LASER BASED ISOTOPE-SELECTIVE PHOTOIONIZATION STUDIES ON LITHIUM

Homi Bhabha National Institute

Recommendations of the Viva Voce Board

As members of the viva voce board, we certify that we have read the dissertation prepared by Vinod Kumar Saini entitled **"Laser Based Isotope-Selective Photoionization Studies on Lithium"** and recommend that it may be accepted as fulfilling the dissertation requirement for the degree of Doctor of Philosophy.

Chairman – **Prof. J. A. Chakera**		Date: 23/06/2020
Guide/ Convener – **Prof. S. K. Dixit**	S.K. Dixit	Date: 23/6/2020
Examiner - **Prof. K. N. Uttam**	KNUttam	Date: 23/6/2020
Member 1 - **Prof. S. R. Mishra**	SRMishra	Date: 23/6/2020
Member 2 - **Prof. S. K. Majumder**		Date: 23/6/2020
Member 3 – **Prof. S. G. Nakhate**		Date: 23/06/2020

Final approval and acceptance of this dissertation is contingent upon the candidate's submission of the final copies of the dissertation to HBNI.

I hereby certify that I have read this dissertation prepared under my direction and recommend that it may be accepted as fulfilling the dissertation requirement.

Date: 23/06/2020

Place: RRCAT, Indore

S.K. Dixit

Prof. S. K. Dixit (Guide)

CONTENTS

Chapter 5: Studies on Selective Li Photoionization using Thermionic Diode Detector 141-173

Chapter 6: Isotope Selective Photoionization of Li using TOF Mass-spectrometer 175-215

Chapter 7

Summary and Future Scope

7.1 Summary

In the present thesis, a systematic and comprehensive study on laser based isotope-selective photoionization of lithium is carried out using three different kinds of atomic vapour sources and ion-detectors such as hollow cathode discharge lamp, thermionic diode and the time-of-flight mass-spectrometer. Most of the sub systems, i.e. lasers, atomic vapour sources, detection and data acquisition systems are developed as the part of research work. The research work is followed in chronological order with the inputs obtained from one step, is utilized to facilitate the next step.

In the first step, the tunable pulsed dye lasers pumped by the copper vapour lasers and nitrogen laser are developed and characterized for Li photoionization studies at high and low repetition rate, respectively. Dye laser wavelength calibration and suitable schemes for Li photoionization studies have been carried out in a test setup based on OG effect in HC lamp. In the first study, it is established that hollow cathode lamp is very convenient, cost effective and suitable device for selective photoionization studies on lithium. The developed Li HC lamp has the features of being demountable, see-through, large bore size, adjustable low gas pressure and capability to operate upto high current of 75 mA. The design, construction, assembly and electrical/optical characterization of the developed Li HC lamp are presented in detail. The designed HC lamp provided wide positive resistance region found suitable for discharge oscillations free OG spectroscopy. This enabled the stable operation of developed HC lamp for large operational currents and over large fill gas pressure range. High resolution and high signal to noise ratio (Li/Ne) OG signals have been obtained in HC lamp with optimized hollow cathode parameters. An OG line recorded in the vicinity of 670.80 nm, assigned to Li ($^2S_{1/2} \rightarrow {}^2P_{1/2,3/2}$) transitions, is fairly resolved for its two close by fine structure lines. The HC lamp generated an accurate and rich OG resonance spectrum of Li and Ne lines over full wavelength tuning range (627 - 676 nm) of the dye laser used. Many transitions of buffer gas (Ne) are clearly detected by OG effect which were not even observed through its recorded emission spectra, These OG spectrum transition lines with high accuracy measured upto ~ 0.33 cm^{-1}, provided a quick and easy means of wavelength calibration for scanning dye laser with precision at atomic levels. Time resolved (Li/Ne) OG signals were also recorded and analysed. Next, the Doppler limited OG spectroscopy of Li in HC lamp is carried out to study the Doppler broadening effects in OG signal. Doppler limited OG spectrum clearly resolved the isotopic Li (D_1 & D_2) lines which is used to estimate Doppler broadening (~3.5 GHz) effects and gas temperature (~ 845 ^{0}K) in HC lamp. High resolution Doppler free saturation absorption spectroscopy (SAS) of Li is also carried out to measure the hyperfine structure splitting and isotope-shift at ~ 670.80 nm using single mode CW ring dye laser at linewidth < 10 MHz. Four hyperfine components of ^{7}Li D_1 and D_2 lines and two hyperfine components of ^{6}Li D_1 line are clearly resolved. The hyperfine splitting of ground ($^2S_{1/2}$) state measured as 800 ± 10 MHz for ^{7}Li (D_1 & D_2), and 227 ± 10 MHz for ^{6}Li (D_1) are found in close agreement with literature reported data. The isotopic shift for D_1 lines of ^{6,7}Li is also measured experimentally and found as 10540 ± 12 MHz. The above studies carried out in developed HC lamp provided the essential and valuable data in advance. Later on, this was used in the study of Li isotope-selective photoionization.

Further, in an innovative approach, large dark space width of the developed Li HC lamp is utilized for studies on two-step selective photoionization of Li atoms. High electric field present in dark space region is utilized for the photoionization of selectively laser excited Li isotopes. It is a first study of its kind in HC lamp. This study deals with Li isotopes, their fine structure energy levels and the measurement of photoionization cross-section. This study concluded that HC lamp with relatively large dark space width (~1.6 mm), exhibiting high electric field (~3 kV/cm), acts as a laser ion-source cum detector for investigation of efficient energy pathway $[{}^2S_{1/2} \rightarrow {\sim}\,\underline{671\text{ nm}} \rightarrow {}^2P_{1/2,3/2} \rightarrow \underline{{\sim}337\text{ nm}} \rightarrow \text{Li}^+\ ({}^1S_0)]$ for Li photoionization. The strong photoionization signals measured with reasonably good SNR ~14 establishes the sensitivity of HC lamp as a photo-electron/ions detector. Further, photoionization cross-section and atom density of ^{7}Li measured as ($\sigma = 18.5 \pm 2.4$ Mb) and ($N_0 \sim 1.7 \times 10^9$ atoms/cm^{-3}), respectively for ($2p\,^2P_{3/2}$) excited state is an excellent outcome of this experiment. In another research study, three-step Li photoionization scheme, with first and second steps through selective excitation followed by a third non-resonant/collisional ionization is explored by OG method. This study is carried out in the negative glow region of hollow cathode discharge with optimized ionization pathway, ($0 \rightarrow 14904$ cm^{-1}) at 670.8 nm, ($14904 \rightarrow 31283$ cm^{-1}) at 610.4 nm and ($31283 \rightarrow > 43487.11$ cm^{-1}) for 610.4 nm. Later on, the same scheme was implemented in TOF mass-spectrometer based Li isotope-selective photoionization experiment.

The Li selective photoionization studies have also been carried out by another complimentary route by employing thermionic diode based atomic vapour source cum detector setup. Thermionic diodes are basically the high gain ion-detectors as compared to HC lamps. The diode operated in space charge limited region enables the high detection sensitivity for the excited atoms, particularly lying in higher excited states. Therefore, a long thermionic diode with built in ion-detection is developed for Li photoionization spectroscopy. The design, construction, assembly and electrical/optical characterization of the developed thermionic diode are presented in detail. Its large gain ($\sim 10^4$) enabled the high SNR ($\sim 10^6$) detection of photoionization signal for two-photon excitation ($2s\,^2S_{1/2} \rightarrow 3d\,^2D_{5/2}$) of Li even for its small absorption cross-section. For two-photon excitation and ionization at 639.145 nm, the measured value of photoionization cross-section ($\sigma = 7.8 \pm 1.6$ Mb) of Li near its first ionization threshold agree well with that published earlier. One more study in thermionic diode is carried out to measure the photoionization cross-section of Li (2p, 3d) excited states corresponding to single-photon excitation ($^2S_{1/2} \rightarrow {}^2P_{1/2,3/2}$) at 670.780 nm and two-photon excitation ($^2S_{1/2} \rightarrow {}^2D_{3/2,5/2}$) at 639.145 nm followed by non-resonant ionization at 337.1 nm radiation. The experimental results are compared with two-step model calculations of photoionization signal saturation curve. The photoionization cross-section (σ) determined for both the states Li ($^2P_{1/2}$, $^2D_{5/2}$) are as 15.40 ± 2.8 Mb and 8.04 ± 1.6 Mb, respectively. These are in close agreement with reported data obtained by other methods. The device enabled high SNR photoionization signals for both the photon excitation schemes. The study concluded that for investigation of the efficient energy pathways for Li photoionization, the thermionic diode based ion-detector is a simple, sensitive and cost-effective device.

After generating required data on Li spectroscopy in HC lamp and on different photoionization schemes in thermionic diode and HC lamp, more advanced atomic beam based mass-spectrometry system is setup for further studies. The in-house built linear time of flight mass-spectrometer (TOFMS) is used for isotope-selective photoionization studies to measure the Li natural isotope ratio, photoionization cross-section and enrichment of its isotopes. Basically, two important experiments are carried out using mass-spectrometry setup. First, the laser assisted isotope separation of Li by two-step photoionization. Second, the laser based enrichment of Li isotopes by three-color photoionization. First experiment is dedicated to measure the relative natural abundance of Li isotopes, to measure accurately their photoionization cross-section and to separate the isotopes using simplest two-step photoionization approach. Measured natural isotopic abundance (^{6}Li / ^{7}Li $\approx$ 0.080) and their photoionization cross-sections for 2p excited state, ^{6}Li (15.53 ± 2.1 Mb), ^{7}Li (18.62 ± 2.4 Mb) closely matched with reported values obtained with other methods. This experiment uses the low repetition rate pulsed tunable dye laser pumped by the nitrogen laser. It is found that abundance of ^{6}Li is enhanced from 7.5 % to over 72 %. This results from precise tuning of dye laser wavelength around ^{6}Li (${}^2S_{1/2} \rightarrow {}^2P_{1/2}$) resonance level. The chosen photoionization pathway $[{}^2S_{1/2} \rightarrow \underline{\sim 671\ \text{nm}} \rightarrow {}^2P_{1/2,3/2} \rightarrow \underline{\sim 337\ \text{nm}} \rightarrow {}^1S_0\ (Li^+)]$ offered large (~10 folds) enhancement in ^{6}Li isotope abundance with high (~ 32) selectivity. Further three-step, three-color Li photoionization scheme is studied with TOFMS. In this scheme, two narrowband pulsed dye lasers are used for successive step-wise first and second resonant excitations of the Li atoms via single photon transitions. These dye lasers are pumped by copper vapour laser master-oscillator power-amplifier (CVL-MOPA) with pulse repetition frequency of 6.5 kHz. A part of CVL-MOPA output (λ~ 578 nm) is utilized for non-resonant third-step photoionization of Li atoms from its excited state. Using this scheme, ^{6}Li concentration is enhanced up to 92% on the TOFMS detector by employing ionization pathway $[{}^2S_{1/2} \rightarrow \underline{\sim 671\ \text{nm}} \rightarrow {}^2P_{1/2,3/2} \rightarrow \underline{\sim 610\ \text{nm}} \rightarrow {}^2D_{3/2,5/2}\ \underline{\sim 578\ \text{nm}} \rightarrow {}^1S_0\ (Li^+)]$. The selected scheme resulted into high photoionization yield, very large enhancement in isotope abundance (> 12 folds) and very high selectivity (S ~ 164). Similarly, by tuning the dye laser wavelengths corresponding to ^{7}Li transitions, very high selectivity leading to (~100%) enrichment in ^{7}Li abundance is obtained. Hence, isotope separation of Li with high enrichment, demonstrated at signal level, by isotope-selective laser photoionization method, is an excellent outcome of detailed and systematic research studies, pursued in the present thesis work.

The abridged summary of the present thesis, titled "Laser Based Isotope-Selective Photoionization on Lithium" is as follows;

- Lithium HC lamp, thermionic diode, dye lasers and associated instrumentation & data acquisition system are developed as the part of present research work.
- Dye laser wavelength calibration, Li atom energy levels, fine/hyperfine structure and isotopic shift are studied in HC lamp.
- Two-step and three-step isotope-selective Li photo-ionization schemes are studied.

- Photoionization cross-section is measured for different excited states of lithium.
- Isotope selectivity and purity are studied, in two-step and three-step photoionization schemes, using in-house built time-of-flight mass-spectrometer.
- High enrichment of the isotopes ^{6}Li (7.5% → 92%) and ^{7}Li (92.5% → ~ 100%) at TOFMS detector is demonstrated by optimized laser photoionization scheme.
- As an outcome of the present research work, a facility is developed for the study of laser based isotope separation processes of different elements.

7.2 Future scope

The future scope is to increase the yield of selected Li isotopes in laser based isotope separation (LIS) method. This will involve still higher repetition rate and higher average power tunable lasers. These are well within the reach of currently available laser technology. The LIS efficiency can be further improved by employing the multi-pass atomic beam source with optimized engineering system design. On the research side, for higher yield and better enrichment, the more efficient photoionization schemes especially targeting auto-ionization levels could be explored using improved design of HC lamp and thermionic diode. In the process side, suitable technique has to be implemented to collect the enriched isotope and then to extract it in the useful form. Future scope of the work, is to utilize the established process and the facility to enrich ^{6}Li isotope in appreciable quantity and finally, to utilize it for several device developments including solid state compact & efficient neutron detector. The developed facility is in ready position to study the isotope separation of other elements especially useful for medical applications which need to be pursued.

STATEMENT BY AUTHOR

This dissertation has been submitted in partial fulfillment of requirements for an advanced degree at Homi Bhabha National Institute (HBNI) and is deposited in the Library to be made available to borrowers under rules of the HBNI.

Brief quotations from this dissertation are allowable without special permission, provided that accurate acknowledgement of source is made. Requests for permission for extended quotation from or reproduction of this manuscript in whole or in part may be granted by the Competent Authority of HBNI when in his or her judgment the proposed use of the material is in the interests of scholarship. In all other instances, however, permission must be obtained from the author.

Vinod Kumar Saini

DECLARATION

I, hereby declare that the investigation presented in the thesis has been carried out by me. The work is original and has not been submitted earlier as a whole or in part for a degree / diploma at this or any other Institution / University.

VKSaini
Vinod Kumar Saini

List of Publications arising from the thesis

Journal

1. "Laser isotope separation scheme of lithium by three-color photoionization", **V. K. Saini**, S. Talwar, V. V. V. Subrahmanyam, R. K. Mishra, P. K. Saini, and S. K. Dixit, *Physica Scripta,* **(2020)**, 95, 075403 (10pp).

2. "Laser assisted isotope separation of lithium by two-step photoionization using time of flight mass-spectrometer", **V. K. Saini**, S. Talwar, V. V. V. Subrahmanyam, and S. K. Dixit, *Optics and Laser Technology,* **(2019)**, 111, 754-761.

3. "Measurement of photoionization cross-section of Li (2p, 3d) excited states using thermionic diode detector", **V. K. Saini**, P. Kumar, V. V. V. Subrahmanyam, and S. K. Dixit, *Jour. of Quantitative Spectroscopy & Radiative Transfer,* **(2019)**, 224, 361-367.

4. "Development of a thermionic diode detector for laser spectroscopy", **V. K. Saini,** P. Kumar, S. Shaikh, and S. K. Dixit, *Measurement Science and Technology,* **(2019),** 30, 065501 (10pp).

5. "Selective photoionization of lithium isotopes in hollow cathode lamp: A feasibility study for laser ion source and detector", **V. K. Saini**, A. Kak, S. K. Dixit, *Applied Optics,* **(2018)**, 57, 6808-6816.

6. "Development of a see-through hollow cathode discharge lamp for (Li/Ne) optogalvanic studies", **V. K. Saini**, P. Kumar, K. K. Sarangpani, S. K. Dixit, and S. V. Nakhe, *Review of Scientific Instruments,* **(2017)**, 88, 093101 (9pp).

7. "Saturation absorption spectroscopy of lithium in hollow cathode discharge lamp", P. Kumar, **V. K. Saini**, G. S. Purbia, O. Prakash, S. K. Dixit, and S. V. Nakhe, *Advanced Science Letters,* **(2015)**, 21, 2548-2550.

8. “Studies on pulsed and CW optogalvanic effects in the in-house developed see-through lithium hollow cathode lamp”, **V. K. Saini**, P. Kumar, K. K. Sarangpani, S. K. Dixit, A. Lala, and S. V. Nakhe, *Advanced Science Letters,* **(2015)**, 21, 2609-2612.

9. “Studies on pulsed OG effect in Eu/Ne hollow cathode discharge”, **V. K. Saini**, P. Kumar, S. K. Dixit, and S. V. Nakhe, *Applied Optics,* **(2014)**, 53, 4320-4326.

Conferences

1. “Two-step photoionization studies of lithium using thermionic diode”, **V. K. Saini**, Krishna Kumar, and S. K. Dixit, *DAE-BRNS, National Laser Symposium (NLS-28), VIT Chennai,* Jan., 8-11, **2020,** (CP-09-02).

2. “Development of a heat-pipe for laser spectroscopy”, **V. K. Saini**, C. T. Sreerag, S. Saleem, R. Khare, and S. K. Dixit, *DAE-BRNS, National Laser Symposium (NLS-27), RRCAT Indore, India*, Dec., 3-6, **2018**, p. 131.

3. “Studies on laser induced selective isotopes photoionization of lithium using in-house developed time of flight mass-spectrometer”, **V. K. Saini**, S. Talwar, K. K. Sarangpani, and S. K. Dixit, *DAE-BRNS, National Laser Symposium (NLS-26), (BARC) Mumbai, India,* Dec., 20-23, **2017**, p. 103.

4. “Development of compact and versatile hollow cathode lamp for Li optogalvanic studies”, **V. K. Saini**, P. Kumar, K. K. Sarangpani, S. K. Dixit, A. Lala, and S. V. Nakhe, *DAE-BRNS, National Laser Symposium (NLS-22), MIT Manipal*, Jan., 8-11, **2014**, p. 1-4.

VSaini

Vinod Kumar Saini

DEDICATIONS

Dedicated to my parents

ACKNOWLEDGEMENTS

I thank the *almighty God* who inspired and enabled me to complete this research work.

It is a matter of great pleasure for me to express my sincere gratitude to all those who have contributed to this work, directly or indirectly. First of all, I express my deep gratitude towards my Ph.D. guide *Dr. S.K. Dixit*, for his invaluable guidance throughout the execution of research work as well as support in shaping the thesis.

I thank *Director, RRCAT* for permitting me to pursue Ph.D. in HBNI. I also thank the members of present Ph.D. doctoral committee (*Dr. J.A. Chakera, Dr. S.R. Mishra, Dr. S.K. Majumder and Dr. S.G. Nakhate*) as well as the past doctoral committee members (*Dr. S.M. Oak, Dr. P.A. Naik, Dr. G.S. Lodha, Dr. H.S. Rawat, Dr. K.S. Bindra, Dr. Anand Moorti, Dr. P.K. Mukhopadhyay, Dr. Aparna Charabarti, Dr. S.M. Gupta, Dr. C. Mukherjee and Dr. Vas Dev*) for their valuable suggestions for improving the quality of research work. I would like to extend my warm gratitude to *Shri. S.V. Nakhe*, Director, Laser and material science group for his constant motivation and support.

I am thankful to *Dr. R. Khare* and *Dr. Om Prakash* for fruitful scientific and technical discussions on the critical issues in CVL, dye laser and optogalvanic studies.

I am deeply grateful to *Sandeep Talwar*, *P. K. Saini*, *R. K. Mishra, C. T. Sreerag* and *Krishna Kumar* for their valuable technical and practical support.

I am thankful to *Dr. Jitendra Kumar, Dr. R. Mahakud, V.V.V. Subrahmanyam, G.N. Tiwari, A. Mokhariwale, Praveen Agrawal, Sachin Agrawal*, *U. Kumbhkar, L. Chandravanshi*, *C.S. Mandloi* and *V.K. Shrivastava* for helping in execution of the research work in different ways.

I acknowledge the support of *Optical Design Lab, Optical Coatings Lab, Chemical Treatment Lab, Mechanical Components Design & Fabrication Lab and Glass Blowing Facility* for fabrication of optical and mechanical components.

I also take this opportunity to thank all *my friends, relatives and well-wishers* for their invaluable moral support during this long journey.

Last but not the least, I express my deep appreciation for *my wife Anita and kids, Aditya & Vidushi* for their understandings, patience, whole-hearted support and co-operation.

Vinod Kumar Saini

Chapter 1

Introduction

1.0 Motivation

Isotopes of different elements find important applications in medical, agriculture, biotechnology and nuclear industries. As most of the elements in their natural form are found as a mixture of the two or more isotopes, therefore separation/enrichment of the isotopes is of prime importance for their wide applications. Laser based isotopic-selective photoionization is a well proven process for separation and enrichment of the desired isotope. Laser isotope separation (LIS) technique has a number of advantages such as highly selective separation, high purity isotope, short start up time and single-stage production with low energy consumption and cost effectiveness. This is in contrast with non-laser based traditional isotope separation technologies such as chemical, electromagnetic, gas diffusion and gas centrifuge. These methods suffer from small isotope separation factor per stage, thus requiring a large cascaded multi-stage operation. These are also of huge size, inefficient, prone to contamination, very costly and produce isotopes of limited purity. Hence, the laser isotope separation (LIS) remains a highly active research area which is continually being upgraded with advancement of laser technology and process modalities. Since LIS research is element specific, different types of laser, different types of spectroscopies, associated tools and different strategies need to be adapted for different elements. In particular, studying the LIS process for alkali metal lithium (Li) with only two stable isotopes ^{6}Li and ^{7}Li with natural isotopic abundance of 7.5% and 92.5% respectively, is highly rewarding both for understanding the key physics involved and the potential applications of these isotopes in nuclear industry. Element wise, Li represent an ideal system to be studied for LIS due to its non-radioactive & non-toxic nature, manageable low melting point (~ 180 ^{0}C), moderate ionization potential (~ 5.4 eV), the large isotopic shift (~ 10 GHz @ 671 nm) and readily available laser system at different wavelengths to pursue the Li photoionization spectroscopy. In applications, both Li isotopes are important for peaceful programs of nuclear industry either in fission or fusion reactors to generate the clean electric power. Nuclear fusion reactors are the futuristic source of unlimited energy for next generation. In fusion process, the isotopes of hydrogen namely deuterium (D) and tritium (T) are forced to combine at appropriate pressure and temperature conditions to subsequently release vast amount of energy. Deuterium, a stable isotope of hydrogen, is abundant in sea water and can be easily recovered. On the other hand, tritium, a radioactive isotope, exists scarcely in nature and found in trace amounts because of its short half-life (12.3 years). Tritium is most commonly produced, in situ, by bombardment of neutrons on Li by Li (n, α) T reaction in fusion reactor. Among the Li isotopes, the productivity of ^{6}Li (n, α) T process is much higher than that of ^{7}Li (n, α) T due to much larger thermal neutron absorption cross section (~ 940 barns) of ^{6}Li as compared to ^{7}Li (~ 45 mili barns). Highly enriched ^{6}Li well above its natural abundance is essential to breed adequate quantity of tritium in fusion reactors with high breeding ratio (TBR > 1) for D-T reaction [1]. The enriched ^{6}Li is also useful in development of compact solid state neutron detectors and finds possible applications in strategic projects to develop thermonuclear weapons. Also enriched ^{7}Li, devoid of highly neutron absorbing ^{6}Li, finds important utilization in molten salt (lithium fluoride) and pressurized water nuclear fission reactors [2]. Thus, the separation/enrichment of both the ^{6}Li and ^{7}Li isotopes is a very relevant research topic.

For separation of Li isotopes, the methods based on isotopes mass difference such as gas diffusion and gas centrifuge are not very practical due to light weight and very small difference in mass of ^{6}Li and ^{7}Li. The mercury-amalgam method of Li isotope separation is the only technology in practical use that can produce the enriched ^{6}Li on industrial scale.

However large amount of toxic mercury used and small isotope separation factor are big issues in the process [3]. There are other chemical methods of Li isotope separation such as membrane separation [4], electro-migration [5], solvent extraction [6] etc. Recently, enrichment of Li isotopes by electrochemical pumping using Li solid electrolyte is reported [7]. All these methods, more or less, suffer by small isotope separation factor per stage. These existing methods can not economically separate more than about 65% of the desired isotope from naturally occurring isotopes. The remaining 35% is left in tails. Therefore, a method of lithium isotope separation with high enrichment factor, less warmup time, free of toxic materials and environment friendly is important. This demand motivates the study on laser based techniques for separation and enrichment of Li isotopes.

1.1 Objectives and strategy to attain the goals of research problem

In the present thesis, atomic vapor laser isotope separation (AVLIS) process is adopted to study the LIS of Li isotopes. The isotope separation by laser method differs fundamentally from other existing methods. It distinguishes between the different isotopes of an atom (same number of protons and electrons but different number of neutrons) not on the basis of mass difference but through precise differences in their electronic structures. This results in different atomic transition frequencies. Although, these differences are small, still they affect wavelength of light absorbed by the atoms. Each isotope absorbs the light of slightly different wavelength. As the laser light is highly monochromatic and has wavelength tunablity, it can selectively excite the energy level transitions of one isotope leaving all others unexcited. The absorbed photon induces the change in electronic configuration of atom and a valence electron is promoted to higher energy state further away from nucleus. The atom is then in excited state. The electron can be raised to higher energy levels by additional photons of appropriate energy. The atom ultimately gets ionized when electron detaches from it. The ionization can be regarded as continuum of free energy states. Selective excitation/photoionization of atoms is the most universal method for separation of the isotopes. For selective photoionization, all the schemes consist of two steps, (1) isotope selective excitation and (2) ionization of the excited atoms. Two-step schemes are relatively simple. Three-step scheme can be used either for atoms with high ionization potential or to increase the selectivity of process. The small photoionization cross-section can be enhanced by tuning the radiation wavelength of last-step to the auto-ionizing states, if present. Lithium is an element with relatively simple electronic structure. Hence Li is an ideal system for detailed understanding of important physics on the photoionization process and measurement of related important spectroscopic parameters. The photoionization cross-section of Li is a crucial parameter for investigating the astrophysical plasma also, as Li is present in solar-type stars. Besides, Li has applications in area such as in laser development and in thermonuclear plasma. Hence, the objective of thesis work, to study the isotope-selective photoionization of Li using different ionization pathways leading to separation/enrichment of its isotopes by laser method, is relevant and justified.

The present research work involves tunable lasers, hollow cathode lamp, thermionic diode ion-detector and time-of-flight mass-spectrometer (TOFMS) for studying different photoionization pathways of Li isotopes, measurement of photo-ionization cross-section & ionization yield and enhancement in Li isotopes abundance. Since most of these systems, required for Li photoionization spectroscopy are either not available commercially or available at exorbitant cost, therefore a strategy is adopted to develop most of these sub systems as the part of present research work. The basic working principle as well as development and characterization of these systems with a pointed aim of pursuing isotopic-selective photoionization studies on Li, are detailed in various chapters of the thesis. Also as a plan of work, Li spectroscopy is first carried out in Li hollow cathode (HC) lamp and thermionic diode to validate the experimental setups, to calibrate the dye laser wavelength, to estimate the laser energy requirements, and to measure the spectroscopic data of Li such as atomic energy levels, fine/hyperfine structures, isotope-shift and photoionization cross-section. Finally the data and the excitation/photoionization schemes, explored with these devices, are implemented in an atomic beam based time-of-flight mass-spectrometer photoionization setup to demonstrate the high enrichment of ^{6}Li and ^{7}Li with high isotope selectivity as detailed in thesis.

1.2 Spectroscopy techniques

1.2.1 Optogalvanic spectroscopy

Optogalvanic (OG) spectroscopy is one of the simplest, economical and sensitive technique for laser spectroscopy of atoms and molecules. It is based on optogalvanic effect detected by Penning [8] first time. It has been extensively used in the spectroscopic studies for investigation of finger prints of molecular, atomic and ionic species in gaseous discharge [9-12]. In OG process, photon induces the change in plasma impedance of discharge medium. This happens when electromagnetic radiation is frequency tuned to the atomic transitions of the species present. The optogalvanic effect originates by laser induced change in population of atomic states (Δn) coupled by laser radiation. The medium undergoes collisional ionization with energetic discharge electrons. This causes, the change in total ionization rate. As a result the impedance of plasma or discharge, changes. This can be recorded as an optogalvanic signal. The signal polarity, either positive or negative, depends upon the energy levels $E_i \rightarrow E_k$ coupled by the laser. If IP (E_i) and IP (E_k) denotes probability of ionization of an atom in E_i and E_k levels respectively, then voltage ΔV (OG signal) induced, is given by

$$\Delta V = R\Delta I = a\,[\Delta n_i\, IP\,(E_i) - \Delta n_k\, IP\,(E_k)] \tag{1.1}$$

There are mainly three processes as listed below which contribute to the ionization of an atom 'A' from an energy level E_i;

(i) Ionization by impact of the electrons,

$$A(E_i) + e^- \rightarrow A^+ + 2\ e^- \tag{1.2}$$

(ii) Collisional ionization by metastable atoms (B),

$$A(E_i) + B^* \rightarrow A^+ + B + e^- \tag{1.3}$$

This process is very effective when E_i is a highly excited state.

(iii) Direct photoionization by laser photons,

$$A(E_i) + h\nu \rightarrow A^+ + e^- \tag{1.4}$$

HC lamps are the miniature atomic vapor source as well as can serve as a sensitive detector for OG spectroscopy [9]. The geometry of HC lamp, due to its high operational current density promotes the oscillations of hot electrons inside HC. This enhances the ionization, ion bombardment and other processes. Numerous theories and mathematical expressions have been developed to understand and quantify the OG effect in HC discharge [13-15]. No agreement is there to accept any one as a unified theory for complete description of all the process in HC discharge. However, a phenomenological approach based on ionization mechanism is widely accepted. Basically, there are two principal mechanisms which can explain the change in impedance of HC discharge upon illumination by resonant photons. The first one is based on enhancement in electron-collision induced cross-section as the energy of final state approaches the ionization limit [16]. In cathode dark space region, this mechanism is believed to be dominant, due to high concentration of available energetic electrons. In negative glow region, the second mechanism is thought to be dominant, due to increase in electron temperature of discharge upon irradiation with resonant photons [17]. The OG effect is readily understood under the assumption that atomic system transfers the excitation energy to the electrons. The equilibrium established between electrons and atoms, resulting from repeated elastic and super elastic collisions in HC discharge, makes the electron temperature nearly equal to atomic excitation temperature. Although, incident laser radiation marginally perturbs the process, the electron collisions are so frequent that a substantial change in levels population does not occur. Thus energy of the absorbed photons is simply delivered to the electrons. This additional energy causes the change in discharge impedance. Both the processes, described above, have been proposed to explain the OG effect in different kinds of discharge. Either of the process can govern the generation of OG signal depending upon the discharge environment. In fact, the discharge plasma is very complex and can't be described by any general theoretical model. In the past, sincere efforts have been made in this direction. Some special theoretical models have been proposed for hollow cathode and other kinds of discharge. These models explain the experimental observations nicely in typical discharge conditions. The discharge-plasma produced in HC lamp is suitable for OG spectroscopy by virtue of its low galvanic noise. The advantageous property of HC discharge is the strong electric field in cathode dark space that accelerates the ionic charge towards cathode. This ensues high sputtering yield at moderate discharge current. Thus, the HC discharge can be used as a good source of free atoms for spectroscopy. The HC discharge lamp can generate high atom density even for refractory elements. The HC discharge enables the plasma density of few orders of magnitude higher than in planar electrodes discharge at same input power [18].

1.2.2 Advantages and applications of OG spectroscopy

OG spectroscopy makes the use of electronic detection with fewer electronics instead of costly and special optical detection techniques generally used in fluorescence spectroscopy. The noise current in discharge can be limited practically up to shot noise levels. The noise current is basically a statistical fluctuation of charged particles in discharge medium. In this condition the noise current is given by

$$(I_N)_{rms} = (2eI\Delta v)^{1/2} \quad (1.5)$$

where I is discharge current and Δv the detection bandwidth. With a typical 30 mA HC discharge current, I_N is ~ 1 nA in 1 Hz bandwidth. The OG detection limit for uranium atom is of an order 10^6 atoms/cm^3 while the concentration as small as 10^5 atoms/cm^3 are routinely detected in alkali atoms [19]. These favorable conditions ascertain the usefulness of OG technique in detection of traces of explosives and impurities. Absorption spectroscopy is limited by optical density of the sample to absorb a detectable amount of incident radiation. The OG technique has many important applications other than in atomic and molecular spectroscopy such as in laser frequency stabilization and in plasma spectroscopy. In present thesis, Li HC lamp has been used for dye laser wavelength calibration, investigation of hyper fine structure/isotope shift and to explore suitable Li photoionization pathways by OG method as detailed in chapters-3 & 4.

1.2.3 Saturated absorption spectroscopy

Saturated absorption spectroscopy (SAS) is an excellent classical pump-probe method used in experimental physics. The technique overcomes the problem of Doppler broadening without cooling down the sample to very low (mili-kelvin) temperatures. In fact, it is a modified form of absorption spectroscopy which is capable of resolving the fine/hyperfine features of atomic transitions that normal absorption spectroscopy can't do. This technique can be used to measure the fine/hyperfine structures and isotopic shift of atomic species present in a HC lamp. In SAS setups, a relatively high intensity laser beam known as the pump, is sent through the atomic vapors. Another weak beam, called the probe, is also sent in counter-propagating direction through the atoms at same frequency. The probe beam intensity is recorded for various frequencies using a photodiode. Both the beams, despite being at same frequency, address the different velocity group of atoms due to their thermal motions. Reddetuned laser beam will be absorbed by atoms moving towards the source. The opposite is applicable for blue-tuned laser. In both the cases, the probe beam will be absorbed by the atoms moving away in opposite direction.

For laser beam, close to resonance with atomic transition, both the beams would address the same velocity group of atoms. These are the atoms having velocity vectors perpendicular in direction to laser propagation. Strong pump beam would move many of atoms to be in excited state. A transition is said to be saturated when number of atoms in ground state and excited state are approximately equal. As the probe laser frequency sweeps the resonance, absorption dips would occur. These are hyperfine resonances. The width and depth of absorption dips is related to the pump beam level. The width of dip can approach the natural line-width of transition. On the system with more than two states, a consequence of this counter-propagating beams method, is the presence of crossover lines. When two transitions share the common ground state within a single Doppler-broadened feature, a crossover peak at a frequency exactly between the two transitions may occur. The crossover peaks can be quite strong. This SAS technique can be utilized for the frequency locking of the lasers.

The SAS studies on Li are carried out in HC lamp and presented in chapter-4.

1.2.4 Resonant ionization spectroscopy (RIS)

In resonant ionization spectroscopy (RIS) methods, an atom or a molecule is selectively excited in steps beyond its ionization potential to form an ion using different wavelengths of the laser radiation [20]. In resonant ionization mass spectrometry, absorption or emission properties of the photons are not important. It is only the resulting ions which are mass-selected and detected [21]. This kind of selective ionization in RIS has excellent potential for isotope separation with number of advantages such as:

1. An electron and/or ion detection is possible with much higher efficiency as compared to detecting photons. Using suitable laser light source, one electron from each atom can be removed that enables high sensitivity to RIS, thereby allowing detection of single atom [22].

2. The elemental selectivity of RIS of atoms is extremely high because of allowed electric dipole transitions involved.

3. If more than one resonant step-wise excitation are induced, the selectivity from each transitions can be multiplied to obtain the total higher selectivity.

4. Overall process selectivity can be enhanced by mass-selective detection of the created ions.

5. The resonance condition met for each excitation steps provides the high elemental as well as isotope selectivity. The isobaric interference, as observed in non-laser mass-spectrometry, is highly reduced. Further, the contamination interference, which is a major issue in conventional methods, can be avoided [23].

6. The effects of background, limited by electrical noise, can be minimized.

1.3 Optical excitation schemes

The electromagnetic radiation interaction with matter is one of the most basic processes in nature. Subject to certain conditions, a part of electromagnetic radiation is absorbed in matter and the process is called as photo-absorption or resonant-excitation. Electromagnetic radiation can be absorbed in any atomic or molecular system through many processes such as single-step, multi-step or multi-photon absorption. In step wise resonance ionization process, a minimum of two steps are used. The first step is a resonance process as illustrated in Fig 1.1. This assures that ionization is not possible unless the laser is tuned to an appropriate wavelength to excite the atoms upto certain high energy states. In continuum, there is no restriction on the energy of free electrons as per quantum mechanics, therefore any photon of minimum threshold energy can be absorbed further to complete the ionization process.

1.3.1 Single-step excitation

In a single-step excitation, the outermost electron of an atom undergoes a transition from initial $|i\rangle$ energy state E_i to another higher $|f\rangle$ discrete energy state E_f due to an absorption of a photon of suitable energy $\hbar\omega_{if}$. In this case,

$$E_f - E_i = \hbar\omega_{if} \tag{1.6}$$

where $\hbar(= h/2\pi)$ is the Planck's constant and ω_{if} the frequency of absorbed photon. Similarly, when an electron jumps from higher to lower energy states, it emits a photon of an energy corresponding to energy difference between the involved states. A simple single-step photo excitation process is shown in Fig 1.1. This process obeys the electric dipole transition selection rules ($\Delta l = \pm 1$, $\Delta S = 0$, and $\Delta J = 0, \pm 1$, $0 \leftrightarrow 0$ forbidden). Here 'l' is orbital angular momentum, '*J*' the total angular momentum and '*S*' multiplicity of the concerned states.

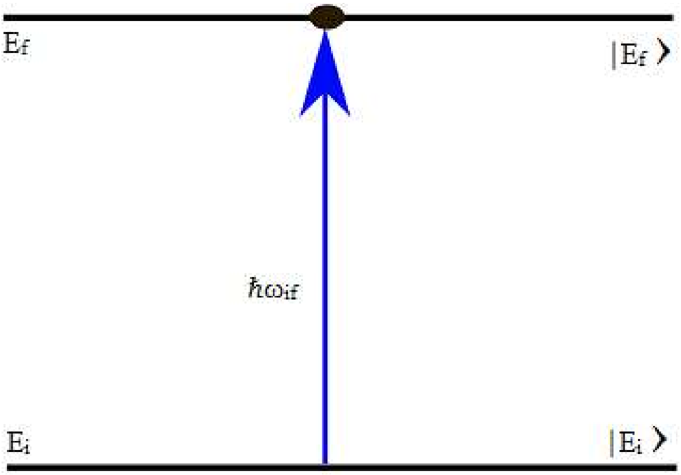

Fig. 1.1 Single-step excitation process

The transition probability per unit time for single-step photo excitation, using the electric dipole approximation [24] is expressed as,

$$P_{if} = \frac{4\,\pi^2}{3\,\eta^2}\frac{\rho(\omega if)}{4\,\pi\,\varepsilon 0}|\langle f\,|er|\,i\rangle|^2 \tag{1.7}$$

Here $\rho(\omega_{if})$ is the radiation density per unit interval of angular frequency (ω). The transition probability depends on the electric dipole matrix element $|\langle f\,|er|\,i\rangle\,|^2$. The initial and the final states must have opposite parity in order to make this term non-zero.

1.3.2 Multi-step excitation

In multi-step photo excitation, an atom sequentially absorbs two or more photons of different frequencies via real intermediate states allowing an electron to make a transition to the states inaccessible by single photon excitation. This technique made it possible to probe the high lying Rydberg states of an atom in VUV region by selecting different intermediate states. The simplest example is the two-step excitation process as shown in Fig. 1.2. In this process, the final atomic state $|\,f\,\rangle$ is reached in two steps via real intermediate $|\,k\,\rangle$ level. In the first step, an electron from initial $|\,i\,\rangle$ state is promoted to an intermediate $|\,k\,\rangle$ level by absorption of a photon of energy $\hbar\omega_1$ and in second step, another photon of energy $\hbar\omega_2$, is absorbed by the electron to attain final state $|\,f\,\rangle$. This process is shown in Fig. 1.2. The excitation from initial $|\,i\,\rangle$ state to final $|\,f\,\rangle$ state through intermediate $|\,k\,\rangle$ state is possible if

$$E_f - E_i = \hbar\,(\omega_1 + \omega_2) \qquad (1.8)$$

Each transition, following this process, obeys the single-photon dipole selection rules as described earlier. The intermediate state possesses an opposite parity to that of the initial and final state. The condition for an effective excitation to final $|f\,\rangle$ state through real intermediate states is that the first-step laser pulse duration must be shorter than the lifetime of intermediate $|\,k\,\rangle$ state and the second-step laser should appear within the lifetime of excited state $|\,k\,\rangle$. This technique needs the two different lasers with an output radiation having the photons of suitable energy for each resonant steps and thus improves the overall selectivity of the process. For the elements those have higher ionization potential, three or four steps scheme are beneficial. Although, the implementation of these are more complex.

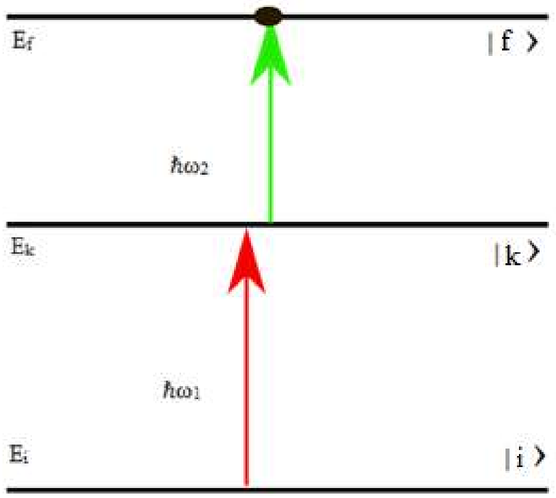

Fig. 1.2 Two-step excitation process

1.3.3 Multi-photon absorption

In 1931, it was theoretically predicted [25] that an atom might absorbs two or more photons simultaneously. Such transitions could practically be observed with the advent of lasers in nineteen-sixties that allows an electron to occupy the energy states inaccessible by a single photon absorption. Since transition probability for such transitions, without intermediate resonance states, is very small, therefore high intensity radiation interacting with atomic system is needed to explore the multiphoton absorption process. The transition probability W_{if} for multi-photon absorption between the energy states | i ⟩ and | f ⟩ can be expressed as,

$$W_{if} = \sigma I^{n} \tag{1.9}$$

Here 'n' is the number of photons involved in the multi-photon absorption, I (watt/cm^2) the radiation intensity and σ (cm^2), the multi-photon absorption cross-section. The first observation of two-photon transitions was observed by Hughes and Grabner in 1950 [26]. The phenomenon attracted much attention on the availability of sufficiently intense light radiation provided by the lasers and opened an area of the multi-photon absorption. The pulsed lasers are most suitable for this process as their peak powers are high. The simplest example of multi-photon absorption is the two photon absorption as shown in Fig 1.3.

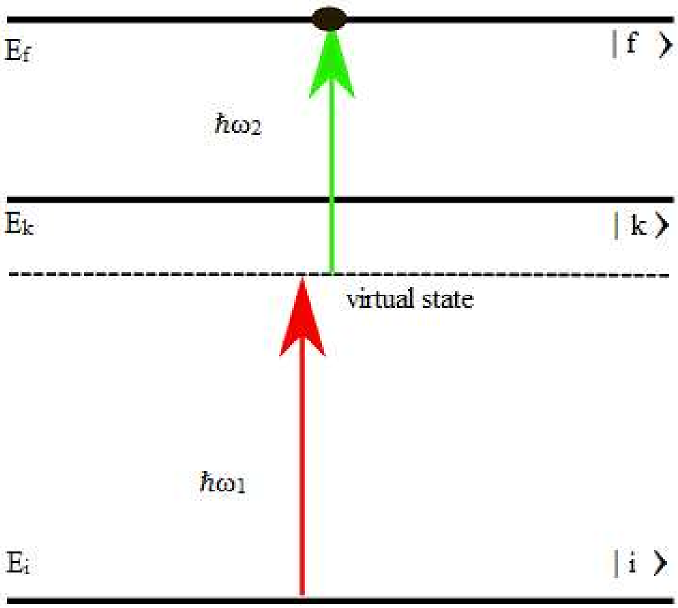

Fig. 1.3 Two-photon absorption process

In this process, two photons are simultaneously absorbed by an atom to undergo a transition between the two levels of same parity via intermediate virtual state. These states do not correspond to any specific ‘n’ or ‘l’ states. These are not the real eigenstates, being merely the superposition of waves and therefore are not populated by the electrons. The two photon absorption process can be expressed as,

$$E_f - E_i = \hbar\,(\omega_1 + \omega_2) \tag{1.10}$$

Here ω_1 and ω_2 are the frequencies of two interacting photons. The two absorbed photons may be of the same or different frequencies. If ω_1 and ω_2 are such that their energy comes close to that of a real intermediate state then the probability of two-photon transition is expected to increase sharply. The selection rules for two-photon process are different from that described earlier for single-photon excitation process. For example, $\Delta l = 0, \pm 2$, $\Delta J = 0, \pm 2$, $\Delta L = 0, \pm 2$ are allowed and $0 \leftrightarrow 0$ transition is forbidden. Transition probability (P_{if}) is given [27] as,

$$P_{if} = I^2 \sum_k \frac{|\langle i\,|er|\,k\rangle\,\langle k\,|er|\,f\rangle|^{\,2}}{(\omega_{ni} - \omega_{ik})^2} \tag{1.11}$$

Where ω_{ni} is the laser frequency. The two-photon process has a number of significant advantages over the conventional single photon excitation. First, the visible light can be used to access the energy states which are lying in UV-region. Secondly, the study of transitions between the states of same parity, for which single photon transitions, are forbidden are possible through two photon process. Another important advantage for obtaining high-resolution data is the minimization of Doppler broadening effects using counter-propagation of laser beams for two photon absorption process. Here the absorption has to occur from two counter-propagating laser beams. This compensates the linear Doppler shift. In the process, very narrow line width Doppler free spectra are obtained. It is advantageous over the other saturation spectroscopy and Doppler free techniques that utilize only a subgroups of velocity atoms to take part in the transition. However, in two photon process all the atoms regardless, their velocity, contribute to the Doppler free transitions.

1.4 Resonance ionization schemes

Fig. 1.4 shows the typical resonance ionization schemes for many elements of research interest. These element group may belong to alkali, alkaline earth, rare earth and actinides. These elements are important in atomic physics, nuclear physics, chemistry and cosmology. The bound atomic states can easily be saturated with continuous wave (CW)/ pulsed laser. This is due to their high optical cross-section ($\sigma = \lambda^2/2\pi$) typically of the order of 10^{-10} cm^2, for resonant transitions. The ionization schemes, such as two or three-step resonant excitation with different colors that cover most of the elements, can be categorize into three basic types. These differ in last step of excitation/ionization. If last step is non-resonant, it usually present a bottleneck to the excitation path due to low photoionization cross-section (σ) of the order of 10^{-17}-10^{-19} cm^2 [20-23]. It can be increased up to four order, by exciting the atoms to Rydberg levels which can further be ionized by applying an electric field (E.F), by collisions with gas molecules or using the photons with wavelength in far-infrared (FIR) range. The larger cross-section of last step transitions provide more efficient ionization of the atoms. Higher cross-section of photoionization can be obtained by tuning the ionizing laser to auto-ionizing states. The feature can be utilized in the lanthanides and actinides elements, due to their high density of auto-ionizing states near the ionization limit.

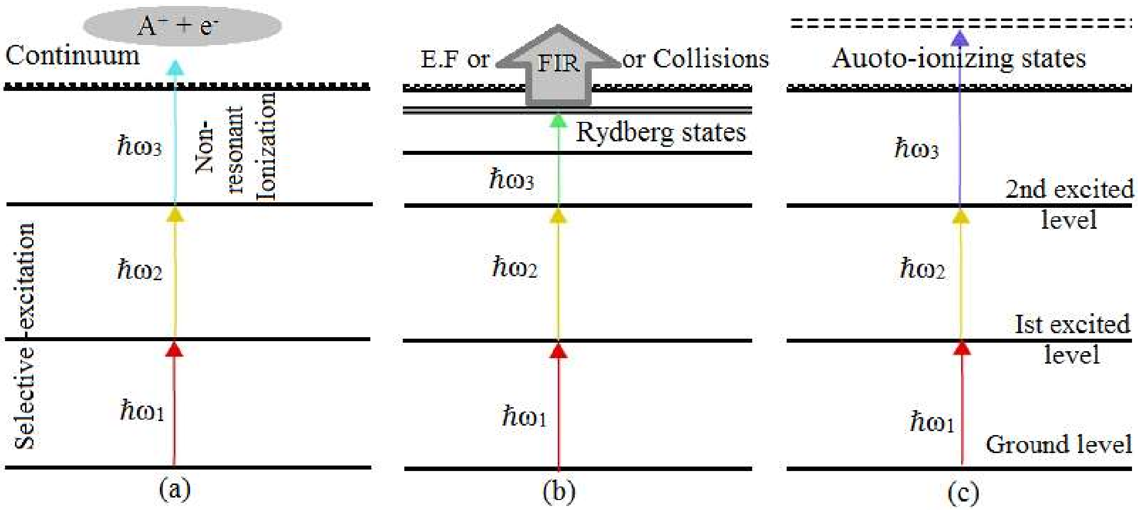

Fig. 1.4 Stepwise resonant ionization techniques: (a) directly to continuum, (b) through Rydberg states, (c) using auto-ionizing states

1.4.1 Classification of ionization schemes

All the possible resonance ionization schemes can be classified by several characteristic features. Few of the important schemes of common interest for a wide variety of applications are as follows;

(1) Two-step ionization in single-frequency field: A [ω_1, ω_1 e^-] A^+, means that in the first step atom ‘A’ can be excited by a photon of frequency ω_1. In the next step, it can be non-resonantly ionized by another photon, giving rise to free electron e^- and positive ion A^+.

(2) Two-step ionization in single-frequency field: A [$2\omega_1$, ω_1 e^-] A^+, indicates that an atom 'A' in its ground state can be excited by two-photon absorption with only one excitation stage being resonant.

(3) Three-step ionization in two-frequency field: A [ω_1, ω_2, ω e^-] A^+, with only two excitation stages being resonant. Third step with frequency 'ω' be non-resonant.

(4) Three-step ionization in two-frequency field: A [$2\omega_1$, ω_2, ω e^-] A^+, with the first (two photon) and second (one photon) excitation stages being resonant.

(5) Two-step ionization in single-frequency field: A [$\omega_1\omega_1$, ω e^-] A^+, note that notation 'ω_1 ω_1' is to designate the two-photon resonance.

In process (5), two-photon allowed transition is driven at frequency ω_1 to a level which is photo-ionized non-resonantly by a photon of same or different frequency. Figure 1.5 show the general schemes. Now, we can address the issues of photoionization scheme and decide, which one is better for an element of interest. It is the energy levels spacing of an atom that determines suitable scheme because lasers operation is restricted to certain specific wavelengths. The characteristics of an atom that guide the type of laser required, are the ionization potential, different energy levels of an atom and whether these are accessible by single or two-photon transitions. These details with other essential specifications of lasers e.g. peak power, pulse energy, pulse duration and beam quality (divergence and coherence) should be taken into account to finalize the schemes. The five basic schemes ordered roughly according to their complexity (Fig. 1.5), are suitable to nearly all the elements of periodic table. The criteria used in finding the simplest RIS scheme is as; 1) the tunable dye lasers should have sufficient power to saturate the photoionization process, 2) their output radiation should lies in 380-750 nm (i.e. 3.25-1.65 eV) range. For the specific elements, those have strong transitions in UV range, the dye lasers can be frequency doubled as, 217-360 nm (i.e. 5.71-3.44 eV). Higher the order of scheme, more is the complexity in process.

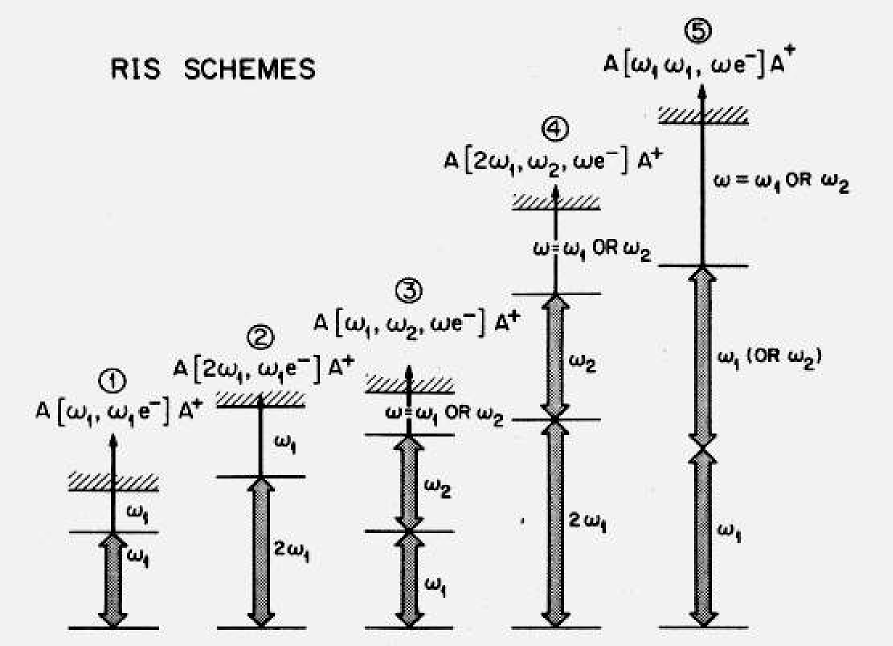

Fig. 1.5 Classification of RIS schemes (Ref. 23)

Schemes ‘1’ & ‘2’ is the simplest and require only one laser, but in scheme ‘2’ frequency doubled laser output is also required. In schemes ‘3’ & ‘4’, two lasers can be used; that involve an additional requirement of time and space coincidence. Two -photon transitions can be utilized where single photon transitions are prohibited. For such applications that involve the scheme ‘5’, the first and higher energy state transitions may involve the photons obtained by doubling, re-doubling, and mixing of the fundamental wavelength.

1.5 Atomic energy levels, width and profile of spectral lines

1.5.1 Decay of excited states

In spectroscopic studies, to deal with observed spectral lines, it is essential to understand their evolution, width and profile. Let us consider a group of atoms lying in the ground state at room temperature. If energy is supplied to the atoms in any form such as through particle collisions, electric current or absorbed light, then the outer electrons those with the highest quantum number are pumped to the excited energy states. These excited electrons eventually decay back down to the ground or lower state when the energy or pumping source is removed as shown in Fig 1.6. After excitation, population density 'N_u' in upper level 'u' decays exponentially. The population is transferred to lower energy levels which could be the ground or other 'N_l' low lying energy levels. In simplest case, lower level is the ground state. If excited state population (N_u) is low enough and none of excited atoms collide during the decaying process, then only the way to energy loss ($\Delta E_{ul} = E_u - E_l$), is a radiation, emitted during the decay process provided energy and momentum remain conserved. The radiative decay is referred to as spontaneous emission, since it is a natural process that occurs without any external stimulus. The population decay rate can be expressed by simple equation as;

$$dN_u/dt = -A_{ul}N_u \tag{1.12}$$

A_{ul} is the rate of population being transferred and referred to as the transition probability.

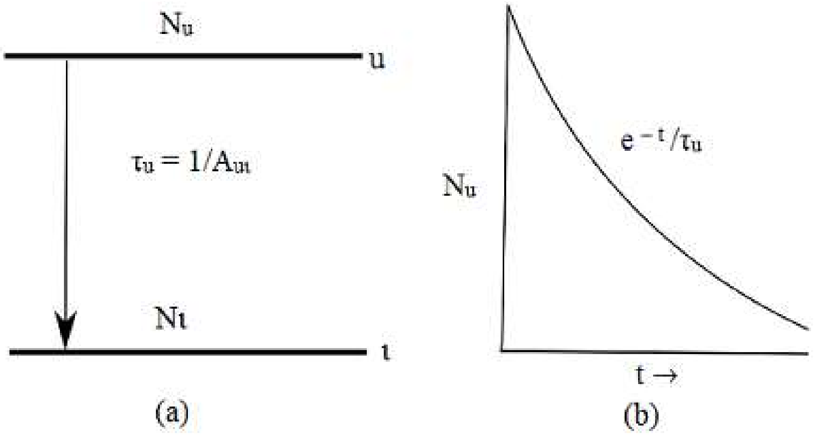

Fig. 1.6 Spontaneous emission decay process

The solution of Eq. (1.12) is,

$$N_u = N_u^0 \exp(-A_{ul})\, t \tag{1.13}$$

$$N_u = N_u^0 \exp(-t/\tau_u) \tag{1.14}$$

When $t = \tau_u$, the population N_u decay to 1/e of its original value and $\tau_u = 1/A_{ul}$ is then referred as the lifetime of level 'u'. The N_u^0 is the initial population density in the level 'u' at the time of excitation pulse. For more general case, in which population in level 'u' decay radiatively to several lower lying levels, the expression for decay is written as,

$$dN_u/dt = -(\sum_i A_{ui})\,Nu \tag{1.15}$$

and the lifetime is expressed as,

$$\tau_u = 1/(\sum_i A_{ui}) \tag{1.16}$$

1.5.2 Line broadening mechanism

Atoms radiate the electromagnetic energy when an excited electron jumps from an upper energy level (E_u) to a lower energy level (E_l), thereby emitting a photon of the frequency $\nu_0 = \Delta E/h$ corresponding to energy difference $\Delta E = E_u - E_l$. The spectral lines observed in an emission/absorption spectrum are never completely monochromatic. I(ν) function in neighborhood of ν_0 is known as the line profile. Frequency interval $\delta\nu = |\nu_2 - \nu_1|$, signifies the line-width. The most commonly used term is full-width at half-maximum (FWHM). This is at $I(\nu_1) = I(\nu_2) = I(\nu_0)/2$, in the line profile. Therefore atomic spectral lines possess a finite frequency (or wavelength) distribution and are not truly monochromatic. The finite width is due to the characteristic decay time and other line-broadening phenomena. The functional form of line broadening profile can be Lorentzian, Gaussian or Voigt distribution, depending upon which type of broadening is being addressed to. The line-broadening can be controlled by chemical or physical environment of the absorbing/radiating atoms. Natural, collisional or pressure and Doppler broadening are the most common line broadening processes.

1.5.3 Natural broadening

The natural broadening (width) of an energy level is always present regardless of the environment of an atom. It is described by Heisenberg uncertainty principle. The principle states that uncertainty in determining the energy width ΔE of an energy level that has minimum uncertainty in its lifetime of Δt is obtained by,

$$\Delta E.\ \Delta t \approx \hbar \tag{1.17}$$

Shorter the lifetime 'Δt' of an excited level, greater be the uncertainty (natural width) in energy 'ΔE'. This in turn means larger uncertainties in frequency $\Delta \nu = \Delta E/h = 1/2\pi\Delta t$ or wavelength of photons associated with the transitions to or from that level.

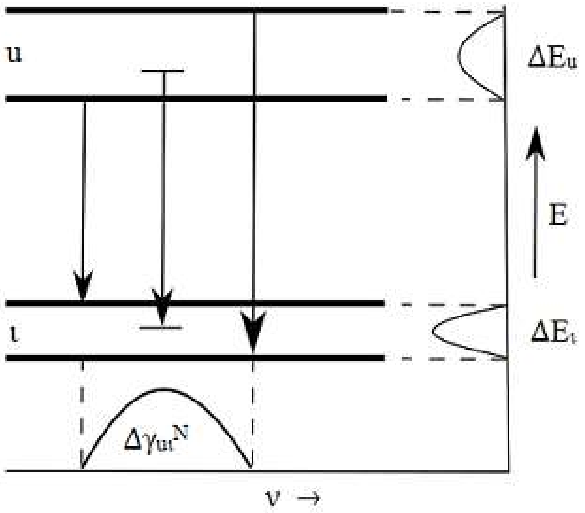

Fig. 1.7 Natural linewidth of atomic transition

If ΔE_u and ΔE_ι are the energy uncertainty associated with radiative lifetime τ_u and τ_ι as shown in Fig 1.7 then,

$$\Delta E_T = \Delta E_u + \Delta E_\iota = \hbar / \tau_u + \hbar / \tau_\iota = \hbar\ (\textstyle\sum_i A_{ui} + \sum_i A_{\iota i}) \tag{1.18}$$

Since $\Delta E_T = \hbar\Delta\omega_{ul} = h\Delta\nu_{u\iota}$, therefore natural emission width is defined as,

$$\Delta\nu_{u\iota}^{N} = (\textstyle\sum_i A_{ui} + \sum_i A_{\iota i})\ /2\pi \tag{1.19}$$

Strong resonance lines ($\Delta t \sim 10^{-8}$ s) have large linewidth. However forbidden lines from long-lived ($\Delta t \sim 1$ s) metastable levels are very sharp.

Lorentzian function describes the spectral profile of a naturally broadened homogenous line. The normalized spectral profile due to natural broadening is given by,

$$S_{\nu N} = \frac{2/(\pi\Delta v_N\ )}{1+\{\frac{[2(v0-v)]}{\Delta v_N}\}^2} \tag{1.20}$$

where $\Delta\nu_N$ is FWHM of naturally broadened line around central frequency (ν_0). Typical width of naturally broadened lines is of an order 10^7 Hz. Their FWHM, $\Delta\lambda_N$ (m) is expressed as,

$$\Delta\lambda_{\mathrm{N}} = \frac{\lambda_0^2}{\mathrm{c}}\Delta\nu_N \tag{1.21}$$

where λ_0 = line center wavelength (meter) and c = speed of light (ms^{-1}). For example for alkali atoms such as sodium Na, at 589.0 nm, $\Delta\lambda_N = 1.16 \times 10^{-14}$ m or 0.0116 pm. The natural linewidth is identical for all the atoms in an ensemble. Such line broadening is called homogeneous. The transitions those have long lifetime (~ ms), such as in case of metastable levels, the transition width is small and the lines are sharp.

1.5.4 Collision broadening

Line profile is affected by collisions of atom with the other atoms. Collisions may be of same kind (Holtzmark broadening) or with foreign species (Lorentz broadening). The effect of collisions broadening enhances with increase in the concentration of collision partners. Hence the collisional broadening is sometimes also called pressure broadening. The collisions, leaving the atoms in the same energy state (adiabatic collisions), are more pronounced. This is in comparison to the collisions that leave the atom in a different energy state. The spectral distribution from adiabatic collisions is given by,

$$\Delta\nu_{\mathrm{a}}(\mathrm{H_z}) = \frac{8\mathrm{KT}}{\pi^3\mu}\,\sigma_{\mathrm{a}}\mathrm{N_x} \tag{1.22}$$

where σ_a is optical cross-section (cm^2) for adiabatic collisions broadening, N_x density (cm^{-3}) of collisional partners, μ reduced mass (g) of the collisional partners and K is the Boltzmann constant (J/K). The normalized spectral profile for collisional broadening ($S_{\nu C}$) is Lorentzian. This is described by equation (1.20) by replacing $\Delta\nu_N$ with collisional trem, ($\Delta\nu_a$). If natural and collision broadening are assumed to be mutually independent, then the resulting FWHM is,

$$\Delta\nu_L = \Delta\nu_C + \Delta\nu_N \tag{1.23}$$

1.5.5 Doppler broadening

The statistical velocities distribution due to thermal motion of the atoms, absorbing radiation along an observation path, is a major cause of line-broadening. This is due to Doppler effect. Since atoms are in motion with respect to observation path, therefore Doppler effects cause a statistical distribution in observed line frequency. This is directly related to the velocity distribution and is temperature dependent. Now, consider the fact that real atoms in our system are not stationary, rather are moving in random directions in space. In non-relativistic limit, an atom travelling with a velocity 'v' parallel to laser beam propagation direction, will experience a shift in frequency (ν_0). This is called Doppler shift (ν_D) and can be described by,

$$\nu_D = \nu_0 (1 + v/c) \tag{1.24}$$

The atoms velocity distribution is governed by Maxwell-Boltzmann probability function as,

$$P(v)\,dv = (m/2\pi kT)^{1/2} \exp(-mv^2/2kT)dv \tag{1.25}$$

The line frequency distribution about central frequency ν_0 is then given by,

$$D(\nu) = [\exp\{-(\nu - \nu_0)^2/2\sigma_v^2\}]/(2\pi\sigma_v)^{1/2} \tag{1.26}$$

which is a Gaussian distribution with a standard deviation,

$$\sigma_\nu = \nu_0 (kT/mc^2)^{1/2} \tag{1.27}$$

This leads to FWHM of the distribution, often called as the Doppler width,

$$\Delta\nu_D = 2\nu_0 [2\ln 2\,(kT/mc^2)]^{1/2} \tag{1.28}$$

In wavelength units, it leads to an expression $\Delta\lambda_D = 7.16 \times 10^{-7} \lambda_0 (T/M)$, where k (J/K), T (K) and M (a.m.u) are Boltzmann constant, temperature and the atomic weight, respectively. The normalized spectral distribution $S_{\nu D}$ is described by Gaussian relation as,

$$S_{\nu D} = [(2/\Delta\nu_D)(\ln 2/\pi)^{1/2}] \exp\{-\ln 2\,(\nu-\nu_0)^2/\Delta\nu_D^2\} \tag{1.29}$$

In general, overall profile of most the absorption lines is a combination of both the Gaussian and Lorentzian distribution, thus a Voigt profile. The predominance of one distribution over another largely depends upon environment of the atoms.

1.6 Hyperfine structure and isotope shift

1.6.1 Fine/hyperfine structure

The mutual electrostatic attraction between the electron and the nucleus fixes the gross energy of an electron in the atom. However, magnetic effects are also present at atomic level. An electron possess intrinsic magnetic moment. The magnetic moment 'μ_s' of the electron is related with its spin angular momentum 's', Bohr magneton 'μ_B' and Lande 'g_s' factor as,

$$\mu_s = - g_s \mu_B s \tag{1.30}$$

The electron, moving in electric field of nucleus, experiences magnetic field B_l. This is proportional to the orbital angular momentum '*l*' of the electron. The electron magnetic moment interacts with the magnetic field created due to its motion, modifies its energy due to perturbation H_{so} as,

$$H_{so} = - \mu_s.B_l = \zeta\, l.s \tag{1.31}$$

The constant ζ is proportional to expectation value of $[\left(\frac{1}{r}\frac{dV}{dr}\right)]$, where V(r) is effective central potential in which valence electron moves. The value of ζ can be estimated by,

$$\zeta = \frac{-e}{2m^2c^2}\left(\frac{1}{r}\frac{dV}{dr}\right) \tag{1.32}$$

using V(r) as calculated by Hartree-Fock method. The *l* and *s* both couples together. Also they precess about resultant *j* with a frequency proportional to the strength of the field. The resultant angular momentum $j = l + s$ with $j^2 = (l + s)^2$ results,

$$2l.s = [j^2 - l^2 - s^2] \tag{1.33}$$

Thus energy shift becomes,

$$\Delta E_{so} = < H_{so} > = \frac{-e\hbar^2}{2m^2c^2}\left[\frac{j(j+1)-l(l+1)-s(s+1)}{2}\right] < \frac{1}{r}\frac{dV}{dr} > \tag{1.34}$$

The spin-orbit interaction leads to small differences in energy of the levels, resulting in the complexities in spectral lines, known as the fine structure. The fine structures are usually of very finely spaced of the order 10^{-6} of the energy difference between the energy levels. The hyperfine structure results from two types of interaction. First, the magnetic interaction between electron and nucleus and second, the electrostatic interaction between the electric quadrupole moment of the nucleus and the electron.

1.6.2 Isotope shift

Spectral lines are the characteristic of an element which generates its spectrum. However, the line energy depends slightly on its isotopes. Energy difference between isotopes are called the isotope shift. Different isotopes have changes in the energy of transition. If the two isotopes are labelled 'H' for heavy and 'L' for light then

$$E_{1H} - E_{2H} = \hbar\omega_H \text{ and } E_{1L} - E_{2L} = \hbar\omega_L \tag{1.35}$$

$$\hbar(\omega_H - \omega_L) = \hbar\delta\omega = (E_{1H} - E_{2H}) - (E_{1L} - E_{2L}) \tag{1.36}$$

is known as the isotope shift (IS). An atomic level is described by the angular momentum and energy. Every level has a definite value of angular momentum. Hence, if due to additional neutrons, the mass of atomic nucleus varies, as the case in the isotopes of an atom, the energy of the levels will change in order to preserve the angular momentum. This energy change, named as mass-shift (MS), is one major component of the isotope shift. The isotope shift ($\Delta\nu$) is given as,

$$\Delta\nu \sim \nu\,(m\,\Delta M/M^2) \tag{1.37}$$

where m = electron mass, M = nuclear mass and ΔM = isotopic mass difference. For light nuclei such as lithium, the mass-shift is the significant contributing component. This is due to $1/M^2$ factor. Addition of one neutron to the light nucleus has much larger effect as compared to that in a heavy nucleus. Then linear combination of normal mass-shift and specific mass-shift approximate the total mass-shift. The normal mass-shift, is the transition frequency dependent and always positive for heavier isotope. Specific mass-shift caused by correlation between the electrons, can be both positive and negative. Its evaluation is difficult because of correlation integrals. The size and shape of electric charge distribution of nucleus guide the energy of an atomic level. This effect is another major contributing part of the isotope shift. Different isotopes have the same number of protons. However, the charge proton distribution in a nucleus is affected by the number of neutrons present. The nuclear charge distribution modifies the Coulomb interaction with the electrons. The resulting electric field determines the energy of atomic electrons. The energy level shift, arising in different isotopes, due to different electric field is termed as field-shift (FS). The field-shift is sometimes also named volume-shift. However field-shift term is more preferable as the changes in shape and nuclear charge distribution can lead to isotope shift. For heavier element isotopes, the dominated effects are variation in hyperfine structure, in nuclear and electronic angular momentum and in nuclear volume. Energies of ‘s’ electrons are altered by change in nuclear volume. This in turn produces substantial isotopic shift for transitions involving ‘s’ electrons. The total isotope shift (IS), to a good approximation, is the sum of these two effects,

$$\mathrm{IS} = \mathrm{MS} + \mathrm{FS} \tag{1.38}$$

Thus differences in electronic absorption frequencies among the isotopes of an atom due to their isotope-shift could be used for isotope separation by selective photoionization methods.

1.7 Photoionization cross-section

An atom can be ionized by a single photon whose energy ‘hν’ is higher than the ionization energy (U_i) of the atom. The kinetic energy of generated photoelectrons, is given by ($h\nu - U_i$). The probability of photoionization of an atom to its ionic state is proportional to photoionization or photoelectron cross-section. The cross-section is usually denoted by $\sigma(\omega)$. The photoionization is dipole transition between initial Ψ_i and final Ψ_f states. Final state lies in the continuum where photo-electron can occupy any state. For each energy value ($E > 0$) there is a solution in Schrödinger equation. The solution corresponds physically to an electron asymptotically free as the wave-function does not decay at infinity, but oscillates periodically. The transition probability for such an event is obtained by the dipole transition moment and given by,

$$M_{fi} = \Psi_f | r | \Psi_i\rangle \tag{1.39}$$

The cross-section is proportional to sum of squares of dipole transition moment and given by,

$$\sigma \propto \sum_f | M_{fi} |^2 \tag{1.40}$$

over all the final states. Selection rules hold as $l_f = l_i \pm 1$. For 'ns' orbital ionization, only the ns → np process contributes. The ionization of 'np' orbital happens through the channels np → nd and nd → nf. Generally, $l \rightarrow l+1$ transition contribute dominantly. When the vacated orbital and photoelectron wave are in same spatial region, both the interaction and cross-section will be maximum. Near the ionization threshold, the cross-section is usually highest and after then decays with excess photon energy. The electron wave becomes more oscillatory as its kinetic energy increases. In this situation the cross-section suffers rapid decay, as the positive and negative parts of the dipole matrix element tend to cancel one another. Different approaches, theoretical as well as experimental, have been developed for determination of photoionization cross-section of atoms and molecules. However, photoionization cross-section data of the excited states are not widely available. In present thesis work, an alternate saturation technique has been used to evaluate the excited state photoionization cross-section near the ionization threshold of lithium.

1.8 Review on lithium spectroscopy

Lithium is a light, soft and silvery metal of many practical uses and day to day applications. Whether in medicine, smart phone battery or large energy bank for auto-vehicles, it is one of the most widely used elements. According to the current cosmological models, lithium in the universe was formed first time during the Big Bang. It is assumed that Big Bang produced the five lightest elements: H, He, Li, Be, and B. Lithium is the lightest element in universe after hydrogen and helium, having the simple atomic structure. It has been therefore studied extensively both theoretically [28-30] and experimentally [31-39] using different approach by various research groups. As far as the selective excitation and photoionization of lithium is concerned, Aymar et al. [28] have theoretically investigated the lithium photoionization through its Rydberg states. Other important parameters such as oscillator-strength and photoionization cross-section, essentially needed for laser isotope separation of lithium are theoretically determined by Yan et al. [29] and Yue-Ying et al. [30]. Shimazu et al. [31] demonstrated the two-step selective photoionization of Li atoms using an experimental setup in a Li cell. Lahiri et al. [32] studied the radiative recombination of Li and calculated the photoionization cross-section from its excited state. Karlov et al. [33] carried out Li photoionization spectroscopy and suggested its applications. Kramer et al. [34] explored the detection of single Li atom by step-wise resonance ionization and measured its photoionization cross-section for excited (n = 3) atoms. Saloman [35] compiled an extensive report on resonance ionization spectroscopy/ resonance ionization mass spectrometry data for lithium including other elements (Be, In, Li, K, Rb, Ag, Ti and V). Because of its high selectivity and sensitivity, the RIS technique [20-23] is considered to be the most useful for laser based isotope separation. Baig et al. [36] reported observations on Rydberg states of atomic Li. This study was pursued by two-color and three-photon resonance ionization technique utilizing thermionic diode based detection. Resonance ionization spectroscopy of the lithium using cost-effective diode laser based setup was demonstrated by Olivares et al. [37]. Anwar ul Haq et al. [38] reported new experimental data on the highly excited Rydberg states of Li by two-step laser excitation and thermionic diode detection. Amin et al. [39] measured the photoionization cross-section from the excited states of lithium using thermionic diode ion detector.

In the LIS studies, use of time-of-flight mass-spectrometer (TOFMS) improves the overall selectivity of photoionization process based on the mass difference of isotopes. Li isotopes photoionization in two frequency scheme by TOFMS and ionizing radiation at 266 nm was studied by Il'in et al. [40]. Arisawa et al. [41] studied the two-step selective photoionization scheme of lithium and carried out its isotope separation using the ultra-narrow bandwidth (~ 0.036 cm^{-1}) dye laser. Saleem et al. [42] obtained 47% enhancement in ^{6}Li isotope concentration. This study was based on two-step laser photoionization scheme using TOF mass spectrometer.

1.9 Theme and layout of thesis

The work presented in the thesis mainly focus on isotope-selective photoionization studies of Li leading to separation/enrichment of its isotopes by laser method. Main thrust is on the studies related with separation/enrichment of naturally low abundant ^{6}Li isotope either by two-step or three-step selective excitation method using in-house developed lasers, atomic vapors and ion-extraction systems. To achieve the designated target, the whole work is divided into small milestones. These are executed step by step by a well-planned and systematic approach. The second chapter of thesis describe the design and construction details of different types of atomic vapor sources, time-of-flight mass spectrometer, wavelength scanner & data logger unit and the laser systems that have been used for experimental studies in present work. The third chapter deals with the development of hollow cathode discharge lamp for Li spectroscopic studies and dye wavelength calibration. The fourth chapter presents detailed photo-excitation studies on Li atoms investigated by optogalvanic (OG) and saturation absorption spectroscopy methods using the developed HC lamp. It also discusses the possibility of selective photoionization studies of Li in HC lamp. The fifth chapter concentrates on two-step selective photoionization studies with single and two-photon excitation to measure the Li photoionization cross-section using a sensitive in-house built thermionic diode ion-detector. In sixth chapter, the experience gained from previous studies using the hollow cathode lamp and the thermionic diode detector is implemented for two-step isotope-selective photoionization studies of Li using time-of-flight mass-spectrometer. Three-color, three-step isotope-selective photoionization is demonstrated for obtaining separation/ enrichment of Li^6 isotopes. In seventh and the final chapter, the overall summary and future scope is given.

Chapter 2

Experimental Systems

2.0 Introduction

For isotope-selective photoionization and laser isotope separation/enrichment studies on Li, the experimental system mainly consists of narrowband tunable lasers, atomic vapour sources and photo-ion detection systems. This chapter presents developmental details of the laser systems, dye laser wavelength calibration system, basic theory of thermionic diode (TD) and the time of flight mass-spectrometer (TOFMS) as employed to accomplish the targeted thesis works. On lasers side, the laser systems consist of dye lasers tunable in suitable wavelength range (for Li spectroscopy) pumped either by kHz repetition rate copper vapour laser (CVL) or few Hz repetition rate nitrogen laser. The CVLs used are developed in-house, whose working principle and construction details are described. Two similar CVLs having positive branch unstable resonator in oscillator are configured as master oscillator power amplifier (MOPA) for high average power operation. This is needed for simultaneous pumping of two dye lasers operating in synchronism required for Li three-step photoionization studies. Brief details of a commercial excimer laser which is refurbished to operate as a nitrogen laser are also presented. The basic photo-physics of organic dye molecule, working principle and detailed construction of the developed tunable dye lasers with optimized output at ~ 671 nm and ~ 610 nm wavelength along with their cavity layout and tuning mechanisms are described. On instrument side, a computer controlled data acquisition system, especially developed for dye laser wavelength automated tuning and logging of experimental data is described. Basics of time-of-flight mass-spectrometer along with its design & fabrication details are presented. The integration of its sub components such as atomic beam source, ion extraction & acceleration, ion-detector and associated instrumentation for functioning of TD and TOFMS as a whole are also described.

2.1 Copper vapour laser (CVL)

2.1.1 CVL energy level diagram and kinetics

The CVL is a pulsed metal vapour laser excited by electric discharge. The technology of CVL is quite matured and is well reported [43]. Its active medium is produced by heating the pieces of solid copper (Cu), kept in laser tube and the added buffer gas, for sustaining the discharge. The operation of CVL requires an operating temperature of laser tube in excess of 1400 ^{0}C. The same electric discharge that heats solid Cu pieces upto desired temperature to generate its atomic vapour also excites the Cu atoms. The partial energy level diagram for CVL lasing is shown in Fig. 2.1. With atomic number (Z = 29), the electron distribution of Cu into various shell and subshell is $1s^2$, $2s^2$ $2p^6$, $3s^2$ $3p^6$, $4s^1$ $3d^{10}$ with ground state 4s $^2S_{1/2}$ configuration. The next higher excited energy states are $^2D_{3/2,5/2}$. Since orbital (d) is more than half filled, so as per Hund's rule, the energy levels are inverted i.e. line $^2D_{5/2}$ has lower energy (1.39 eV) than the line $^2D_{3/2}$ energy (1.64 eV). The next higher energy states $^2P_{3/2}$ and $^2P_{1/2}$ lie at 3.82 eV and 3.79 eV respectively. The electric discharge preferentially populates the first two upper resonance levels of the copper. The electron impact excites the Cu atoms from ground state to upper $^2P_{3/2}$ and $^2P_{1/2}$ laser levels with effective radiative lifetime of 110 ns and 90 ns, respectively as the phenomena of radiation trapping between ground and upper laser levels is operative. The transitions from upper levels to lower $^2D_{3/2,}$ and $^2D_{5/2}$ metastable levels having lifetime of an order 130 μs [43], generate the laser output radiation (Fig. 2.1). The transitions 4p $^2P_{3/2} \rightarrow$ 4s $^2D_{5/2}$, 4p $^2P_{1/2} \rightarrow$ 4s $^2D_{3/2}$ gives the lasing at 510.6 nm and 578.2 nm respectively. As the lower levels ($^2D_{3/2,5/2}$) are metastable and optically forbidden to ground state, therefore restrict the CVL operation in pulse mode only. The population in these levels can decay through slow diffusion process to discharge tube wall or via collision with electrons. The laser repetition rate in such cases is governed by the time needed for metastable population to decay into ground state and thus limited in typical range of 5-7 kHz.

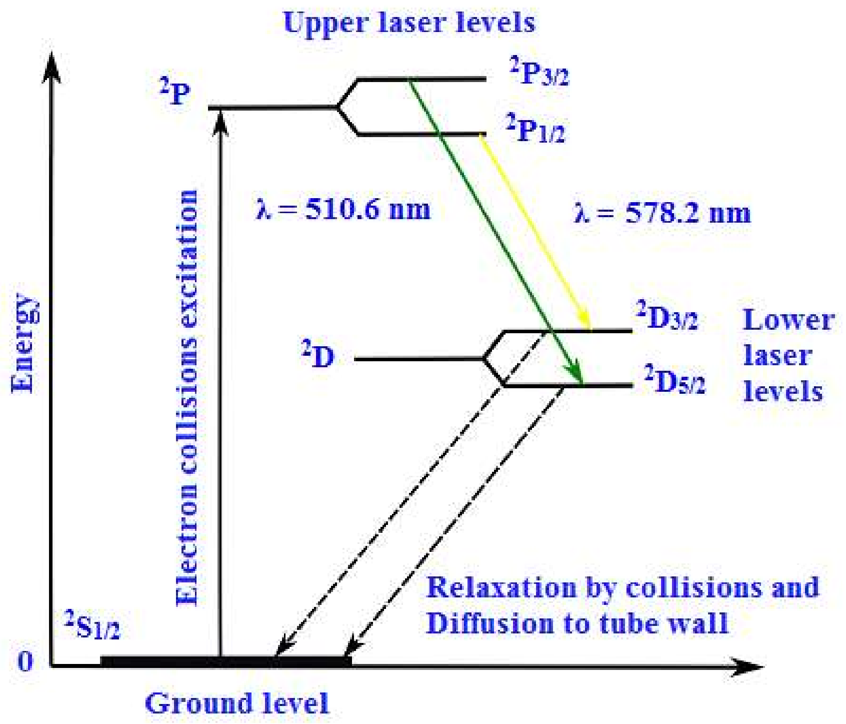

Fig. 2.1 Energy level diagram for laser action in copper vapour laser

2.1.2 CVL design, assembly & electrical excitation

The layout of in-house developed CVL system for the present studies, is shown in Fig. 2.2. The design of laser head is similar to that used by many other researchers for copper vapour lasers [44-46]. The CVL needs a high temperature enclosure to vaporize the copper atoms up to suitable partial vapour pressure (~ 0.4 Torr) for the lasing. The laser head (Fig. 2.2) is constructed using high purity alumina (Al_2O_3) discharge tube with 4.7 cm internal diameter and 150 cm length as a high temperature enclosure. Around 50 to 60 gram of copper (OFHC) in small granules form are placed at equal distance (~ 10 cm) in the discharge tube. This tube is wrapped by bulk alumina fiber at packing density ~ 300 kg/m^3 and placed coaxially in 150 cm long borosilicate glass tube with internal diameter 150 mm and wall thickness 5 mm. Alumina fibre with thermal conductivity of 0.26 W/m ^{0}C provides the required thermal insulation for maintaining the desired CVL working temperature (~ 1500 ^{0}C).

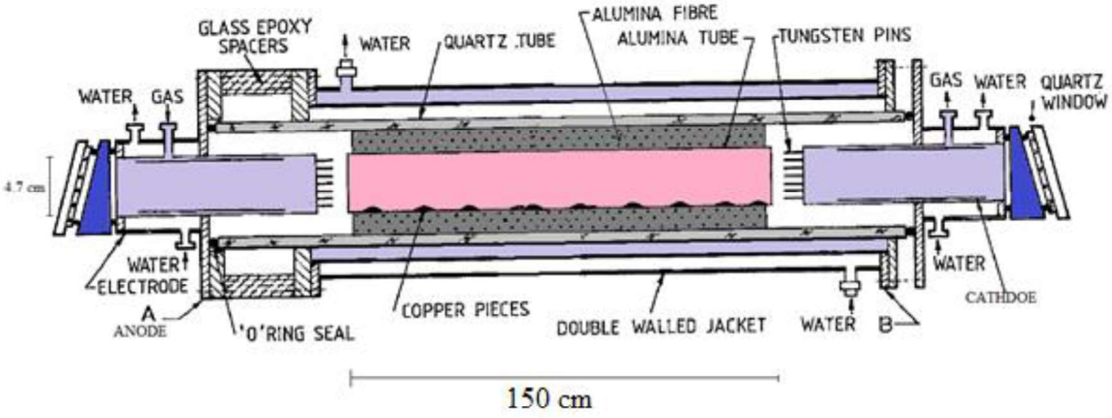

Fig. 2.2 Schematic of in-house developed copper vapour laser

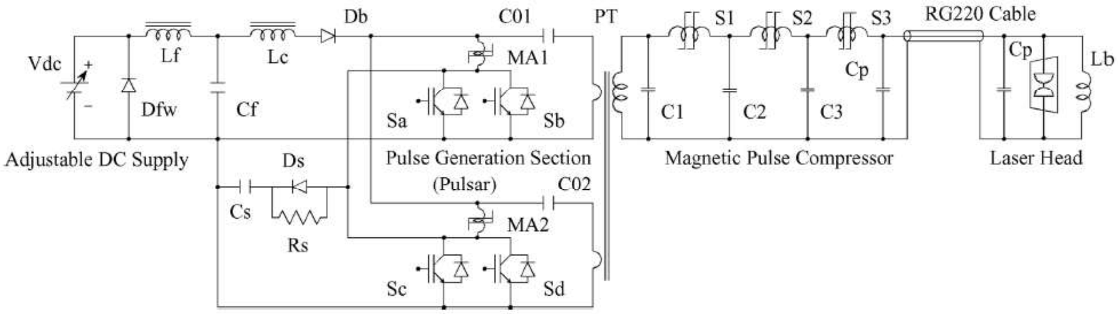

Fig. 2.3 CVL solid state power supply circuit diagram (Ref. 47)

The alumina tube can sustain a temperature upto 1950 ^{0}C. This alumina tube with effective fiber thermal insulation is kept in borosilicate glass tube and safely placed into water cooled double-wall stainless-steel metal jacket. The laser electrodes are fitted to both the ends of glass tube. The high quality rubber 'O' rings are used to seal the laser head from atmospheric surroundings. For minimizing sputtering of electrodes, the discharge is allowed to terminate on refractory material sharp pins. The tungsten pins of length 25 mm and diameter 2.4 mm are guided into electrodes with even gap of ~1.5 cm. A small spacing ~ 25 mm is left in between alumina tube and tungsten pins at both the ends for free expansion of discharge tube at higher temperature. The electrodes of CVL are externally cooled with flowing water (Fig. 2.2). The high voltage side laser head electrode is supported on two nonconductive glass epoxy spacers that provide good electrical insulation. These spacers are attached firmly to the water cooled external metal jacket. The metal jacket is grounded electrically. It provides a return current path to laser power supply electrical circuit to minimize the inductance of laser head. The laser electrode of ground side is fitted with mounting screws on end flange of the metal jacket. The borosilicate tube is supported on two metal flanges with the help of soft cushion, mounted at the metal jacket ends. Fused quartz windows inclined at 6^0 angle with tube axis, are mounted to both the laser electrodes. A tedious and time consuming conditioning process, for newly assembled laser tube, is required. Later on, for routine laser operation only a simple and easy conditioning is sufficient. During conditioning period, the discharge tube is heated repeatedly followed by fast evacuation. In this way the released impurities are flushed out from laser tube head. The buffer gas pressure and flow in discharge tube are controlled by vacuum/gas handling unit having precision needle valves. This laser design enables an easy assembly and high reliability as there is no mounting stresses on discharge tube. Once properly assembled and conditioned, the CVL requires only routine maintenance for its long term operation.

The CVL, being a self-terminating laser requires the fast electrical discharge pulse excitation. The CVL employed in the present research work used an indigenous developed solid state power supply based on insulated gate bipolar transistor (IGBT) switches [47]. The advantage of using solid state power supply over conventional thyratron switch based power supply is its higher electrical power handling capabilities and larger meantime between failures (MTBF). Figure 2.3 shows a circuit diagram of the utilized solid state power supply. Basically, it consists of a switch mode power supply (SMPS), filters, pulse-transformer and three-stage pulse compressors connected to laser head. Variable voltage (325 to 550 V) DC power supply with a current upto 20 Ampere is used. Capacitor banks C01 and C02 form the storage capacitor. These capacitor banks are resonantly charged by DC source upto approximately twice of its value through charging inductor ‘Lc’, blocking diode ‘Db’ and primary coil of pulse-transformer. The pulse-transformer has two primary windings each of one turn connected independently to IGBT and storage capacitor banks. The energy stored in capacitor banks is discharged through pulse-transformer by triggering both the IGBT simultaneously and immediately transferred to high voltage capacitor ‘C1’ connected across the secondary windings. The IGBT are turned-on for 5 μs time interval at 6.5 kHz repetition rate. To reduce the turn-on losses in the IGBTs, the magnetic assist (MA) is connected in the discharge path. The rise time (~ 2 μs) of pulse energy build ups across capacitor C1, is compressed by three-stage magnetic pulse compressors (MPC) and the finally generated voltage pulse of ~ 20 kV with rise time of ~ 90 ns applied to the laser head through a shielded RG-220 electrical cable. The high voltage pulse and its repetition rate are optimized as per the design parameters of CVL. All the power supply components are immersed in transformer oil. The heat dissipated in circuit components is removed by circulating the oil in an oil to water heat exchanger. The power supply has a facility of an external trigger by an optical pulse coupled through an optical fibre and auto trip in case cooled water supply interrupted, MPC oil bath temperature increased beyond set point or the buffer gas pressure deviates from desired working range.

2.1.3 CVL MOPA system

In present research work, the intense radiation (λ_1 = 510.6 nm, λ_2 = 578.2 nm) from CVL output is utilized for optical pumping of the two dye lasers synchronized with each other. These dye lasers are developed for Li multi-step selective photoionization experiment. There is significant power loss due to spatial filtering and beam shaping optics, utilized in above mentioned experimental setups. Therefore, only the CVL oscillator with unstable resonator [48] is unable to provide sufficient output power required to realise the different Li photoionization schemes. A standard way to increase the CVL power with good beam quality, is to employ a master oscillator power amplifier (MOPA) configuration. Such CVL MOPA system has been setup as a part of the research work. A schematic of the used CVL MOPA system, is shown in Fig. 2.4.

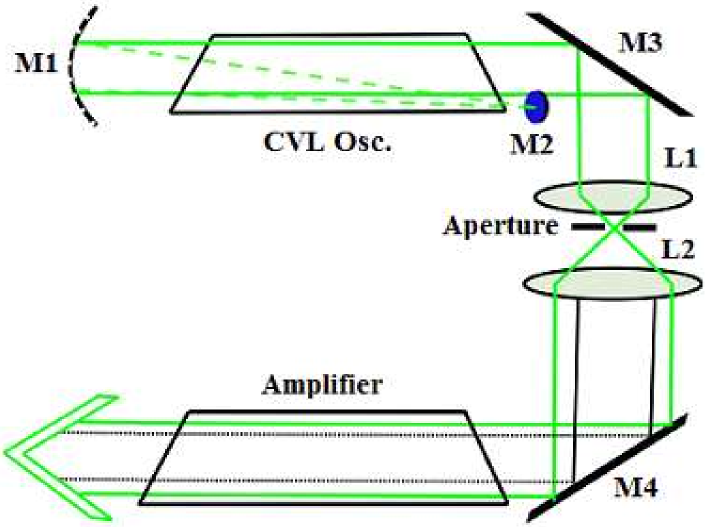

Fig. 2.4 CVL MOPA system

As the CVL is a short inversion time and high gain laser, therefore use of plane-plane (stable) resonator results the large beam divergence output in the range of few mill-radians depending upon the various parameters such as discharge tube diameter, resonator length and laser operating conditions [49]. Such a large diverging oscillator CVL output can't be coupled efficiently with power amplifier as well as can't be focused tightly on dye cell. In the developed CVL-MOPA system, the oscillator is fitted with an off-axis confocal positive branch unstable resonator. The unstable resonator utilizes the large gain volume in single transverse mode leading to a low beam divergence and high spatial coherence [50-52]. To take an advantage of gain appearing initially near the CVL alumina tube wall, an off-axis unstable resonator configuration is adopted. The CVL unstable resonator is formed using highly reflective (> 99.5%) concave mirror M1 of radius of curvature (R1 = 5 m) and button type convex mirror M2 of radius of curvature (R2 = -10 cm).

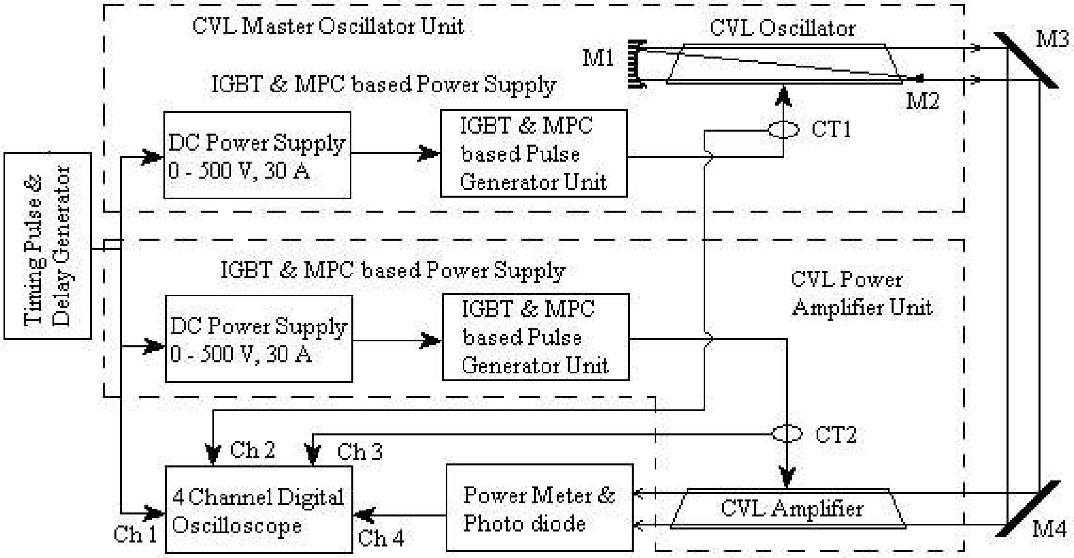

Fig. 2.5(a) Schematic of CVL MOPA system with solid state power supply

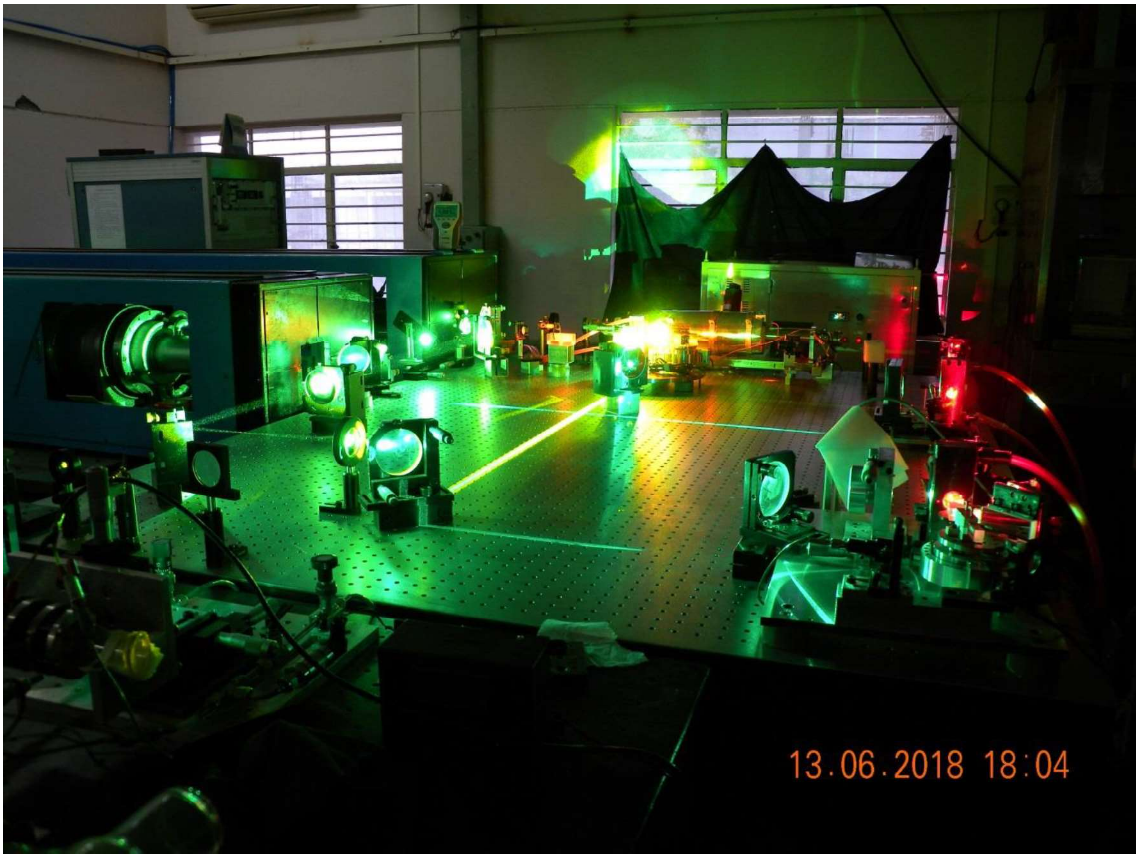

Fig. 2.5(b) CVL MOPA to pump the dye lasers for photoionization experiments

The length of resonator was kept around (R1-R2)/2 to maintain the confocal condition. The resonator magnification M (= R1/R2) was 50. A combination of lens L1 and L2 is used for spatial filtering of ASE from oscillator as well as to match the size of oscillator beam with amplifier tube diameter. Fig. 2.5 (a) & (b) show the schematic of actual working CVL MOPA system and the setup used to pump the dye lasers for Li photoionization experiments. The CVL MOPA output power is optimized by synchronizing the trigger delay between the oscillator and amplifier unit. The CVL master oscillator injected ~ 15 W average power into the power amplifier. The CVL MOPA provided an average laser output power of around 45 watt at 6.5 kHz repetition rate with low beam divergence (< 0.5 mrad) and short pulse duration (~ 40 ns). The yellow beam (~ 578.2 nm) laser pulse is delayed around 20 ns of green (~ 510.6 nm) laser pulse [44]. The CVL MOPA laser power remained fairly stable for continuous eight hours per day operation. The output power of CVL is measured by commercially available power meter (Gentech, PS-310 WB).

2.2 Nitrogen laser system

Nitrogen laser has long been preferred to pump the tunable dye lasers. Nitrogen laser is a gas laser that operates in ultraviolet range (λ = 337.1 nm). Its short pulse duration (~ 10 ns) suits the dye laser excitation as it avoids the triplet state effects in dye laser performance. The fast rise time of laser pulse also helps in populating short lived (5-10 ns) excited dye singlet states efficiently. The short wavelength of pump in UV range allows the generation of tunable dye laser output from 350 nm onward up to near infrared, without any complicated frequency conversion schemes. Its high peak power facilitates dye laser to deliver output at high peak power. In the thesis work, a nitrogen laser is used to pump the dye laser with a laser dye that has good absorption cross section at 337 nm and emits the radiation corresponding to first-step of lithium excitation. For this, an excimer laser (Lambda Physik, EMG 201) is refurbished and operated as a nitrogen laser. Nitrogen laser operates on three level scheme as shown in Fig. 2.6. The active gain medium in nitrogen laser is a nitrogen gas with high purity (~ 99.9%) filled at pressure (~ 40 mbar). Helium is used as a buffer gas. The molecules of nitrogen are excited from ground to excited state by electronic excitation due to fast high voltage discharge pulse populating the upper laser level with lifetime of ~ 40 ns. On decay to lower laser level (lifetime ~10 μs) it emits photons at λ = 337.1 nm. This laser uses the transverse electric discharge excitation. This nitrogen laser provided maximum output energy up to 6 mJ in 10 ns pulse (rise time ~2 ns) at low repetition rate adjustable to 1-5 Hz with beam divergence of about 3.5 mrad. Small pulse to pulse variation in output energy (± 3%) is minimized by optimizing the gas pressure. In present thesis work, this laser is utilized to optically pump the low repetition rate dye lasers for lithium spectroscopic studies carried out in hollow cathode lamp, thermionic diode as well as in time-of-flight mass-spectrometer.

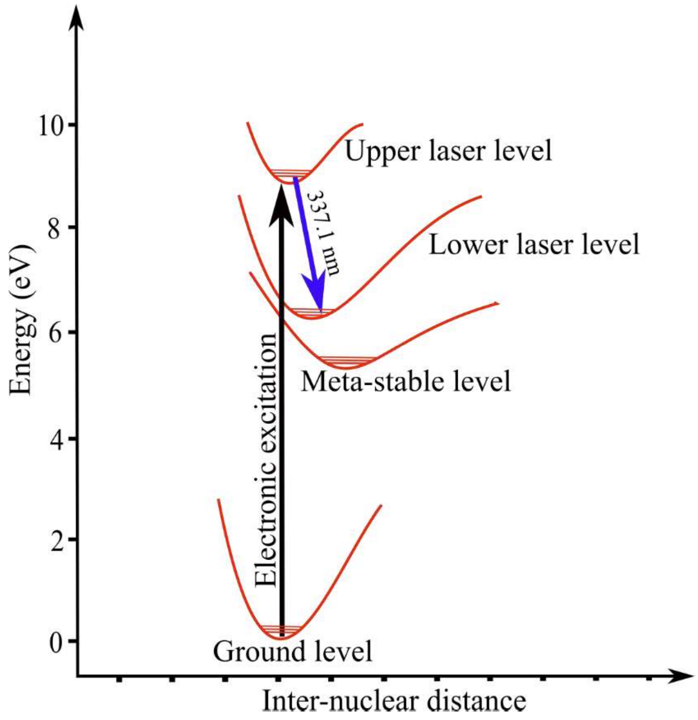

Fig. 2.6 Energy level diagram of nitrogen laser

2.3 Tunable Pulsed dye laser

2.3.1 Dye laser: energy levels and kinetics

Dye laser requires standard components as used in any common laser such as an energy pump source (i.e. CVL or nitrogen laser), an active lasing medium (dye dissolved in solvent) and a resonant cavity (wavelength selective). The laser dyes are the complex organic molecules with large molecular weight. The bond structure of dye is an extended system with alternating single and double bonds. This characteristic allows many organic dyes to absorb strongly in visible and ultraviolet spectrum range. The laser produces the strong fluorescence over a large wavelength range. The energy level scheme of a typical dye molecule in an appropriate dilute solution, is shown schematically in Fig. 2.7.

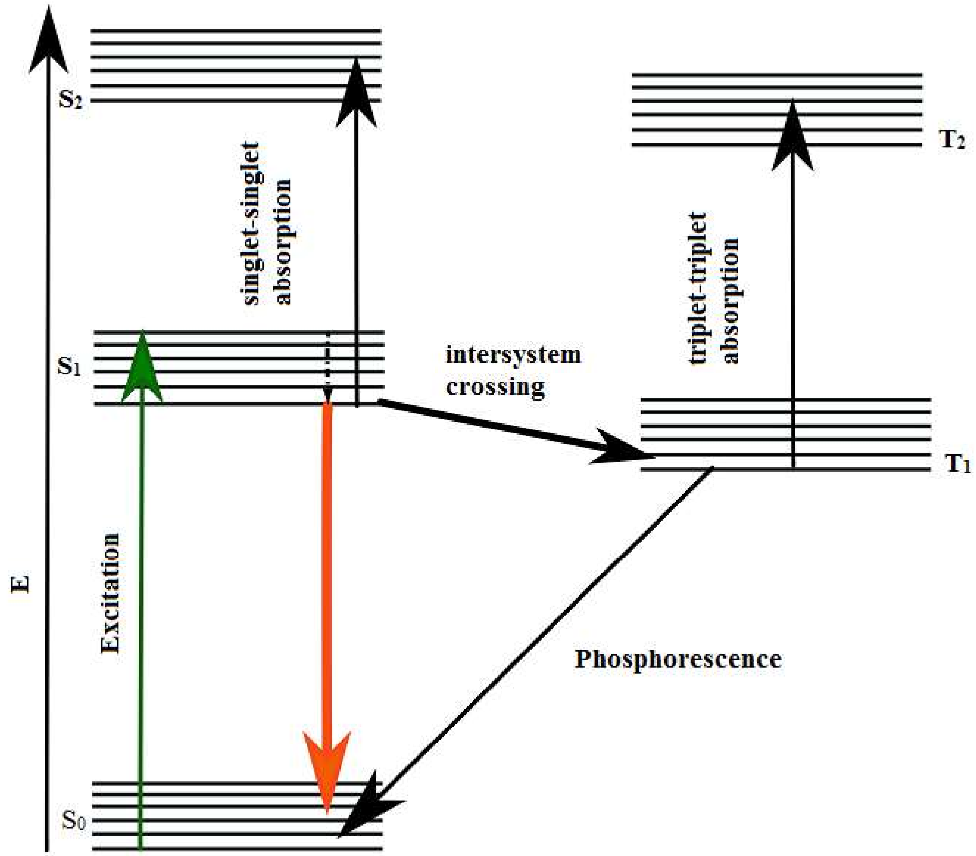

Fig. 2.7 Energy level diagram and basic processes of dye laser

The dye laser molecule consists of a set of electronic levels, each of which has an associated set of closely lying vibrational and rotational states. Singlet states, S_0 and S1 and triplet states, T1 & T2 form the four relevant electronic levels. $S_1 \rightarrow S_0$ transition is used for wavelength tunable lasing. $T_1 \rightarrow T_2$ leads to loss of laser radiation by absorption and need to be avoided. Non-radiative intersystem crossing from the excited singlet (S_1) to the lower triplet (T_1) is energetically allowed and is detrimental for lasing performance. The dye molecules are optically excited from the level S_0 to the excited singlet state S_1, when dye solution is illuminated by light whose wavelength falls in its absorption band. After the excitation, rapid collisions with other molecules dissipate the excess rotational-vibrational energy and the dye molecules relax to the lowest vibrational state of the excited singlet state S_1. This happens in a time scale of ~ 10^{-12} s. Finally, the dye molecules decay via spontaneous emission, to the vibrational-rotational levels of ground state within the radiative emission lifetime (τ_s) of about 10^{-9} s. The emitted light is of longer wavelength than the pumping radiation. The non-radiative relaxation processes return the dye molecules to the ground state. Homogeneous broadening of laser dyes lead to concentration of optical power into a narrow oscillating spectral bandwidth. The population inversion between S_1 and S_0 is attained instantly if the intensity of pumping radiation is very high (~ 100 kW/cm^2). Lasing is then possible almost over entire fluorescence band excluding the part which overlapped with absorption band of dye molecule. Dyes with no or small overlapping of absorption and fluorescence band gives higher laser output efficiency.

2.3.2 Absorption/emission spectrum of DCM dye

Laser grade DCM dye ($C_{19}H_{17}N_3O$) is selected for the first step of Li excitation in photoionization experiments. It is a very efficient laser dye that can be easily pumped by green (510.6 nm) component of the CVL output and emits in the orange-red region of electromagnetic spectrum suitable for Li spectroscopy. Figure 2.8(a) shows its chemical structure. When excited by the light of an appropriate wavelength, the DCM dye display intense, Stokes-shifted broad-band fluorescence spectra, as shown in Fig. 2.8(b).

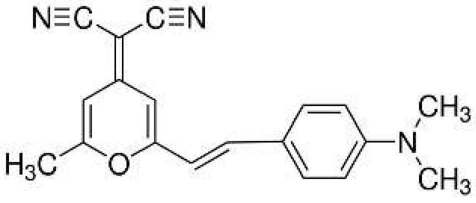

Fig. 2.8(a) Chemical structure of DCM dye ($C_{19}H_{17}N_3O$) molecule (M.W: 303.37)

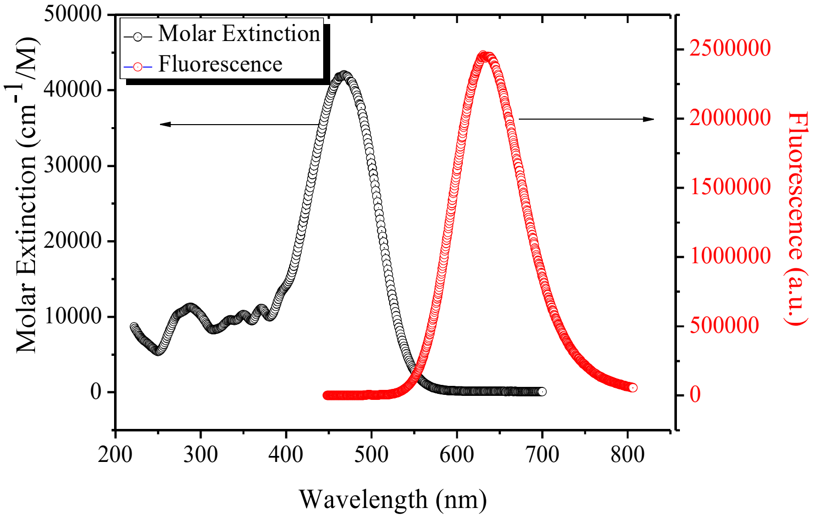

Fig. 2.8(b) Absorption and emission spectra of DCM dye molecule

Efficient dye laser operation, demands high fluorescence yield. Because fluorescence spectrum of few laser dyes overlap with longer wavelength edge of an absorption band, therefore a fraction of an optical output is reabsorbed by dye molecules. The reabsorption by dye molecules in ground state and in its lowest excited singlet, causes a significant loss to dye laser output. Therefore, a small absorption coefficient for ground state as well as excited singlet, is the recipe for efficient laser dyes. In order to further minimise such unwanted re absorption losses, the dye concentration is an important parameter that needs to be optimized with respect to emitted fluorescence and the pump wavelength. The other requirement for efficient dye laser operation is to have a pump source with its wavelength close to the peak of an absorption band of the dye. This makes copper vapour laser with 510.6 nm a good choice as a pump source for DCM dye.

2.3.3 Pulsed dye laser cavity

The simplest pulsed dye laser cavity consists of a linear setup of gain medium, diffraction grating and an output coupler. The first such pulsed dye laser using minimal number of components was demonstrated with spectral width of 150 GHz [53]. Later on more optical components such as beam expanders, wavelength tuning and filters have been added to obtain the narrowband operation [54]. The pulse operation of dye laser can be made using various techniques. The simplest and efficient technique is to use another pulse laser as a pump source. For such purpose nitrogen laser, CVL, frequency doubled and tripled Nd:YAG laser and excimer lasers are popular choices. Laser pumped pulse dye lasers can produce output pulses of upto tens of mJ with typical pulse duration of 10 ns at repetition rate ranging from a few Hz to few KHz. The flash-lamp pumped dye lasers although comes with much higher pulse energy in Joules but produces the larger pulse duration in μs regime at much smaller repetition rate, even less than one Hz. Single mode dye laser operation is possible with short length cavity. The shorter cavity lengths of dye laser increases the free spectral range of longitudinal modes and facilitate the single-mode operation.

2.3.4 Wavelength tuning methods

The important characteristics of the dye lasers are its broad tuning range and narrowband operation. In dye lasers, the wavelength selection as well as its tuning can be accomplished by prism, diffraction grating and/or etalon. Simple representative geometries are shown in Fig. 2.9. The grating based method is the preferred and most widely used technique for the selection and tuning the wavelength in dye lasers.

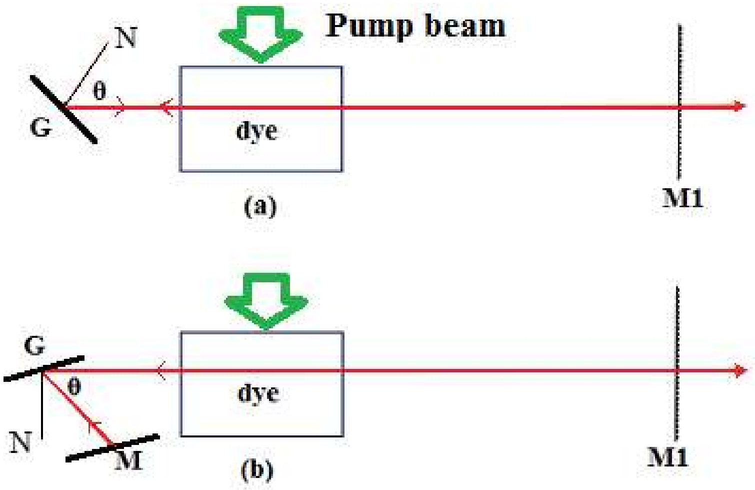

Fig. 2.9 Dye laser tuning with grating in (a) Littrow mode, (b) GIG mode

The grating, diffracts light into specific directions on illumination by a wavelength (λ) and direction of the diffracted light in different orders can be obtained by an expression,

$$d\,(\mathrm{Sin}\ \theta_i \pm \mathrm{Sin}\ \theta_d) = m\,\lambda \tag{2.1}$$

where 'd' is spacing between the grooves which is known as grating constant and angle θ_i, θ_d represents the direction of incident and diffracted beams for an order of diffraction 'm'. In Littrow mode, the light is diffracted back in the direction of incidence (i.e. $\theta_d = \theta_i = \theta$) and grating behave as a wavelength specific reflecting mirror. Desired wavelength can be selected by rotating grating about an axis perpendicular to cavity and parallel to grating ruling lines. The linewidth can be controlled by the angular dispersion of grating. The angular dispersion of grating for a diffraction order 'm' can be obtained by differentiating Eq. (2.1) as,

$$d\theta/d\lambda = m/d\ \cos(\theta) \tag{2.2}$$

The single-pass linewidth (full width) of cavity can be expressed as,

$$\delta\lambda = 2\ \delta\alpha/(d\theta/d\lambda) \qquad (2.3)$$

where $\delta\alpha$ is half the angle of divergence of intra-cavity beam. Above expressions shows that the spectral bandwidth ($\delta\lambda$) directly depends upon '$\delta\alpha$' and can be improved by reducing the angle of divergence and/or by enhancing dispersive power ($d\theta/d\lambda$) of grating. The intra-cavity beam divergence can be reduced by expanding the intra-cavity beam size using beam expanders such as prisms [55] or telescope [56]. Single or a set of prisms are the preferred choice as they offer compact arrangement for the desired beam expansion. The compact layout of prisms also leads to minimized cavity length thereby allowing larger number of cavity round trips in the available inversion time and thereby attaining better dye laser spectral and spatial beam quality. Fig. 2.10 shows the schematic and representation design parameters of a pair of prism with magnification 'M' used in dye laser. The relation (Eq. 2.2) dictates that to reduce the bandwidth, the ratio (d/m) should be small which is possible for higher values of diffraction order (m).

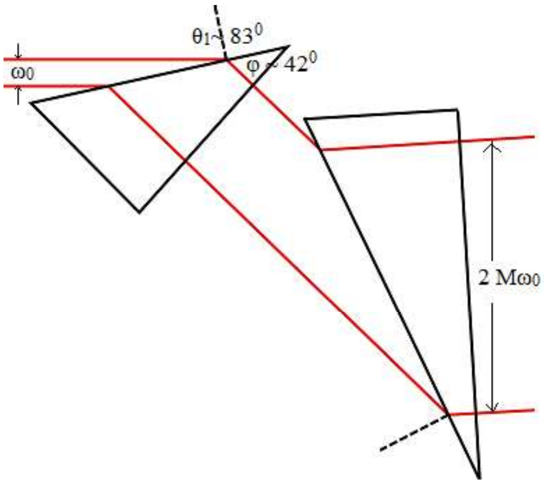

Fig. 2.10 A pair of prism for intra-cavity beam expansion in a dye laser cavity

Another factor that governs the linewidth, is the angle of incidence (θ). It should be as large as possible. All the problems stated above can be tackled by mounting the grating in grazing incidence (GIG) mode in combination with tuning plane mirror (M) as shown in Fig. 2.9(b). In this arrangement, a small part of beam incident at large angle of grazing incidence is diffracted from grating. The diffracted beam is reflected back by tuning mirror. Only a small range of wavelengths are reflected back along the direction of incidence of tuning mirror due to grating effect. Thus wavelength feedback depends upon the orientation of tuning mirror with respect to grating. The reflected beam is diffracted again by grating and returns to the dye cell. The effective angular dispersion from a combination of grating and plane tuning mirror thus can be obtained by an expression,

$$d\theta/d\lambda = 2m/d\cos(\theta) \tag{2.4}$$

where θ is angle between normal to grating and the incident beam. In this configuration, angular dispersion gets double that of Littrow mode under similar conditions. The increase in dispersion occurs due to double diffraction of the beam before returning to the dye active medium. Therefore, single-pass bandwidth of cavity as per Eq. (2.3) can be expressed as,

$$\delta\lambda = \delta\alpha\{d\cos(\theta)\}/m \tag{2.5}$$

which is half of that obtained in Littrow mode. Thus in GIG mode, grating provides improved linewidth that can be enhanced further by replacing the tuning mirror (M) by another grating.

2.4 Tunable dye lasers developed for the present research work

For Li three-step photoionization scheme, two dye laser units namely dye laser-1 and dye laser-2 have been developed. Dye laser-1 (oscillator-amplifier) with average output of ~ 550 mW at 6.5 kHz and 671 nm wavelength is developed for Li first-step resonant excitation. An in house developed dye-cell [57], is used for dye laser-1 and dye laser-2 units (Fig. 2.11). Based on dye laser cavity having a pair of prism and grating in GIG mode with plane tuning mirror, a complete dye laser oscillator mechanical setup is designed and fabricated. Figure 2.12 shows the complete assembly of individual dye laser components with motorized fitting.

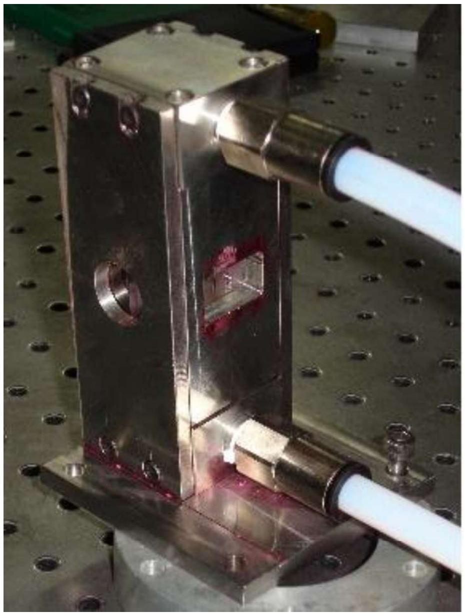

Fig. 2.11 Photograph of flowing type dye cell used in dye laser oscillator

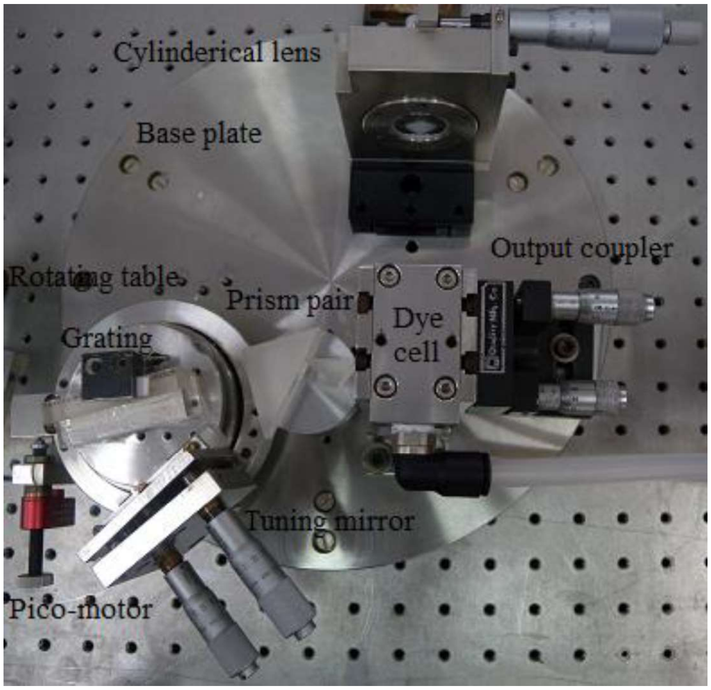

Fig. 2.12 Assembled dye laser oscillator setup

The assembly consisted of a dye cell, held in a suitable housing with ports with provision for circulation of dye. The dye cell flow was confined to attain the required flow velocity of dye solution through the active region (< 1 mm). A cylindrical lens holder is mounted in front of the dye cell. This holder has a provision to rotate the cylindrical lens. This helps in aligning of pump beam with dye cell. The lens holder is mounted on a linear moving carriage. This was very convenient for proper focusing of the pump beam on the dye cell. An output coupler holder is placed on one side of the dye cell. This can easily align the output coupler with the help of two micrometres. A post to hold the prism beam expander is positioned on other side of the dye cell along with a rotating type of circular geometry assembly. This assembly also has a non-rotating platform with fine tilts adjustments in the centre. The grating is mounted on this fixed platform. The outer ring of circular assembly was mounted on ball bearing. It provided rotational movement to the plane reflecting mirror, utilized for tuning the dye laser wavelength, with respect to grating. All these mechanical sub units were assembled on a round thick base plate.

The dye cell has a provision to be simultaneously pumped from transverse opposite side for higher and efficient pumping. The rectangular windows allow the traversal pumping from both the sides. The fluorescence emitted through circular windows along the horizontal axis of dye cell, resonates through the dye gain medium. The dimensions of gain medium are about 0.2 mm x 0.5 mm x 15 mm. The dye laser resonator geometry is of Littman type [58] with a pair of prism beam expander as described above, plane reflecting mirror, output coupler and a grating in GIG configuration. DCM dye in dimethyl sulfoxide (DMSO) solvent whose absorption and emission bands are shown in Fig. 2.8(b), is used to lase at ~ 671 nm. This dye solution served as the gain medium for oscillator & amplifier both. The dye solution concentration was optimized. It was set as 2.6 mM for oscillator and 1.2 mM for amplifier for operation at 671 nm within 630 to 675 nm spectral range. Oscillator-amplifier system is pumped by the 3.5 W & 10 W green (510.6 nm) CVL output, respectively. Short focal length (+ 10 cm) cylindrical lenses are used to focus pump laser into oscillator and amplifier. For optimum inter-pulse replacement (~ 5 times) of dye fluid, the flow velocity of dye solution in pumping region is maintained within 3.5 to 5 m/s range using dye circulators to avoid the degradation of dye. Schematic of dye laser-1 oscillator cavity is shown in Fig. 2.13.

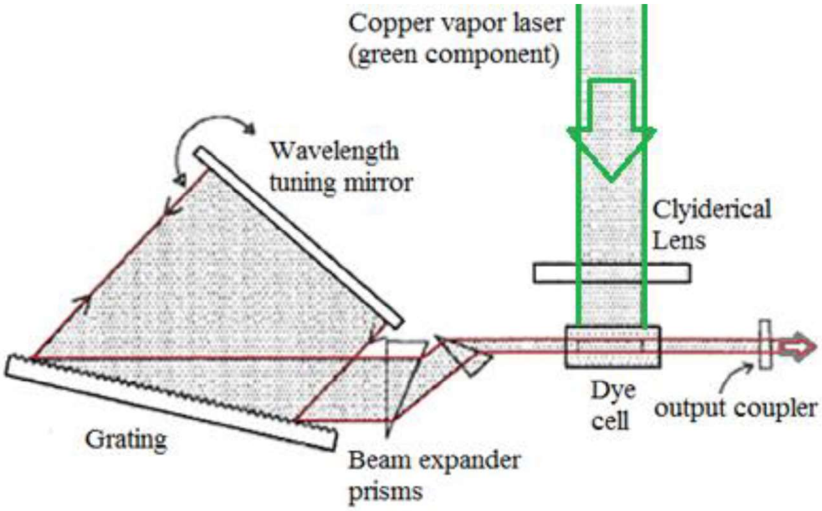

Fig. 2.13 Schematic of dye laser oscillator for Li first-step resonant excitation

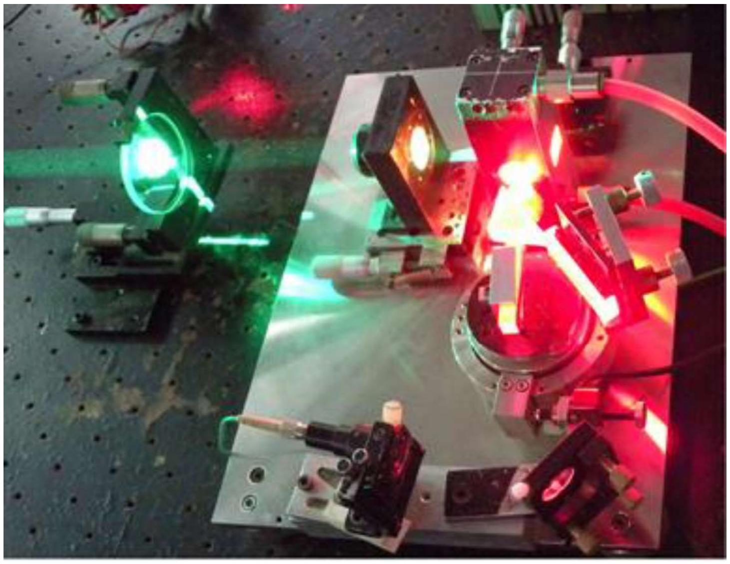

Fig. 2.14 Dye laser oscillator developed for Li first-step resonant excitation

The dye laser resonator contained a holographic grating (2400 l/mm), plane (R ~ 99.9%) tuning mirror, wedged output coupler (R ~ 20%), double prism beam-expander (M = 20) at 83^0 incidence angle as shown in Fig. 2.10. The grating is aligned in grazing-incidence-grating (GIG) mode. The overall resonator length is about 15 cm. The oscillator output is filtered spatially by a 500 μm size pinhole to reduce the amplified spontaneous emission (ASE) component. The filtered dye laser oscillator beam is then focused into amplifier dye-cell by a large focal length spherical lens (f = + 50 cm). An average amplified power of more than 550 mW is obtained at ~ 671 nm. The linewidth of dye laser-1 measured by wavelength meter (HighFinesse, WS-7) was less than 2.5 GHz. The photograph of the developed dye laser oscillator for lithium first step of excitation is shown in Fig. 2.14. On the same lines, another oscillator dye laser-2 (~2.5 GHz, 20 ns, Rh-640 dye, 0.165 mM, avg. power 150 mW, 600-625 nm) pumped by the yellow component (578.2 nm) from CVL-MOPA is also developed (Fig. 2.15) for lithium second-step of resonant excitation.

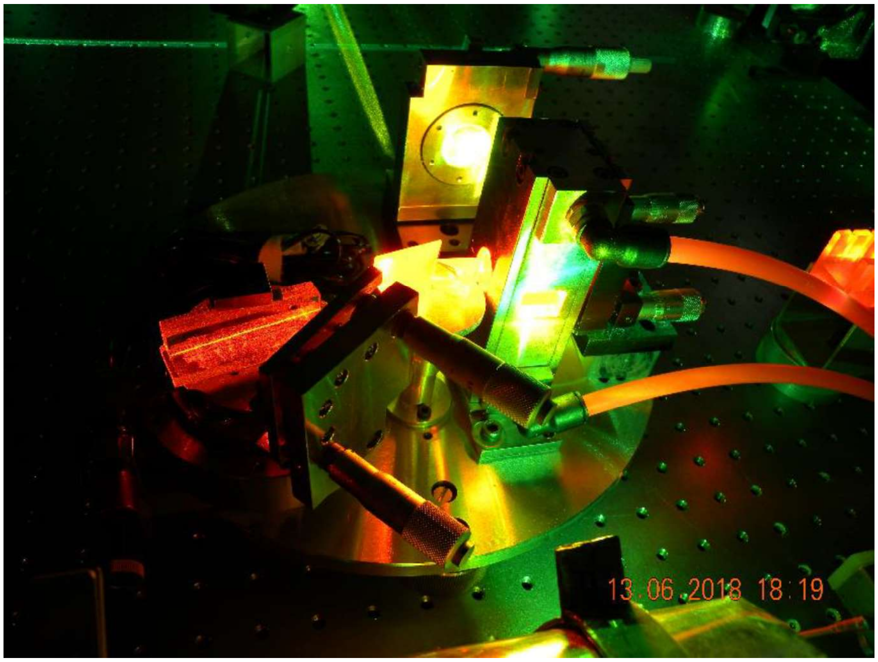

Fig. 2.15 Dye laser developed for Li second-step resonant excitation

Most of the Li photoionization studies in HC lamp, thermionic diode and TOF mass-spectrometer are carried out using nitrogen laser pumped dye laser. However, three-step OG studies in HC lamp and Li selective photoionization studies in TOF mass-spectrometer are, especially, carried out using the CVL pumped dye lasers. Such dye laser with a tuning mechanism with additional grating in Littrow mode, in place of tuning mirror, is used for N_2 laser pumped dye laser to reduce the linewidth further as shown in Figs. 2.16 and 2.17.

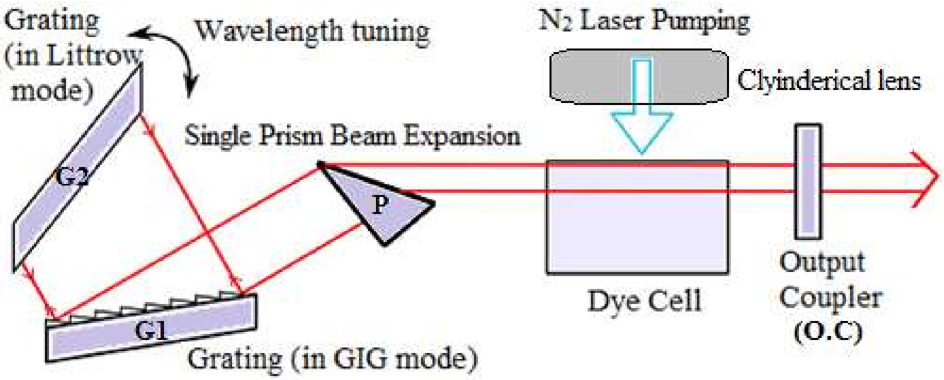

Fig. 2.16 Schematic of nitrogen laser pumped dye laser

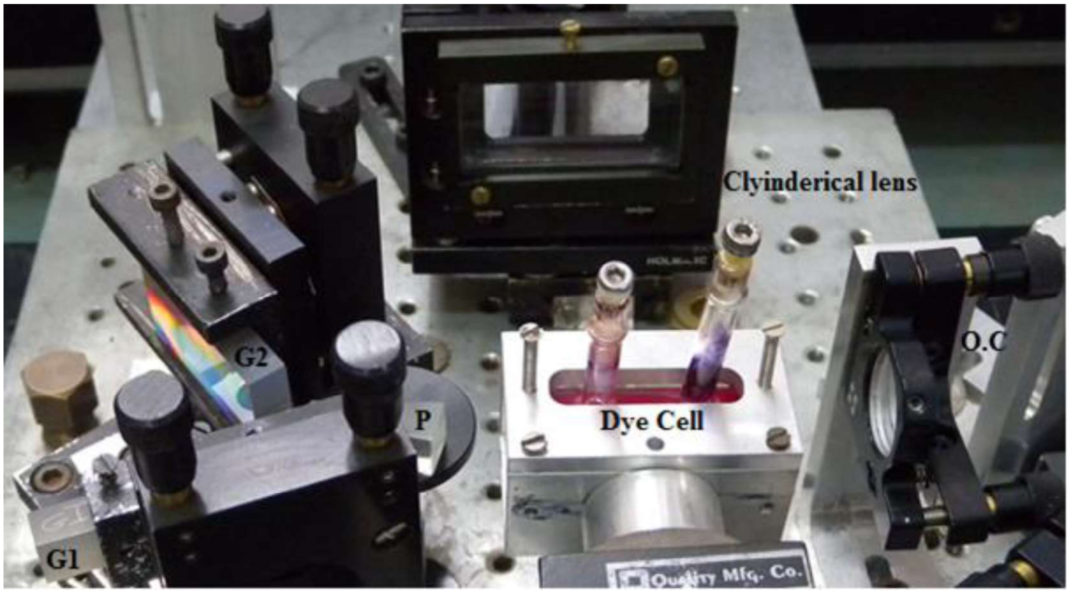

Fig. 2.17 Photograph of nitrogen laser pumped dye laser

2.5 CW ring dye laser

Dye lasers can be operated either in pulsed or continuous wave (CW) mode depending upon the pump source. The CW single mode dye laser that uses a ring cavity configuration is capable of providing the narrowest linewidth in the range of a few kHz. The most common CW single mode dye laser system is commercially available which can be pumped either by the argon-ion laser or by the diode pumped frequency doubled Nd:YAG laser. The CW ring laser makes the use of fine dye jet, birefringence filters, Brewster plate, optical diode, an output coupler and a set of thin and thick etalons as shown in Fig. 2.18 for generating the stable and narrowband laser output. The unidirectional ring cavity avoids the spatial hole-burning effects, which are responsible for the undesirable multimode oscillations in homogeneously broadened dye laser gain medium.

For the experiments that require extremely narrow linewidth, the use of CW dye laser is essential. A commercial (Radiant dye laser, GmbH) narrow linewidth (10 MHz) ring dye laser pumped by the second harmonic of Nd:YAG laser is used for saturation absorption spectroscopy (SAS) experiment in hollow cathode lamp for the measurement of Li fine, hyperfine structure and isotope-shift. As CW dye laser is a relatively low gain laser, resonator losses, triplet state losses and heating effects must be taken care of for efficient lasing. In CW dye lasers, the triplet state plays an important role as it may quench the population inversion. In CW dye lasers, two types of quenching processes, either chemical or mechanical are used in order to quench the triplet state population. Mechanical quenching is a very popular technique for the triplet state quenching. Therefore, a high flow velocity dye jet is generally used in CW dye lasers. A drawback of CW dye lasers with standing wave cavities, is the spatial-hole burning. This impedes the single-mode operation. This process can be eluded by unidirectional travelling wave operation in ring resonators using an optical diode. The schematic layout of the used CW ring dye laser is shown in 2.18.

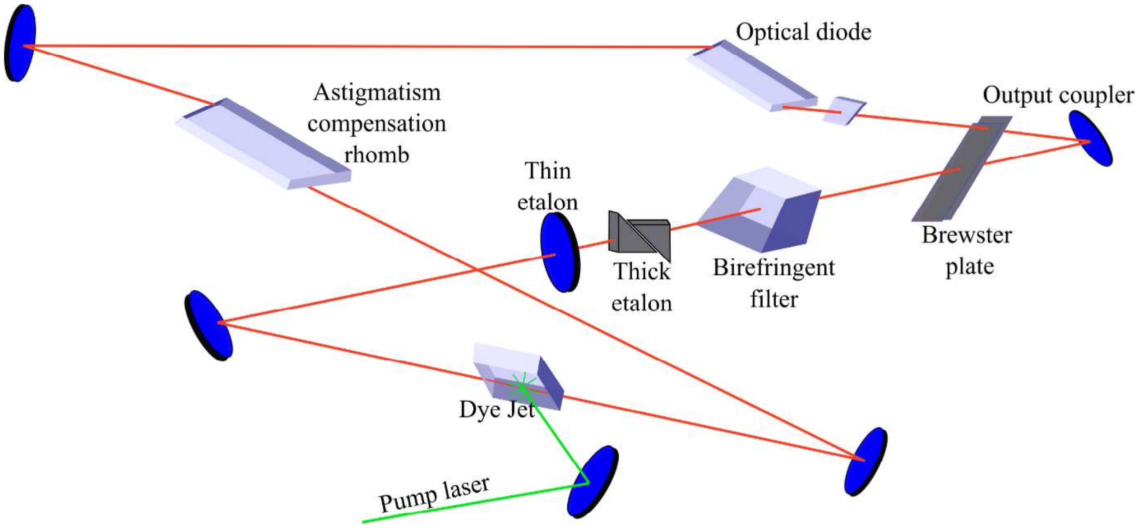

Fig. 2.18 Schematic of Nd:YAG pumped CW ring dye laser

2.6 Wavelength scanner for precision tuning of dye laser

The precise wavelength tuning of dye laser and corresponding data logging are required to record an OG or photoionization spectrum. This could be obtained by passing a tunable dye laser beam into an OG cell and monitoring the produced OG signals along with control of dye laser tuning mechanism see, Fig. 2.19. This setup uses the CVL pumped dye laser, Eu/Ne HC lamp, motorized scanning, wave-meter, boxcar integrator and data acquisition card.

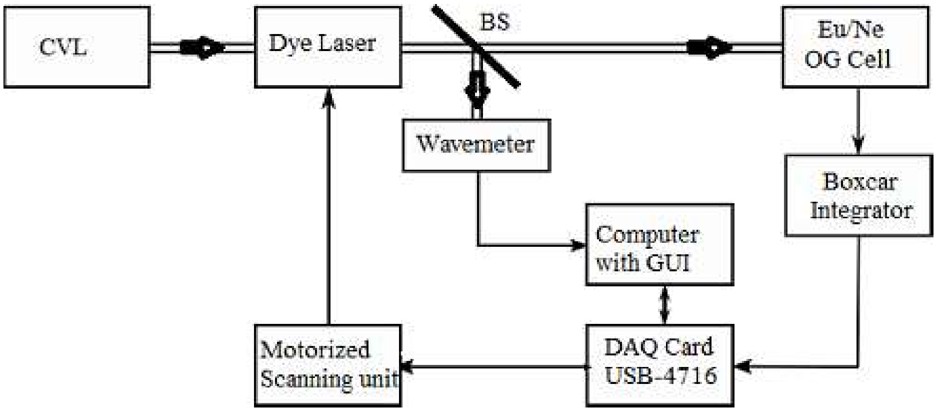

Fig. 2.19 Block diagram of developed wavelength scanner unit

Manual control of dye laser tuning setups is a tiring job and not very much accurate. It is practically impossible to achieve a precise control on tuning and its speed without computer. Therefore, a wavelength scanner and its control based on Lab-View software is developed for accurate tuning of dye laser to desired transitions of the species present in HC discharge to obtain the corresponding OG signals. User selectable wavelength tuning range at controlled speed is an important requirement in spectroscopy experiments. The dye laser wavelength can be scanned within its tuning range by changing an angle of tuning mirror fitted in a high precision mount. In present setup, the tuning mirror is mounted on a rotating table which is driven by a pico-motor coupled to it, as shown in Fig. 2.12. The table rotates around a concentric fixed disc on which dye laser grating is mounted in grazing incidence configuration. The computerized control of pico-motor actuator is developed for controlling the precise movement of tuning mirror. A graphical user interface (GUI) provides the user friendly interface with soft panel controls to select the wavelength scanning range with starting and ending wavelengths, wavelength scanning speed and a particular wavelength to lock the dye laser. The tuned wavelengths and corresponding signals obtained from OG cell (HC lamp) are plotted in the form of online graph on display panel. A particular area of interest of this graph can be zoomed in another opening screen window. It also provides real time graph between wavelength and OG signal intensity. The pico-motor actuator (New Focus, model: 8302) used, has movement resolution of 30 pm/step. A data acquisition card (Advantech, USB-4716) is used for acquiring the OG signal and generating control signals for driver of pico-motor. The flexibility to reach the desired wavelength at a fast speed and then scanning over the range of interest at a very slow user selectable speed, enables the detection of very closely spaced absorption lines with ease which otherwise may be overlook. The setup provides several advantages over manual operation of dye laser such as speed, precision and post processing of recorded data. In this setup, the wavelength scanning and control for pulsed dye laser are established using the CVL pumped dye laser as described earlier in text. A commercial Eu/Ne HC lamp (Heraeus), is used to generate the OG signals. The europium (Eu) has only two stable isotopes with large isotope-shift similar to lithium. The dye laser with Rh-6G dye is operated at pulse repetition rate of 6.5 kHz. A Fizeau interferometer based wavelength meter (WS-7) is used to monitor and display the laser wavelengths. This wavelength scanner can be used with pulsed as well as CW dye lasers. The scanner GUI with an excerpt of Eu/Ne OG spectrum recorded within small wavelength range (~ 1 nm) is shown in Fig. 2.20. A Eu/Ne OG spectrum is also recorded using the boxcar integrator for full dye tuning range to calibrate the dye laser developed (Fig. 2.21). The sharp and clearly resolved OG spectrum obtained with high signal to noise ratio proves the efficient working of wavelength scanner for precision tuning of dye laser and experimental data logging. It is anticipated that similar setup with minor changes would be useful for laser wavelength calibration and frequency stabilization frequently needed in spectroscopy labs.

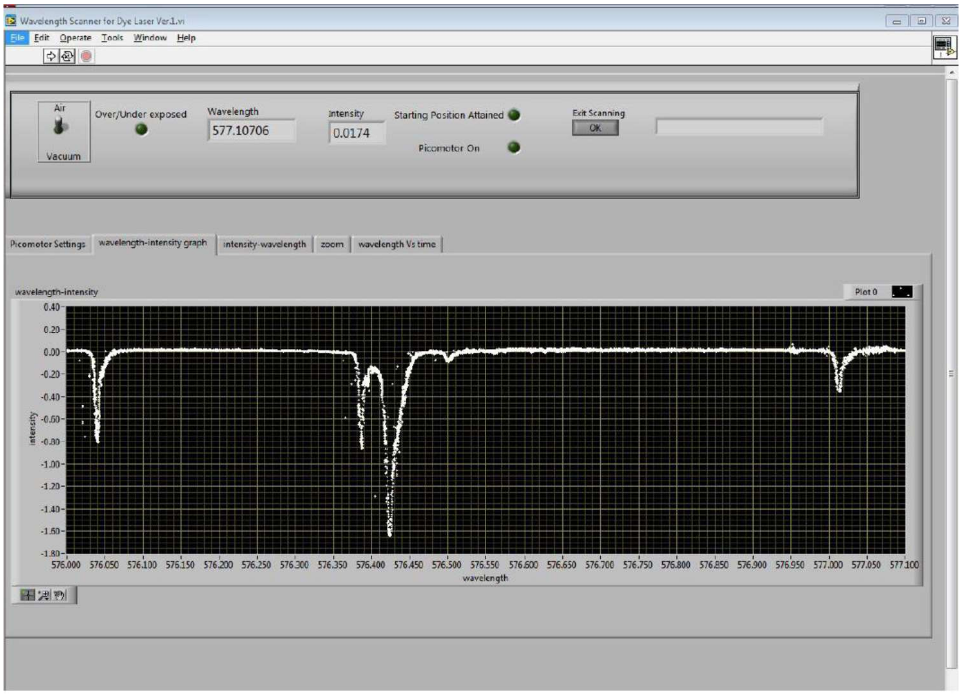

Wavelength Scanner for Dye Laser Ver.1.vi

Wavelength: 577.10706

Intensity: 0.0174

Fig. 2.20 User interface of wavelength scanner unit with recorded OG spectrum

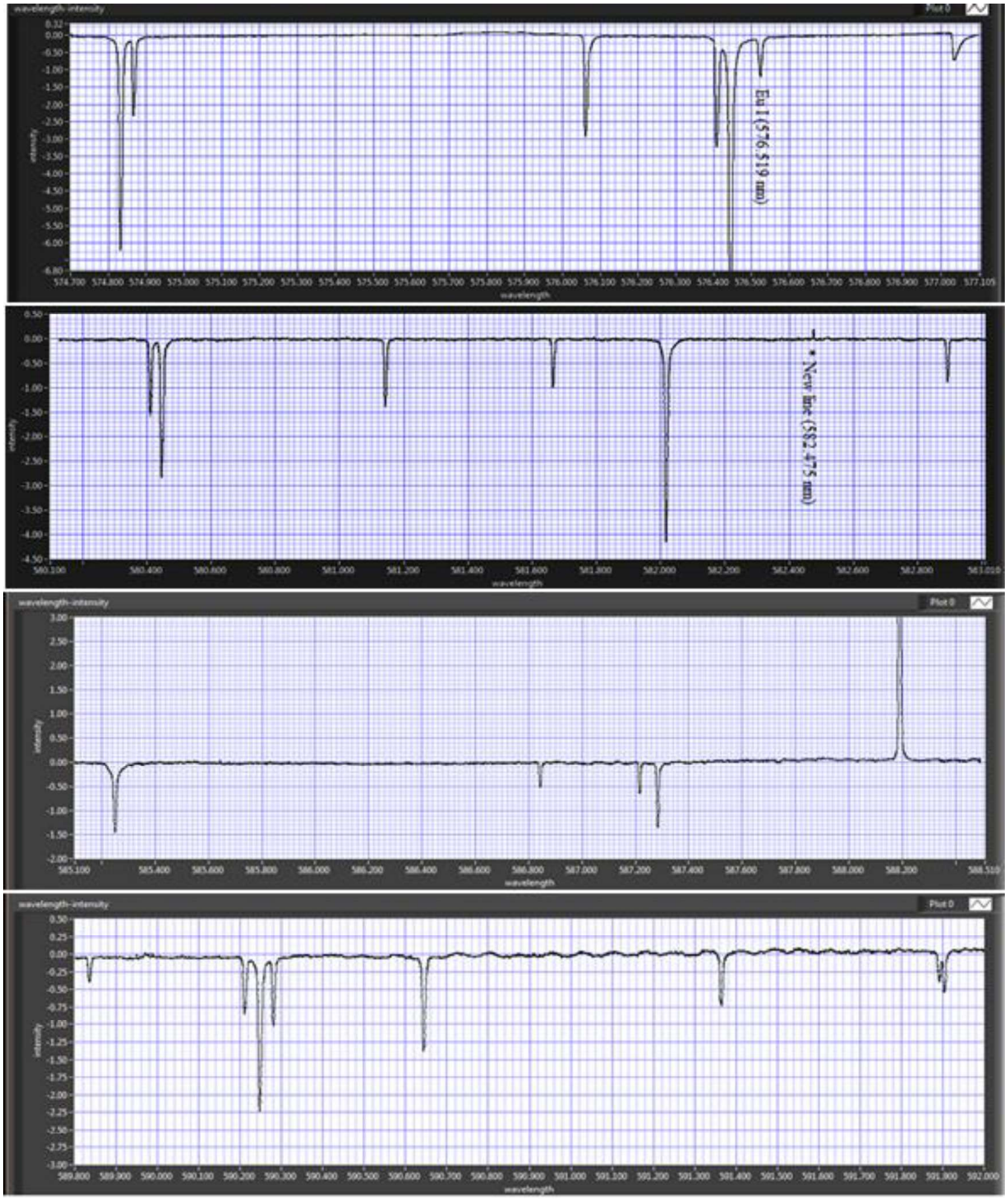

Fig. 2.21 A complete Eu/Ne OG spectrum recorded within full dye laser tuning range

This wavelength scanner unit, however in association with another Li HC lamp, is utilized for calibrating the dye lasers developed, as described in chapter-3. Also, it has been used in precise tuning of dye laser wavelengths, needed for the Li selective photoionization in thermionic diode and TOF mass spectrometry experiments, as described in chapters-5 and 6.

2.7 Thermionic diode detector

Thermionic diode can be used as a sensitive ion-detector that has many advantages over conventional ion detectors. In seeking the detection method of step-wise lithium excitation and measuring of its photoionization cross section, a thermionic diode turned out to be most suitable device for the present experiments. It is a positive ion detector with low background noise. It makes possible counting of the each ions produced during the photoionization process. It also suits well to detect the high lying Rydberg atom transitions [59].

2.7.1 Space charge in thermionic diode

A thermionic diode is a space charge based device similar to an ordinary vacuum diode tube with two electrodes, an electron emitting cathode and the electron collecting coaxial cylindrical anode. The form of such thermionic diode may vary but working principle is essentially the same. Thin metal wire used as a cathode of thermionic diode emits the electrons when heated to high temperature. The emitted electrons move towards the anode. The emission rate of electrons from cathode depends upon type of material used, heating temperature and its surrounding gas. The fresh electrons emitted from cathode experience the push back effect from earlier emitted high speed electrons due to repulsion between similar charges before they reach the anode. At sufficiently high temperature, a cloud of electron or space charge forms in between the cathode and anode in a steady state condition. This space charge develops a potential well between the electrodes which impedes the further flow of electrons and detector in this condition is said to be in space charge limited mode.

2.7.2 Thermionic diode as an ion-detector

The space charge limited thermionic diode mode of operation can be used as a sensitive ion detector. When a positive ion enters into the space charge region, the potential well between the cathode and anode is lowered because of space charge neutralization effect by the positive ion. This decrease in potential well allows more electrons to cross through the space charge region and thus results in an increase in electron current. If the positive ion is supposed to stay for a reasonably longer period (Δt_{ion}) than electron (Δt_{el}) into the space charge before combining with electrons or deposits on the cathode, the increased electron current offers a substantial gain to the ion signal. During its stay period it compensates the negative space charge and thus allows additional number of ($M = \Delta t_{ion}/ \Delta t_{el}$) electrons to move out of the space charge zone. If N number of ions are produced/sec, then increment in diode current is governed by a factor 'eMN'. The magnification in current can attain the values up to $M = 10^5$. The actual gain (i.e. the magnification factor) of a detector depends upon many factors including its geometry, cathode and anode materials, temperature and operating conditions etc. The cathode emission current is related with temperature [60] as,

$$I_0 = AT^2 \exp(-U/kT_c) \qquad (2.6)$$

Where A & U are the constants dependent upon material and T_c is cathode temperature. The relation between anode current and potential is given [61] by,

$$I = K(V_a^{3/2})/ R\beta^2 \qquad (2.7)$$

where $K = (2/9)[2e/m]^{1/2}$, 'm' is the mass of electron and 'β' is given as,

$$\beta = \gamma - (2/5)\,\gamma^2 + (11/120)\,\gamma^3 - \ldots\ldots \qquad (2.8)$$

$$\text{and } \gamma = \ln (R/a) \qquad (2.9)$$

where 'R, a' are the radius of coaxial anode and cathode filament, respectively. The value of β^2 approaches to unity if 'R' is much greater than 'a'. In our design, it is kept greater than 100. The anode current therefore increases with anode potential in space charge limited mode. The potential distribution along radius of cylindrical anode and position of minimum point depend on various parameters, such as the cathode temperature, anode potential (V_a), radius (R/a) ratio of anode to cathode and the material of anode and cathode both.

2.7.3 Advantages of thermionic diode detector

The thermionic diode detector is simple and cost-effective device for laser spectroscopy with high gain, good linearity and time stability. Its sensitivity is very high, although limited by the shot noise and the flicker noise. These device offers large dynamic range for strong photoionization signals without saturation effects, particularly suited for the spectroscopy of high lying Rydberg states atom and photoionization [59]. There is also a statistical advantage of measuring the photo-ions rather than attenuated photons as in classical measurements (photographic or photo-electronic). The more details on thermionic diode working and its utilization for selective Li photoionization spectroscopy are given in chapter-5.

2.8 Time-of–flight mass-spectrometer

The time of flight mass-spectrometer (TOFMS) is basically a crucial tool for mass analysis. It can separate the ions of different masses based on time of flight principle. Mass spectrometry contributed a lot to the understanding of structure of elementary matter and their isotopic abundance. The concept of TOF mass spectrometer was presented first time by William Stephens [62] in 1946. The design of a linear TOF mass spectrometer was first published in 1955 by Wiley and McLaren [63]. After 1990, the TOFMS gained significant popularity. The availability of fast electronics, data acquisition along with pulsed ionization sources finally pushed the TOFMS to one of the top mass spectrometric technique. The TOF mass analyser are thoroughly reviewed by Cotter [64], Guilhaus [65] and Mamyrin [66] in different years. A linear TOFMS is used in the present thesis work for the study of Li isotope separation.

2.8.1 Principle of time-of-flight mass-spectrometer

The simple and straightforward TOFMS consist of an ion source and detector at the opposite end of flight tube evacuated to low pressure of 10^{-7} to 10^{-8} mbar. The species to be analysed are usually laser ionized in ion source. The ions so created are extracted from ion source and accelerated towards the detector by means of an applied electric field. These ions get separated according to their mass to charge (m/z) ratio in flight tube field free region. Ions reach the detector according to their masses. The heavier ions reach after lighter ions. The unique advantage of TOFMS is its speed. It can record complete mass spectrum every few microseconds. The entire mass spectrum can be obtained for each laser or accelerating pulse.

2.8.2 Linear time-of-flight mass-spectrometer

The most commonly used TOF mass spectrometers are of linear type. Their design is similar to Wiley and McLaren model [63]. A linear TOFMS consists of a pulsed ion-source that produces and focuses the ions in time and space coordinates on detector placed at field free drift path end. A linear TOF mass spectrometer with low mass resolution is simpler in design, however a careful choice on geometrical arrangements and applied voltages are needed to achieve high mass resolution [63]. A typical TOF mass spectrometer with single field grid consisting of a pulsed ion source with small source-extraction region (s), drift region (D) and ion-detector is shown in Fig. 2.22. An electric field (E = V/s) with potential V of same polarity as that of the ions is applied to ion source region. The drift region is bound by an extraction grid and the grid just before the detector. Both the grids at ground potential make the drift region field free, otherwise linear trajectory of the ions may be affected.

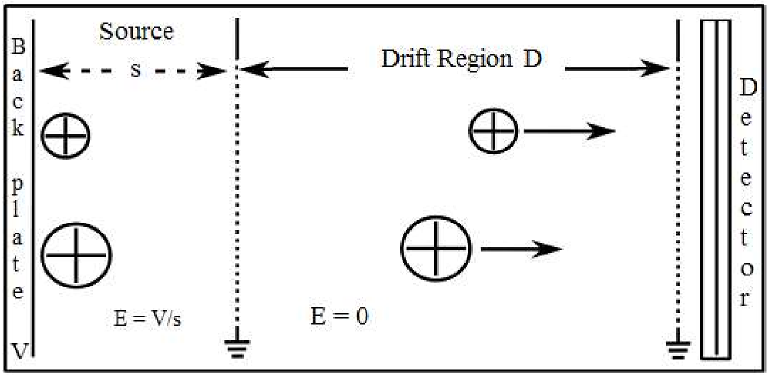

Fig. 2.22 Schematic of a linear TOF mass-spectrometer

2.8.3 Mass-resolution

Ions in gas phase are produced either by electron impact or photoionization in the centre of ion source or directly on surface of back plate by the action of laser ablation. For the simplest case, let us first assume that all the ions are produced with zero initial velocity (v_0) on surface of back plate at potential 'V'. Thus applied electric field accelerate the ions with charge q through the source-extraction region and energizes to the same kinetic energy (K.E). Therefore,

$$K.E = (mv^2)/2 = qV \tag{2.10}$$

The ions would drift in the field free region with velocity

$$v = (2qV/m)^{1/2} \tag{2.11}$$

and the flight time is given by

$$t_D = D\ (m/2q.s.E)^{1/2} \tag{2.12}$$

If the ions are generated at distance 's' away in source region and these ions spend a short time interval where their velocities are not constant. Then this time (t_s) also contribute to their overall flight time and the total flight time would be

$$t = t_s + t_D = (m/2q.s.E)^{1/2}\ [2s + D] \tag{2.13}$$

that again shows square root dependence of flight time upon ion mass which gives an expression for mass-resolution as

$$m/\Delta m = t/2\Delta t \tag{2.14}$$

where Δt is measured as full width at half maximum at detector. Resolution is defined as the largest mass with adjacent masses separated completely. As the mass resolution is inversely proportional to time resolution Δt, therefore many factors such as laser focal spot, pulse width and detector response that influence the Δt should be optimum. Time spread in ion formation results in the ions which enter the drift zone at different times but maintain a constant time difference Δt as they reach the detector. The effect due to uncertainty in time of ion formation on mass resolution can be minimized using longer flight tubes [64]. This will have the effect of increasing time (t), while maintaining constant Δt. The same can be true for real time distribution that arises from laser pulse width.

Now, consider actual case of the ions formed at position 's_0' located approximately at a midpoint of extraction field; these are subjected to Boltzmann distribution of velocity (v_0) with initial translational energy U_0. The ions move in all direction and are guided by an applied electric field. The ions which initially move towards detector reach there earlier as compared to those moving away from the detector. The latter ions are first decelerated to zero speed. Then again re-accelerated and pass through the original position. The deceleration time and re-acceleration to reach up to their original position is referred as turnaround time and is given by,

$$t_{\pm} = 2\,|v_0|\,m/q.E \qquad (2.15)$$

$$\text{or } t_{\pm} = (2/q.E)\,(2mU_0)^{1/2} \qquad (2.16)$$

These two ions with same speed but moving in opposite direction will exit the ion source with same energy ($q.s.E + U_0$) as those of initially moving in forward direction. But they remain separated by turnaround time ($t_{\pm}$). As drift region length is increased, this time separation becomes smaller as compared to total flight time. Equation (2.16) also shows that turnaround time, hence the resulting peak broadening can be minimized by decreasing the initial velocity distribution of the ions by increasing accelerating field strength. The time (T_s) for an ion to travel a distance 's' from initial position 's_0' to the beginning of drift region can be obtained from an equation of ion motion as,

$$s = s_0 + v_0 t + (q.E/2m)\,t^2 \qquad (2.17)$$

$$T_s = [\{2m\,(U_0 + q.s.E)\}^{1/2} \pm (2mU_0)^{1/2}]/q.E \qquad (2.18)$$

and drift velocity $V_D = [2(U_0 + q.s.E)/m]^{1/2}$ for drift length 'D' gives the drift time as,

$$t_D = (2m)^{1/2}[D/2(U_0 + q.s.E)^{1/2}] \qquad (2.19)$$

Therefore, total time an ion would take to reach the detector can be obtained by the sum (T_S + t_D), which gives a well-known equation as given by Wiley and McLaren[63],

$$t = [(2m)^{1/2}\{(U_0 + q.s.E)^{1/2} \pm (U_0)^{1/2}\}]/q.E + (2m)^{1/2} D/2(U_0 + q.s.E)^{1/2} \qquad (2.20)$$

The effect of turnaround time can be minimized by increasing D, however long drift length also creates technical problems such as need of large size detector and strong vacuum system.

2.8.4 Spatial resolution

The focusing of spatially distributed initial ions depends on two opposing factors: (i) ions initially more distant from detector, spend larger time in acceleration region, (ii) these distant ions have shorter drift time. This is because, they get higher drift velocity as they spend more time in acceleration region. If $U_0 = 0$, then differentiation of Eq. (2.20) gives,

$$dt/ds\ (U_0 = 0) = (m/2q.s.E)^{1/2}\,[1- D/2s] \qquad (2.21)$$

This function reaches minimum, when D = 2s. Hence, the spatial focusing is obtained, on plane at distance 2s along drift region, where ‘s’ is the distance from extraction grid to the centre of ionization zone. This focusing condition is same for all the ions and is independent of their total energy. It is evident, that location of space-focus plane is mass independent. On the other hand, ions of different mass are focused at space focus plane at different times. However, mass dispersion for this small distance (2s) is not sufficient to allow the location of a detector at this point. Thus, one solution is to move the space focus plane to much farther away from the ions source by using dual-stage extraction method.

2.8.5 Time-of-flight mass-spectrometer with dual-stage extraction

There are two ways to correct the loss of resolution due to spatial distribution of ion formation. Either, devise a two-stage extraction system or consider the space focus plane to be virtual source with ions differing only in kinetic energy and then focused them using reflectron geometry [67]. In Fig. 2.23, dual stage extraction scheme is depicted. This scheme pushes the space focus plane to an entrance of detector to more distant point. In instruments that utilize two stage extraction, the second stage extraction field (E_d) is much larger than first (E_s) with larger ratio (E_d /E_s) to move the space-focus plane farther away from source [64]. The flight time of ions reaching the detector for dual stage extraction can be obtained using the gas kinetic theory that will also determine the physical parameters of mass spectrometer. These include spacing between the grids, the acceleration potential and the drift tube length.

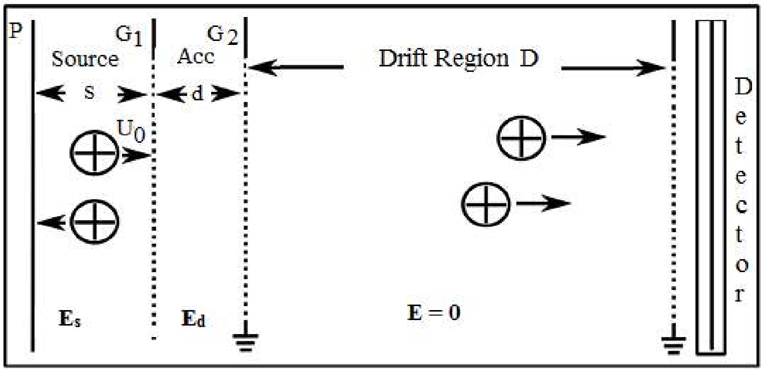

Fig. 2.23 Schematic of TOFMS with dual-stage extraction

If V_0 is the potential difference applied between back plate P and grid G_1 and the V_1 between grid G_1 and G_2. The ions produced by photoionization in source region will be first extracted by an electric field ($E_s = V_0/s$) which then will experience a second field ($E_d = V_1/d$) in acceleration region. If U_0 be initial energy of the ions, then total energy U gained before entering into the drift region would be,

$$U = U_0 + q.s.E_s + q.d.E_d \tag{2.22}$$

and time of flight is obtained [68] by an expression,

$$T(U_0, s) = T_s + T_d + T_D \tag{2.23}$$

where

$$T_s = [(2m)^{1/2}\{(U_0 + q.s.E_s)^{1/2} \pm (U_0)^{1/2}\}]/q.E_s \tag{2.24}$$

$$T_d = [(2m)^{1/2}\{(U)^{1/2} - (U_0 + q.s.E_s)^{1/2}\}]/q.E_d \quad (2.25)$$

$$T_D = (2m)^{1/2} D/2\, U^{1/2} \quad (2.26)$$

The + and − sign in T_s expression correspond to initial velocities away from and towards the detector. If initial energy $U_0 = 0$ and the ions are formed at $s = s_0$, then Eq. 2.22 gives total energy of the ions after the acceleration in two stage extraction/acceleration regions as,

$$U_t = q.s_0.E_s + q.d.E_d \quad (2.27)$$

Thus expression for time of flight becomes as,

$$T\,(0, s_0\,) = \sqrt{\frac{m}{2U_t}}[2s_0\sqrt{k_0} + 2d\,\frac{\sqrt{k_0}}{\sqrt{k_0}+1} + D] \quad (2.28)$$

$$\text{where,}\;\; k_0 = 1 + \frac{dE_d}{s_0E} \quad (2.29)$$

For constant electric field and grid spacing, the mass of ions can be calibrated from time of flight as $m\ \alpha\ T^2$, which determines the mass resolution as $R\ (m/\Delta m) = T/2(\Delta T)$. In this case, condition (Eq. 2.21) for first order space-focus plane or the plane of catch up where energy difference (ΔU) between iso-mass ions due to initial spatial distribution vanishes, can be found by setting $\frac{dT}{ds} = 0$. That yields,

$$D = 2s_0k_0^{\frac{3}{2}}(1 - \frac{1}{k_0 + \sqrt{k_0}}\frac{d}{s_0}) \quad (2.30)$$

Here, all the parameters except k_0 are constant. Thus k_0 can be used to determine the position of detector where all the ions with same (m/q) ratio produced without any time lag and zero initial velocities reach at the same time. This will gives suitable position of the detector where broadening of the ion peak will be reduced drastically. Since accurate mechanically fitting of the detector in focal plane is difficult, therefore k_0 makes it possible and easy to achieve the ions space focusing at the plane where the detector is already positioned, by adjusting the electric field values of extraction and accelerating field regions. The advantage of dual stage acceleration over single acceleration region TOF mass spectrometer is that one can adjust an additional control parameter E_d to obtain the better resolution in an easier way.

2.8.6 Fabrication of time-of-flight mass-spectrometer

A typical layout of linear time-of-flight mass-spectrometer that has been utilized for Li selective photoionization studies, is shown in Fig. 2.24. A vacuum compatible high quality steel (SS 304), is used to fabricate key components of the TOF mass-spectrometer. These are the TOF vacuum housing, laser ion source, grid assembly and the flight tube. It consists of a back plate (P) followed by the two acceleration grids (G_1, G_2) and an ion-detector. These lies at distance s = 8 mm, (s + d) = 43 mm and (s + d + D) = 1243 mm, apart from the back plate. In TOF vacuum chamber, coupled with 1.2 meter long, field free flight tube, the low pressure of an order 10^{-6} mbar is generated using the two oil diffusion pumps driven by rotary pump.

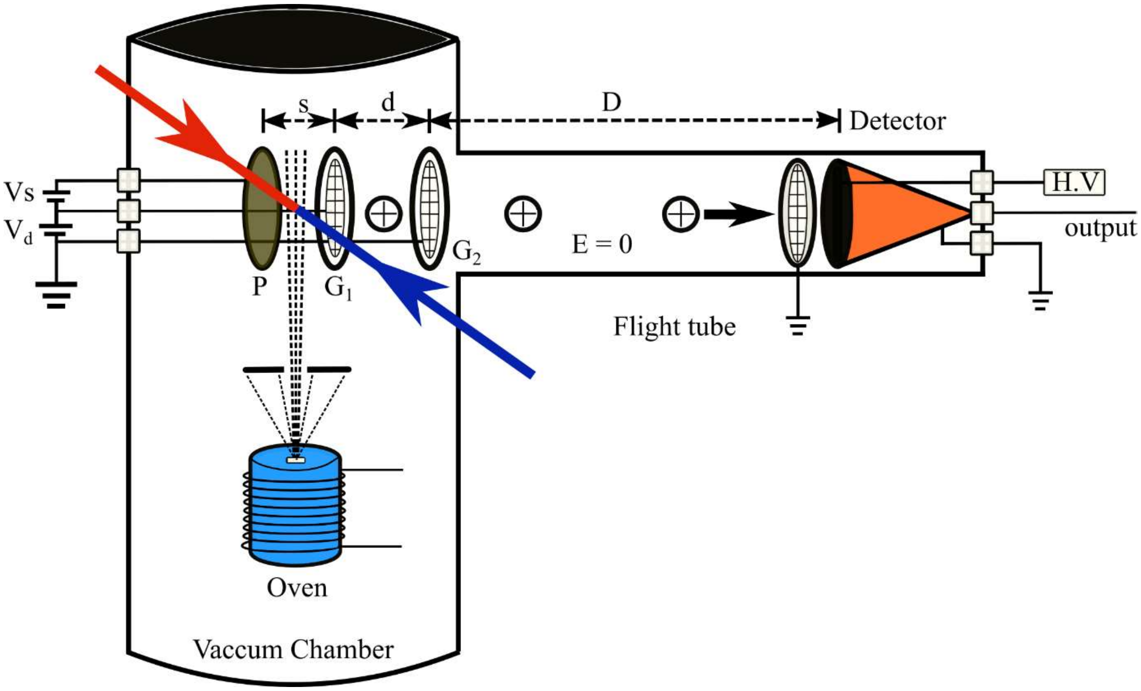

Fig. 2.24 Layout of two-stage extraction/acceleration TOFMS

An effusive type of atomic beam source [67,68] as described below is installed in TOF vacuum chamber. Li atomic beam emanating from an oven reaches the extraction/ionization region of mass spectrometer. Here, it orthogonally interacts with incident exciter (red) and ionizer (blue) laser beams from opposite sides (Fig. 2.24). In this process, Li photo-ions are produced those are extracted with application of an electric field ~ 300 V/cm in s = 8 mm ionization region. The electric field ~ 450 V/cm in d = 35 mm long region, accelerate the created ions to high kinetic energy. These photo-ions are separated according to their mass to charge ratio (m/z) after travelling through 1.2 meter long field free flight region (D). The positive charge, thus produced, is collected by the ion-detector (KBL-25). This detector is operated in the linear region at negative potential of ~ 2 kV. The photo-ion current is measured directly on digital oscilloscope. The delay between ionizing and exciting laser pulse should be optimized to extract all the excited population before its decay to ground state, to achieve the high photo-ionization efficiency for each isotopes. The ion-detector output is averaged over 100 or more acquisitions in order to compensate the effects of pulse to pulse variations in laser energy. To average out the noise, the signal from detector is processed through boxcar integrator. It is then further acquired on oscilloscope and computer to analyse the signals. The oscilloscope is triggered by a fast Si photodiode. The ion detector assembly and the connecting cable wires are shielded and grounded properly. In this way, the effects of laser generated electro-magnetic and background noise can be minimized.

2.8.7 Atomic beam source

A well collimated lithium atomic beam is generated to reduce the Doppler broadening effects. In this direction, the atomic beam source is designed with cylindrical stainless steel oven of inner diameter 12 mm, volume (~ 2800 mm^3) and lithium holding capacity ~ 1.5 gm. Corrosion resistant high quality stainless steel (316 SS) is used for its construction. Figure 2.25 shows the design of atomic beam source. It is compact and can be detached from TOF vacuum chamber to reload and replace the Li sample, easily. The oven is installed just below the ionization/extraction region of TOFMS. Its repair is also easy and less time consuming.

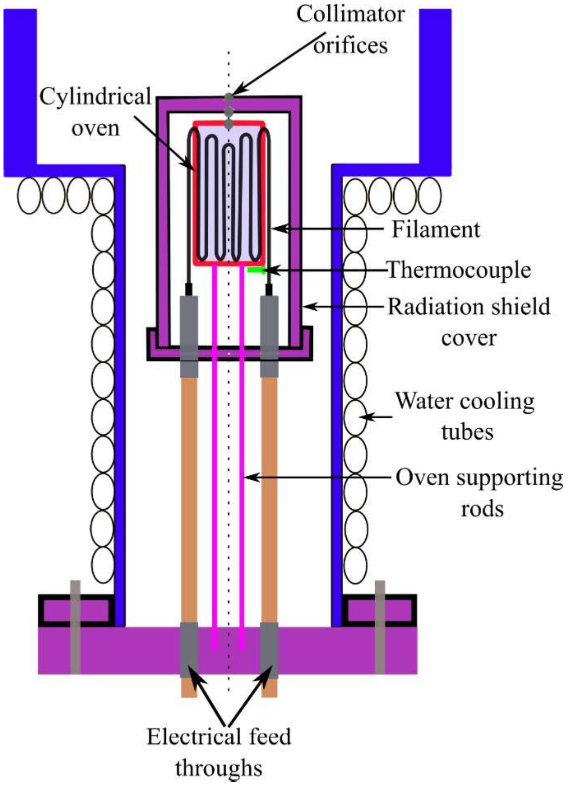

Fig. 2.25 Li atomic beam source

The Li atomic gas temperature is monitored using the ‘K’ type thermocouple with an accuracy of ± 1 ^{0}C. It is directly mounted on outer surface of the oven. The small fluctuations in atomic beam flux are controlled precisely by monitoring dc heating current in filament using PID controller. The oven is surrounded by a multilayer molybdenum radiation shield to minimize radiative heat losses. The Li atomic beam exit through a hole of 1 mm diameter. The filament current is set at 16 A to attain the working temperature of 525 ^{0}C. The atomic collisional mean free path of ~ 24 cm, calculated as ($L = 1/n\sigma$), is found much higher than the diameter of exit hole. This confirms the transparent flow of lithium atoms. The oven jacket is surrounded by copper water cooling tubes. This is carried out to suppress any possibility of thermal ions emission or the electrons which may otherwise register the undesired background events on ion-detector. The number of the atoms that effuse without collisions at an average speed of 1.35 x 10^5 cm/sec, are calculated as ~ 3.7 x 10^{16} atoms/sec. The atom density in the oven is estimated from its temperature and the available Li vapour pressure curves. The main limiting factors that may restrict the efficiency of TOF system are the temporal and spatial overlap mismatch of atomic beam with incident laser beams. The possible error in temporal overlapping can be found as a small fraction,

$$F_t = d_L (\nu_{rep}/\bar{\upsilon}) \tag{2.31}$$

where ν_{rep} is the laser pulse repetition rate, d_L the laser beam diameter in interaction region, and $\bar{\upsilon}$ the average thermal speed of the atoms. Therefore, an average speed $\bar{\upsilon}$ = 1.35 x 10^5 cm/sec, beam diameter d_L ~ 1 mm, repetition rate of laser pulse ν_{rep} ~ 6.5 kHz, contribute the temporal fraction F_t = ~ 0.005. Similarly, the spatial overlap 'F_s' can be estimated as,

$$F_s = (\kappa/\pi)\, \Delta\Omega \tag{2.32}$$

where F_s is fraction of the atoms that enter into the region of laser interaction within a small solid angle $\Delta\Omega$ ($\Delta\Omega \leq 2\pi$) at $\theta \approx 0^0$, out of total number of the atoms evaporated. The factor κ depends upon the geometry of atomic source [68] and θ is the angle with beam limiting diaphragm symmetry axis. For the effusion of atoms from a small oven channel (r = 0.5 mm, l = 25 mm), the evaporated number of atoms into the solid angle ($\Delta\Omega$) increases by a factor κ = $3l/8r$. For an area of interaction d_L x s (with s ≥ d_L, s = FWHM of atomic beam,) having a separation 'b' from atomic source, the fraction of atoms that enter into the interaction zone is,

$$F_s = (\kappa/\pi)\, [d_L\, s/\pi b^2] \tag{2.33}$$

For s = 5 mm, d_L = 1 mm, b = 5 mm and κ = 18.7, the Fs value is ~ 0.012. In this way, a total fraction of evaporated atoms into the interaction zone is, $F_{tot.} = F_s \times F_t \approx 5.7 \times 10^{-5}$. It gives an estimate of overall atom density (~ 10^{12} atoms/cm^3) that undergoes interaction with laser. The photographs of different elements of the time-of-flight mass-spectrometer are shown stage-wise in the Figs 2.26 to 2.30. Figure 2.26 shows the assembly of atomic beam source as described above. In TOFMS, the atomic beam source needs frequent maintenance because of corrosion problems due resistive heating at high current and clogging of vapour source, therefore it is made detachable and compact for easier maintenance and sample loading. The vertical mounting design of heating filament benefits in two ways; first it can sustain higher current without sagging, secondly magnetic effects due to high current are also minimized.

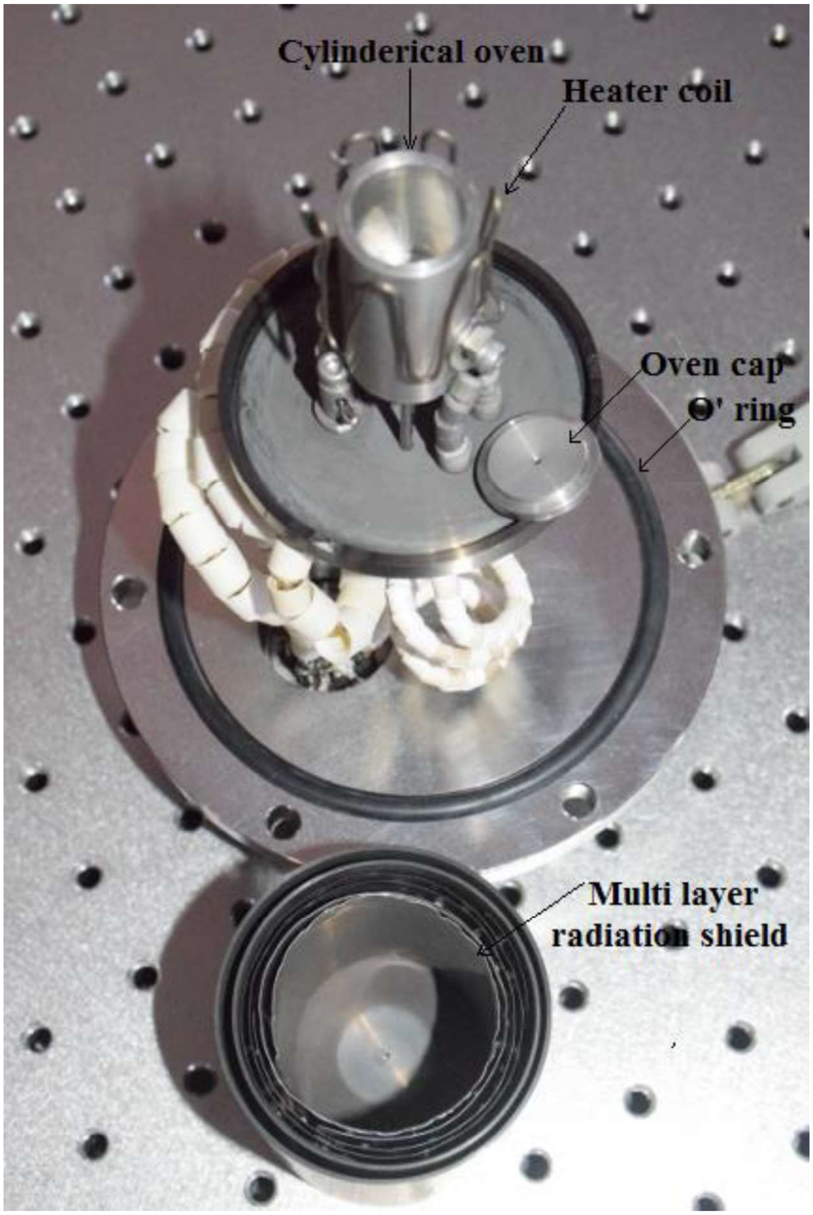

Fig. 2.26 Lithium atomic beam source assembly

The oven is heated by electrical heating of the tantalum filament of 0.8 mm diameter by radiative heat transfer mechanism. The oven get heat directly from the filament as well as heat reflected by the multilayer molybdenum radiation shield. A round tray is mounted just below the oven to collect the remaining condescend material after evaporation. The whole assembly is further mounted on a thick stainless steel disc which is clamped through 'O' ring to vacuum chamber of the TOF mass spectrometer. Good quality home built electrical feedthroughs are used to supply the high current into filament. The ceramic beads provide good insulation to the connecting wires from feedthrough to filament. The design of the oven cap is push fit type. Two atomic beam collimators 5 mm apart and with orifice size of 2 mm are welded at the top of radiation shield cylinder just, above the oven cap. Its precision mechanical alignment eliminates the possibilities of collimator and oven cap orifice mismatch. A thermocouple is directly mounted on outer curved surface of oven to measure its temperature.

Figure 2.27 shows open cross-section of laser ion-source vacuum chamber. The atomic beam source is mounted vertically from bottom side. Two oppositely located quartz windows allow the laser beams to interact axially with orthogonal atomic beam in the centre of vacuum chamber. Third top window is intended to collect the fluorescence emitted during the selective excitation of the atoms. Two extra ports at an angle of 45^0 are given that can be used for an extra laser beam as generally required for multistep of photoionization spectroscopy. An external water cooling to the atomic beam furnace is provided by multi-turn copper tube. The TOF laser ion vacuum chamber is coupled with oil diffusion pump driven by rotary pump. Figure 2.28 shows the dual stage ion-extraction/acceleration grids assembly with proper insulation and mount, fitted at one end of the flight tube. First stainless steel (SS) disc 'P' of 68 mm diameter and 2 mm thickness acts as a back plate that reflect back the lithium positive ions.

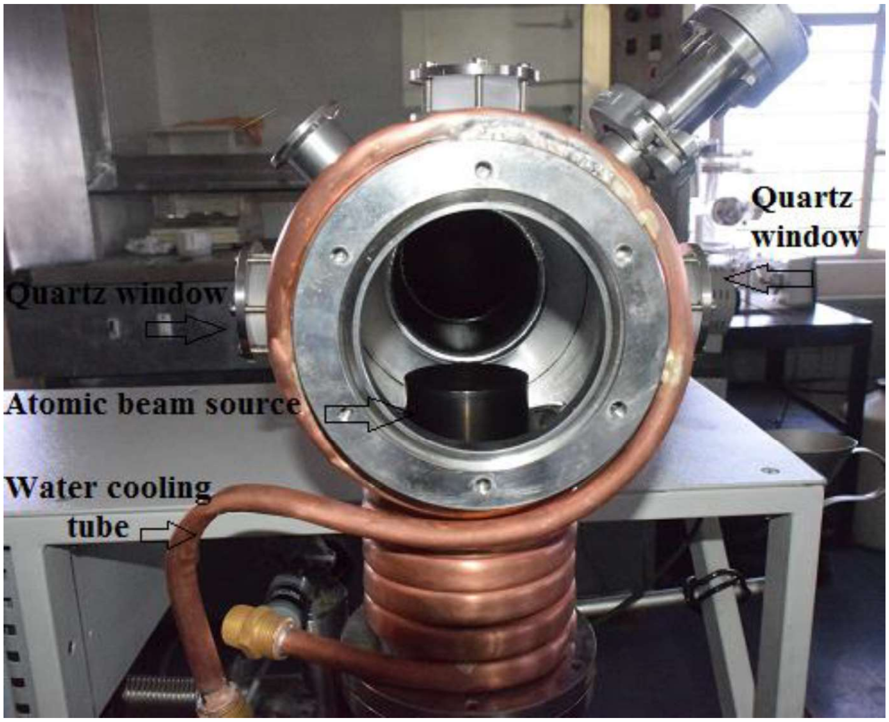

Fig. 2.27 Atomic beam assembly fitted in TOF laser ion-source vacuum chamber

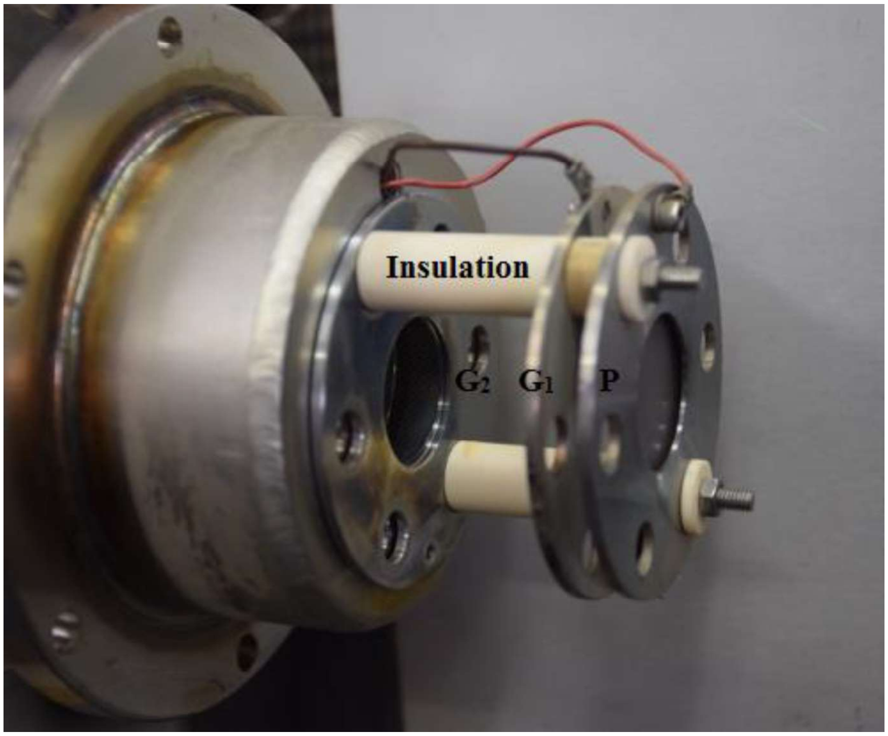

Fig. 2.28 Dual stage ion-extraction/acceleration grids assembly

Another disc type G_1 grid with 30 mm internal diameter holds a fine nickel mesh (precision E-forming) with 90% ion transmission. The mesh is sandwiched between the two thin SS rings which are spot welded together to fix the mesh in place. This arrangement results in stretching of thin mesh. Each square mesh simulates an electrostatic lens for ion extraction. It is electrically separated 8 mm apart from back plate 'P'. Positive ions of lithium are generated by laser photoionization method in between P and G_1. Third similar acceleration grid G_2 separated by MACOR holder and around 35 mm apart from the extraction grid G_1 is mounted axially on flight tube flange at ground potential. High voltage in the range of few kV (typ. 1.5 to 3 kV) are applied to back plate and grid G_1. A long flight drift tube of 1.2 meter length is coupled with dual stage ion-extraction/acceleration grids assembly as shown in Fig. 2.29. At the extreme end of flight tube an ion detector of diameter 25 mm in size with assembly, as shown in Fig. 2.30 is mounted axially with ion optics.

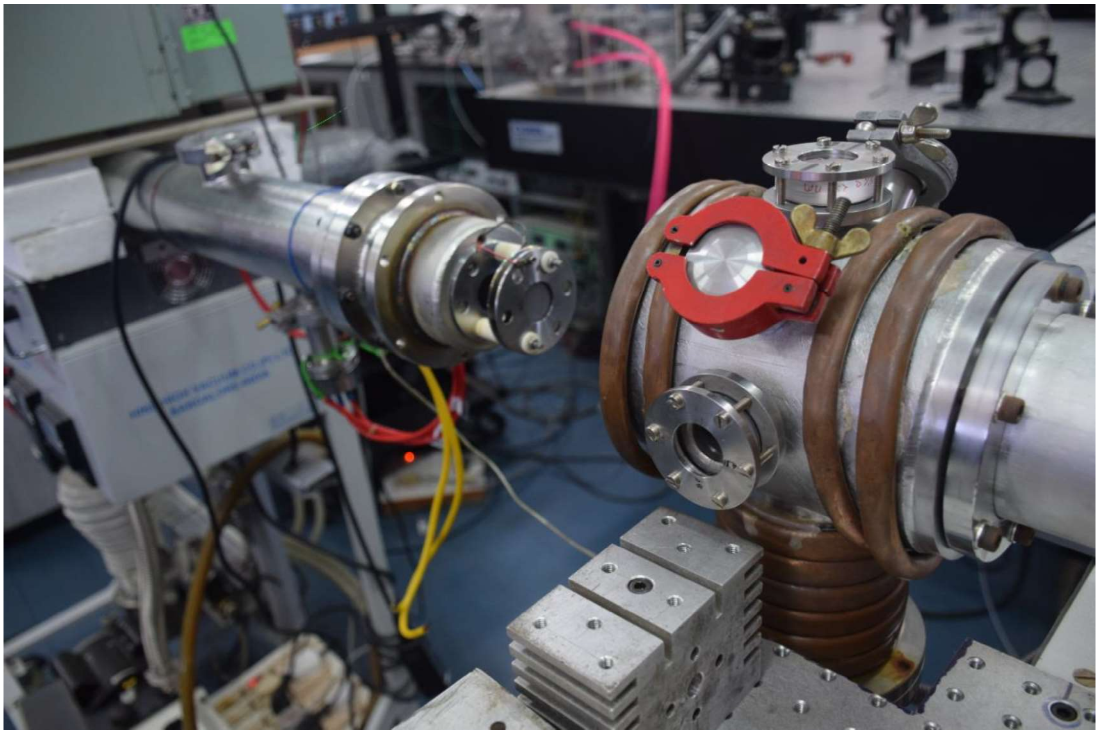

Fig. 2.29 Laser ion-source and ion extraction/acceleration grids fitted with flight tube

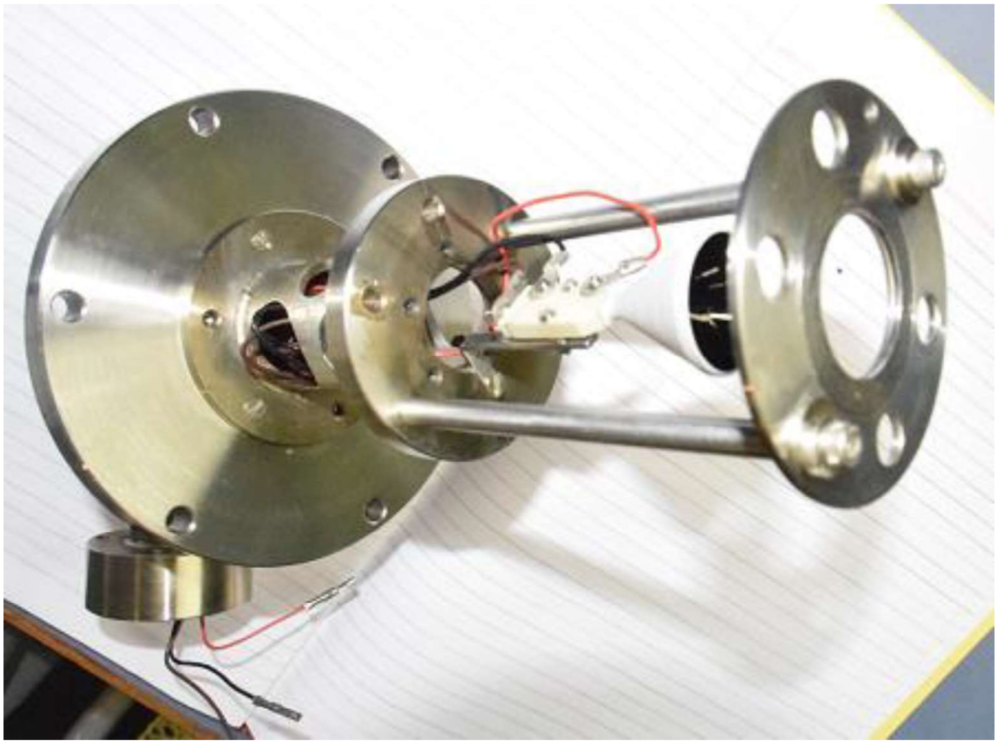

Fig. 2.30 Mechanical assembly of ion-detector

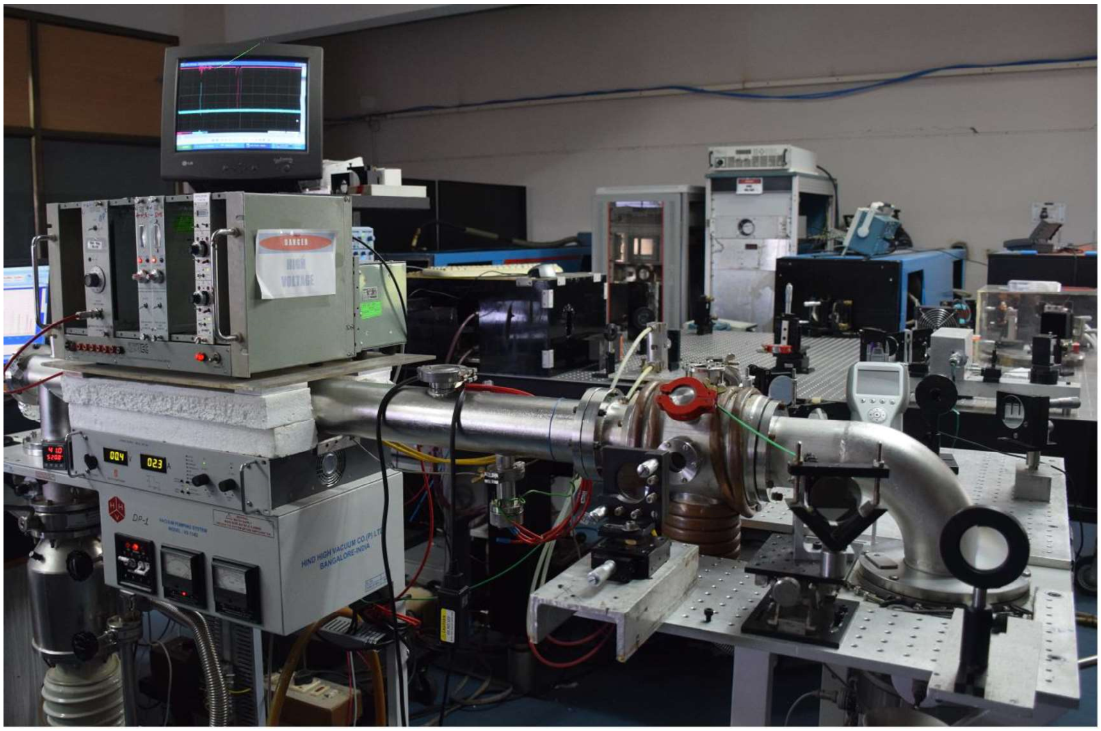

Fig. 2.31 Photograph of in-house built linear TOFMS

To ensure field free drift region, one more similar grid with nickel mesh at ground potential is mounted just before the ion detector, biased in closed configuration. The secondary electron multiplication takes place in the detector and gives an output pulse of charge with ~10^7 electrons for each ion particle. Figure 2.31 shows the complete assembly of developed linear TOF mass-spectrometer. In order to demonstrate the performance of TOF mass-spectrometer, lithium atoms emitted in the form of atomic beam are first resonantly excited by photon of 670.78 nm wavelength then subsequently photo-ionized from its excited state using different photons of 337.1 nm wavelength obtained from nitrogen laser. Both the exiting and ionizing laser beam are focused in laser ionization chamber at a common point where they intersect with orthogonal lithium atomic beam as shown in Fig. 2.24. The photo ions, thus produced, are separated and detected as described above.

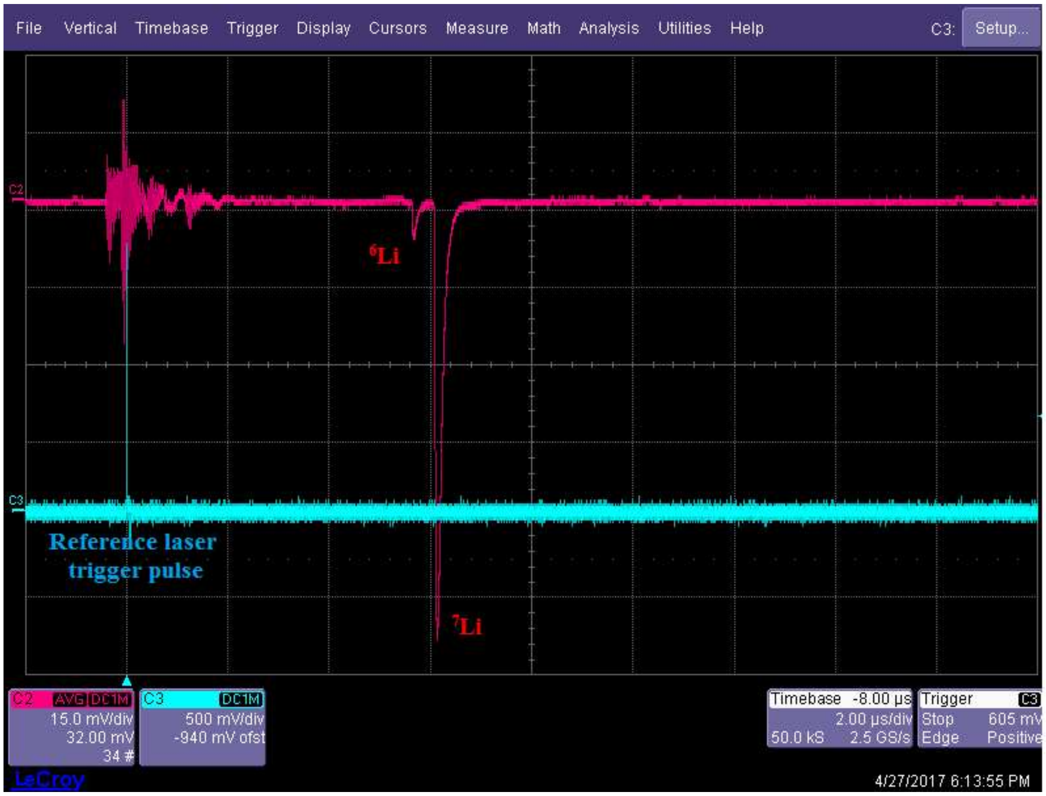

C2 AVG DC1M
15.0 mV/div
32.00 mV
34 #

C3 DC1M
500 mV/div
-940 mV ofst

Timebase -8.00 µs
2.00 µs/div
50.0 kS 2.5 GS/s

Trigger C3
Stop 605 mV
Edge Positive

4/27/2017 6:13:55 PM

Fig. 2.32 Li isotopes signal produced by two-step photoionization using TOFMS

The voltages applied to accelerating grids and the detector are optimized to obtain a smooth distribution of lithium isotopes (Fig. 2.32). For accurate isotopic abundance measurement, the ion detector has to be operated in a linear mode and the vacuum inside TOF chamber and flight tube has to be ensured better than 10^{-5} mbar. The isotope-selective photoionization studies using TOF mass-spectrometer are described in chapter-6 with focus on lithium isotopes.

2.9 Signal recovery instrumentation

The current signal from OG cell and ion-detectors such as thermionic diode or channeltron electron multiplier used in TOFMS is first converted into voltage signal passing through a filter with appropriate value of resistors and capacitors. The load resistor in case of thermionic diode detection varied from 10-100 kΩ depending upon the strength of signal. Then signal is processed either through boxcar integrator (SRS-250) or lock-in amplifier (EG&G-5209) that filters outs the noise from signal. The boxcar integrator is more suitable to signal recovery of the repetitive and small duty cycle signals. The SRS-250 comprises, a fast gated integrator, gate generator and the exponential averaging circuitry. The gate generator triggered externally or internally, provides an adjustable delay of few nanoseconds to 100 milliseconds, practically 2 ns to 15 μs in SRS-250. Boxcar averager integrates the input signal during the gate-width starting at predefined delay after the applied trigger. Each of these integrated samples of input signal are averaged using either analogue exponential averaging circuit or by digitizing each sample and then averaging the resulting digital values. The delay can be set from a potentiometer on front panel or scanned automatically by a rear panel input voltage in order to record an entire waveform. The position and width of gate window are a very important aspect of signal recovery. Position of gate sampling window with respect to desired signal achieves the temporal separation from noise, and it is often the biggest single contributor in improving signal to noise ratio. Noise/ interference in signal at the frequencies higher than reciprocal of gate-width will be completely suppressed. The output from SR-250 serves as an input to the computer interface SR-245, which provides the variety of functions such as scanning, counting and data communication to computer. This unit can be interfaced to PC through RS 232 link and the GPIB cards.

Chapter 3

Development and Characterization of Li Hollow Cathode Lamp

3.0 Introduction

Hollow cathode (HC) discharge finds important technological applications in laser spectroscopy, plasma spectroscopy and semiconductor industries [69]. The HC discharge based devices e.g. HC lamps, offer an extraordinary sharp and bright emission line spectrum [70].Various kinds of HC lamps have been used widely by spectroscopy research community since its discovery in 1916 by Paschen [9] to analyse the intricate molecular and atomic spectrum. These HC lamps can produce high atom density (~ 10^{12} cm^{-3}) even for high melting temperature and low vapour pressure elements by sputtering method. Hence, HC lamp may be used as special atomic vapour source appropriate for all kinds of spectroscopy in gas form particularly for photoionization and OG spectroscopy [9]. In an OG setup, when hollow cathode lamp is irradiated by an optical radiation with wavelength tuned to the atomic transitions of gaseous discharge species, the impedance of discharge varies and thus voltage across hollow cathode changes, consequently. These OG signatures can be obtained by means of electrical method and may form the strong base of spectroscopic analysis, stabilization and calibration of laser power and wavelength [71-75]. The wavelength calibration is a crucial and vital process and regularly needed in spectroscopy labs. The HC lamp with OG effect can provide laser's wavelength calibration in the easiest way [9]. The HC lamp provides OG signal detection for single as well as two-step laser excitation process. It is highly sensitive and can detect the weak OG transitions of inert gases to study their intricate electronic structure, Penning ionization and transitions from excited state [76-80]. The OG technique sensitivity is very high. It depends upon an appreciable change in the impedance of discharge prompted by resonance optical radiations. No additional detector such as PMT or photodiodes is required to detect the OG signal. Therefore, it is relatively cost-effective. It is also insensitive to scattered radiations. This makes it a sensitive technique for probing the atomic or molecular transitions.

In this chapter the development, assembly and characterization of a see-through HC discharge lamp, suitable for Li spectroscopy by OG method, is presented. The HC lamp is characterized for discharge oscillations free OG effects by electrical and optical means. The large strength OG signals of both Li as well as Ne are generated during the passage of tunable dye laser radiation into HC lamp. The HC lamp generated an OG resonance spectrum in the available tuning wavelength range (627 – 676 nm) of CVL pumped dye laser with DCM dye. About 28 resonant OG lines are explicitly observed as a part of the dye laser wavelength calibration studies. Most of them are identified by mixed j&l coupling and allocated to the Ne transitions. An OG line which corresponds to ~ 670.8 nm wavelength is assigned to Li and resolved partially for its ($^2S_{1/2} \rightarrow {}^2P_{1/2,3/2}$) fine structure. The discharge current and fill-gas pressure effects are also studied on temporal evolution of the Li OG signal. The developed HC lamp is further utilized to find the appropriate selective photoionization pathways of lithium as described in the next chapter.

3.1 Design of Li/Ne HC discharge lamp

The low pressure hollow cathode discharge lamps are the most appropriate and adaptable opto-electrical devices among the different kinds of atomic and ionic emission line sources. The electrical excitation of HC lamp can produce sharp and intense spectral lines; whereas, the optical excitation can generate the strong OG signals from cathode species [76,77]. The HC lamps are commercially available for most of the elements and the OG studies of these are documented in literature [9]. However, the OG studies of Li in HC discharge are scantily reported [78,80]. The reason may be that Li is highly reactive and has the low melting point (180.5 ^{0}C). It may be difficult to operate a commercial HC lamp with high spectral purity. The available commercial Li HC lamps are designed for small current (~ 12 mA) and constant gas pressure (~ 10 mbar) operation. These are not always the optimized parameters to produce the faithful OG signals for cathode species. These HC lamps are also constrained to the studies of specific preloaded elements. There is no way to change the material to be analysed and also the fill gas pressure. To remove these problems in present work, a see-through hollow cathode lamp with variable filled inert gas pressure, is developed for Li OG and photoionization studies. The developed hollow cathode is also suitable for various combinations of the elements & inert gases. Our design permits the change in cathode element also. It is by virtue of its demountable nature. The design of such HC lamp is shown in Fig. 3.1(a). It is labelled for parts nos. 1 to 10 as; 1) HC cathode, 2) Anodes, 3) Macor round disc, 4) Electric connections, 5) Bottom flange, 6) Kodial window, 7) Alloy tube, 8) Upper flange, 9) Glass tube, 10) Vacuum attachments. The dimensions of the anode and cathode are of 5 and 17 mm in length and 6 mm in bore-size, respectively. These are fabricated from high quality steel (304 L) to resist the corrosion and Li reaction with cathode wall. The anode and cathode inter spacing of ~ 5 mm permits the Ne gas discharge-breakdown at small voltage (~ 350 V) and at low gas pressure (~1 mbar).

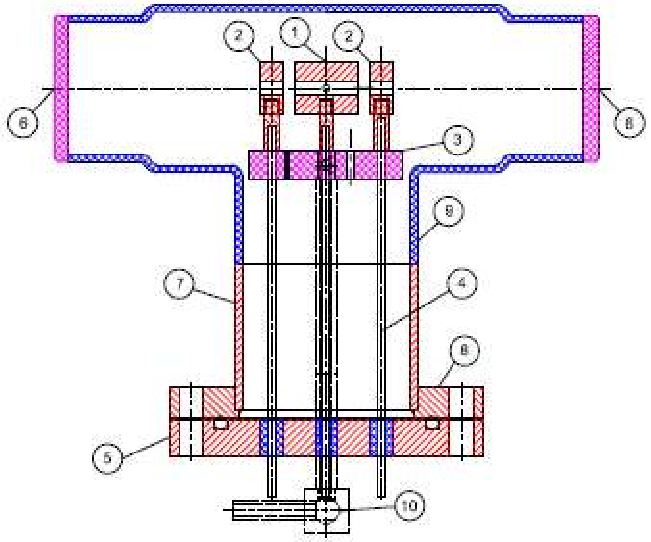

Fig. 3.1(a) Schematic view of hollow cathode lamp

Fig. 3.1(b) Electrical feedthroughs, Bottom flange and MACOR disc assembly

Three electrical feedthroughs are fabricated from kovar material and mounted in bottom stainless steel flange as shown in Fig. 3.1(b). High vacuum, with leak rate < 10^{-9} lit-mbar/sec, is achieved in HC lamp by developing unmatched type of kovar compression seals in bottom SS flange for mounting electrical feedthroughs. A thick MACOR disc of 4 cm in diameter, is used to guide the feedthroughs for griping the HC electrodes assembly. A glass vessel of ‘T’ shape with 4 cm diameter, 0.25 cm thickness and 10 cm length, fabricated from special kodial glass, is fused with upper SS flange by matched seal using a mixed (Ni, Co, Si, Cr) composition pipe of 5 cm diameter and 1.5 mm thickness. Thick glass windows (~ 0.3 cm) of 4 cm diameter are cut from a special optical glass with high transmission (> 92 %) at around 670 nm wavelength. A bottom stainless-steel (SS) flange with rubber ‘O’ ring is used to mount tubular glass vessel. The fine needle regulators are utilized to monitor the fill gas pressure and the vacuum in hollow cathode. Before making its use, it is essential to condition the hollow cathode for the stabilized discharge operation. HC electrodes and electrical-feedthroughs are made in greasy and dusty environment of mechanical workshop and glass blowing unit. Hence, these need effective scrubbing to remove out the deposited grease, glass dust, and oil impurities. Hence, all the HC lamp sub components are initially washed properly by organic agent such as acetone and then re-assembled. Highly pure Ne fill gas (~ 99.995%) is used at low pressure (1 to 5 mbar) to obtain stable discharge. The hollow cathode is suitably baked and flush out constantly for at least few days at ~ 100 ^{0}C. Prior to characterization of HC lamp, a thin Li foil of ~ 0.32 mm thickness purchased from Sigma-Aldrich is loaded into the cylindrical hollow cathode. To eliminate the mineral oil traces in which Li sample was preserved originally, an electrical discharge is applied at low current and pressure for at least of an hour. The discharge is observed to be extremely uneven and unstable, initially. This happens due to residual impurities still present inside the freshly prepared cathode cylinder which displays the bright scintillations on its surface for few minutes. However, after long continuous operation of 5 to 6 hours, stable discharge is attained. Frequently, it is detected that after extended use of hollow cathode, the vaporised cathode material get deposited on glass windows and its exterior surface. It may cause severe complications such as discharge instability and opaqueness to emitted or incident light. In such circumstances, the HC lamp has a facility of dismantling for removing the unwanted deposits using weak acid-wash. Around twenty minutes typical warmup time is required to achieve the steady state discharge in conditioned HC lamp.

The large bore-size, see-thoroughness, demountablity and variable gas pressure are the main features of the developed Li HC lamp. Our designed HC lamp has better features than that available. These HC lamp qualities are more appropriate, especially to Doppler free spectroscopy which needs the pump and probe counter propagating laser beams interacting with atom in a low pressure discharge. The negative glow is the most significant region for optogalvanic spectroscopy as it does not perturb the energy levels of species present in hollow cathode discharge. The developed hollow cathode is so designed that it produces a uniform negative glow, restricted to cathode bore only. No irregular and intermittent discharge occurs on its exterior surface. Otherwise, the strong discharge striations and oscillations may take over that can mask the OG and photoionization signals. A snapshot of developed hollow cathode is displayed in Fig. 3.2. It is observed that negative glow is merged from all over inner sides of cathode in the centre and remain restricted within hollow cathode diameter. The negative glow is a nearly field free region unlike the high electric field present HC dark space region. It is an important region of hollow cathode discharge for OG spectroscopy [9].

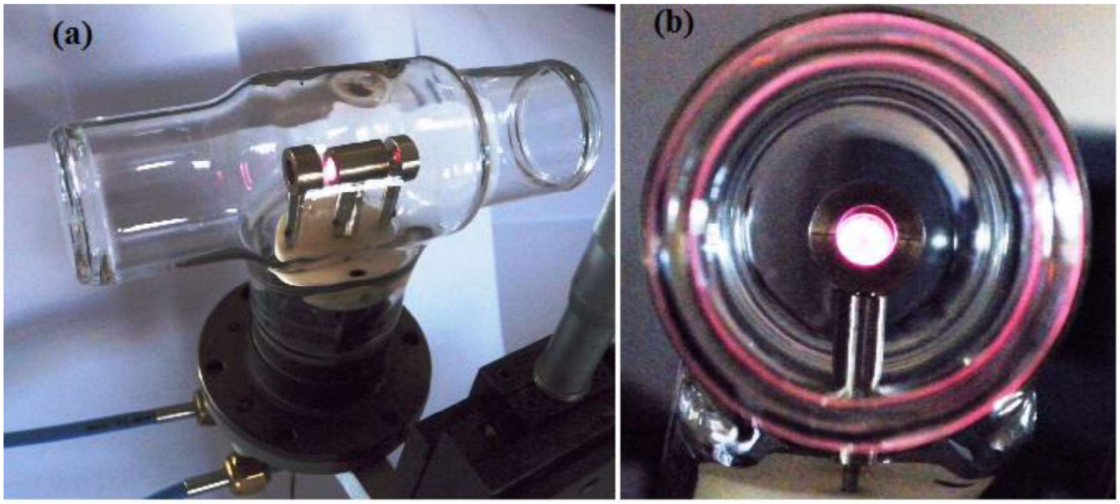

Fig. 3.2 Electrically excited HC lamp (a) Side on, (b) Front end views

3.2 Characterization of Li HC lamp

The hollow cathode lamp is characterized electrically by mapping its current & voltage (I-V) characteristics for discharge oscillation free operation. Figure 3.3(a) shows the I-V characteristics of 6 mm bore diameter hollow cathode. It is observed that developed Li HC lamp generates the desired positive resistance region for wide current range at low gas pressure (0.5-5 mbar) values. This is beneficial, as the negative resistance is not suitable to produce normal OG signals due to dominating large discharge oscillations [10,81]. In commercial Li HC lamp (with bore size ~ 2 mm), the small dips in I-V curve shows a negative resistance in its specified typical operating range, see Fig. 3.3(b). Negative resistance generated by HC discharge along with its inductive and capacitive reactance simulates discharge-OG circuit. This generates oscillations in optogalvanic signal upon dye laser excitation pulse impulse [82].

It means, the HC discharge generating a negative resistance is more prone to discharge instabilities. Such hollow cathodes are not suitable for OG and photoionization spectroscopy.

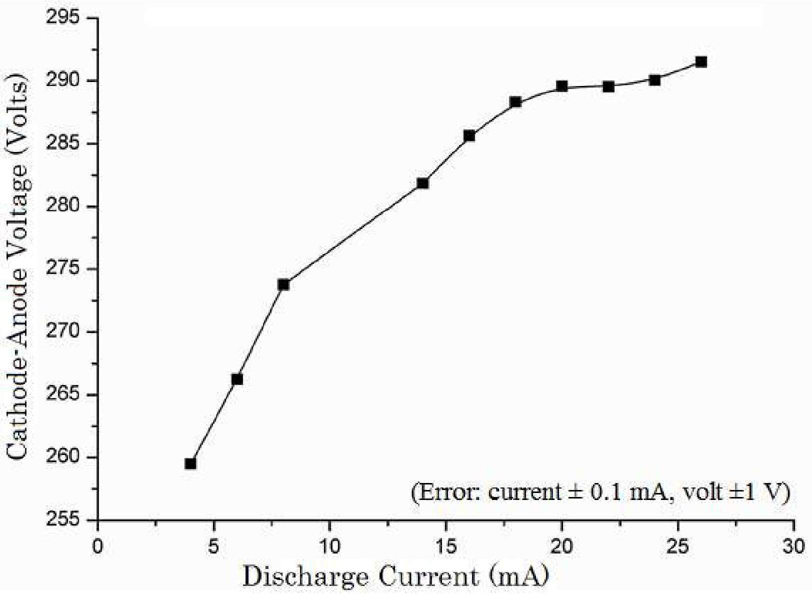

Fig. 3.3(a) I-V characteristics of developed Li HC lamp

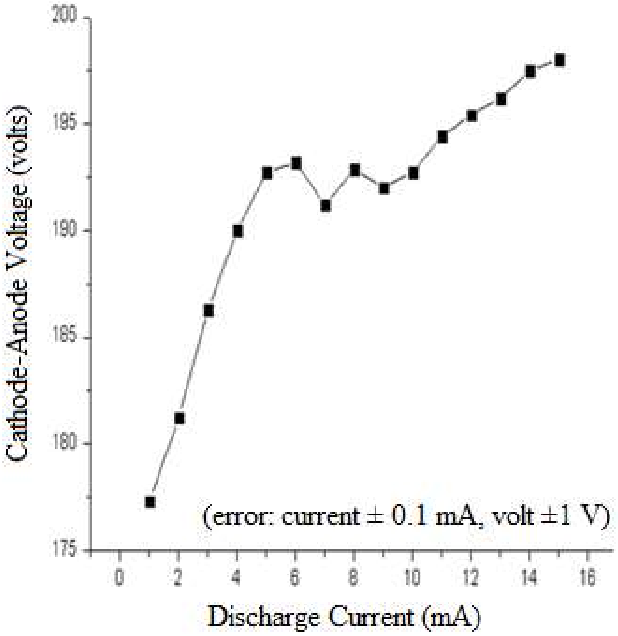

Fig. 3.3(b) I-V characteristics of commercial Li HC lamp

For its optical response, a photosensitive device based detector having good resolution (~ 0.02 nm) with double grating spectrophotometer (Ava-specs, 3648/2), is used to measure spectral line spectrum of hollow cathode in desired range of emission wavelength (610-673 nm). It is noted that higher current density of 30 mA at 1.0 mbar pressure in HC lamp, produces a sharp and intense line emission spectrum for Li as well as Ne gas (Fig. 3.4). The intensity of Li and Ne lines are found to rise almost linearly with increment in gaseous-discharge current; however, nonlinear increment is also noticed for Li at larger currents beyond 30 mA.

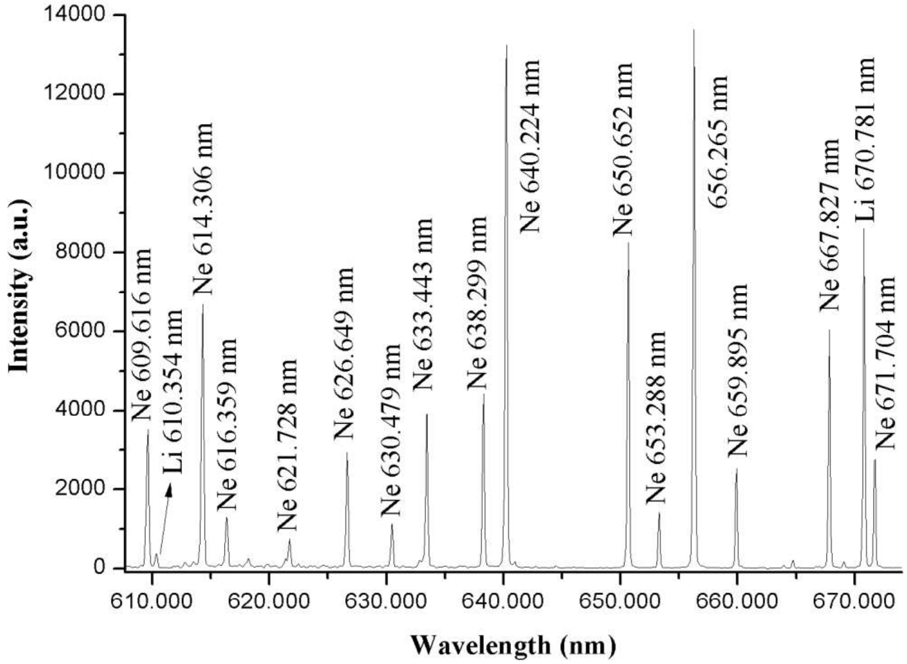

Fig. 3.4 Li HC lamp emission spectrum (at 30 mA current, 1 mbar gas pressure)

In HC discharge, the higher energy states are supposed to be occupied due to electronic excitations [80]. At moderate current (≥ 30 mA) and pressure lower than ~ 2 mbar, faint line is noticed from Li ($^2D \rightarrow {}^2P$) excited state at 610.35 nm wavelength. This opens a door for Li OG spectroscopy from excited states in HC lamp. It is noticed that Li emission line intensity improves multifold on slight decrease in pressure still at low currents. The gas pressure vs intensity plot is shown in Fig. 3.5. When the pressure of inert gas is decreased from 1.35 to 0.25 mbar, the Li line intensity at 670.78 nm, increased remarkably. On other hand, the Ne line intensity at close by transition at 671.70 nm reduced as pressure is decreased. These investigations helped in the understanding of temporal evolution of OG signal at different values of discharge current and gas pressure in Li HC lamp.

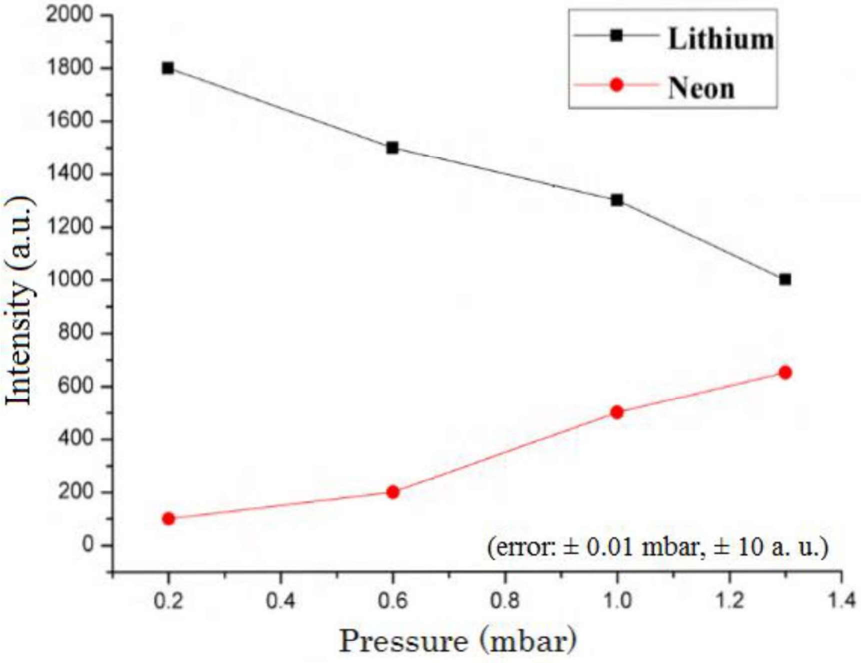

Fig. 3.5 Li HC lamp gas pressure dependent emission intensity

3.3 Detection of Li OG signals

Figures 3.6(a) & (b) shows the schematic and actual setup for OG studies in developed HC lamp. This setup uses an indigenously developed CVL pumped tunable dye laser system. The HC optical excitations are obtained using dye laser of ~2.5 GHz linewidth and ~ 100 mW average power, tunable in the wavelength range of 627 – 676 nm with DCM (Exciton) dye. The duration and repetition rate of dye laser pulses are ~ 20 ns and 6.5 kHz, respectively. The hollow cathode is electrically excited using an indigenously developed high voltage power supply. It sputters the Li neutral atoms into neon glow discharge. An OG circuit with ballast resistance 4.7 kΩ, 17 Watts heat dissipation and 10 nF polypropylene capacitance enclosed in a metal box, is used to measure the OG signals. The OG-circuit metal box and connecting electrical wires & cables are properly sealed and grounded for acquiring noise free OG signals.

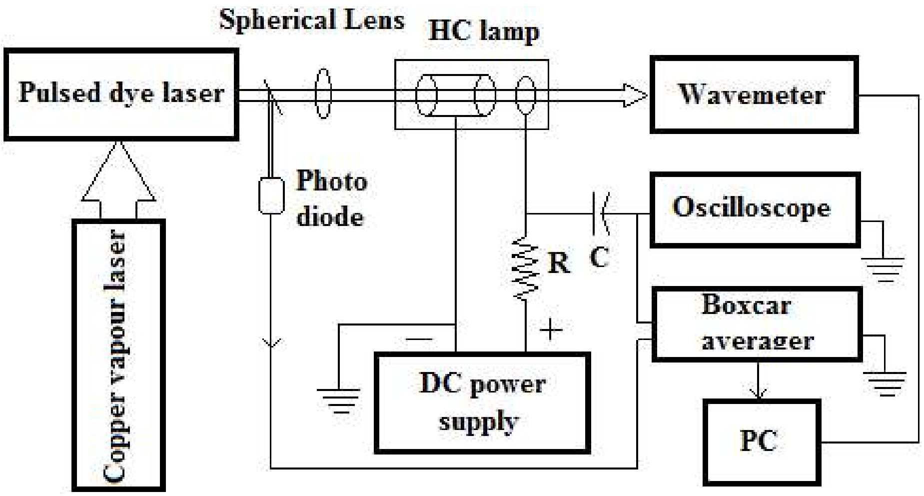

Fig. 3.6(a) Schematic of OG setup, R = 4.7 kΩ, C = 10 nF

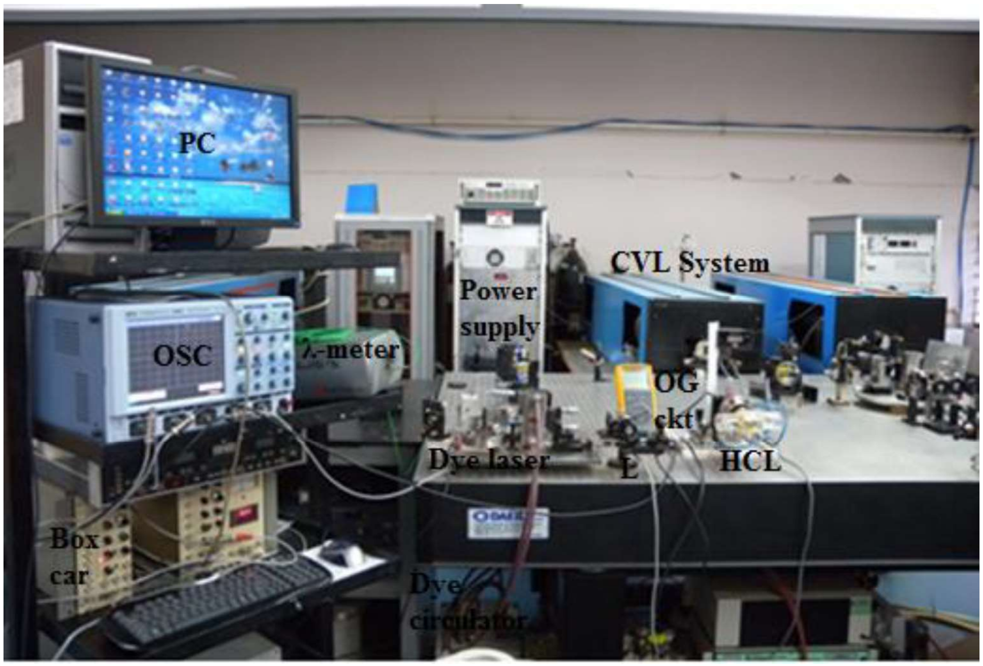

Fig. 3.6(b) Complete OG setup with laser systems, HC lamp and associated instrumentation

A convex lens of focal length 25 cm, is utilized to focus the beam of dye laser into negative glow of HC discharge. Appropriate steps are taken to exclude the risk of photoemission from interior cathode wall. Upon passing the dye laser beam into negative glow region, a small variation in the impedance of discharge medium, is noticed at resonant transitions, as an OG signal. For recording temporal evolution of the OG signals, a digital oscilloscope is used. However, to retrieve the time integrated OG spectrum, box-car integrator from Stanford research system, is used. The OG signal triggering is provided from Si-photodiode output. A dye laser wavelength scanner as described in chapter-2 is employed for continuous tuning of dye laser wavelengths and data logging [83]. It has a picomotor (New/Focus-8302) and data acquisition card (USB-4716) which is precisely controlled by a computer. The picomotor actuator with linear displacement resolution of 30 nm/step and drive torque of 0.018 Nm enables the fine change (~ 0.001 nm) in laser scanning wavelength. The slow scanning rate (~ 0.10 nm/ min) of tunable laser permits the smooth recording of continuous optogalvanic resonance spectrum. The optogalvanic transition wavelengths are monitored by a high accuracy wave-meter (Angstrom, WS-7L).

3.4 Temporal evolution of Li OG signal

The evolution of Li OG signals, at its respective excitation wavelengths, can be understood from its atomic structure. Figure 3.7 shows the Li energy level diagram relevant to explain Li OG signal in HC lamp. The electronic configuration of Li can be designated by 'RS' coupling with ground state as '$^2S_{1/2}$' which originates from its even parity configuration $1s^2 2s^1$ (2^2S). Upon optical excitation, its outer ($2s^1$) shell can leave one electron easily as compared to fully filled inner $1s^2$ shell. It gives rise to $1s^2 2p^1$ (2^2P) excited state configuration, where the symbols 2^2S and 2^2P represent the respective ground state and excited state terms. The electronic transition, in between the two energy states, is accountable for a broad structure of Li, D lines.

The sub features of a D line are the two D_1, D_2 lines that evolves from an interaction of the intrinsic spin and the orbital angular momentum. The angular momentum's spin-orbit interaction, splits the single D line into two D_1 & D_2 lines, which is called fine structure of Li.

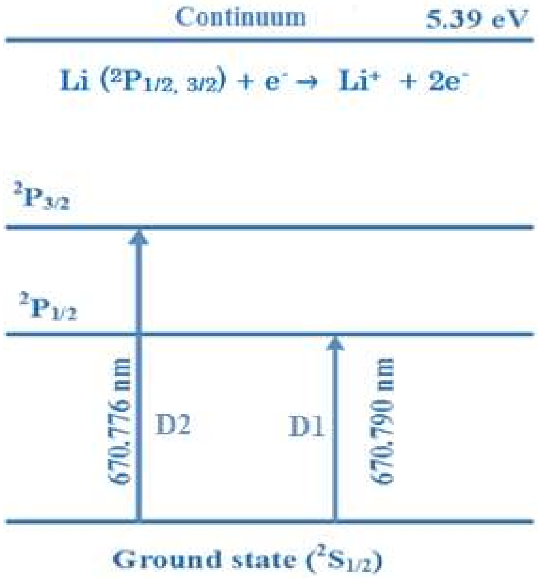

Fig. 3.7 Partial energy level diagram of lithium for OG signal

Figure 3.8 shows the time resolved OG signal for D_2 line which is originated from irradiation of dye laser pulse to Li ($^2S_{1/2} \rightarrow {}^2P_{3/2}$) transition at 670.776 nm at 50 mA and 5 mbar pressure. Generally, a fast rising negative peak followed by positive part are the characteristic OG signatures of cathode species in HC discharge. Similar is the case with lithium. The mechanism of Li OG signal evolution can be understood as follows; in hollow cathode discharge, all ionized inert gas atoms, accelerated by applied field, sputter the Li atoms. These now turn into vital part of the HC discharge. Since, rate of sputtering depends upon the square of discharge current [73], thus it leads to strong OG signals at higher current. The Li atoms are now excited to higher $^2P_{1/2,3/2}$ energy states by resonance absorption of dye laser wavelength tuned around 670.80 nm. These excited states are closer to the limit of Li ionization (~ 5.4 eV) [84]. Thus, the ionization collision probability of Li atoms increases multi folds due energetic (~ 3 eV) electrons present in low pressure gas discharge [85]. In this manner, the improved effective ionization rate decreases the gaseous discharge impedance. This results in negative optogalvanic signal across the hollow cathode discharge as shown in Fig. 3.8. The characteristic OG signal retrieval time (~ 3 μs) depends upon the applied discharge current, fill gas pressure and anode-cathode separation [9]. The lithium ions created during resonance absorption get accelerated in cathode fall region. This further liberates more Li atoms by sputtering means. Thus boosted Li atom density leads to a minor increase in HC impedance and therefore a relatively slow (~ 3 μs) positive part of OG signal is noticed. Besides ionization, the ongoing recombination process ultimately leads the OG signal to reach its steady state.

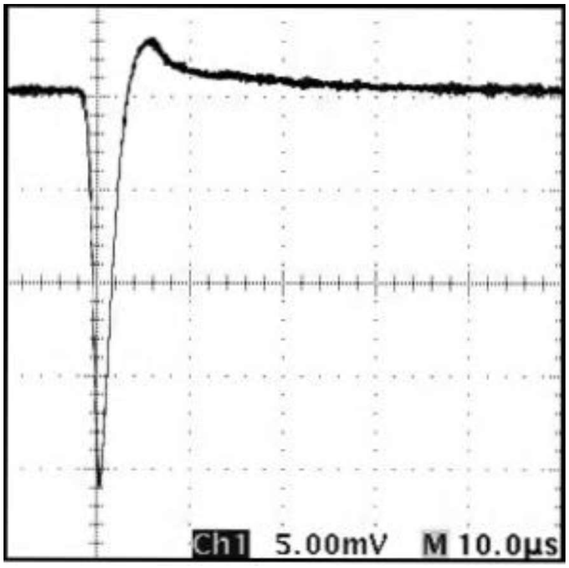

Fig 3.8 OG signal for Li transition ($^2S_{1/2} \rightarrow {}^2P_{3/2}$) at 50 mA current, 5 mbar pressure

We could not observed Li OG signals of significant strength, in commercially available hollow cathode at their rated operational current and fill gas pressure. Probably, it is due to low Li sputtering yield. This yield is very low for Li due its very low density and high surface binding energy [86]. However, we succeeded to observe a small (~ 10 mV) OG signal in developed Li

HC lamp. The explicit Li OG signal is observed at high current and low pressure. At increased current, improved sputtering rate as well as boosted ionization collisional rate generates superior and strong OG signals (Fig. 3.8). The HC lamp heat ups significantly beyond 70 to 80 mA current operation and needs external cooling. It is also noticed that Li OG signal grow many fold on reducing gas pressure. As the pressure of inert gas in HC lamp is decreased (2.5 to 0.5 mbar), the strength of OG signal is improved around 1.5 times, see Fig. 3.9 and Fig. 3.10.

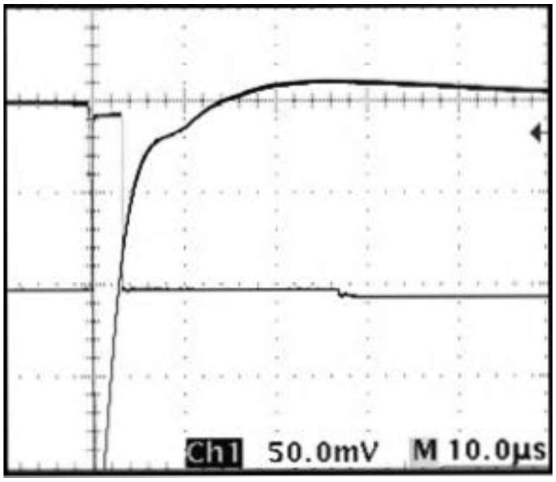

Fig 3.9 OG signal for Li transition ($^2S_{1/2} \rightarrow {}^2P_{3/2}$) at 65 mA current, 2.5 mbar pressure

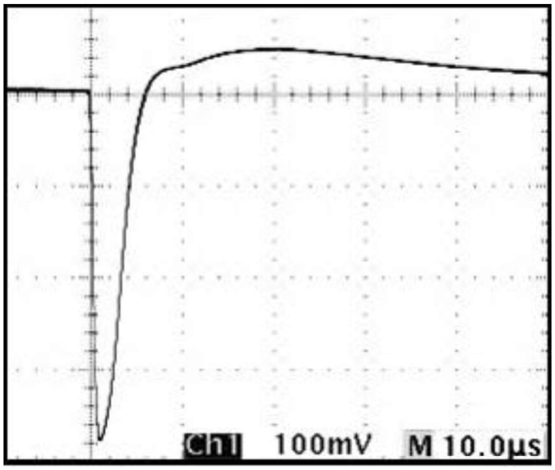

Fig 3.10 OG signal for Li transition ($^2S_{1/2} \rightarrow {}^2P_{3/2}$) at 65 mA current, 0.5 mbar pressure

The large increase in Li OG signal can be ascribed to the availability of more Li atoms because of effective sputtering at low gas pressure. When the HC lamp fill gas pressure is reduced, the discharge species collisional mean free path increased. Thus when it becomes nearly comparable to HC bore size, an efficient sputtering occurs [9]. This phenomena agrees well with previously observed increased Li emission line intensity at reduced pressure (see Fig. 3.5).

3.5 Lithium-Neon OG spectrum

The known atomic transitions of an atom can be utilized as absolute wavelength marker provided these are capable to produce OG signals of comparable temporal characteristics. The evolution of Ne signal in hollow cathode is directed by collision ionization rate as well as by population relaxation rate of respective states coupled through laser pulse [87]. Both the aspects are governed by operational HC current and gas pressure. Therefore, OG temporal profiles, from different energy state, can be somewhat dissimilar. For adjusting effects of HC discharge parameters, an optogalvanic spectra is recorded at threshold current 25 mA and 5 mbar gas pressure as shown in Figs. 3.11(a) & (b). Altogether, twenty eight lines are observed within entire dye laser scan range (626- 676 nm). Of these, one spectral line near the 670.80 nm wavelength, is allocated to Li. Amplitude wise, Li OG signal is weak; though, detected clearly as shown in Fig. 3.11(b). The enhanced view of the Li OG spectrum is shown in Fig. 3.11(c). It is to be noted that developed hollow cathode lamp with Doppler limited OG setup is capable to resolve nearby Li fine structure $^2S_{1/2} \rightarrow {}^2P_{1/2,3/2}$ transitions detected on 670.791 and 670.776 nm, separately, see Fig. 3.11(d). These atomic transitions at ~ 15 pm apart lies within ~ 10 GHz of Li energy level separation [84]. These also nearly match with Li D_1 & D_2 lines as described earlier. This permits calibration of the used tunable dye laser wavelength upto ~ 0.33 cm^{-1}. The precision of laser wavelength calibration in OG setup is mainly limited by dye laser bandwidth and various types of broadening in line transition.

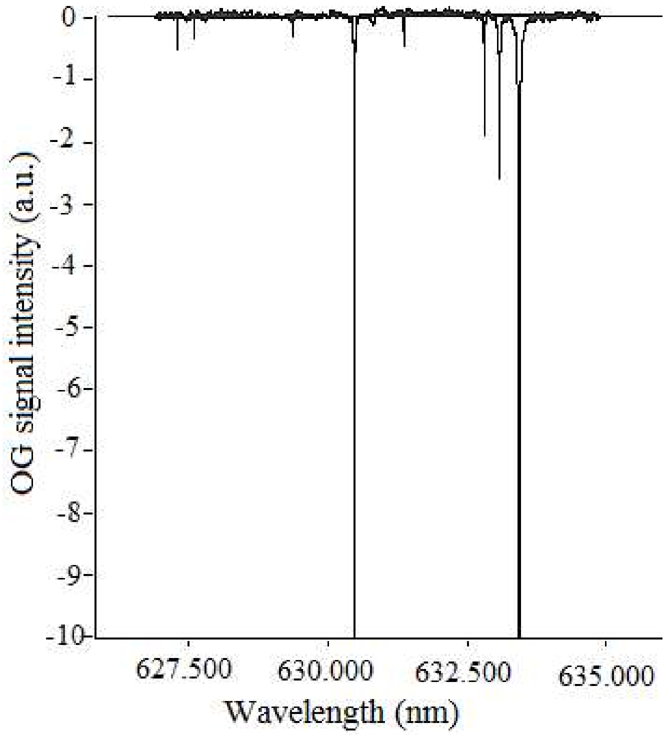

Fig. 3.11(a) Li/Ne OG spectrum for dye laser wavelength range 627-635 nm

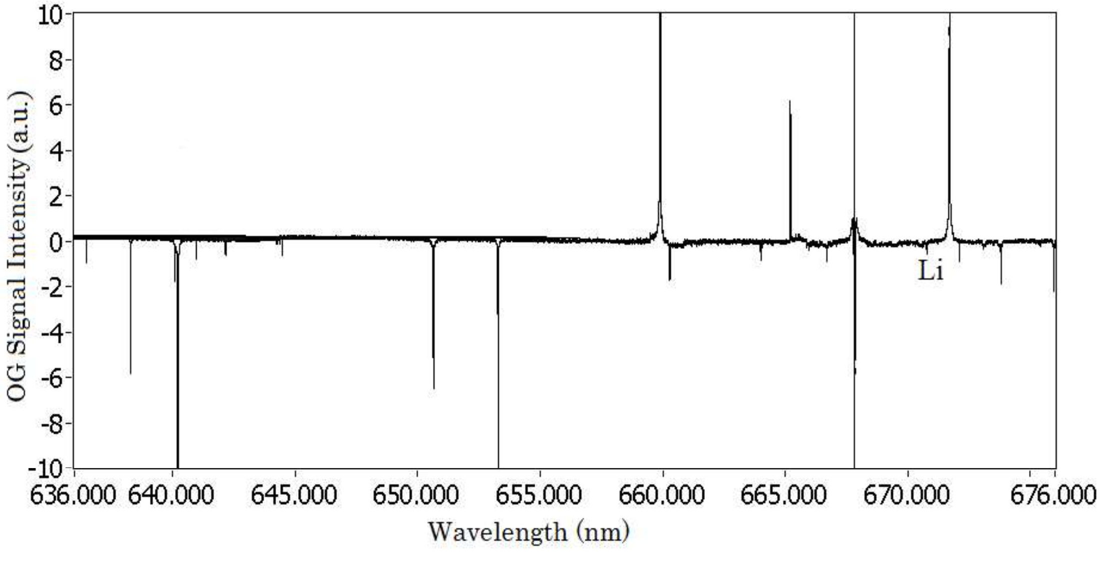

Fig 3.11(b) Li/Ne OG spectrum for dye laser wavelength range 636-676 nm

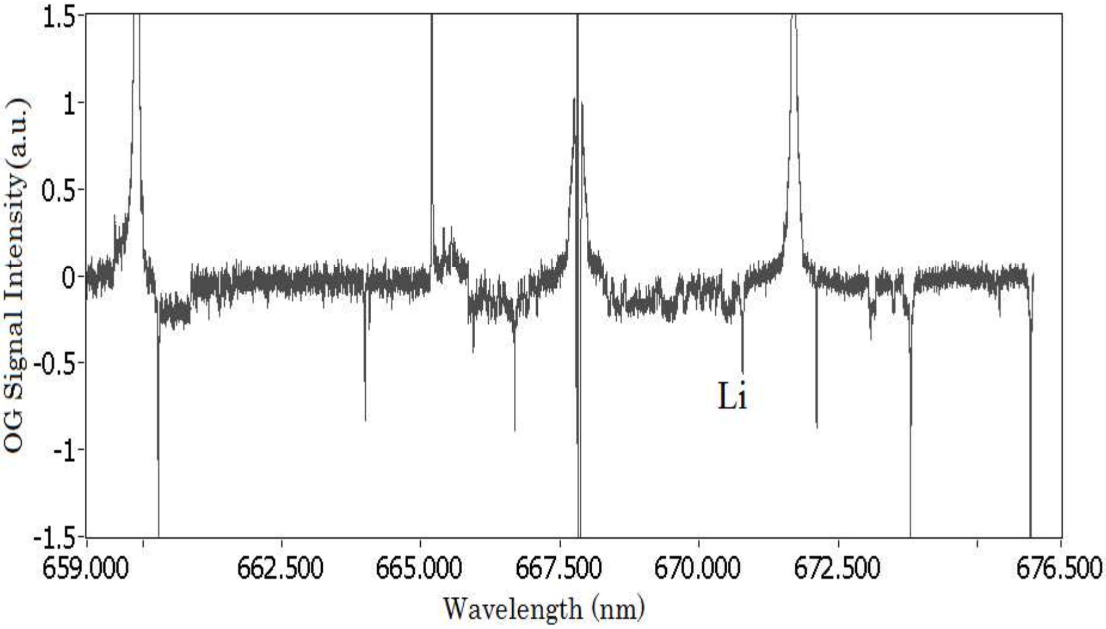

Fig. 3. 11(c) Enlarged view of OG spectrum with same Li OG line nearby 670.80 nm

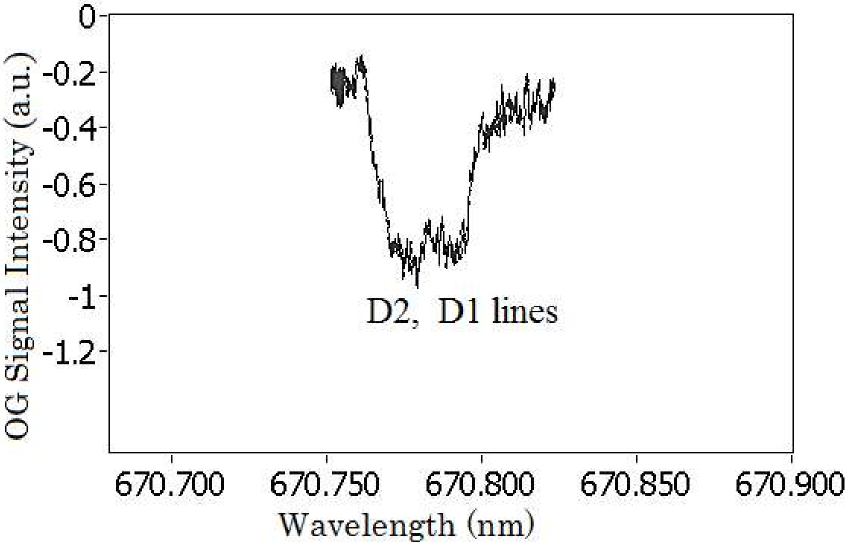

Fig 3.11(d) Partially resolved D_1 & D_2 lines for Li transition ($^2S_{1/2} \rightarrow {}^2P_{1/2,3/2}$)

The Doppler broadening for Li transitions, in developed hollow cathode, is measured as ~ 3.5 GHz. It is relatively large because of light mass of lithium atoms. For an accurate measurement of the energy levels, the broadening in line transitions should be minimized. The major line broadening can be significantly improved in Doppler free OG experimental setups [88]. Further improvements in wavelength calibration accuracy is possible by using the Doppler free inter-modulated optogalvanic and saturation absorption spectroscopy setups.

The remaining 27 OG lines as listed in table 3.1 are recognized by means of special '*j-ℓ*' coupling scheme and allocated to Ne transitions. This scheme is used because two common type of L-S and j-j coupling schemes do not provide real understanding of vector coupling for inert gases such as Ne, henceforth of their energy levels. So, an intermediate *(j- ℓ)* coupling proposed by Racah [89] is used to account for the energy of levels for detected Ne transitions. Generally 'j-ℓ' coupling occurs, when electronic electrostatic interaction is feebler compared to parental ion spin orbit interaction, however stronger than spin coupling of exterior electron. Therefore, Ne excited states are notified as $n\ell[K]J$, here ℓ is exterior electron angular momentum while K describes net angular momentum occurring due to coupling of ion core's total angular momentum (j_c = 1/2, 3/2) and electron angular momentum ℓ, i.e. $K = |j_c \pm \ell\,|$ and $J = |K \pm s|$. It is to be noticed that all the OG lines closely match with NIST [90] reported emission line transitions. The mechanism of neon OG signal origin is well explained and reported in the literature [87,91-94]. The same is true and applicable for our HC lamp. Most of the Ne optogalvanic signals are of negative polarity; though, few spectral lines that evolved from metastable energy states such as Ne transition $3s[1/2]^o_1 \longrightarrow 3p[1/2]_1$ at 659.89 nm, $3s[1/2]^o_1 \longrightarrow 3p[1/2]_0$ at 665.21 nm, $3s[1/2]^o_1 \longrightarrow 3p[3/2]_2$ at 667.82 nm and $3s[1/2]^o_1 \longrightarrow 3p[3/2]_1$ at 671.70 nm exhibit positive polarity. Inverted polarity of signal lines at these transitions may be correlated to their collisional ionization cross-sections. In general, Ne OG signals from non-metastable states are observed negative for both the rare gases as well as Li cathode element.

Table 3.1: 27 Ne OG lines and their spectral notations

Wavelength (in nm)	Spectral notations with 'j-ℓ' scheme
627.603	$3p[1/2]_1 - 4d[1/2]^{o}_{0}$
629.373	$3p[3/2]_1 - 5s[1/2]^{o}_{1}$
630.479	$3s[3/2]^{o}_{1} - 3p[3/2]_2$
631.369	$3p[3/2]_1 - 5s[1/2]^{o}_{0}$
632.817	$3p[3/2]_2 - 5s[1/2]^{o}_{1}$
633.089	$3p[3/2]_1 - 5s[3/2]^{o}_{1}$
633.443	$3s[3/2]^{o}_{2} - 3p[5/2]_2$
635.185	$3p[1/2]_0 - 5s[1/2]^{o}_{1}$
636.499	$3p[3/2]_1 - 5s[3/2]^{o}_{2}$
638.299	$3s[3/2]^{o}_{1} - 3p[3/2]_1$
640.108	$3p[1/2]_1 - 5s[1/2]^{o}_{1}$
640.225	$3s[3/2]^{o}_{2} - 3p[5/2]_3$
640.975	$3p[3/2]_2 - 5s[3/2]^{o}_{1}$
642.171	$3p[1/2]_1 - 5s[1/2]^{o}_{0}$
644.471	$3p[3/2]_2 - 5s[3/2]^{o}_{2}$
650.653	$3s[3/2]^{o}_{1} - 3p[5/2]_2$
653.288	$3s[1/2]^{o}_{0} - 3p[3/2]_1$
659.895	$3s[1/2]^{o}_{1} - 3p[1/2]_1$
660.290	$3p[3/2]_1 - 5s[3/2]^{o}_{1}$
664.001	$3p[3/2]_1 - 5s[3/2]^{o}_{2}$
665.210	$3s[1/2]^{o}_{1} - 3p[1/2]_0$
666.689	$3p[1/2]_0 - 5s[3/2]^{o}_{1}$
667.827	$3s[1/2]^{o}_{1} - 3p[3/2]_2$
671.704	$3s[1/2]^{o}_{1} - 3p[3/2]_1$
672.113	$3p[1/2]_1 - 5s[3/2]^{o}_{2}$
673.803	$3p[1/2]_0 - 4d[3/2]^{o}_{1}$
675.958	$3p[1/2]_0 - 4d[3/2]^{o}_{1}$

In OG effect, signal intensity is largely governed by lower levels population, probability of transitions and ionizing rate of lower and upper energy level. The OG signal strength and transition oscillator strength 'f' may be correlated as [$\Delta z/I = fg\lambda$], here 'Δz' denotes a change in gaseous discharge impedance and '*I*' is intensity of dye laser beam at wavelength λ. The factor 'g' is degeneracy of lower energy level. Hence, the strength of OG signal exhibits a correlation with intensity of emission line [95] that should follow the HC emission spectrum.

Though, practically it was noticed that intensity and polarity of signal in optogalvanic spectrum are ruled by boxcar setting. So, one to one relation of OG strength and emission intensity is scarcely possible. The OG signal could follow emission line intensity if boxcar parameter setting are adjusted to every individual signals. This is barely possible in full single wavelength scan. Therefore, to record a true OG spectrum following strategy is adopted. The boxcar sampling parameters, with respect to evolution of temporal OG signal, are augmented in such a way that both the feeble as well as high strength signals could be recorded, altogether. Wavelength as well as intensity scales in OG spectrum are adjusted as and when required to record the every feeble lines clearly. It is noticed that both of intensity and polarity of time integrated OG signal depend on gate width and its position with reference to incident laser pulse. For precise calibration accuracy, the signals are sampled at suitable delay and gate width far from zero-crossing region; otherwise, slight change in signal temporal behavior might significantly affect wavelength of OG line also. In present experiment, the gate width (~ 3 μs) of boxcar integrator is precisely adjusted with synchronized incident laser pulse so that all the OG signals in entire wavelength scanning range can be recorded with least alterations and wavelength shift. For improvement in signal to noise ratio, higher sampling rate at 1K, is used for averaging the OG signals. A specific neon $3s\ [1/2]^{o}_{1} - 3p[3/2]_{2}$ transition, detected at 667.827 nm, created an OG signal with dual polarity behavior (+ ive as well as - ive). Possibly, it occurs due to dynamic nature of OG signal growth and inaccurate gate width setting. Though, for reproducible wavelength calibration, such type of inconsistencies should be avoided. As the OG signal evolution time depends on HC current, inert gas pressure and laser power etc. [9]; therefore, these hollow cathode discharge parameters should be constant for fixed boxcar settings, otherwise setting of parameters have to be changed accordingly, during the full wavelength scan of OG spectrum. It means to record the OG signals accurately, proper setting of boxcar parameter are important for such long and continuous OG spectrum.

3.6 Conclusion

In summary, the development details of see-through type large bore size HC lamp for Li and inert gas optogalvanic spectroscopy is described. The developed hollow cathode produced time dependent as well as time integrated continuous OG signals of both Li and Ne. The experimental data shows that hollow cathode broad positive resistance expanse, attained for long range of discharge current and gas pressure, is desirable for discharge oscillation free optogalvanic effect. Many neon transitions, not even detected in (Li/Ne) recorded emission spectrum, are clearly measured by OG effect. This establishes the fact that developed HC lamp is more sensitive in OG process than as a discrete emission lines source. Similarly, scarcely observable Li OG signals in commercially HC lamp are explicitly detected with good signal to noise ratio in developed hollow cathode lamp. It clearly shows the sensitivity of in-house built Li hollow cathode lamp. The experimental result outcomes also specify that HC lamp fill gas pressure greatly affects the Li OG signal. This leads to high strength OG signals for decreased (~ 0.5 mbar) pressure. Optogalvanic line noticed nearby 670.80 nm and allocated to Li ($^2S_{1/2} \rightarrow {}^2P_{1/2,\,3/2}$) transition is partially resolved. These two resolved closely spaced lines belongs to the Li fine structure. The developed hollow cathode generated true, accurate, and rich Li/Ne OG spectrum over entire wavelength tuning range (627 – 676 nm) of the dye laser. These OG lines with an accuracy of ~ 0.33 cm^{-1}, in addition to previously recorded OG lines, by other researchers [71, 95-97], would be useful in wavelength calibration of a scanning type of dye laser at precision of atomic levels. The intention behind the development of large bore size and see-through Li hollow cathode lamp was also to study the selective excitations of Li. This study helped in atomic beam based mass-spectrometry photoionization process, as described in chapter-6. The important features of developed hollow cathode lamp such as, see-through and variable fill gas pressure, also makes it more suitable to be employed in Doppler free spectroscopy experiments.

Chapter 4

Photo Excitation Studies in Li Hollow Cathode Lamp

4.0 Introduction

This chapter presents detailed photo-excitation studies on lithium atoms investigated by OG method in the developed HC lamp. Interlinked studies are performed with final aim of investigation into efficient photoionization pathways of lithium isotopes by multistep excitation. In the first study, Li OG signals with good S/N ratio are produced and optimized with respect to discharge current and fill gas pressure at moderate incident laser power. This study is carried out to ascertain suitability of the developed Li HC lamp for photoionization studies. Further, CW OG studies are carried out in Li HC lamp using a commercial single mode CW ring dye laser to estimate the Doppler broadening in Li transition of interest. This study is extended further to elucidate the lithium fine & hyperfine structure and isotope shift, as required for selecting efficient photoionization scheme. For this purpose, the Doppler free saturation absorption spectroscopy (SAS) of lithium at ~ 670.8 nm has been carried out using single mode CW dye laser. The effect of buffer gas pressure on the line broadening is also studied. Four hyperfine components of ^{7}Li, D_1 & D_2 lines and two hyperfine components of ^{6}Li D_1 line are clearly resolved at reduced buffer gas pressure. The hyperfine splitting of ground state ($^2S_{1/2}$) for ^{7}Li D_1 & D_2 lines, and the ^{6}Li D_1 lines are calculated from SAS spectrum. The isotopic shift for D_1 lines of ^{6,7}Li is also measured.

Next, two-step selective photoionization of Li isotopes is studied in the dark space region of HC lamp. The high electric field present in dark space is used to collect the fast charge generated by an interaction laser pulses with sputtered Li atoms. It enables the detection of photoionization. In photoionization spectrum, the ^{6}Li D_1 line at 670.805 nm is clearly observed and the ^{7}Li D_1 and D_2 lines at 670.790 and 670.776 nm are fairly resolved. This work is further extended for studying the Li photoionization by opto-galvanic method through two-steps selective excitation followed by third non-resonant/collisional ionizations. This study is carried out in negative glow region of HC discharge. The photoionization spectrum has been recorded using two dye lasers and boxcar integrator interfaced with wavelength scanner cum data logger. The knowledge and experience gained from isotope-selective two-step resonant excitation in HC discharge is implemented further in Li three-step photoionization studies using atomic beam and time-of-flight mass-spectrometer as described in chapter-5.

4.1 Pulsed and CW OG effects in Li HC lamp

4.1.1 Pulsed OG studies

Pulsed OG effect in Li/Ne hollow cathode lamp on Li transition $^2S_{1/2} \rightarrow {}^2P_{1/2,3/2}$ is carried out with a focused aim on selective photo-excitation and studying the D_1 & D_2 lines. The experimental setup for this study is similar to that shown in chapter-3 (Fig. 3.6) except different ballast resistance and coupling capacitance values (R = 15 kΩ, C = 100 pF). The fill gas pressure of neon in Li HC lamp is adjusted and maintained around 0.3 mbar to obtain high OG signal strength. The CVL pumped pulsed dye laser (~ 2.5 GHz, 20 ns) system, generating an average output power of more than 100 mW, is used to excite the Li transition in HC lamp. The excitation wavelengths are obtained from dye laser using a tuning mirror driven by pico-motor. The dye laser beam is properly aligned and passed through the hollow cathode without interacting with cathode wall to avoid the possibility any spurious signal. This is carried out using a convex lens of 25 cm focal length. The 4% reflectivity wedge glass plate, is utilized for sending a small portion of an output from dye laser to a wavelength meter (WS-7L). It is coupled with a personal computer for monitoring the wavelength of dye laser. A regulated high voltage (Aplab, India) power supply, in conjunction with homemade metal shielded OG detection circuit, is used to acquire the OG signals. When dye laser beam is absorbed by Li or

Ne species present in HC discharge, the resulting change in plasma impedance is monitored through a coupling capacitance (C = 100 pF) on a digital oscilloscope (TDS-3052B, Tektronix) as an optogalvanic signal. To acquire the feeble signals faithfully, oscilloscope is synchronously triggered by reference laser pulse utilizing fast Si photodiode. Figure 4.1 shows the Li OG signals corresponding to D_1 and D_2 lines for ($^2S_{1/2} \rightarrow {}^2P_{1/2,3/2}$) transitions at (b) 670.791 and (a) 670.776 nm, respectively. The OG signal has negative polarity for both the transitions. The partial energy level diagram of Li as shown in Fig. 3.7, can be used to explain the observed pulsed OG signals.

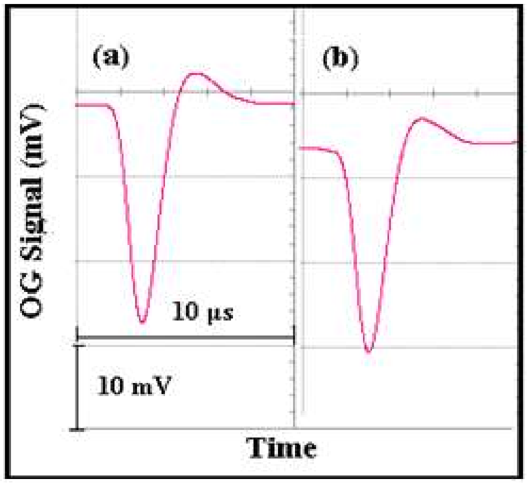

Fig. 4.1 Li OG signals for ($^2S_{1/2} \rightarrow {}^2P_{1/2,3/2}$) transitions at (a) 670.776, (b) 670.791 nm

In Li/Ne HC discharge, the sputtered Li atoms are excited to higher state $^2P_{1/2,3/2}$ from ground state. This is due to resonance absorption of dye laser beam in the vicinity of 671 nm wavelength at their respective transitions. These excited states are closer to Li ionization limit. Hence, ionization probability of lithium atoms increases due to the collisions with energetic (3-5 eV) discharge electrons that alters the net effective rate of ionization. The overall effect of resonant absorption, followed by subsequent ionization reduces the discharge impedance. This is reflected as a negative voltage (OG) signal (Fig. 4.1) monitored across HC lamp electrodes.

It is observed that Li OG signal increases with the increment in discharge current at constant pressure (~ 0.3 mbar). This is correlated with higher excitation rate at the increased current. The effect of neon fill gas pressure on Li OG signal, at constant current, is also observed. When gas pressure in HC discharge is varied from 5 to 0.3 mbar, the Li OG signal intensity increases (0.32 to 1 arbitrary units) similar to as shown in Fig. 3.8 to Fig. 3.10 in chapter-3. It can be correlated to the increased mean free paths of charge carriers (neon ions). This in turn increases the effective sputtering of Li atoms. Therefore, it is required to operate the HC lamp at reduced gas pressure and increased discharge current to obtain the good strength OG signals.

As in Li/Ne HC discharge, the buffer gas plays the role of sputtering agent for Li as well as participating in the kinetics of HC discharge, it is instructive to study the OG effects for neon transitions also. The OG signals obtained are the culmination of physical processes such as electron collisional excitation, radiative depopulation, electron collisional ionization and collisional population redistribution upon resonant excitation by laser pulse. The evolution of two prominent neon OG signals for ($1s_2 \rightarrow 2p_2$) transition at 659.895 nm and for ($1s_2 \rightarrow 2p_5$) transition at 671.704 nm are shown in Fig. 4.2 with their energy level diagram. The polarity of Ne OG signals is observed positive similar to that obtained by Shuker et al., in Ca/Ne hollow cathode discharge [94]. In general, polarity of neon OG signals in HC discharge, originated from ($1s_i$) states, are negative [9]. The cause of inverse sign OG effect is very well documented in literature [98] and also explained by Mirage et al. [99]. In fact, the effect of laser interaction on any atomic system that it would stimulated either by absorption or emission depends upon population difference of the two energy levels involved. Consequently this results in decrease or increase in higher energy level population. Higher energy levels exhibit the larger ionization cross-section. Thus, an increase in excited state population leads to higher ionization rate owing to both the increase in population as well as change in electron distribution function [98,100]. Thus, the resultant OG effect is a decrease in voltage across the HC discharge electrodes.

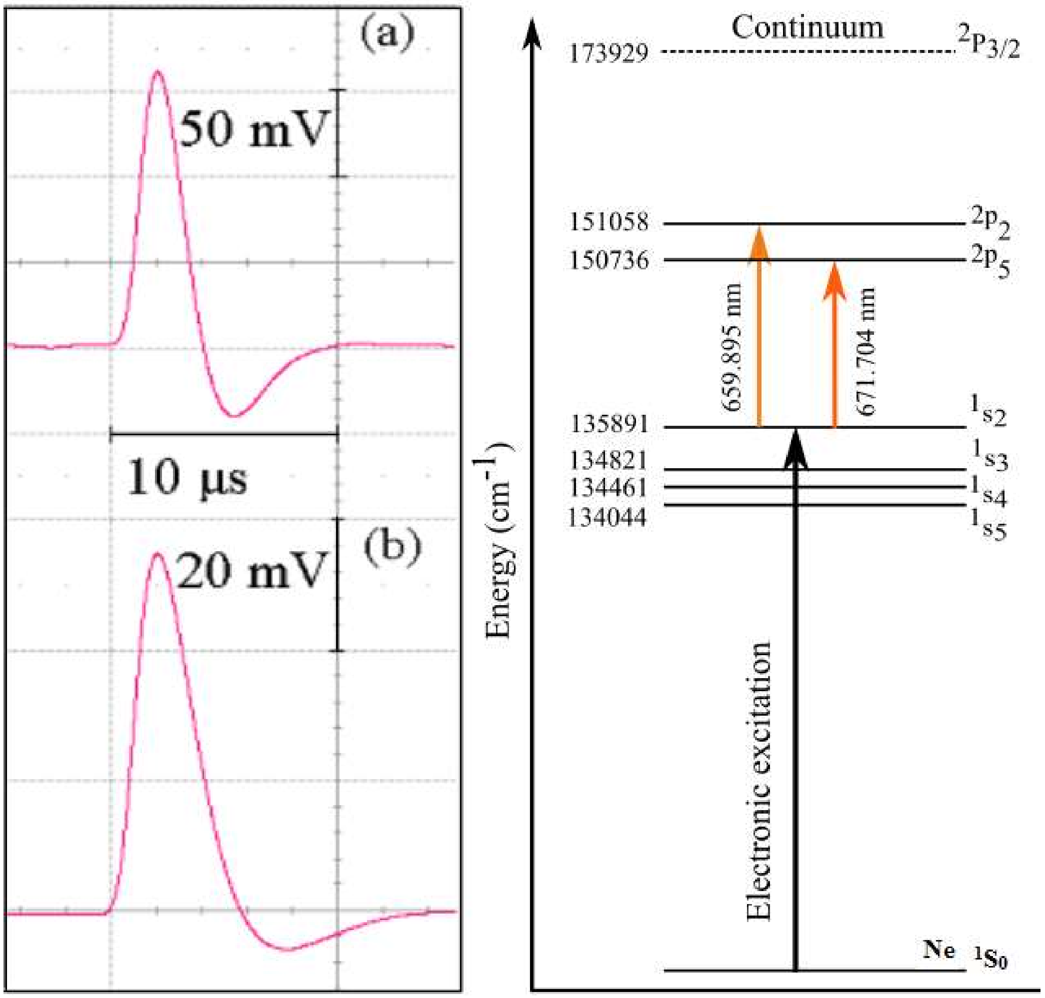

Fig. 4.2 Ne OG signals at (a) 659.895 nm, (b) 671.704 nm and energy levels diagram

Such OG studies, based on atomic/molecular process with discharge OG-circuit model in miniature neon discharge plasma are covered in our earlier work [10,82]. Conversely, the inverted population results in decrease in number density of higher ($2p_i$) levels due to stimulated emission. Hence, net effect is the decreased ionization [94]. Thus, the polarity of neon OG signal is very much sensitive to the population difference (see Eq. 1.1) in the two energy levels coupled together by the laser radiation. Signals in Fig. 4.2 also exhibit such typical inverted OG signatures. Both the Ne transitions ($2p_2 \rightarrow 1s_2$) and ($2p_5 \rightarrow 1s_2$) terminate at common lower level. There is a large difference in the lifetime of upper ($2p_j$) levels and lower ($1s_2$) level. The lifetime of $2p_j$ levels is shorter than $1s_i$ levels [98]. As the energy state $1s_2$ has strong electric dipole allowed transition, it is coupled effectively to the ground state, while $2p_j$ level transitions are even parity forbidden. Also, the transition probability (5.32×10^7 s^{-1}), for radiative transition from $2p_2$ state is an order magnitude lower than transition probability (6.64×10^8 s^{-1}) of $1s_2$ state [101]. Therefore, the similar relationship should exist between the transition cross-sections for electron impact. Accordingly the de-excitation rate of $1s_2$ state should be higher than $2p_2$ state, in spite of, radiation trapping in discharge. Thus, energy levels dynamics and the population governed by electron-collision and de-excitation rates, are responsible for the inverse sign OG effect for ($2p_2 \rightarrow 1s_2$) transition at 659.895 nm. Similar is the case observed for ($2p_5 \rightarrow 1s_2$) transition at 671.704 nm transitions as both share the same lower ($1s_2$) state and the higher energy ($2p_5$) state is having radiative lifetime and transition probability similar to $2p_2$ state [101,102].

4.1.2 CW OG studies

Figure 4.3 shows the schematic of CW OG setup. This mainly consists of the developed Li HC lamp, Nd:YAG, 2nd harmonic pumped CW ring dye laser with DCM dye, wave-meter and a computer (PC). A data logging software developed, in Lab-View, is used to extract the OG signals and to display on computer. The Li atomic vapours are produced in similar way as described earlier using the same Li HC lamp by sputtering means in Ne gas discharge. The Li Doppler limited OG spectrum is recorded using CW ring dye laser setup and lock-in amplifier to measure the Doppler broadening effects in HC discharge lamp. A mechanical chopper is used to chop the CW dye laser beam to obtain the lock-in reference and time integrated OG signals. The used CW ring dye laser with ~ 10 MHz linewidth provides mode-hop free scan of ~ 30 GHz. During the scan, isotopic Li D_1 & D_2 lines are clearly resolved, however ^{7}Li (D_1) & ^{6}Li (D_2) lines are undistinguishable as shown in Fig. 4.4. The isotopic shift for these two undistinguished Li lines is so small that it is dominated by cumulative line broadening effects generally observed in gaseous discharge. The main source of line broadening, in present case, is the Doppler broadening as the fill-gas pressure (0.3 mbar) in HC lamp is kept low enough.

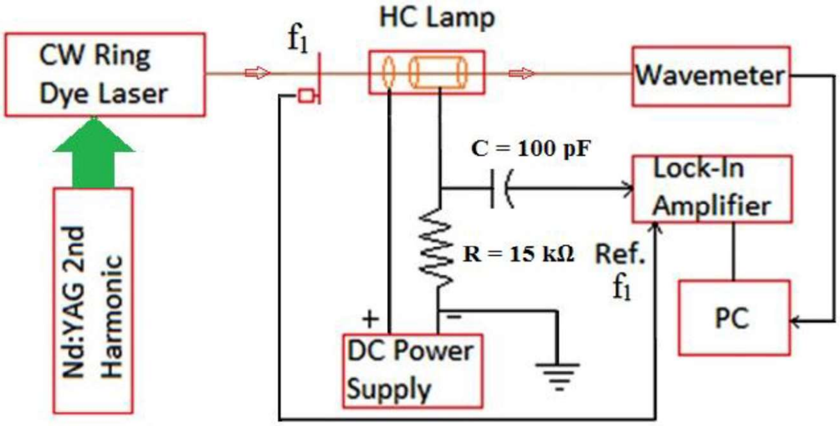

Fig. 4.3 Schematic of experimental CW OG setup

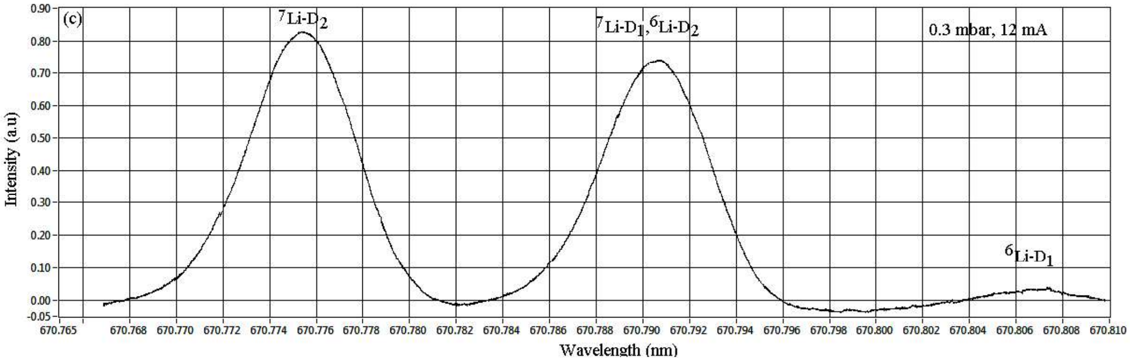

Fig. 4.4 Doppler limited OG spectrum of ^{6,7}Li in the vicinity of 671 nm

The Doppler broadening (inhomogeneous), in the transitions, occurs due to the thermal motion of atoms or molecules. As any specific atom or molecule could either move along or perpendicular or both to dye laser beam, therefore every OG spectral line is Doppler shifted resulting in a slight change in wavelength or frequency absorbed. The shift in resonant frequency (ν_0) is governed by,

$$\nu_D = \nu_0 (1 \pm v/c) \tag{4.1}$$

that generate Doppler broadened line profile. As the broadening effects, due small natural lifetime and low pressure (0.3 mbar), is expected to be low enough, therefore OG line intensity profile is nearly Gaussian type and can be represented by I(ν) as,

$$\mathrm{I}(\nu) = \mathrm{I}_0 \sqrt{\frac{4\ln 2}{\pi}} \frac{1}{\Delta\nu_{\mathrm{D}}} \exp[-4\ln 2 \frac{(\nu-\nu_0)^2}{\Delta\nu_{\mathrm{D}}^2}], \tag{4.2}$$

$$\text{where } \Delta\nu_{\mathrm{D}} = \frac{2\nu_0}{\mathrm{c}} \sqrt{\frac{2\ln 2\,\mathrm{kT}}{\mathrm{m}}} \tag{4.3}$$

The broadening in spectral line depends on frequency (ν_0), atomic mass (*m*) and temperature (*T*) of the absorbing atoms/ molecules. For Li, it is significantly higher since it has lower atomic mass and therefore higher thermal velocity. From OG signal profile, Doppler broadening effect is estimated to be 3.53 GHz. This gives fill gas temperature as 845 ^{0}K. The recorded OG spectrum can be used to study the Li fine structure and to estimate its isotope-shift as both the parameters are important in laser isotope separation. Hence, these pulsed and CW OG studies provide the guidelines for the utilization of developed Li HC lamp for further research work in terms of operating discharge current, fill gas pressure, spectral resolution, incident laser power and their linewidth and the control of laser wavelength.

4.2 Saturation absorption spectroscopy of Li in HC lamp

In present study, Doppler free saturation absorption spectroscopy (SAS) of Li at ~ 671 nm is carried out to study its hyperfine structure splitting as well as isotopic shifts corresponding to Li D_1 and D_2 lines. Figure 4.5 shows the schematic of an experimental set-up for saturation absorption spectroscopy. It consists of the same CW ring dye laser coarsely tuned around in narrow spectral range nearby about 671 nm wavelength. The desired wavelength is obtained using DCM laser grade dye dissolved in ethylene glycol. The λ/2 plate in conjunction with cube beam polarizer (CP) is utilized to split CW laser output into probe and pump beams with needed intensity ratio. The high intensity pump beam (~ 100 mW/cm^2) is chopped using an optical chopper (OC) while passing through the HC lamp. The weak probe beam (~ 100 μW/cm^2) is sent through the Li HC lamp in counter-propagating direction. A Si-PIN photodiode (PD) is used to detect the probe beam. The intense pump beam generates the Bennet hole in Doppler broadened medium population, which is detected by using the counter-propagating probe beam as shown in Fig. 4.5. The photodiode output is given to digital lock-in amplifier (SR830, USA) referenced to chopping frequency of high intensity pump beam.

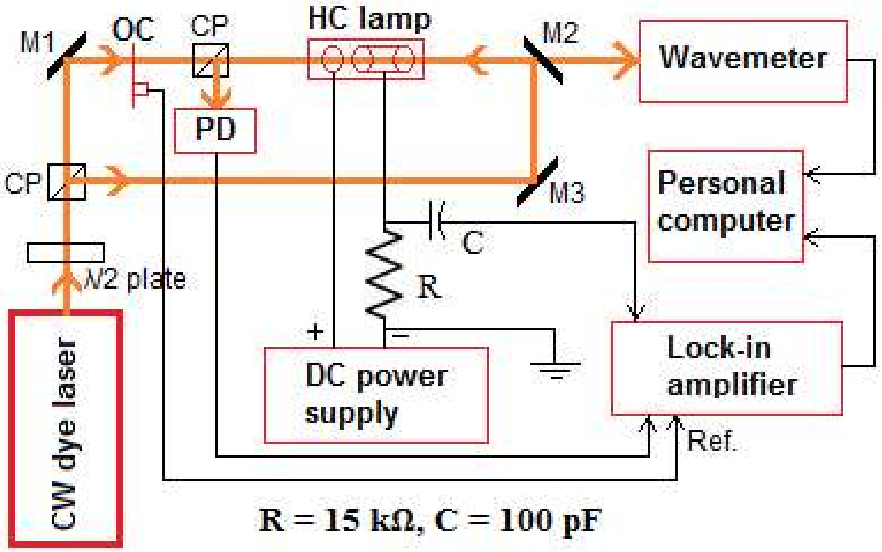

Fig. 4.5 Experimental setup for saturation absorption spectroscopy

A part of the dye laser beam, through partial beam splitting mirror M2, is sent to high precision wave-meter (W-S7, HighFinesse) for monitoring the transition wavelength. The saturation absorption spectra is recorded using a data acquisition card and LabVIEW developed program.

The non-zero nuclear spin of ^{6}Li and ^{7}Li as $I = 1$ and $3/2$, respectively are responsible for its hyperfine energy level splitting [103]. The coupling of total orbital angular momentum ($J = L \pm S$) with nuclear spin (I) generates the hyperfine structure. Figure 4.6 shows the possible Li fine/hyperfine energy levels and its corresponding transitions. The ground and first excited state of Li are described by the term values ^2S and ^2P. The ground state ^2S splits further into two hyperfine levels with energy shift governed by magnetic dipole interaction. Also the first excited state ^2P splits into the $^2P_{1/2}$ and $^2P_{3/2}$ state owing to spin orbit interaction. Of these, $^2P_{1/2}$ (D_1) line splits again into two hyperfine levels with shift in energy governed by magnetic dipole interaction term. Another, electric quadrupole interaction is only effective when $J, I \geq 1$. Therefore, this interaction does not influence the above state. On the other hands, the $^2P_{3/2}$ state splits into four hyperfine levels with shifts in energy governed by both the interactions.

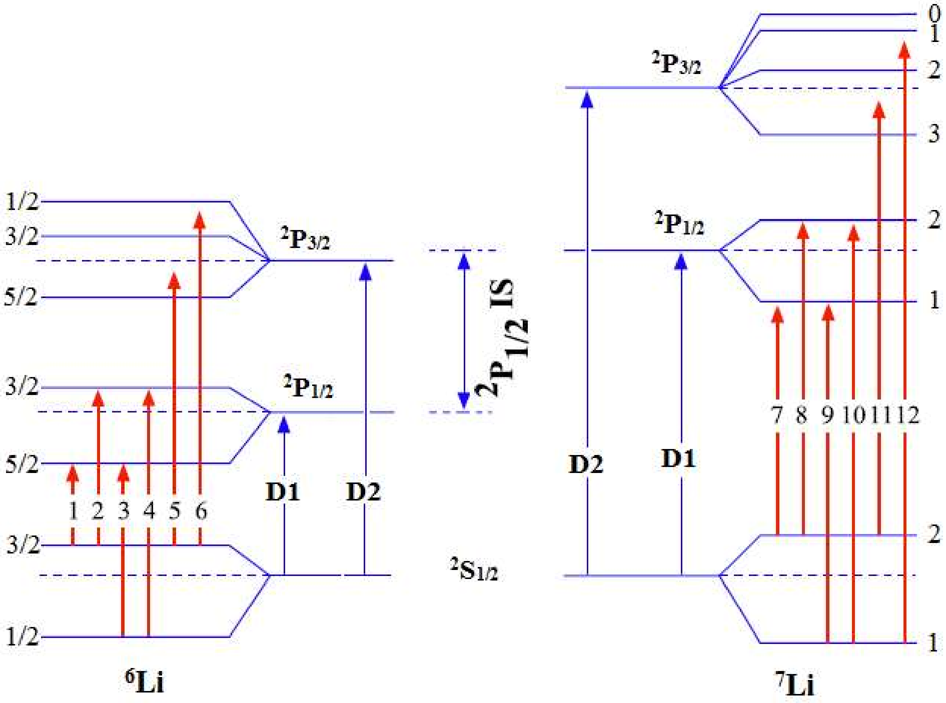

Fig. 4.6 Hyperfine energy levels and the transitions of ^{6,7}Li, D lines

Figure 4.7(a) shows the measured saturation absorption spectrum of lithium at ~ 671 nm with fill gas pressure of 5 mbar. The two hyperfine components of ^{7}Li, D_1 and D_2 lines are fairly resolved. However, the ^{6}Li D_1 line is not resolved. This is due to the effect of velocity changing collisions highly dependent upon fill gas pressure. The fill gas pressure is reduced and the spectrums are again recorded. Figures 4.7(b) and 4.7(c) shows the lithium SAS spectrum with reduced gas pressure of 1 and 0.3 mbar, respectively. In these figures, four hyperfine components of ^{7}Li D$_1$ & D$_2$ lines and the two of ^{6}Li D$_1$ line are clearly resolved.

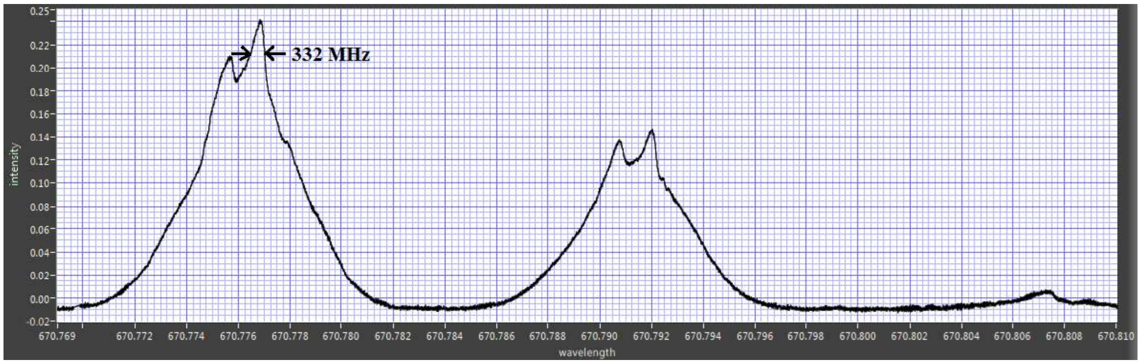

Fig. 4.7(a) SAS spectrum of ^{6,7}Li at ~ 671 nm (5 mbar Ne gas pressure)

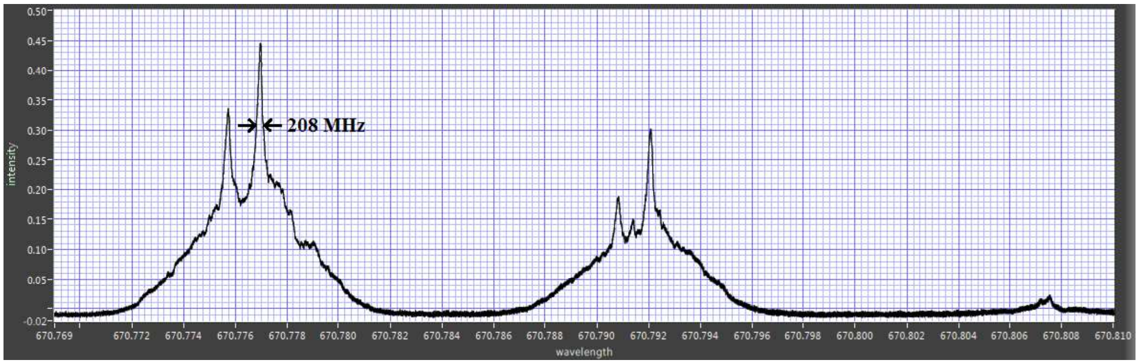

Fig. 4.7(b) SAS spectrum of ^{6,7}Li at ~ 671 nm (1 mbar Ne gas pressure)

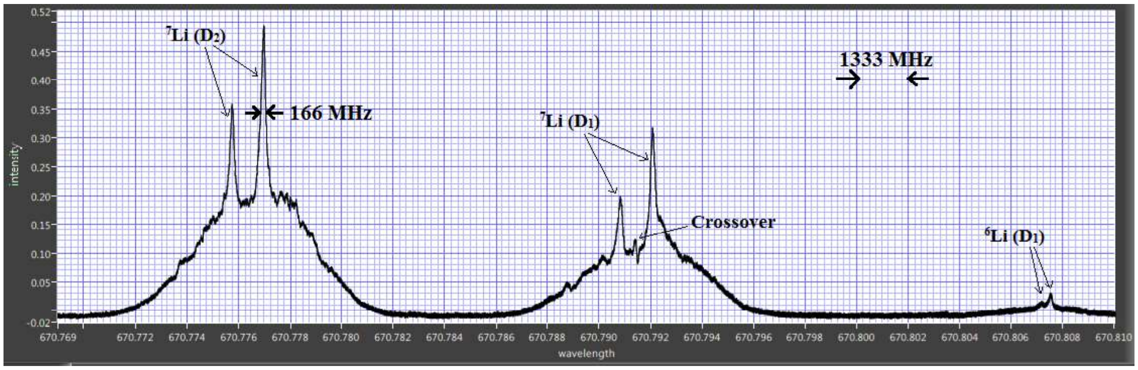

Fig. 4.7(c) SAS spectrum of ^{6,7}Li at ~ 671 nm (0.3 mbar Ne gas pressure)

The observed line shape shows a Lorentzian type of profile superimposed onto a broad Gaussian pedestal caused by velocity changing collisions effects. The lines profile of measured spectrum is ruled by the following equation [104],

$$S(\Delta\nu) = \frac{\sigma_o \gamma_o d}{2\sqrt{\pi}\Delta\nu_d}\left\{\frac{\left(\frac{1}{2}\gamma_o\right)^2}{\left(\frac{1}{2}\gamma_o\right)^2 + \Delta\nu^2} + C\ \mathrm{exp.}\left[-\left(\frac{\Delta\nu}{\Delta\nu_d}\right)^2\right]\right\} \mathrm{x}\ \frac{N\ \mathrm{exp.}\left[-\left(\frac{\Delta\nu}{\Delta\nu_d}\right)^2\right]}{1 + D + C\ \mathrm{exp.}\left[-\left(\frac{\Delta\nu}{\Delta\nu_d}\right)^2\right]} \tag{4.4}$$

Where γ_o denotes the homogeneous linewidth of transitions, σ_o the resonant cross-section and d is the absorption length. N is total atomic density and the $\Delta\nu_d$ Doppler width. The parameter C specifies the relative contribution of Lorentzian and Gaussian terms and D tells about the non-linear dependence of line-shape on collisions and pump intensity. The fine/hyperfine energy levels spacing and isotopic shift are calculated from the obtained spectra. The peak values are estimated by taking the average of twelve spectrums recorded. The observed fine structure splitting ($^2P_{3/2}$, $^2P_{1/2}$) of ^2P state is 10052 ± 10 MHz. Table 4.1 shows the measured lithium hyperfine splitting in HC discharge. The hyperfine splitting of ground state ($^2S_{1/2}$) is 800 ± 10 MHz for ^{7}Li (D_1 & D_2), and 227 ± 10 MHz for ^{6}Li (D_1). The isotopic shift for ^{6}Li and ^{7}Li, D_1 line is observed to be 10540 ± 10 MHz. These results are in good agreement with literature reported values [105]. Both the measured parameters play important role in the selection of an efficient photoionization scheme for lithium. The large isotope-shift favours high selectivity of photoionization process leading high enrichment of the desired isotope. Larger the isotope-shift, smaller be the constraints imposed on parameters of dye lasers, especially from linewidth side.

Table 4.1: Li ($^2S_{1/2}$) ground state hyperfine splitting obtained from recorded SAS spectra

Isotope	F values	Experimental values (MHz)	Reported values (MHz)
^{6}Li	3/2 – 1/2	227 ± 10	228.205
^{7}Li	2 – 1	800 ± 10	803.504

4.3 Selective photoionization of Li isotopes in HC lamp

This section of chapter presents an extensive study on two-step selective photoionization of Li isotopes as carried out in Li HC lamp. In a very special scheme, the dark space region of HC discharge is utilized for Li photoionization studies. Hence, this section start with basics of HC dark space region, it merits for implementation of photoionization process and the relevant kinetic process. Then, the results on Li selective photoionization, across 670.780 nm ($^2S_{1/2} \rightarrow {}^2P_{1/2,3/2}$) transition with respect to precise tuning of dye laser and effect of ionizing laser pulse energy is presented. Further using an important saturation technique, photoionization cross-section and Li atom density for ^{7}Li ($^2P_{3/2}$) excited level are measured.

4.3.1 HC dark space and its merit in photoionization studies

In hollow cathode, space charge is created near the inner cathode wall surface. It occurs because of difference in mobility of electronic and ionic charge carrier present in discharge. HC positive space charge creates the high electric field of an order of few kV/cm. This decays in linear fashion from cathode to negative glow where it vanishes [106]. Owing to HC special geometrical dimensions, discharge medium is mainly restricted to the dark space and negative glow region. In fact, the voltage applied to hollow cathode drops considerably across thin dark space width (d ~ 1 mm). This is possible if negative glow perform as an electrical conductor. Then the region in between dark space and negative glow may be used as an effective or virtual anode. Thus for analysis purpose, the dark space enclosed by the cathode and virtual anode can be assumed as an ionization compartment [107-109]. The charge carriers generated by interaction of exciting and ionizing laser beams with sputtered atoms, are accelerated by dark space electric field. This results in photoionization signal because of slow and fast moving ions and electrons, respectively. Vas Dev et al. [110] used HC dark space for studies of uranium two-colour photoionization and observed fast (~ ns) signature of photoionization signal.

Generally, pulse and CW laser based intricate photoionization setup has been utilized for studying resonance energy pathway [111-114]. This kind of experimental setup generally uses laser ablated or very high temperature resistive or electron beam heating atomic source, in combination with expensive mass-filters for study of photoionization process. These type of atomic beam based setups offer higher isotope selectivity and also could generate highly precise and resolved hyperfine mass spectrum. These nevertheless suffer by low density of atoms (~ 10^8 atoms/cc) or interference because of ablated surplus ions generated in laser interaction zone. Furthermore, the ionic charge collection by mass-analyser detector is restricted due to poor transmission (~ 85%) through fine-mesh electronic grids. Nevertheless, numerous experiments have been carried out utilizing atomic beam setups equipped with economical electron multipliers without any mass-analyser. Both the atomic source and detector are even shared in these experiments. The design of atomic beam sources are more complex at higher temperature, such as for refractory elements. Also, the electron multiplier ionic detectors are more fragile as per their structural design. Also the detection efficiency deteriorates slowly over a time-interval due to the aging and humid environmental conditions. Thermionic diode based devices, relatively simpler in design and highly sensitive detection wise. These have also been used for studying Rydberg atoms, oscillator strength and photoionization process [115]. This kind of detector has also been focussed in present research work as detailed in chapter-5. In thermionic diode device, the energy of ionizing laser photons needs to be distributed uniformly throughout the device due to its longer laser-interaction path. Other devices such as parallel plate capacitor type heat cell have been also utilized by Ambartzumian et al. [116], Shimazu et al. [117] and Olivares et al. [37]. However, their use is limited by metallic coating on plates, resulting slow decrease in detection efficiency and increased background noise over the period of time. Other type of encouraging device for laser photoionization studies on atoms, is the HC lamps. In these, atomic vapour can be easily generated at high density by sputtering rather than heating or ablation in other devices. High atom density (~ 10^{11} atom/cc) has been measured in dark space of hollow cathode within laser-atom interaction zone [118]. The typical atom density generated in hollow cathode discharge is nearly thousand times larger than as expected in thermionic diode, heat-pipe and atomic beam sources. Besides ground level, high energy metastable levels are also populated in HC discharge lamps. So, studies on photoionization from the excited states are also possible in hollow cathode. Thus multi-step photoionization schemes may reduce to fewer excitation steps especially in case of filled inert gases. This in turn reduces the complexity and cost of experimental setups.

4.3.2 Kinetics in dark space region of HC discharge

For an interpretation, the dark space region restricted by the effective anode and cathode of hollow cathode lamp can be treated as a miniature ionization chamber [109]. In ideal case, the electric field in HC ionization chamber which drives laser created electronic & ionic charges, can be acquired from Poisson's equation and applied hollow cathode potential (V_0) as,

$$\frac{dE(x)}{dt} = \frac{e}{\epsilon_0}(n_i^s - n_e^s), \tag{4.5}$$

$$\int_0^d E(x)dx = -V_0\,, \tag{4.6}$$

$$E\,(x) = -\frac{2V_0}{d}\left[1 - \frac{x}{d}\right], \tag{4.7}$$

Here, e is the electronic charge, ϵ_0 the permittivity of free space. The V_0 denotes applied HC voltage, while d represents the dark space width measured from origin assumed at cathode. The n_i^s and n_e^s are ionic and electronic charge densities, respectively that exist in hollow cathode discharge. Position dependent field *E(x)* drives the charge carriers created by an action of step-wise photoionization of sputter atoms and their motion is regulated by,

$$\frac{dv_i(x,t)}{dt} = \frac{e}{M}\,E(x) - \beta_i v_i\,(x,t) \tag{4.8}$$

$$\frac{dv_e(x,t)}{dt} = -\frac{e}{m} E(x) - \beta_e v_e (x,t) \tag{4.9}$$

here, M and m are the mass of ions and electrons, while β_i and β_e denotes respective collisions repetition rate. Laser induced photo-ion current signal could be attained from energy conservation principle. The work carried out by HC dark space electric field on photo created charges should be equal to energy delivered by applied voltage (V_0). Thus, the laser photo prompted current i(t) can be obtained as below, provided the magnetic effects due to charge motion are ignored,

$$V_0\, i(t) = e \int E_0 \,(n_i\, v_i - n_e v_e)\, d\tau \tag{4.10}$$

Here, E_0 represents the space charge electric field due to voltage (V_0) across the hollow cathode and τ is the volume enclosed by virtual anode and cathode in which electrons and ions are travelling. In Eq. (4.10), the variation in electrostatic energy and work done on charge due to field E_0 is not involved, as these are mutually cancelled out [119]. In pure atomic beam based mass-spectrometry setups, the laser created ion current are generally measured by separate detector positioned at few tens of centimetres away from ionic source. This is done through special ion optics such as acceleration grid and the einzel lens. It offers an added mass selectivity, though at the cost of lower charge collection efficiency. While, in hollow cathodes, no such isolated detector is needed and the charges so generated are collected and detected by cathode itself at few millimetres away from laser generated ions. Hence, better charge collection efficiency is expected in hollow cathode that would produce strong photoionization signal. However, this occurs at the cost of poor selectivity, unlike the mass-spectrometry photoionization setups. In hollow cathode lamp based setup, the selectivity is mostly governed by the laser linewidth and line broadening in atomic transitions. Previously, hollow cathode has been utilized by Babin et al. [120] to generate an atomic beam of refractory element and extracted the same into a separately attached glass chamber for fluorescence studies. Applying minor change in hollow cathode geometrical design, the laser created photo-ions can be extracted in a similar way as done by Alessi et al. [121] and Carazzato et al. [122] in glow-discharge ion source. The use of hollow cathode for resonance ionization spectroscopy is beneficial for discovering novel energy pathways and to compute photoionization cross-section. Hollow cathode based photoionization setups are simpler and relatively inexpensive in design over huge and intricate atomic beam based mass spectrometry photoionization systems. Because these bulky systems need big vacuum chamber, high temperature oven and delicate ion-detector. In HC lamp, major benefit is its ease of operation. Past studies in hollow cathode dark space, especially related to photoionization, were limited to few elements such as uranium [107,108] and Copper [109]. Recently, Scarpa et al. [123] explored more than ten ionization pathways for Ge using hollow cathode. Similarly, two-colour photoionization of Sn has been performed in hollow cathode and compared with signal from TOF mass-spectrometer [124]. In present work, the dark space has been used to study isotope-selective photoionization of lithium. The large bore size, see-through, in-house built HC lamp is used in present study.

4.3.3 Two-step laser photoionization scheme of Li

Li has only two isotopes. As per energy levels and ionization potential (I.P), the separation of its isotope (^{6,7}Li) appears to be feasible. This can be carried out by two step photoionization using narrowband dye laser with an output at ~ 671 nm and N_2 laser at 337.1 nm in UV range. The applicable energy levels diagram for Li isotopes with suitable atomic transitions [125] is presented in Fig. 4.8. Both the Li isotope has doublets. The energy separation between fine structure levels $^2S_{1/2} \rightarrow {}^2P_{3/2}$ and $^2S_{1/2} \rightarrow {}^2P_{1/2}$ for both isotopes is ~ 0.33 cm^{-1}. It is almost matching with isotopic shift ~ 0.35 cm^{-1} for resonant line at 670.78 nm [117]. It shows $^2S_{1/2} \rightarrow {}^2P_{1/2}$ line of ^{7}Li approximately overlaps with $^2S_{1/2} \rightarrow {}^2P_{3/2}$ line of ^{6}Li. Hence, a dye laser of linewidth (< 0.33 cm^{-1}) is prerequisite for selective excitation of Li doublets ($^2P_{1/2}$ or $^2P_{3/2}$) of each isotopes. The linewidth of dye laser utilized in present setup is ~ 0.2 cm^{-1}. Hence, it is a good choice to selectively excite either of the two isotopes by dye laser tuning to $^2S_{1/2} \rightarrow {}^2P_{3/2}$ line of ^{7}Li or $^2S_{1/2} \rightarrow {}^2P_{1/2}$ line of ^{6}Li. This is to measure the ionization cross-section of Li. The I.P of Li is ~ 5.39 eV [126]. As energy of excitation (~ 14908 cm^{-1}) for Li ($^2P_{1/2,3/2}$) states is ~ 1.84 eV, therefore excited atoms can be ionized by the photons with wavelength ≤ 349 nm. Thus, a dye laser with ~ 0.2 cm^{-1} linewidth and tunable at ~ 671 nm along with N_2 laser with its energy of photons ~ 3.68 eV, is a feasible combination for the studies of two-step Li isotope-selective photoionization.

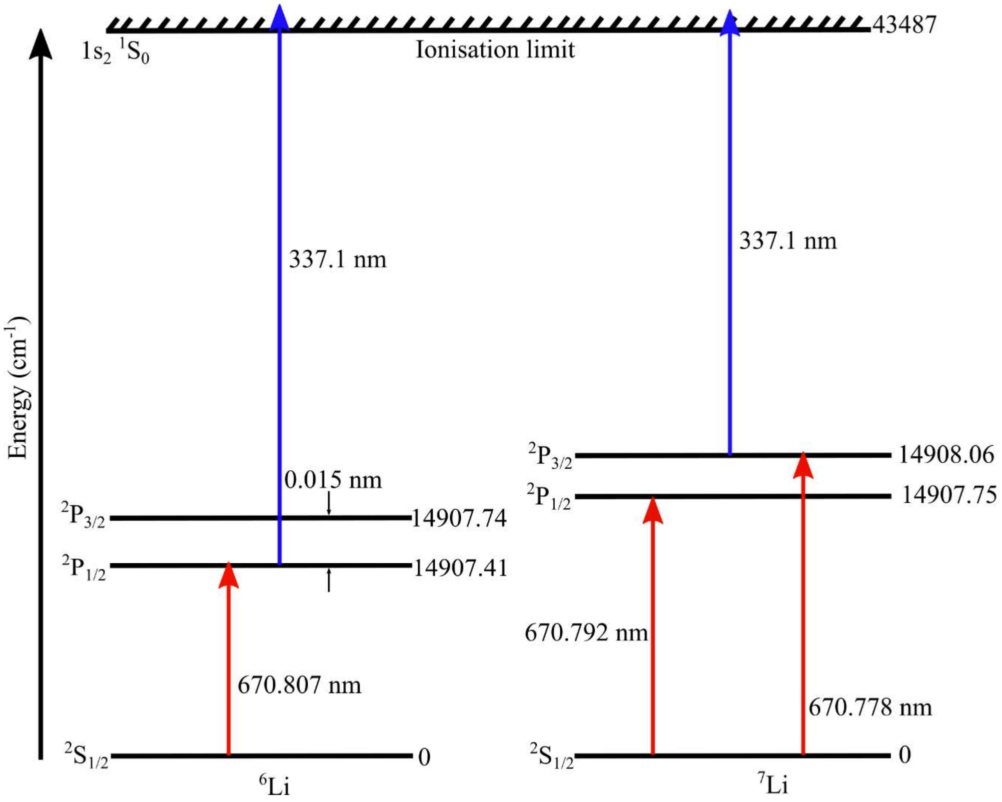

Fig. 4.8 Isotope multiplets diagram for two-step photoionization of Li atoms

4.3.4 Experimental details for two-step Li photoionization in HC lamp

The experimental details for two-step selective photo-ionization of Li atoms using hollow cathode is shown in Fig. 4.9. It has an in-house built dye laser pumped by the nitrogen laser of wavelength in UV range at 337.1 nm. Nitrogen laser with 10 ns pulse has peak output power ~

350 kW. Its repetition rate is adjustable from 1 to 5 Hz as per requirements in experiment. The design of dye laser cavity with single prism beam expander and grating in GIG configuration is similar to that of Littman [58] already described in chapter-2. In brief, a small and cylindrical non-flowing dye cell is made from good quality quartz tube. A 3.5 mM DCM dye solution is made in DMSO solvent to produce an output in 640 to 680 nm range. This is as required for the excitation of desired Li transitions. Dye laser output peak power is measured ~ 14 kW in 6 ns pulse. The dye laser linewidth is reduced further upto ~ 0.2 cm^{-1} by using double grating in grazing-Littrow mode. Using suitable reflectivity mirrors, around 60% of nitrogen laser output is dedicated for optical pumping of dye laser and rest of ~ 40% is used for ionization of the excited lithium atoms. The Li vapours are produced in homemade hollow cathode by sputtering method. The details of hollow cathode is given in chapter-3. An inert gas most suitably neon is used at low pressure (~1 mbar) to get steady gas discharge. A dc power supply (PS) with high voltage is utilized to create steady and uniformly distributed discharge in hollow cathode. The hollow cathode is held in precision translational stage. This helps in aligning laser beams parallel as well as closer to inner cathode wall. Both of exciting and ionizing laser beams are overlapped temporally and spatially and then passed cautiously through hollow cathode dark space region from the opposite sides. The extended view of laser interaction with sputtered lithium atoms and typical distribution of electric field (E.F) in hollow cathode dark space is shown in Fig. 4.10. Both slow (10 kΩ, 10 nF) and fast (50 Ω, 0.47 nF) electronic circuitry with a pair of opposite polarity fast diodes are used to detect the photo electron/ions current. The detection electronics is properly enclosed in sealed metal box. A computer controlled dye laser wavelength scanner cum data logger [83], described in detailed in chapter-2, is utilized to obtain accurate wavelength scanning data in small spectral range. The wavelength λ-meter (WS-7), photodiode (PD), oscilloscope (Lecroy, 500 MHz), boxcar integrator (SRS-250) and personal computer (PC) are main constituents of the scanner.

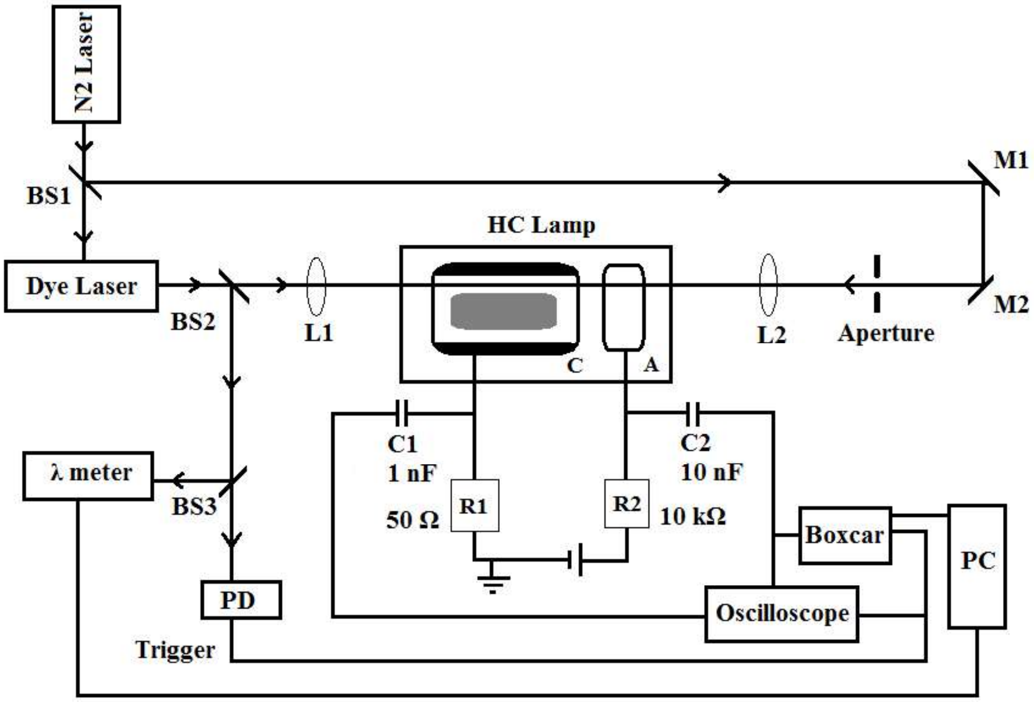

Fig. 4.9 Experimental setup for two-step selective photoionization of Li atoms

A: Anode; C: Hollow cathode; PD: Si-Photodetector; BS1, BS2, BS3: Beam Splitters;

L1, L2: Convex lens (Focal length = 30, 50 cm); M1, M2: Mirrors; PC: Personal computer

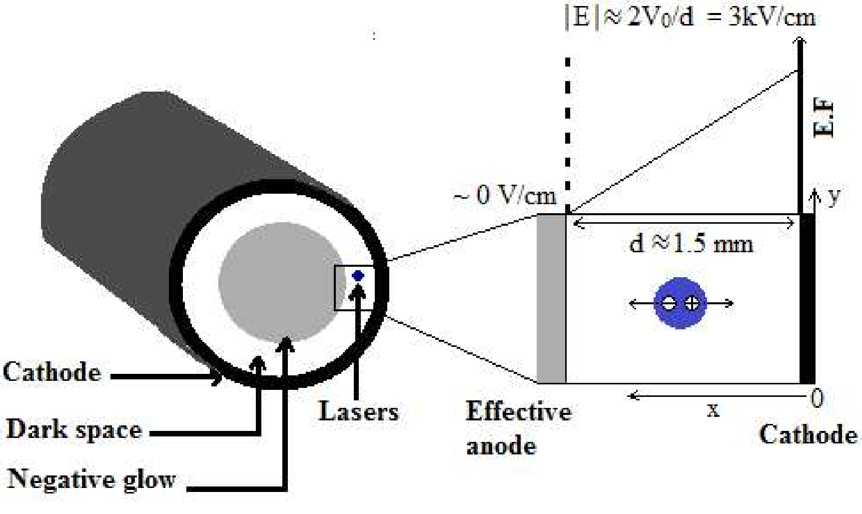

Fig. 4.10 Laser-atom interaction and electric field distribution in HC dark space region

4.3.5 Results on Li photoionization

A. Measurement of photoionization signal

The signal due to selective photoionization of ^{7}Li for a transition ($^2S_{1/2} \rightarrow {}^2P_{3/2}$) that corresponds to 670.778 nm is recorded using two different kinds of circuit. The slow time response (R = 10 kΩ, C =10 nF) circuitry regularly, utilized for measurement of normal optogalvanic effect, generated strong photoionization signal as observed in Fig. 4.11. The signal has collective contribution. It is due to fast and slow moving electrons and ions respectively, created during photoionization. For estimating signal to noise (S/N) ratio of photoelectron/ion detector; first, overall backgrounds noise in absence of exciting and ionizing laser beams is measured. The curvy type of ~ 4 mV peak-peak noisy signal superimposed on base line is noticed. Most likely, it is because of electromagnetic interference due to high energy dump into the discharge of nitrogen laser and the operation of rotary motor used for vacuum. The shot noise (typ. ~ 0.2 mV) generated by OG circuit ballast resistance (10 kΩ) and discharge current passing through hollow cathode is negligible in comparison of external noise (~ 4 mV). Now, only the exciting laser beam tuned ~ 670.778 nm is permitted to pass through dark space to excite ^{7}Li ($^2S_{1/2} \rightarrow {}^2P_{1/2,3/2}$) transition. However, the predicted Li optogalvanic signal could not be detected. It may be because of inadequate energy acquired by electrons just freed from the cathode. These electrons are accountable to generate an optogalvanic signal through collisions with excited Li atoms. The Li multiphoton ionization probability is also ruled out owing to very low power from dye laser. When both the excitation (λ_1 = 670.778 nm) and ionizing (λ_2 = 337 nm) laser pulses are permitted to interact altogether with Li atoms in dark space, the electron-ions pair created by selective photoionization produced high strength Li photoionization signal at 15 mA and 1 mbar gas pressure (Fig. 4.11). A reasonable large signal to noise ratio (S/N ~ 14) obtained, indicates the high charge collection efficiency of the hollow cathode lamp as a detector. In the last stage, first step excitation laser wavelength is completely mistuned from 670.778 nm in presence of second step non-resonant ionizing laser beam. It is noticed that no signal arises except backgrounds noise. The above described procedure validates the sanctity of step-wise photoionization in hollow cathode lamp.

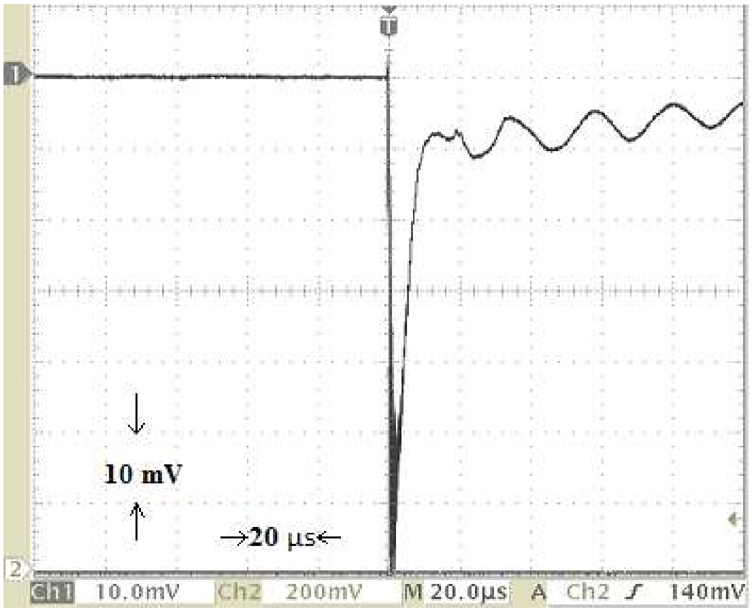

Fig. 4.11 Two-step Li photoionization signal by OG method in developed HC lamp

B. Temporal profile of Li photoionization signal

Another fast response electronic circuit (R = 50 Ω, C = 0.47 nF) having smaller time constant is used to monitor true involvement of electronic and ionic parts, separately in recorded photoionization spectrum. The measured profile of lithium photoionization signal in Fig. 4.12, shows the sufficiently resolved contribution of both electronic (peak '1') and ionic part (peak '2'), separately with their pulse width and amplitudes. Both the signal parts are explicitly observed. The signal produced by ionic and electronic charge start to evolve after an interval of 80 and 20 ns, respectively from reference trigger pulse. It arises due to the difference in mobility of created charge carriers. To differentiate clearly these signals from background noise, the ionizing as well as exciting laser beams are allowed and blocked, simultaneously and it is ensured that these signal peaks appear and disappear, accordingly.

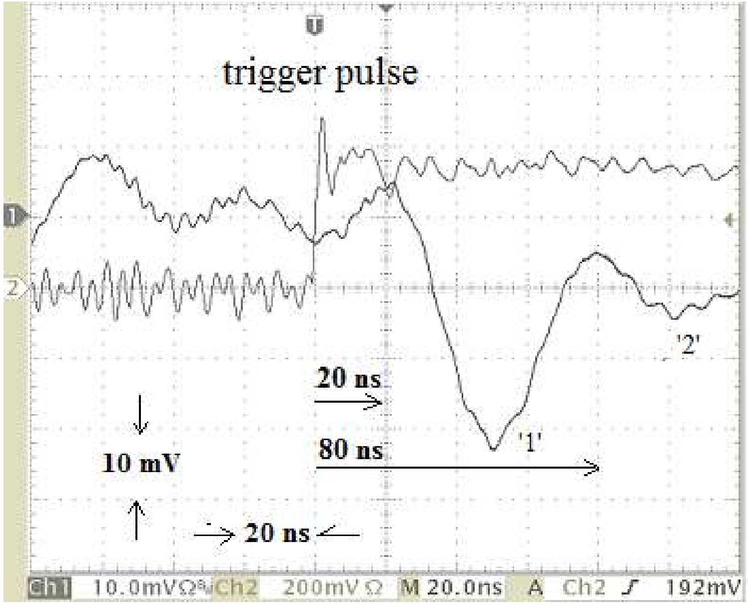

Fig. 4.12 Temporal profile of Li two-step photoionization signal

Broglia et al. [108] had obtained the similar results. They measured temporal behaviour of the photoionization signals for different positions of laser beam and examined closely intensity of the slow and fast signals in hollow cathode dark space. It is noticed (Fig. 4.12) that fast signal due to negative electronic charge follow the pulse of dye laser in shape and nano-seconds duration unlike 'µs' duration normal OG signal [9,12]. In our case, the observed photoionization signal pulse duration (~ 20 ns) is larger than the pulse width (~ 6 ns) of dye laser. Possibly, it is because of lengthy interconnecting coaxial cables used in experiment and the capacitive behaviour of hollow cathode discharge. The cumulative effect of both the factors is due to large time constant of an equivalent OG circuit. In switched-on condition, discharge capacitance is estimated from the rise time of photoionization signal as ~ 8 pF. While, the capacitance measured across hollow cathode electrodes in switched-off condition is ~ 6 pF only. The, increased value of capacitance ~ 2pF, in switched-on condition is attributed to capacitance of the generated ion chamber. The impedance of hollow cathode used, is considerably higher than input termination of 50 Ω at oscilloscope. Hence, the effect of back reflection on signals because of mismatch in impedance is observed. Thus energy reflection causes minor distortions in the shape of pulse and strength of signal. The photoionization signals are measured at different currents and 1 to 3 mbar range of gas pressure. No significant change except in signal amplitude is observed.

C. Radial profile of Li photoionization signal

Besides temporal behaviour, change in photoionization signal amplitude with respect to various laser interaction positions in hollow cathode is measured also by shifting the lamp parallel to laser beam. The signal polarity is observed negative. Although for radial position dependent profile, the polarity does not matters and thus only the strength of signal is plotted. Such co-ordinate dependent evolution of signal acquired during smooth scanning of laser beam in hollow cathode is shown in Fig. 4.13. In this figure position '0' represents the centre of hollow cathode. The small flat region of ~ 1 mm across the centre indicates the width of negative glow region and the arrows mark the dark space width. From Fig. 4.13, it is evident that strength of signal nearby cathode inner surface is maximum and decreased promptly just before negative glow region. The negative glow acting as an effective anode is approximately electric field free zone [9]. The motion of laser created charge carriers in this zone is controlled by slow process of diffusion. The quick fall observed in signal amplitude, follows the dark space electric field [106,108]. The hollow cathode lamp developed is capable to produce relatively large width of dark space (d ~1.6 mm) and negative glow region of around 1.0 mm for 15 mA current and 1 mbar inert gas pressure. It is noticed that width of dark space depends on both the fill gas pressure and HC discharge current. Predominantly, it is heavily dependent on gas pressure and increased with decrease in pressure. The laser interaction of ionizing and exciting beams is guaranteed in this dark space width within ~ 10 mm length of cathode. The ionized Li atoms volume is governed by the dimensions of focussed laser beam spot size and dark space region.

Thus, the hollow cathode can be utilized in both ways, as a laser ion source as well as photo electron or ion detector for investigating appropriate energy pathways for Li photoionization efficient schemes and to measure the photoionization cross-section.

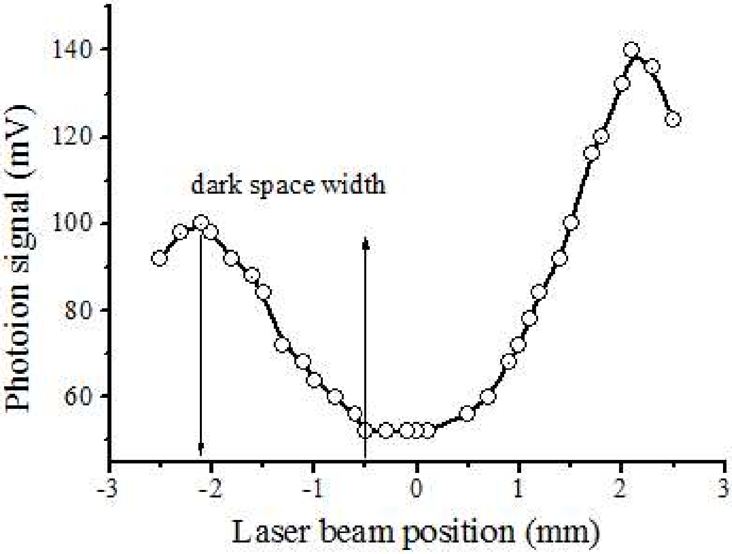

Fig. 4.13 Radial profile of Li two-step photoionization signal

D. Li isotope-selective photoionization

The objective of this work is the investigation of suitability of hollow cathode lamp as an ion source as well as detector for laser selective photoionization of Li and to explore the relevant spectroscopic data such as its isotopic-shift, fine-structure and cross-section of photoionization. As per outlined scheme of laser excitation, the produced sputtered Li atoms are first excited optically from ground state $^2S_{1/2}$ to $^2P_{1/2,3/2}$ excited states by dye laser tuning across 670.780 nm wavelength. The dye laser delivers high enough energy (~ 50 μJ) to saturate the used transitions; though, it may leads to the saturation broadening in line transitions. Hence, dye laser output is reduced by neutral density filters near the saturation point of resonant transition. This is important for measurement of photoionization cross-section when the saturation method is used. The ‘2p’ level population is subsequently ionized by absorbing an extra photons from ionizing nitrogen laser radiation at 337 nm. The effect of precise dye laser tuning on photoionization signal, in hollow cathode across 670.780 nm ($^2S_{1/2} \rightarrow {}^2P_{1/2,3/2}$) transition, is recorded. The dependence of Li photoionization signal on dye laser exciting wavelength is shown in Fig. 4.14. This recorded spectrum is the boxcar averaged output of both the isotopes monitored by highly precise (WS-7) wavelength meter.

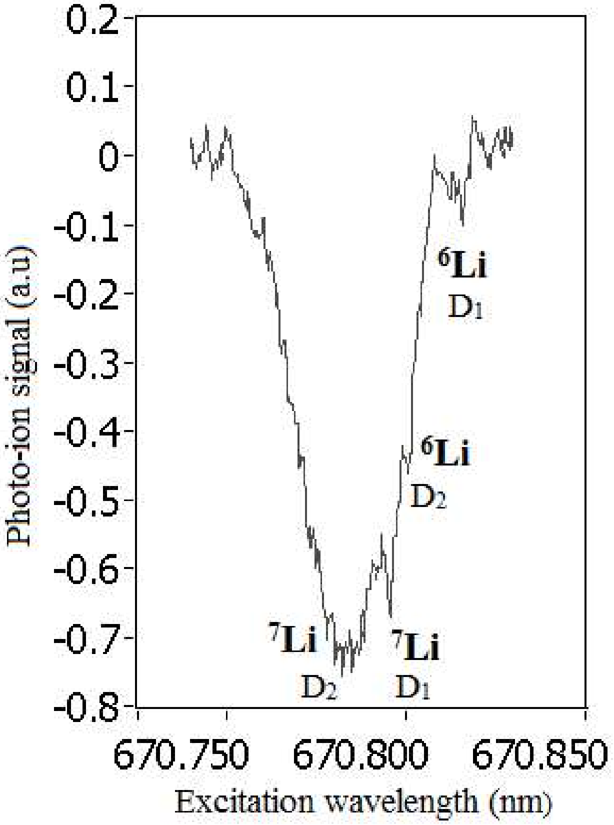

Fig. 4.14 Li two-step photoionization signal in HC lamp with precise dye laser tuning

No amplification is used to process the photoionization signals. The boxcar integrator gate width is so adjusted that both the ionic and electronic parts of signal are acquired explicitly. The photoionization signal is measured at 5 mV sensitivity and averaged over 100 samples. The fine structure spectrum of both the isotopes (^{6,7}Li) are observed clearly. Signatures at isotopic level, consistent with ^{7}Li, D_2 line ($^2S_{1/2} \rightarrow {}^2P_{3/2}$) and ^{6}Li, D_1 line ($^2S_{1/2} \rightarrow {}^2P_{1/2}$) are fairly resolved. However, ^{7}Li, D_1 line ($^2S_{1/2} \rightarrow {}^2P_{1/2}$) and ^{6}Li, D_2 line ($^2S_{1/2} \rightarrow {}^2P_{3/2}$) overlaps significantly. It is because linewidth (~ 0.2 cm^{-1}) of the used dye laser is broader than gap of energy between them. For higher resolution spectra, further improvements in dye laser linewidth is needed. The energy spacing measured between $^2P_{3/2}$ and $^2P_{1/2}$ excited states for the both isotopes ^{6}Li and ^{7}Li are measured as ~ 0.34 cm^{-1}. The experimentally measured isotopic shift of Li isotopes for '2p' states is as ~ 0.35 cm^{-1}. Both the data well agree with the literature reported data [117,126,127]. The energy spacing between hyperfine energy levels could not be measured because of large Doppler broadening (~ 3.5 GHz) in the atomic transitions [128].

E. Measurement of Li photoionization cross-section

The Li photoionization cross-section has been measured, in past by many researchers using various types of atomic source and techniques. Rothe [129] carried out an experiment on Li photoionization cross-section measurement for its excited 2p state near ionization threshold using ion-electron recombination in the shocked plasma. Karlov et al. [130] individually measured the excited state atom density and the number of ions generated using UV ionizing wavelength. Saleem et al. [111] reported the photoionization cross-section near the ionization threshold for ^{7}Li ($^2P_{3/2}$) state using laser based TOF mass spectrometry. In present study, the photoionization cross-section for ^{7}Li ($^2P_{3/2}$) state, with an ionizing radiation at 337.1 nm, is measured by using the simple and inexpensive hollow cathode based photoionization setup. A popular method as described by Burkhardt et al. [131] is used. This is an attractive method as the absolute number of atoms ionized and the excited state atom density, need not to be known, as in case of Karlov et al. [130] studies. This method is based upon the photoionization signal saturation with regard to ionizing laser energy. It has been extensively used to quantify the photoionization cross-section of alkali metals [111] and the other elements [112].

From two step photoionization kinetics [131], it is easy to get an expression for charge carriers (N_i) density generated per ionizing pulse simply by solving the rate equations as,

$$N_i = \frac{Q}{eV_{vol.}} = N_0 \left[1 - \exp\left(-\frac{\sigma E}{2\hbar\omega A}\right)\right] \tag{4.11}$$

where N_0 (cm^{-3}) represents the density of excited atoms, Q the total charge, e the electronic charge, A(cm^2) the area of cross-section of ionizing laser beam. E *(Joule)* denotes energy of ionizing laser and $\hbar\omega$ *(Joule)* the ionizing energy per photon. The term $V_{iol.}$ (cm^3) is laser interaction volume and σ (cm^2), the absolute cross-section for photoionization. In this Eq. (4.11), most of the parameters are either known or can be found except σ and N_0. These can be obtained from least square fitting of Eq. (4.11) to photoionization signal measured as a function of ionizing radiation energy density. The above expression is valid under few assumptions such as resonance transition should be saturated, exciting laser pulse duration should be less than lifetime of excited state and spontaneous decay rate of the excited atoms should be negligible. In this experiment, the dye laser output energy is enough to saturate the lithium ($^2S_{1/2} \rightarrow {}^2P_{1/2,3/2}$) transitions and its pulse duration (~ 6 ns) is smaller than the lifetime (27.2 ns) of Li (2p) state [29,126]. The area (A) of cross-section for ionizing laser beam is measured by photographic film burn spot technique. Similar technique has been used by R. Cong et al. [112] for ionization cross-section measurement of Co, Sn and other elements by laser photoionization method. They found this method equally suitable to two knives method. For measurement of ionization cross-section, the strength of Li photoionization signal, with respect to ionizing laser intensity, is measured. The signal strength is measured by varying the intensity of ionizing laser (337.1 nm) using the neutral density filter, keeping the intensity of exciting laser at 670.778 nm, fixed. Figure 4.15, shows the experimental photo-ionization data for ^{7}Li ($^2P_{3/2}$) excited atoms. The strength of photoionization signal increased first with the increase in ionizing laser energy and then shows a trend of near saturation at higher laser energy. Triangle represents the experimental data and the solid line is the least square fit to Eq. (4.11).

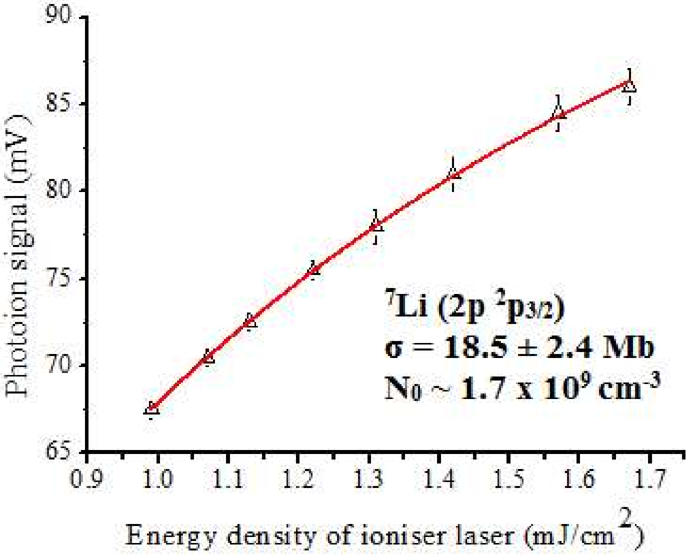

Fig. 4.15 Photoionization cross-section data for ^{7}Li (2p $^2P_{3/2}$) state

To avoid the two-photon ionization possibility, the energy of ionizing laser is kept marginally below the saturation level. That's why complete saturation is not obtained. By extrapolating the fitted curve to higher energy values, the energy of saturation is estimated. The solid line which passes through experimental data point is the least square fitting to Eq. (4.11). This gives the photoionization cross-section value as 18.5 ± 2.4 Mb. This cross-section is in good agreement with earlier reported data [111,132]. The main cause of errors in results are the uncertainty in measurement of ionizing laser pulse energy (E) and interaction cross-section area (A). The measurement uncertainty in laser interaction cross-sectional area is ~ 20%, while the ionizing laser energy measurement error due to the energy meter is around ± 3%. Pulse to pulse variation in the energy of ionizing as well as exciting laser and the error in measurement of photoionization signal further add around ± 5% and ± 2% uncertainty, respectively. The overall rms value of cumulative error in measurement of photoionization cross-section, is found to be less than 27%. The net charge (Q) generated per pulse by laser photoionization, can be correlated to photoionization signal measured across the load resistance R as,

$$Q = \left(\frac{\text{Voltage signal}}{R}\right)\Delta t \tag{4.12}$$

where Δt (s) represents signal pulse width. The N_i can be calculated from net charge created per ionizing pule as described above. An asymptote to the plotted data curve as per Eq. (4.11) provides a relation $N_i \rightarrow N_0$ when $E \rightarrow \infty$. It gives the atom density as $N_0 \sim 1.7 \times 10^9$ (cm^{-3}).

4.4 Three-step OG spectroscopy for photoionization of Li in HC lamp

Laser isotope separation of Li needs the knowledge of its energy levels and the absorption wavelengths. The Li has an ionization energy of 5.39 eV [84,102]. This is suitable for three-step photoionization by laser radiation tuned in the visible spectrum. The present study focuses on to investigate the photoionization pathway for lithium atoms by multistep excitation technique using OG spectroscopy. Although, the energy levels of alkalis are well reported [84,90,126], however their utilization for multi-step photoionization is rarely reported [133] and many details are lacking. Then to find an efficient route of selective photoionization using a particular laser system, it is essential to perform the concrete experimental research. Although, the photoionization schemes suitable for Li can be carried out using more advanced atomic beam based mass spectrometry setups. However, due to their bulky size and more complexed arrangements, the hollow cathode lamp based OG setup is preferred because it is simple, easy and economical. Hollow cathode lamp has been used by Victor et al. [134] for two-step OG spectroscopy of Nd. In recent past resonant laser photoionization of Ge has been also reported in a hollow cathode lamp [123]. We used the home built HC lamp to study the Li photoionization pathway through its intermediate resonant states with transitions (0 → 14904 cm^{-1}) at 670.8 nm, (14904 → 31283 cm^{-1}) at 610.4 nm and (31283 → > 43487.11 cm^{-1}) for < 819 nm by OG method. In order to reduce the complexity of experimental setup, we planned to use a portion of the same dye laser output that has been utilized for 2nd resonance excitation at 610.4 nm, for the third non-resonant step. This is of course lower than the needed ionizing wavelength of 819 nm. This serves the purpose of Li photoionization from its excited (3d) state.

4.4.1 Three-step photoionization pathway for Li

Figure 4.16 shows the pathway for resonance ionization of Li atoms through its intermediate energy states. The lithium atoms available in 2s($^2S_{1//2}$) ground state are resonantly excited to first 2p ($^2P_{1/2,3/2}$) energy state using pulse laser light of 670.791 and 670.776 nm wavelength for ^{7}Li isotope and in similar way for ^{6}Li at 670.805 and 670.793 nm (not shown in Fig. 4.16).

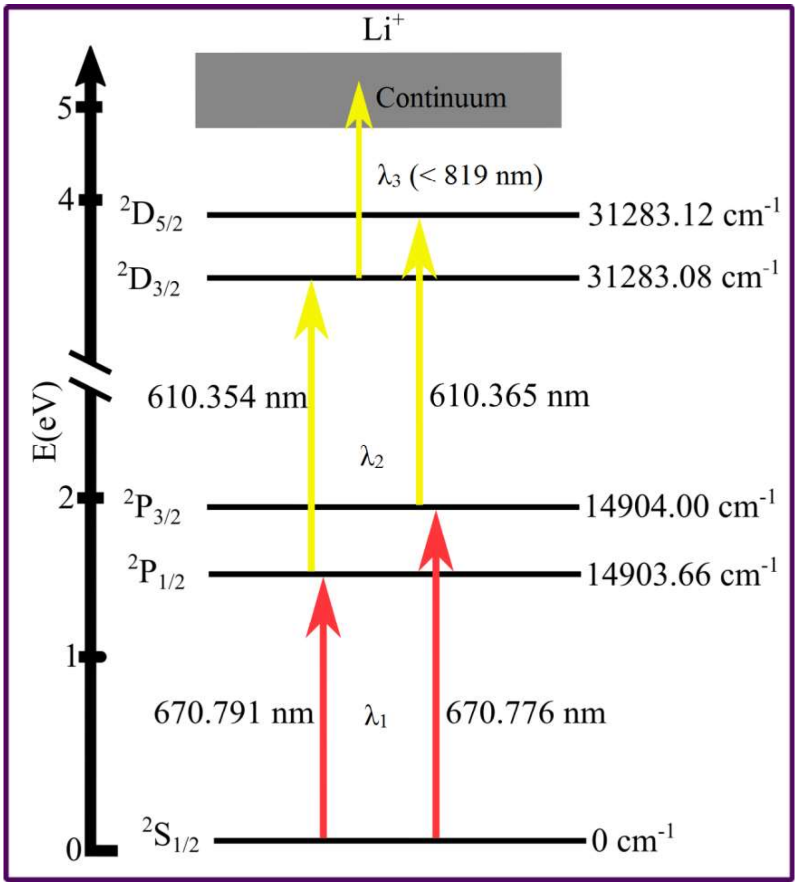

Fig. 4.16 Three-step selective photoionization pathway for Li by OG method

Subsequently, in second step, the population from 2p state with lifetime 27.1 ns [135] is further excited into higher energy 3d ($^2D_{3/2,\ 5/2}$) state with lifetime of 16.7 ns by another laser pulse of photons with wavelength ~ 610.35 nm. The lifetime of these states are comparable to the laser excitation pulses. These single-photon transitions ($^2S_{1/2} \rightarrow {}^2P_{1/2,3/2}$) and ($^2P_{1/2,3/2} \rightarrow {}^2D_{3/2,5/2}$) are viable as per electric dipole selection rules $\Delta l = \pm 1$, $\Delta J = 0, \pm 1, \pm 1$, $\Delta L = \pm 1$, $\Delta S = 0$ and even ↔ odd parity. As the first ionization potential of Li is 5.39 eV and the excitation energy corresponding to first step and second step transitions are around 1.84 and 2.03 eV respectively [126], therefore excited Li atoms from 3d state can be readily ionized by the photons with wavelength shorter than 819 nm. In the present experiment, either of the first or second step dye laser pulse can serve the purpose to photo ionize the Li atoms as their energy is sufficient to bridge the gap between the Li ionization and 3d excited state. However; for third step, a suitable energy photon of wavelength ~ 819 nm from another laser can also be used to reach the Li ionization threshold for efficient photoionization.

4.4.2 Experimental details for three-step Li photoionization in HC lamp

The schematic view of an experimental setup used to realize the above described photoionization scheme, using OG spectroscopy by laser multi-step excitation technique, is shown in Fig. 4.17. In-house developed HC lamp as described in chapter-3 with neon as buffer gas and lithium as cathode is used to generate the lithium atomic vapour. An electrical discharge is applied to HC lamp by a high voltage power supply through a 10 kΩ ballast resistor. The resulting signal due to three-step ionization is coupled to boxcar integrator (SRS-250) through 47 nF capacitor. The signal is recorded by a data acquisition system as described earlier in chapter-2, using computer controlled dye laser wavelength scanner and data acquisition card (Advantech, USB-4716). The CVL pumped two independent dye laser system in synchronization with each other, as described in details in the chapter-2, are used to excite the step-wise Li transitions. The layout of experimental setup is arranged keeping in mind the optical delay between green (510.6 nm) and yellow (578.2 nm) components of CVL pump laser and the delay (~ ns) required in between first and second resonant step of lithium excitation.

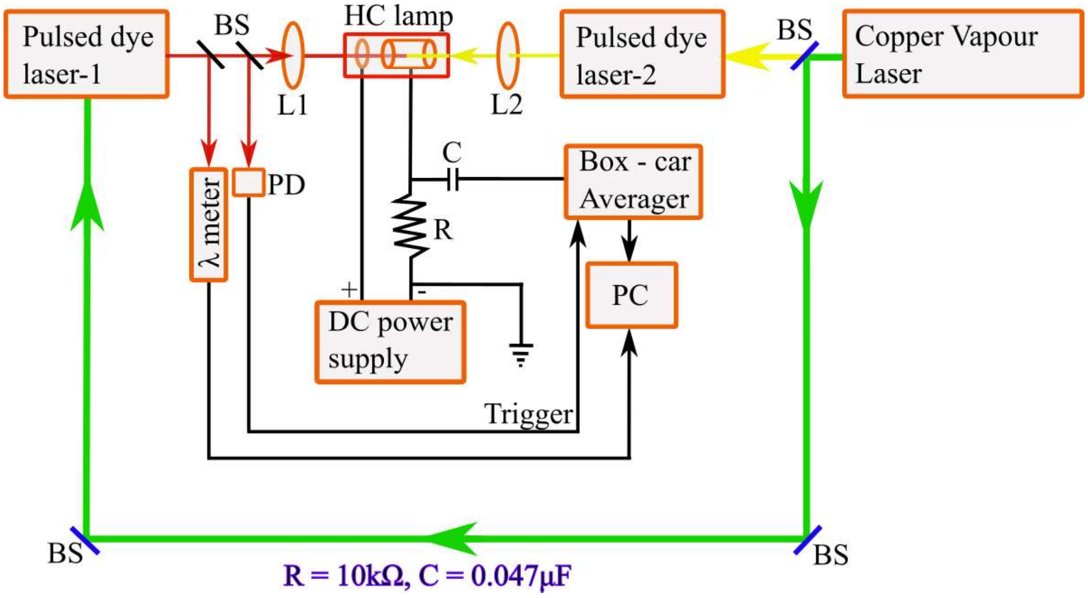

Fig. 4.17 Setup for three-step OG spectroscopy for Li selective-photoionization

In the present CVL laser system, yellow component appears after ~ 20 ns time interval of green laser pulse. The used system delivers the laser output powers of around 100 mW from dye laser-1 (~ 2.5 GHz, 635-680 nm, DCM dye, 2.6 mM) and 150 mW from dye laser-2 (~ 2.5 GHz, 600-625 nm, Rh-640 dye, 0.16 mM) at 6.5 kHz repetition rate. These are sufficient to saturate the respective first and second step of Li transitions as shown in Fig. 4.16. Two spherical lenses L1 and L2 each of focal length 30 cm are used to focus the laser beams into HC discharge from opposite sides. For accurate and precise tuning of the dye laser wavelengths corresponding to respective Li transitions, a computerized motor control is provided to each of the dye laser. The first beam splitter 'BS' placed near the copper vapour laser is a dichoric mirror that has been used to split the CVL green and yellow beams for pumping the respective dye lasers. Second and third beam splitters 'BS' are used to a split ~ 4% of dye laser-1 output for λ meter and photodiode. A precise λ meter (WS-7) with high accuracy is used to monitor dye laser wavelengths. A Si PIN photodiode (PD) is used as a trigger to generate gate window to retrieve the OG signals from HC lamp through boxcar-integrator (SRS-250) on a computer.

4.4.3 Results on three-step Li photoionization

In HC discharge, the origin of optogalvanic (OG) effect can be understood by two different mechanisms. First one, the excitation of atoms by laser from lower to higher electronic states leads to an increased electron impact ionization cross-section. The excited atoms thus get ionized. The ionization of excited atoms results in the decrease of HC discharge impedance and results an OG signal. In second mechanism, laser excitation of the atoms to higher energy states increases the electron temperature through supper elastic collisions between the electrons and the excited atoms. Therefore, the decrease in discharge impedance results in an OG signal. Both mechanism operate simultaneously and domination of either of the process depends upon the discharge and atomic excitation conditions. This first mechanism is important for multi-step excitation photoionization scheme for lithium in hollow cathode discharge [136] and its detailed explanation is given in chapter-3. At first, the experiment is carried out by Doppler limited single-step OG spectroscopy using the first-step Li ($^2S_{1/2} \rightarrow {}^2P_{1/2,3/2}$) excitation at λ_1 by scanning the dye laser-1 wavelength across 671 nm keeping the light from second-step dye laser-2 at wavelength λ_2 blocked or mistuned. Initially, no OG signal is observed at low discharge current up to 20 mA and buffer gas pressure of 5 mbar. However, when hollow cathode is operated at higher current beyond its threshold value (> 25 mA) and at low buffer gas pressure of 1 mbar, the noticeable OG signals are obtained as shown in Figs. 4.18(a) & 4.18(b). These results are consistent with already observed results in chapter-3 with a difference of isotope-selective signatures. Figure 4.18(a) shows the two peaks corresponding to D_1 & D_2 lines of ^{7}Li for excitation wavelengths 670.791 and 670.776 nm respectively. These lines are not well resolved because of Doppler broadening (~ 3.5 GHz) of the transitions in HC lamp. Similarly in Fig 4.18(b) these two lines are observed for ^{6}Li corresponding to its excitation wavelengths 670.805 and 670.793 nm respectively. Peak height for ^{6}Li is observed to be smaller roughly one tenth of ^{7}Li and seems to follow their natural abundances. At higher discharge current values, the electron temperature is expected to be larger [136] and thus both the OG mechanisms are supposed to contribute the OG signal.

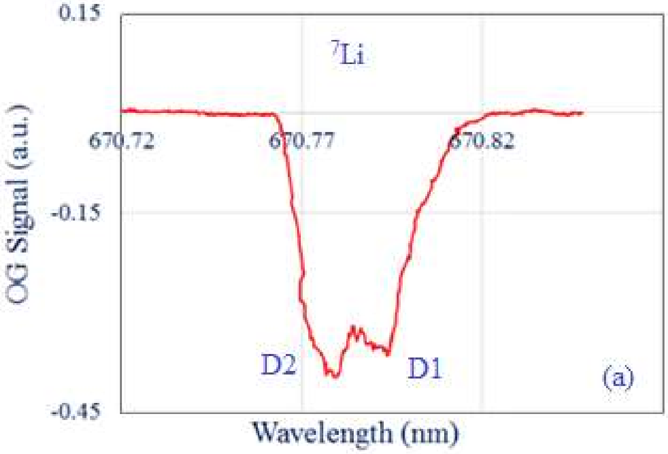

Fig. 4.18(a) ^{7}Li OG signal with fairly resolved D_1 & D_2 lines in HC lamp

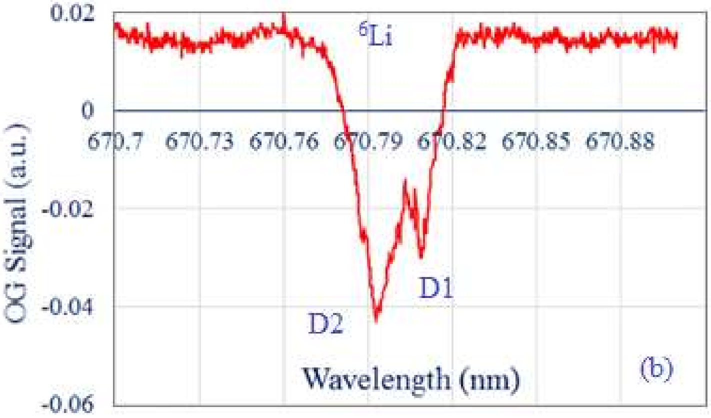

Fig. 4.18(b) ^{6}Li OG signal with fairly resolved D_1, D_2 lines in HC lamp

When HC discharge current decreased up to threshold current (~ 25 mA) and dye laser-1 is scanned from 670.70 to 670.95 nm, an OG spectrum as shown in Fig. 4.19(a) is observed with slightly reduced strength of ^{7}Li signal however with clear D_1 and D_2 components. ^{6}Li components could not be seen because of its weak strength. This spectrum is noisy because of instant background disturbance present in the lab, although OG signal is still clearly retrieved.

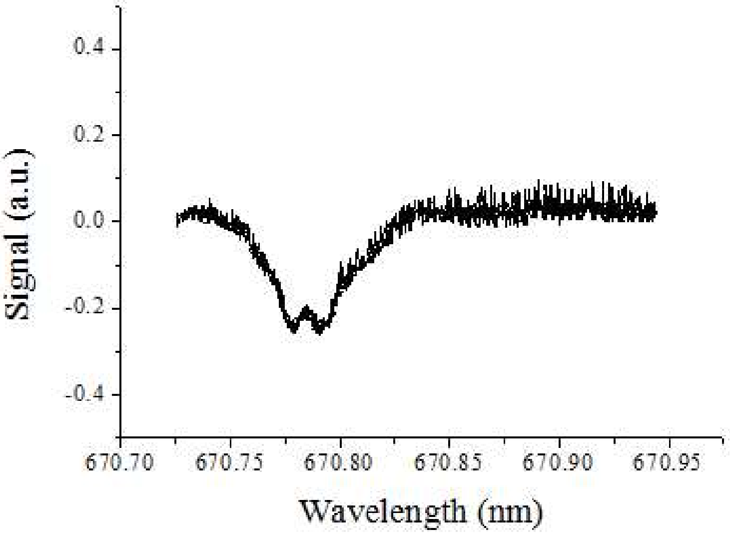

Fig. 4.19(a) Li OG spectrum, when dye laser-1 scanned and dye laser-2 blocked

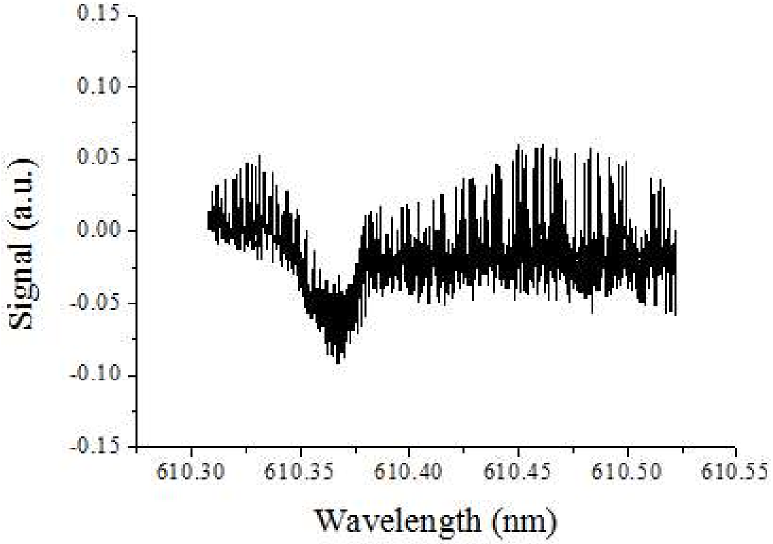

Fig. 4.19(b) Li OG spectrum, when dye laser-2 scanned and dye laser-1 blocked

Similarly, the dye laser-2 is scanned from 610.30 to 610.52 nm across 610.365 nm wavelength. This corresponds to second-step for Li ($^2P_{1/2,3/2} \rightarrow {}^2D_{3/2,5/2}$) excitaion from its excited state, in absence of laser light from dye laser-1. An OG spectrum with weak signal strength at 610. 365 nm is observed as shown in Fig. 4.19(b). The fine structure components and isoptopic signature are not clear, however a cumulative signal is explicit. This signal occurs from Li excited state transistion, possible in HC discharge because few higher enegy states close to ground state, are populated by the elctronic impact excitaion in HC lamp [9]. Now, experiment is repeated with light from both the dye lasers allowed to pass through the negative glow region of HC lamp, keeping the dye laser-2 wavelength fixed at 610. 36 nm and scanning the wavelength of dye laser-1 in the range of 670. 70 to 67.90 nm. An intersting result with remarkable enhancement (~ 10 fold) in Li signal with fairly resolved D_1 & D_2 lines is observed as shown in Fig. 4.20.

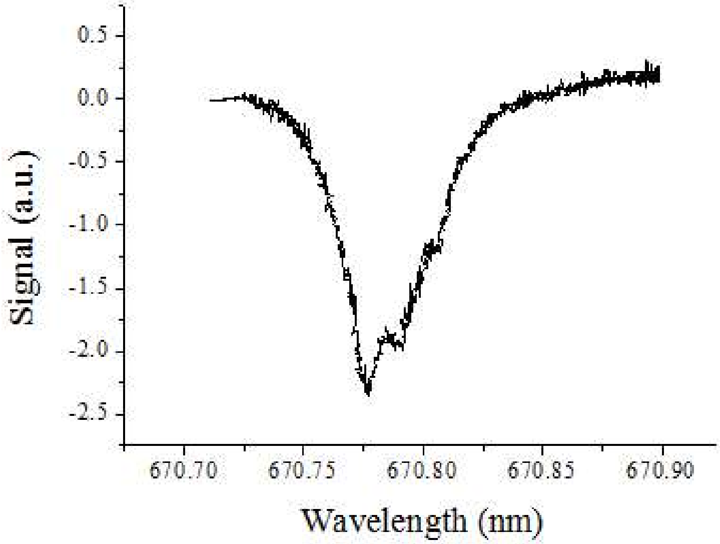

Fig. 4.20 Li OG signal by two-step excitaion followed by third-step ionization at 610.35 nm

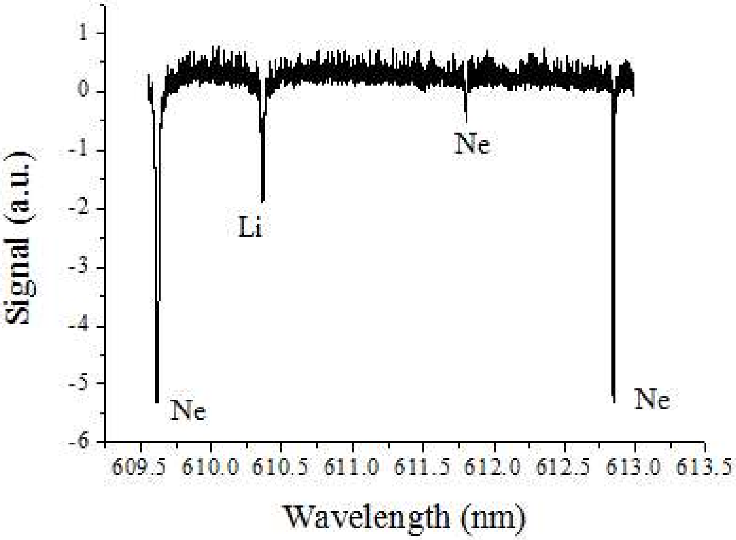

Fig. 4.21 Li/Ne OG spectrum with dye laser-2 scanned and dye laser-1 tuned at 670.78 nm

The enhanced OG signal is observed when both the first and second step transitions are excited simultaneously with a few nano-second delay between them followed by non-resonant third-step ionization at same the wavelenth of 610.365 nm. Similarly, the experiment is repeated again by scanning wavelength of dye laser-2 in the range of 609 to 613 nm and keeping wavelength of dye laser-1 fixed at 670.78 nm corrsponding to Li first step resonant transtion ($^2S_{1/2} \rightarrow {}^2P_{1/2,3/2}$). In addition to three-step enhanced Li OG signal at 610. 365 nm , few lines at 609.608, 611.804 and 612.844 nm are also obserevd that correspond to single-step excitation of well known buffer neon gas transitions (see Fig. 4.21). The effect of dye laser-2 power is observed on Li enhanced OG signal. The enhancement is observed only at higher power levels that ensure about the cascaded three-step photoionization of Li in HC lamp by OG effect. Later on, similar scheme has been applied in time-of-flight based photoionization experiment in chapter-6.

4.5 Conclusion

In summary, pulsed and CW OG effect have been studied in the in-house developed (Li/ Ne) hollow cathode lamp. Lithium OG signals in the vicinity of 671 nm are clearly observed with good S/N ratio at moderate incident laser power (~50 mW) obtained from copper vapour laser pumped dye laser (~2.5 GHz, 20 ns, 635-680 nm). In addition to OG signals from cathode material, strong neon buffer gas OG signals are also observed. Doppler limited OG spectrum clearly resolved the isotopic Li (D_1 & D_2) lines which is used to estimate the Doppler broadening (3.53 GHz) effects and gas temperature (845 ^{0}K). For resolving Li (D_1 & D_2) lines further, Doppler free saturation absorption spectroscopy of lithium at ~ 671 nm has been carried out to study the hyperfine structure splitting. The effect of fill gas pressure on SAS spectrum is also studied. Four hyperfine components of ^{7}Li D_1 and D_2 lines and two hyperfine components of ^{6}Li D_1 line are clearly resolved at lower gas pressure. The observed hyperfine splitting of ground state ($^2S_{1/2}$) is 800 ± 10 MHz for ^{7}Li (D_1 & D_2), and 227 ± 10 MHz for ^{6}Li (D_1). The measured isotopic shift 10540 ± 12 MHz for ^{6,7}Li is in close agreement with reported values. In addition, Li isotope-selective two-step photoionization is demonstrated in hollow cathode lamp, designed especially for photoionization spectroscopy. Most likely, it is a first study of its kind in hollow cathode which deals with Li isotopes and its fine structure splitting along with measurement of photoionization cross-section. The result outcomes validate that hollow cathode with relative large dark space width (~ 1.6 mm) which offers the high electric field (~ 3 kV/cm), can be utilized as an ion-source for an investigation of Li suitable $[^2S_{1/2} \xrightarrow{\sim 671\ \mathrm{nm}} {}^2P_{1/2,3/2} \xrightarrow{\sim 337\ \mathrm{nm}} Li^+ ({}^1S_0)]$ energy pathway. Suitably high signal to noise ratio of the photoionization signals obtained without using any amplifying device, shows the sensitivity of hollow cathode as a photo-electron or ion detector. Moreover, it leads to an easy way of photoionization cross-section and atom density measurement for ^{7}Li (2p $^2P_{3/2}$) excited state as ($\sigma = 18.5 \pm 2.4$ Mb) and ($N_0 \sim 1.7 \times 10^9$ atoms/cm^{-3}), respectively. Overall, the results acquired conclude that hollow cathode based photoionization setup is much simpler. In efficiency, these are at par with atomic beam apparatus usually used for photoionization spectroscopy. The hollow cathode discharge lamp provides an inexpensive and easier way to the studies of selective photoionization and it can also be extended to the other class of elements. The idea of using intrinsic high electric field produced in hollow cathode dark space for resonance photoionization spectroscopy is creative in itself. The hollow cathode lamp developed, has been also used successfully for three-step OG spectroscopy to realize the proposed three-step, two-colour selective photoionization scheme [(0 → 14904 cm^{-1}) at 670.8 nm, (14904 → 31283 cm^{-1}) at 610.4 nm and (31283 → > 43487.11 cm^{-1}) at 610.4 nm] for lithium by OG method. This study demonstrated that simple and inexpensive hollow cathode based setup can be used efficiently to realize the different possible photoionization schemes for any element.

Chapter 5

Studies on Selective Li Photoionization using Thermionic Diode Detector

5.0 Introduction

Following the essential spectroscopic and photoionization studies of Li carried out by hollow cathode lamp (Chapter-4), the next logical step was to employ a more sensitive device, i.e. the developed thermionic diode. It is capable of generating a long column of Li vapour with uniform atom density and operates in space charge limited region of diode that ensures its high gain and sensitivity required for precision laser spectroscopy. It is an easy to operate and low cost device. The present chapter is focused on studies of selective Li photoionization using thermionic diode detector (TDD). This chapter starts with a short review on thermionic diode ion-detectors. Since as a part of present research work the TDD is developed, its design, construction and characterization are presented in details. In-house built TDD photoionization setup enabled the high gain and high signal to noise ratio for Li photoionization signals generated by the two-photon excitation mechanism. The gain of TDD is measured in an accurate way by spectroscopic method using single-color, three-photon ionization of lithium. In the second work, Li selective photoionization studies are carried out to measure the photoionization cross-sections of its 2p ($^2P_{1/2,3/2}$) and 3d ($^2D_{5/2}$) excited states via two different photoionization pathways. First one is the measurement of Li photoionization cross-section near the first ionization threshold using single photon (2s $^2S_{1/2} \rightarrow$ 2p $^2P_{1/2}$) excitation at 670.78 nm followed by non-resonant ionization at 337.1 nm wavelength. Second scheme uses two photon excitation (2s $^2S_{1/2} \rightarrow$ 3d $^2D_{5/2}$) followed by non-resonant ionization at 337.1 nm. Photoionization signals with high signal to noise ratio (SNR) are produced, for both the single and two photon excitation schemes, using thermionic diode detector. The measured value of Li photoionization cross-sections are in agreement with literature reported data obtained with other methods.

5.1 Development of thermionic diode detector for Li spectroscopy

5.1.1 Brief review on thermionic diode detector (TDD)

High atom density and long absorption path is needed for the detection of weak atomic transitions by absorption method. Fluorescence technique is a good alternative of it. In this technique the fluorescence occurs as a result of absorption with minimum path length and atom density, and it can be monitored easily. Though, the excited atoms may be ionized rapidly before begun to fluoresce, ensuing in reduced fluorescence. In such circumstances, the atoms ionized could be detected effectively by using the negative space charge effects in vacuum diodes. The diode space charge enables the high detection sensitivity for excited atoms, especially lying in Rydberg states [137-144]. Such a device is called as thermionic diode detector (TDD). Structure-wise, basically it is a heat pipe. Its metal body acts as cylindrical anode of diode having coaxial and the stretched straight hot wire as cathode. Alternately, it may be named as a heat pipe diode. This way, device serves the double purpose. In heat pipe mode, it can produce uniform density metal vapour extended isotherm. In action, it is analogous to a vacuum diode tube in which excited atoms could be ionized by laser photoionization or thermal collisions. The +ive ions created this way are electrostatically trapped for a longer period (~ 10 ms) in a potential well formed around hot cathode. This further controls current through the diode. The space charge potential well and trapping time of the ions orbiting around the cathode enables a gain of 10^4 to 10^6 or still higher [142]. Thermionic diode gain can be defined as increase in diode current per photo-ion generated. Ions trapping time in space charge is accountable for extraordinary boost in the sensitivity of diode. This results in nearly 100% detection efficiency [138]. Such high efficiency is required in the detection of ultra-trace elements. In earlier studies, Li trace detection in Ca and Cu samples were reported in literature upto pico-gram levels [143]. At first, Kingdon [145] in 1923 had demonstrated the use of thermionic diode space charge limited mode of operation for efficient ion detection. Afterward, the use of space charge reduction effect was made to determine the ionization potential of inert gases. However, the thermionic diode was used practically first time by Mohler et al. [146] for spectroscopy purpose. Thermionic diode became a powerful tool for laser spectroscopy after the availability of tunable dye lasers in early 1970s [141,143,147-151]. Exclusively, thermionic diode is a special type of ion detector, in the sense that signal current multiplies manifold (~10^5). This is due to space charge neutralization effect of the ions created by laser. However, in normal ion-detectors such as gas filled parallel plate detectors, the signal is not intrinsically amplified and directly evolves from the ion current produced. That's why, no gain is possible in ordinary ion-detector, while very high gain can be attained in thermionic diode based detector. High voltage is required for ordinary ionization detectors to boost the secondary electrons or to ionize the excited atoms and finally to move them towards collector. In the TDD, the excited atoms can be ionized either by direct photoionization or thermal collisions. A very small potential (near the zero volt) is adequate to drift the thermally emitted electrons through the space charge up to its anode. A long thermionic diode was designed by Herrmann et al [142] for a special experiment on parity measurement and its gain was estimated from the calculated potential distribution and the trapping time of ion. To minimize the effects of electric and magnetic fields, they utilized indirectly heated cathode to shield the interaction volume electrostatically that made its design complex.

Thermionic diodes can be utilized for the investigation of highly excited atoms especially present in Rydberg states. The spectroscopy of Rydberg atoms is a highly rich and diverse field and still emerging [152]. Particularly, the alkaline earth and alkalis metals have been studied by means of Doppler free two photon using the thermionic diode [153-157]. Moreover, the energy levels and Rydberg states of lanthanide have been explored using thermionic diode [158,159]. It can be used in photoionization spectroscopy. An important spectroscopic parameter that has direct connection with photo ionization process of highly excited atoms, is the cross-section of photoionization. The photoionization cross-section can be defined as a measure of probability of ionization by a photon. In fact, in laser isotope separation process, the photoionization cross-section plays a vital role. That's why, as a part of the present research work, an inexpensive and simple thermionic diode is developed for lithium photoionization spectroscopy and for the measurements of its photoionization cross-section.

5.1.2 Design and construction of TDD

An engineering drawing of the developed thermionic diode is shown in Fig. 5.1. Its various parts are labelled as; 1. Cylindrical furnace, 2. Heat-pipe, 3. Radiator, 4. Filament cathode, 5. Electrical-feedthroughs, 6. Window flange, 7. Glass window, 8. Heating coil, 9. Clamps, 10. Gas-inlet, 11. Vacuum-outlet, 12. Sample. The main body of diode includes a long heat pipe of length 70 cm with inner, outer diameters 3.0 and 3.3 cm respectively. This is enclosed by the coaxial heating furnace. Furnace and heat-pipe are both casted from high quality steel (SS 340 L). At both ends of heat pipe two SS flanges (ID: 2.2 cm, OD: 4.6 cm) are welded. Just before window flanges, fine grooves of width 1.5 mm and depth 2.5 mm are cut on both the heat-pipe ends in a long region of ~ 10 cm. This is for removal of excess heat to save the rubber 'O' rings as well as quartz glass windows from metallic coating. Further, coaxial mini heat radiators with multi-thin fins as shown in Fig. 5.1 are mounted externally for efficient cooling. The furnace has a special design to heat the 30 cm long central part of heat-pipe containing Li.

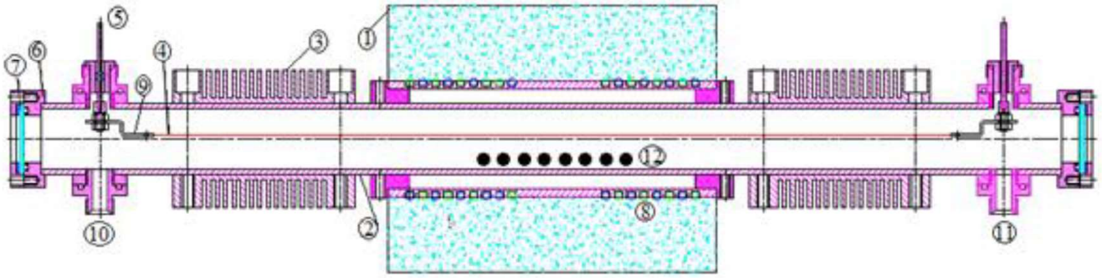

Fig. 5.1 Engineering drawing of thermionic diode detector

To maintain a symmetry of Li atomic vapours column and its temperature profile, the furnace is made coaxial with heat-pipe. Kanthal wire of ~1 mm thickness is used for resistive heating. The insulated heating wire is wrapped firmly into the spiral grooves made on outer furnace surface which is a hollow pipe of SS with diameter: 5 cm, length: 30 cm and thickness: 0.4 cm. To nullify the magnetic effect of multi-turn heating coils, the wiring of heating element is essentially of bifilar type, otherwise it may perturb the energy levels of analytic sample. Two small cooling fans near the glass windows are used to dissipate the extra heat that otherwise can damage the 'O' rings. The glass windows always remain protected from metallic coating as the Li atomic vapours get condensed well in advance due to fan's cooling. High atom density is anticipated at low temperatures typically at 550 ^{0}C, as the melting point (~180 ^{0}C) of Li is low. A photograph of the developed thermionic diode is shown in Fig. 5.2. A thermocouple of 'K' type with an accuracy ± 1°C in conjunction with PID control is used to measure the temperature profile of Li vapour column generated over its 30 cm long central part.

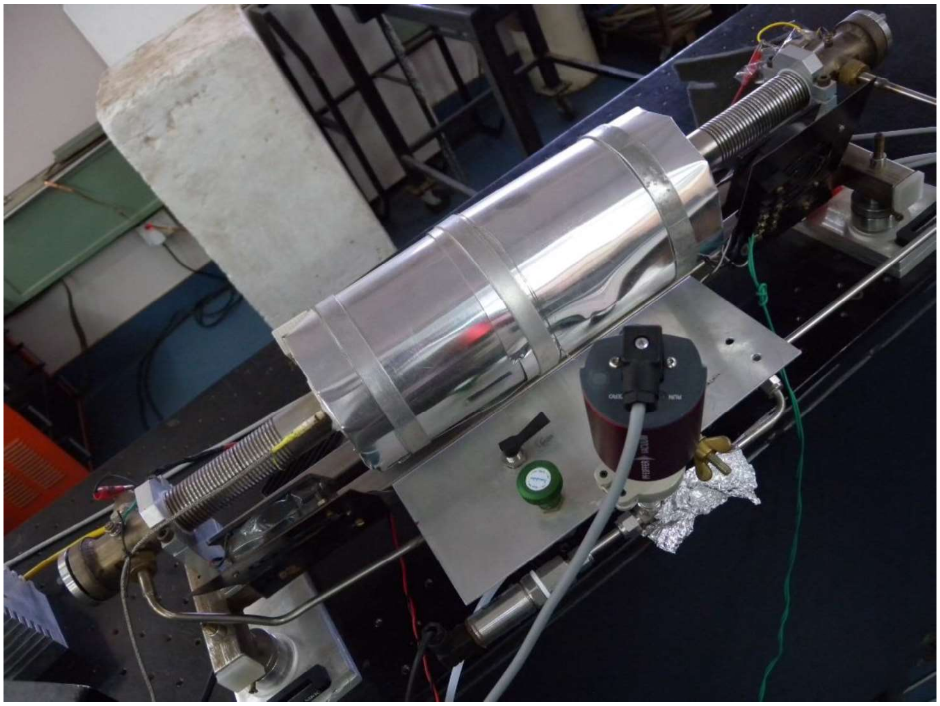

Fig. 5.2 Developed thermionic diode detector for Li spectroscopy

For an easy alignment of the incident laser beams into the diode space charge region, the heat-pipe diode is supported well by an adjustable levelling stand. Otherwise, poor alignment of the lasers and diode space charge may deteriorate the working performance and gain of the device.

5.1.3 Thermal characterization

First, the heat-pipe is baked and flushed out continuously for at least 12 hours by flowing an inert gas to remove the residual impurities. After that a proper vacuum of ~ 10^{-6} mbar is established using an oil diffusion pump driven by rotary pump. Then the diode is inflated with neon buffer gas preferably at low pressure. The heat-pipe central portion is heated by an electrical resistive heating furnace as described above. When the temperature of furnace is increased gradually, Li starts to vaporise just beyond its melting point and the vapour pressure get increased accordingly. The Li vapours moved away from central heating zone and get condensed near the colder region in heat-pipe, eventually. This act sweeps out the buffer gas by the atomic collision between the lithium and neon gas. Practically, the buffer gas is excluded almost from heating central region except in short transition regions near the heat pipe ends. The transition region thickness depends on kind of metal vapour, buffer gas and the partial vapour pressure of the both [160-162]. Since, the Li vapours are well confined by the buffer gas, therefore long column of Li vapour has a well-defined boundary layer. In order to keep the boundary layers sufficiently thin, the pressure of buffer gas is kept marginally greater than vapour pressure of lithium. As the furnace electrical heat power is increased, the rate of Li fluid evaporation also increases its vapour pressure along with temperature. At ~ 200 W electrical power, Li vapour pressure nearly get balanced by neon fill gas pressure. The evaporation zone now holds a pure Li metallic vapour column with its pressure nearly equal to fill gas. The condensation of metallic vapour occurs just before to reach the glass windows. This limits Li vapour diffusion at fill gas boundaries due to effective cooling. Thus, Li viscous condensate again proceeds to heat-pipe central hot zone through its internally fabricated micro-capillaries and evaporates again slowly. In this way, a cycle of Li evaporation and condensation takes place repeatedly. An isotherm of metal vapour column of uniform density is generated, eventually. By this act, the metal vapour gets purified itself through the continuous condensation and evaporation cycles. We succeeded to obtain a well-defined isotherm of Li metal vapour column, when heat-pipe is operated at ~ 500 ^{0}C and at very low gas pressure 0.01 mbar. The temperature distribution for the developed column of lithium vapours in the central of heat pipe is shown in Fig. 5.3. A perfect isotherm could be obtained only if there is an outward continuous diffusion of Li vapours and the fill gas ousted entirely from heating zone. It may take place when rate of Li evaporation and condensation reach the equilibrium. It is possible only by good mechanism of the capillary pumping through a well-designed wick structures [161]. Since, in present design there is no such wick structure except the micro-grooves fabricated into heat-pipe's inner wall, therefore the temperature distribution is not perfectly uniform all over its length. Still, a good isotherm (Fig. 5.3) is observed at very low gas pressure (~ 0.01 mbar) over its long central part.

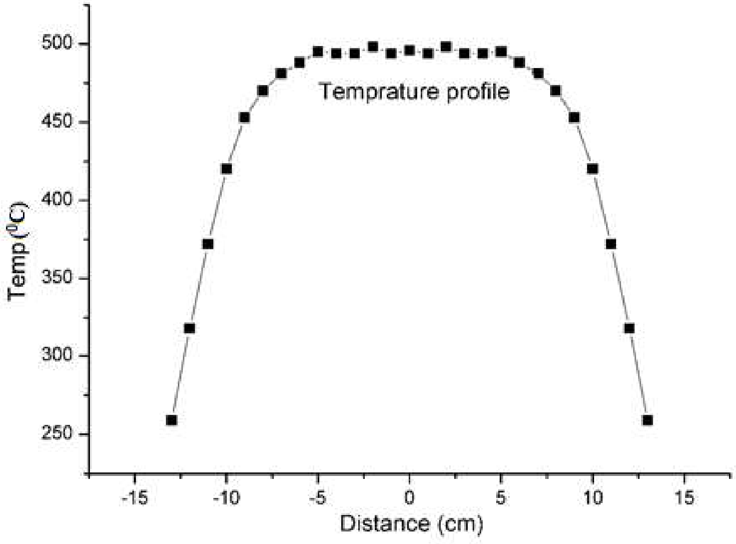

Fig. 5.3 Axial temperature profile with Li loaded heat-pipe diode

5.1.4 Optical characterization

In first part, heat pipe diode is characterized through absorption spectroscopy experiment. The atomic vapours are produced by resistive heating of research grade Li sample of ~ 2.0 gm purchased from Sigma-Aldrich. In this experiment, N_2 laser pumped dye laser, tunable in the wavelength range of 645-675 nm at pulse energy of ~ 100 μJ, is used. The collimated dye laser output tuned to Li ($^2S_{1/2} \rightarrow {}^2P_{1/2,3/2}$) transition is passed through Li atomic vapour generated inside heat pipe at 500 ^{0}C and gas pressure of 0.01 mbar. The terminology used as $^2S_{1/2}$ and $^2P_{1/2,3/2}$ are purely the spectroscopic notations and denote the lithium ground state and excited states lying at ~ 1.84 eV above, respectively. The energy of laser absorbed is measured by a silicon PIN photodiode. The precise dye laser wavelength scanning across 670.78 nm created a strong Doppler broadened absorption peak covering both the Li isotopes overlapped substantially (Fig. 5.4). A capacitance based low pressure gauge (CMR362) is used to measure the partial vapour pressures of lithium and neon buffer gas. The temperature is recorded by a thermocouple sensor along the axis of heat-pipe in close proximity of its wall. The real temperature of the Li vapour inside the heat pipe may be about 1 ^{0}C higher.

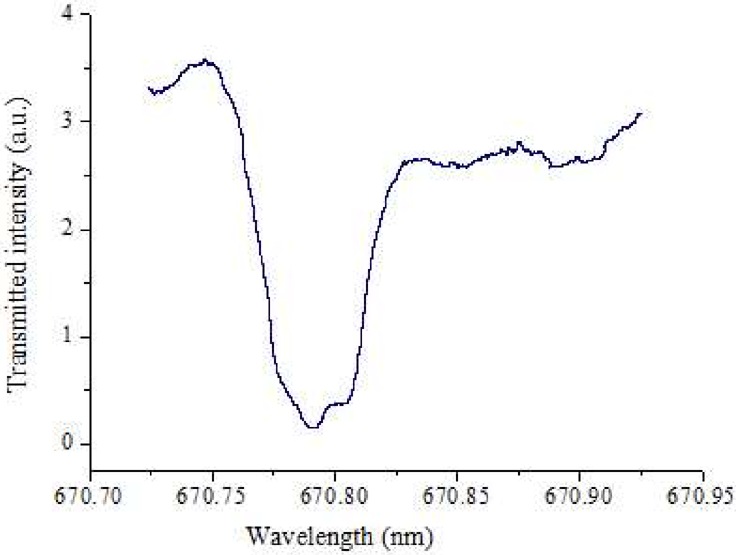

Fig. 5.4 Li absorption spectrum around 670.78 nm wavelength

Absorption type neutral density filters are used to reduce the intensity of incident laser beam in order to preclude nonlinear absorption which is most probable at high laser intensity. The intensity of transmitted and incident laser beam both are measured for different values of fixed fill gas pressure and temperature (Fig. 5.5). The line integrated Li atom density (N_0L) is obtained using the following Beer-Lambert law,

$$N_0 L = \frac{-\ln\left(\frac{I}{I_0}\right)}{\sigma_{abs}} \tag{5.1}$$

where σ_{abs} represents absorption cross-section (7.85×10^{-12} cm^2) at resonant 670.78 nm wavelength and 'L' is the length of vapour column produced. Here, it is assumed that produced Li atomic gas medium is thin and maintain the linear absorption. Therefore, the Beer-Lambert law is applicable in this experiment. The optical depth, which is the ratio of intensity of transmitted to incident (I/I_0) laser beam, are calculated from the experimental data. The Li atom density (N_0) in ground state $^2S_{1/2}$, for typical operating range of heat pipe temperature at around 500 ^{0}C is measured as ~ 9.5×10^9 atoms/cc. For low incident laser intensities nearly a straight line is observed in the temperature range of 500 to 550 ^{0}C.

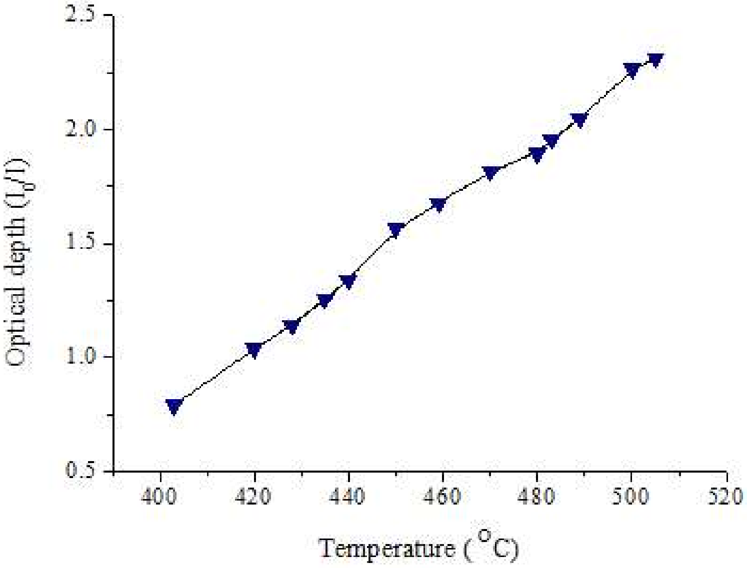

Fig. 5.5 Li optical depth vs heat-pipe temperature plot

5.1.5 Measurement of TDD electrical characteristics

In second part, thermionic diode overall functionality is confirmed. From adaptability point of view, the heat pipe design permits an easy conversion into sensitive thermionic diode for detection of ions created as a result of selective laser photoionization. To convert, an electrical diode, having small work function cathode, has to be inserted into heat pipe, see Fig. 5.1. A thin (~ 0.25 mm diameter) and straight long filament with high melting point made of tungsten is stretched axially into heat pipe and then functional working of the diode is ensured.

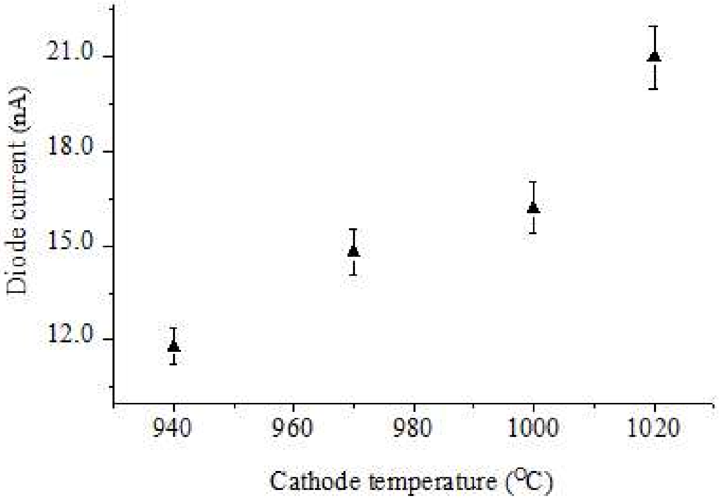

Fig. 5.6(a) Diode current at constant anode voltage without Li charged into heat-pipe

For 4.5 to 5.2 Ampere filament current range that generates a cathode temperature in between 900 to 1000 ^{0}C, a feeble diode current of only few tens of nano-ampere (nA) is detected initially at fixed anode voltage (V_A) of 30 volts, see Fig. 5.6(a). However, when heat-pipe is charged with Li sample, a remarkable enhancement (~10^3 fold) in diode current is observed even at low filament currents and cathode temperatures as shown in Fig. 5.6(b). It is due to the substantial decrement in cathode work function because of a thin coating of Li get deposited. The Li work function is fairly low (~ 2.4 eV). It is just nearly the half of tungsten work function (~ 4.5 eV) [163]. For cathode filament current (I_C) ranging from 0.4 to 1.2 A, an exponential increment in diode current is observed followed by a near saturation region till ~ 2A. It is observed that for low current values (upto 1.2 A), all the cathode electrons emitted in small quantity, reach the anode, immediately, without any constraints. Although, due to increased emission flux emitted from cathode at higher filament current (such as 1.2 to 2.0 A), a negative space charge rise to build-up that limits further increase in thermionic diode current. At considerably higher current beyond 2.0 A, the Li deposited on cathode starts to evaporate. Thus, all of a sudden work function again starts to increase resulting in less thermal electrons emission. Thereby, a decrease in diode current is observed. This concludes that diode space charge is governed by the dense electron clouds emitted from cathode in the range of 1.2 to 2.0 A cathode current at low anode voltage (V_A), This is called as limited space charge region for diode operation. We explored this region to detect lithium photo ions produced by three photon ionization. A drastic fall in diode current is observed beyond 2.0 A. It is essentially ascribed to high vaporization rate of Li from cathode. Although, the fill gas required to generate a confined metallic vapour column affects the above filament current range. The diode current is observed to increase by increasing fill gas pressure, at fixed anode voltage and cathode current.

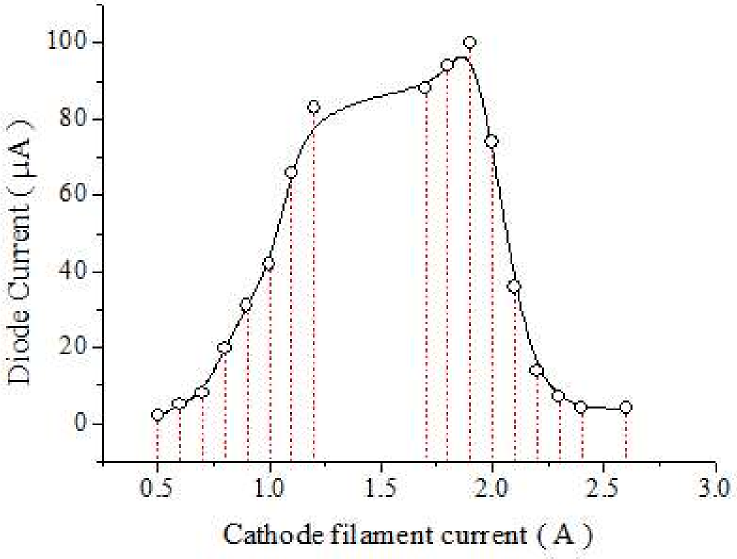

Fig. 5.6(b) Plot for diode current when heat-pipe is charged with lithium

5.1.6 Performance of thermionic diode detector

Thermionic diode performance is judged by an experiment on Li photoionization using two photon excitation (2s $^2S_{1/2} \rightarrow$ 3d $^2D_{3/2,5/2}$) having small (6.25 x 10^{-31} cm^4 s) absorption cross-section [164]. Although, the two photon transitions are weak in nature, still we could succeed to produce a strong Li photoionization signal by taking an advantage of negative space charge developed around cathode. An experimental setup for such single colour, three photon Li ionization is shown in Fig. 5.7. It has an in-house built dye laser pumped by the UV radiation at 337 nm obtained directly from nitrogen laser as described in chapter-2. Its pulse width is ~ 6 ns, linewidth ~ 0.2 cm^{-1}/ 6 GHz and the pulse-energy ~150 μJ. The 5 mM concentration dye solution of Rh-640 perchlorate is freshly prepared in ethanol for generating a tunable output in small wavelength range across 640 nm to excite the desired Li two photon transition.

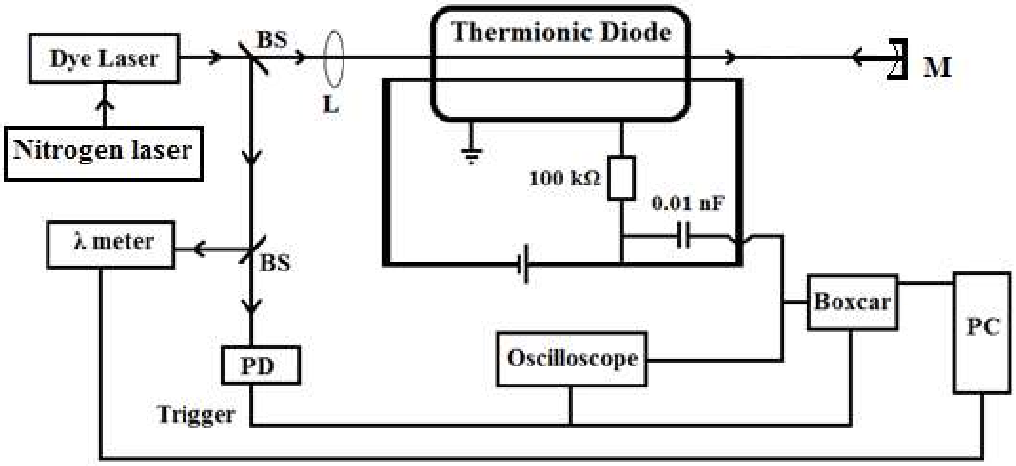

Fig. 5.7 An experimental setup to measure thermionic diode performance

M: Concave mirror, BS: beam splitters, L: Convex lens, PD: Si-PIN photodiode

The Li excited energy state (3d $^2D_{5/2}$) is reached through intermediate virtual energy state using two photons excitation at ~ 639.15 nm and photo-ionized subsequently by one more photon of the same energy. In fact, the virtual state is not an actual energy state. It is a part of formalism related to perturbation theory and can be assumed of as short lived transient state. The Heisenberg's uncertainty principle ($\Delta E. \Delta t \geq \hbar/2$) can be used to explore about the possibility of virtual states. To produce an ion-signal, both the retro-reflected ionizing and exciting laser beams are spatially overlapped into heat pipe diode in proximity of cathode filament. The photo-ion signal is measured across a load resistor of 100 kΩ, and fed through 0.01 nF capacitor to signal recovery instruments having a boxcar integrator (SRS-250), wave meter (WS-7), an oscilloscope (Lecroy-500 MHz) and a computer (PC).

The following mechanism that makes the use of two-photon resonant absorption followed by a non-resonant ionization is possible for Li.

$$\mathrm{Li\ (2s) + 2h\nu\ (639.145\ nm) \rightarrow Li\ (3d)\ (two - photon\ absorption)} \tag{5.2}$$

$$\mathrm{Li\ (3d) + h\nu\ (639.145\ nm) \rightarrow Li^{+} + e^{-}\ (non - resonant\ ionization)} \tag{5.3}$$

or by collisional and associative ionization from two atoms in 3d level [152]

$$\mathrm{Li\ (3d) + Li\ (3d) \rightarrow Li^{+} + Li\ (2s) + e^{-}} \tag{5.4}$$

$$\mathrm{Li\ (3d) + Li\ (3d) \rightarrow Li_2^{+} + e^{-}} \tag{5.5}$$

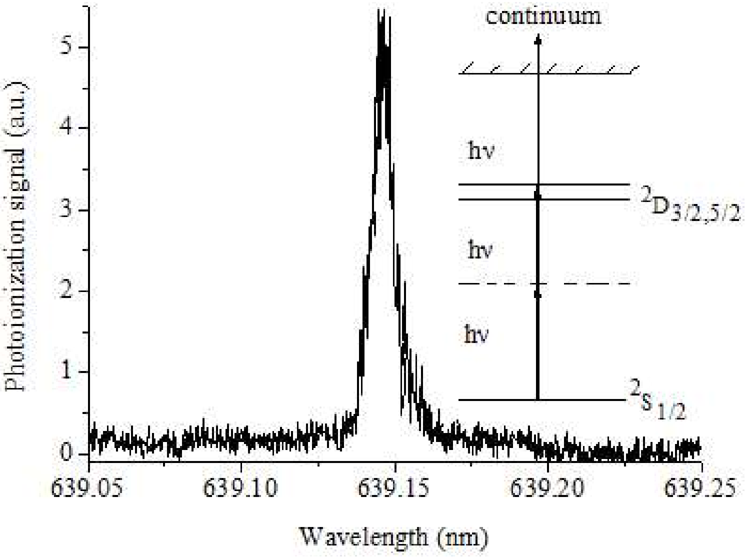

Fig. 5.8 Single colour, three-photon Li photoionization signal at 639.145 nm

The narrow profile of lithium photoionization spectrum (Fig. 5.8) measured by using two-photon excitation ($^2S_{1/2} \rightarrow {}^2D_{5/2}$) at 639.145 nm does not display any molecular transition signature. It means molecular channel does not attribute to Li ionization in the present experimental environment. The time based profile of photo-ion signal is shown in Fig. 5.9. A high strength ionization signal is noticed for filament cathode current 2.7 A, 5.3 mbar gas pressure and 500 ^{0}C heat pipe temperature. The signal rising time is observed as ~ 0.66 ms. This is roughly the time needed for diffusion of lithium ion into space charge detection region from the field free region where Li phot-ions were created. The signal pulse width (~ 3.9 ms) should be essentially the typical orbiting time of Li ions around the cathode to lower the space charge potential barrier height. The ion signal increased exponentially when the cathode current is increased from 1.0 to 2.7 A (see Fig. 5.10). It means the gain of diode increases as the current in cathode is increased. However, for filament current beyond 2.7 A, the gain fall promptly and follow the characteristics of diode as described in Fig. 5.6(b). This is attributed to the increased evaporation rate of Li deposited on cathode filament. This results in fewer emission of cathode electrons and thus lowers the gain of diode accordingly.

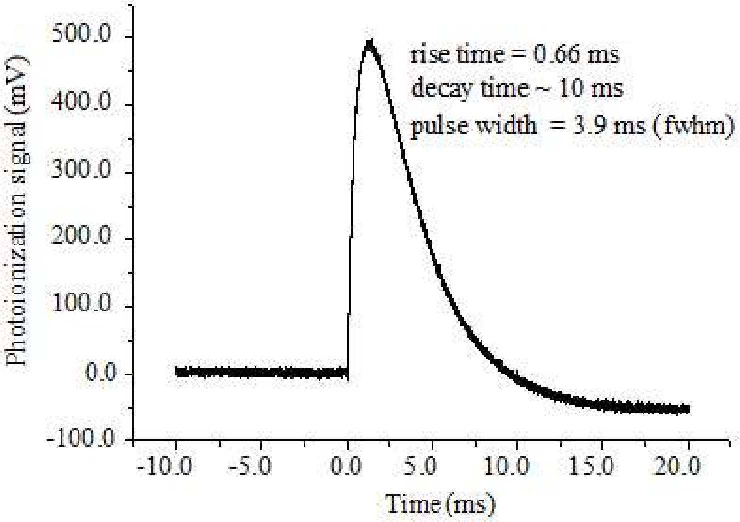

Fig. 5.9 Time resolved single colour, three-photon Li photoionization signal at 639.145 nm

Nearly, a linear increase is observed in the signal when temperature of heat-pipe is increased at fixed filament current and gas pressure (Fig. 5.11). This is attributed to the generated higher atom density, consistent with increased Li vapour pressure, at increased high temperature.

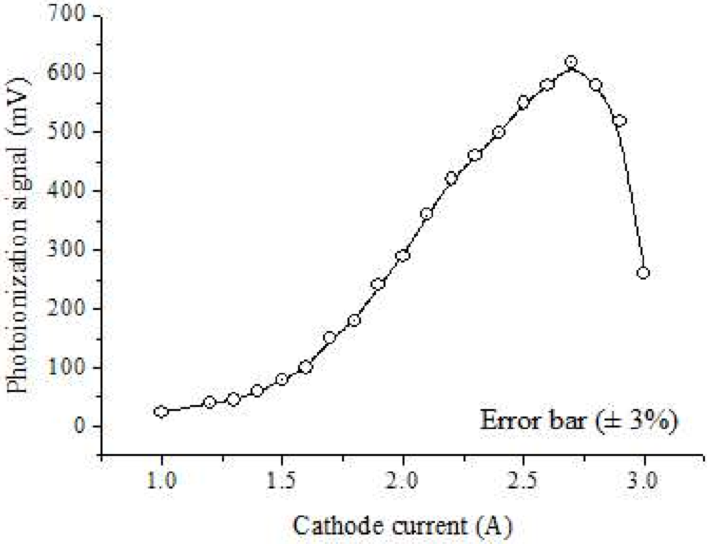

Fig. 5.10 Plot of Li photoionization signal vs cathode filament current

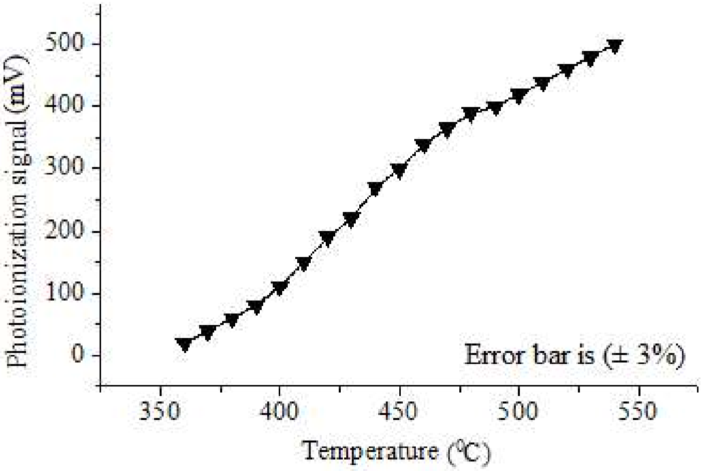

Fig. 5.11 Plot of Li photoionization signal vs heat-pipe diode temperature

Similarly, the fill gas pressure effect on Li ionization signal, at fixed value of heat pipe temperature and cathode filament current, is also observed (Fig. 5.12). In a short span of filled gas pressure (typ. 1 to 20 mbar), the strength of photoionization signal increases in a linear fashion initially (from 1 to 5 mbar) than achieve saturation onwards. The rise in ion-signal strength with fill gas pressure can be explained based on increased collision rate of Li with fill gas atoms in its ^{2}D excited state that just lies ~1.5 eV below the Li first ionization potential. Mostly in such conditions, ionization through collision seems to contribute to ionization signal predominately [141]. That's why, the TDD gained wide popularity in laser spectroscopy work and suited for high resolution spectroscopy of Rydberg atoms [139].

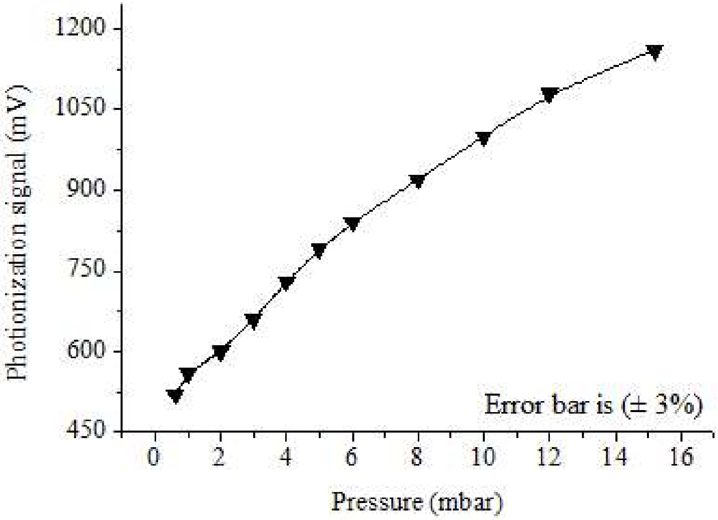

Fig. 5.12 Plot of Li photoionization signal vs buffer gas pressure

In spite of the large strength signals, the sensitivity of detector is restricted by its inherent noise. The main sources of typical noise are the shot noise due to the flow of charge carriers, noise due to thermal motion of the electrons in load resistor and flicker noise due to fluctuations in cathode emission. As the cathode emits large electron flux at typical operating filament currents, therefore due the discrete nature of charge carriers, the statistical fluctuations in thermionic diode current is given as,

$$\Delta I_{rms} = (2\Gamma^2 eI\Delta f)^{1/2} \tag{5.6}$$

Where, ΔI_{rms} denotes the root mean square fluctuations in current, Γ^2 the space charge reduction factor, 'I' the average diode current and Δf bandwidth over that noise is considered. For a typical value of 50 µA diode current, $\Gamma^2 \leq 1$ and detection bandwidth of 0.1 Hz, the value of I_{rms} shot noise is estimated less than 1.2 pA. Similarly, the random thermal motion of charge carriers produces a noise voltage across load resistor (R) that can be obtained as;

$$\Delta V_{rms} = (4k_B T R \Delta f)^{1/2} \tag{5.7}$$

For practical 100 kΩ, load resister, thermal noise current ($\Delta V_{rms}/R$) is calculated as ~ 0.4 pA. Here, both the shot and thermal noise do not depend on frequency. However, an excess noise other than shot or thermal noise also called the flicker noise is observed in many electronic devices. It is very difficult to explain the flicker or excess noise. It is observed that flicker noise power increases with the square of thermionic diode current. In cathode filament, having low work function or coated by low work function material, the flicker noise occurs due to fluctuation in electron emission properties of cathode coating. It is very difficult to predict the amplitude of excess noise, however it may be approximately estimated from noise power spectrum of the signals.

5.1.7 Gain measurement

In earlier reports, thermionic diode gain were estimated from its operating electrical parameters and geometrical design [138,142]. In the present work, the gain of thermionic diode is measured spectroscopically. A more precise way of absolute photoionization cross-section (σ) measurement is used for calculating the gain of thermionic diode. This involves an important term known as the ground state atom density (N_0). The Li photoionization cross-section from its (3d $^2D_{3/2,5/2}$) excited state is measured experimentally by using two-photon excitation scheme as shown in Fig. 5.8. It uses the single colour, three photon ionization of lithium at 639.145 nm. The relation as given by Eq. 4.11 between the photoionization cross section (σ), ionizing laser energy (E) and strength of photoionization signal (ΔV) as described in chapter-4, is used to estimate the ground atom density (N_0) and the TDD gain factor. In this expression all the factors are either known or can be measured except N_0 and σ. These can be dig out from least square fit of the Eq. 4.11 to photoionization signal measured with respect to ionizing laser energy. This fitting expression is practical with few assumptions, for example resonance transition should be saturated and the spontaneous decay rate from excited state during short duration exciting laser pulse should be negligible. In the present experiment (Fig. 5.7), exciting laser pulse duration (~ 6 ns) is less than lifetime of Li (3d) excited state. The pulse energy of dye laser is reasonably high to saturate the Li ($^2S_{1/2} \rightarrow {}^2D_{5/2}$) desired transition. The area of cross-section (A) of the ionizing laser beam is estimated by photographic film burn spot technique. The size of burn spot is zoomed by a microscope having a magnification of 20 to deduce the cross-sectional area (A) correctly. The burned spot diameter is measured ~ 280 µm. For photoionization cross-section, the strength of generated ion-signal is measured with respect to ionizing laser energy.

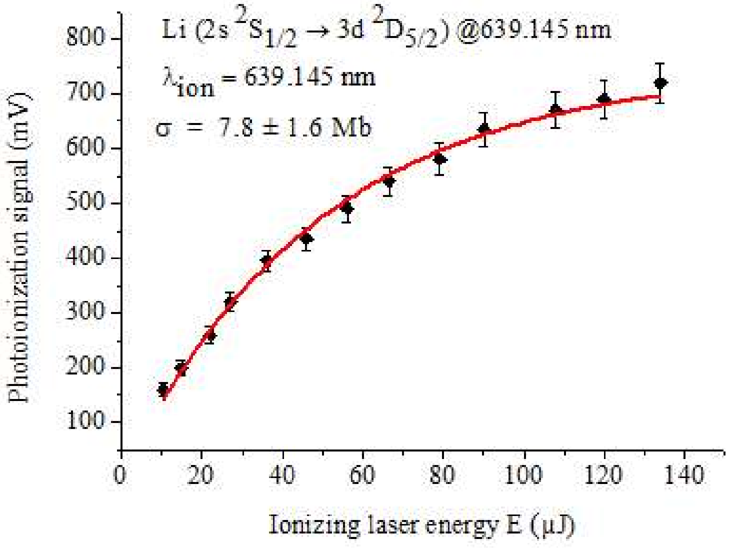

Fig. 5.13 Effect of ionizing laser energy on Li photoionization signal

For that purpose, the lithium atoms are excited from its ground state ($^2S_{1/2}$) to the higher excited (3d $^2D_{3/2, 5/2}$) states by tuning the dye laser wavelength to 639.145 nm. As per electronic transition selection rules (even to even parity transition), only the ($^2D_{5/2}$) state can be accessed from ground state by two photon excitation. The population in $^2D_{5/2}$ state is photo-ionized sequentially by using one more photon of suitably energy. In present case, it is obtained from retro-reflected ionizing laser beam at 639.145 nm. The ion-signal is monitored by varying the ionizing laser intensity using the neutral density filters. The experimental photo-ionization data for excited Li (3d $^2D_{5/2}$) atoms is shown in Fig. 5.13. Initially, the strength of ion-signal is observed to increase with the increase in ionizing laser energy. Onwards, it shows a saturation behaviour at higher energy. The solid squares represent the experimental data points and the curved line which passes through the experimental data is the least square fit to Eq. (4.11). It gives photoionization cross-section value $\sigma = 7.8 \pm 1.6$ Mb. This data agrees well with previous reported values [35]. The source of error, occurred in our results are largely the measurement uncertainty in ionizing laser energy *(E)* and interaction cross-section area *(A)*. The cross-sectional area measurement uncertainty is ~ 20% and the uncertainty in ionizing laser energy measurement due to energy meter is ± 3%.

As per Eq. (4.11), the photo-ions generated ($N_i = Q/ eV_{vol.}$) can be measured from lithium photoionization signal using an expression Q = (photoionization signal/ R) Δt, (see Eq. 4.12). In present experiment, *R* represents a load resistor (100 KΩ) across which the photoionization signal is measured while Δt is the pulse-width (~ 3.9 ms) of ionization signal. According to Eq. (4.11), the $N_i \rightarrow N_0$ as the $E \rightarrow \infty$. At suitably high ionizing laser energy the ion-signal saturates. The determination of N_0 is independent of ionization cross-section, while σ is linked to shape of N_i vs E data. As per above prevailing conditions, the Li atom density in ground state is estimate as $N_0 \sim 9.5 \times 10^{13}$ (atoms/cc). This value is around 10^4 times larger than ground state atom density ($\sim 9.5 \times 10^9$) measured by previous absorption experiment (see

Fig. 5.4). This factor is attributed to high gain of thermionic diode and could be explained based on neutralization of the negative space charge effects due to Li positive ions created by single colour, three photon ionization [141]. In a real sense, thermionic diode gain is defined as the increase in current of diode per generated photo-ion. It means, each generated photo-ion allows the $\sim 10^4$ more electrons to reach the anode of diode upon space charge neutralization by decreasing the build-up potential barrier. Thermionic diode gain depends upon many factors such as its cathode temperature, the electron temperature and thermionic diode geometry. Typically, it varies from 10^4 to 10^6. The coaxial cathode and anode geometries with large diameter ratio ($r_A/r_C \approx 120$) are used to achieve the high gain in present design. As both the cathode and anode are sufficiently long, therefore the charge density and potential distribution largely depend on radial distance only. Since the cathode is directly heated by an electric current, therefore a non-radial field component may arise due to Ohmic voltage drop. However, it is negligible in our case owing to very small resistance of tungsten filament used. The experimental result (Fig. 5.10) indicates that as the cathode current increases, the electron emission rate and hence the negative space charge increases. It causes the ions to be trapped for a longer period in the potential well and thus the gain is increased significantly. After the development and characterization of thermionic diode, it has been used for more studies on selective lithium photoionization as required in laser isotope separation.

5.2 Studies on Li photoionization and photoionization cross-section measurement

Photoionization cross-section is a quantification of ionization probability of an atom by a photon. This is the most important spectroscopic data required to investigate the laboratory as well naturally produced astrophysical plasma. Its value from the ground state is well known for most of the elements, however photoionization cross-section of their excited states sparingly reported. This is also important for laser isotope separation. It can be measured from ionizing laser pulse energy required to saturate the photoionization signal. It was Rothe [129] who first designed an experiment using radiative electron-ion recombination in shocked plasma for ionization cross-section measurement of Li (2p) states. Earlier, the Li photoionization cross-section has been also measured by Saleem et al. [111] using TOFMS for ^{7}Li (2p $^2P_{3/2}$) state for ionizing radiation 335 nm. Using the hollow cathode lamp, Saini et al. [165] measured Li photoionization cross-section of the same excited state using an ionizing radiation at 337.1 nm. In the present study, thermionic diode (TD) is used to measure the photo-ionization cross section. TD generates a long column of uniform atomic vapour density of Li and is a relatively simple, low cost, easy to operate, and extremely sensitive device. This is in contrast to the complex atomic beam TOFMS setups or the magneto-optical traps [132], used for same purpose. Present study describes the measurement of Li photoionization cross-section. This is carried out for excited 2p ($^2P_{1/2,\ 3/2}$) and 3d ($^2D_{5/2}$) states near the ionization threshold. Two different ionization pathways are studied. These are single-photon and two-photon excitation followed by a non-resonant ionization. Mostly thermionic diodes have been used to study the properties of an atom in Rydberg states [153,159]. However, use of these devices for measurement of photoionization cross-section are rarely reported. In this study, in-house developed thermionic diode as described above in section 5.1 is utilized. Out of several, this study shows one important application of the developed device for laser photoionization spectroscopy. However, it is mostly used for the highly excited Rydberg atoms spectroscopy.

5.2.1 Experimental setup for Li two-step photoionization in TDD

Figure 5.14 shows a schematic of an experimental setup, used for Li two-step photoionization in thermionic diode. Atomic vapours of Li are generated in the heat-pipe of diode. The diode is loaded with ~ 1.0 gm research grade sample of Li. TD is based on a long SS hollow pipe (length = 70 cm, dia. = 3 cm). Both the ends of pipe are sealed with quartz windows. A straight and thin tungsten wire of diameter ~ 0.25 mm, is stretched off-centre through the heat-pipe.

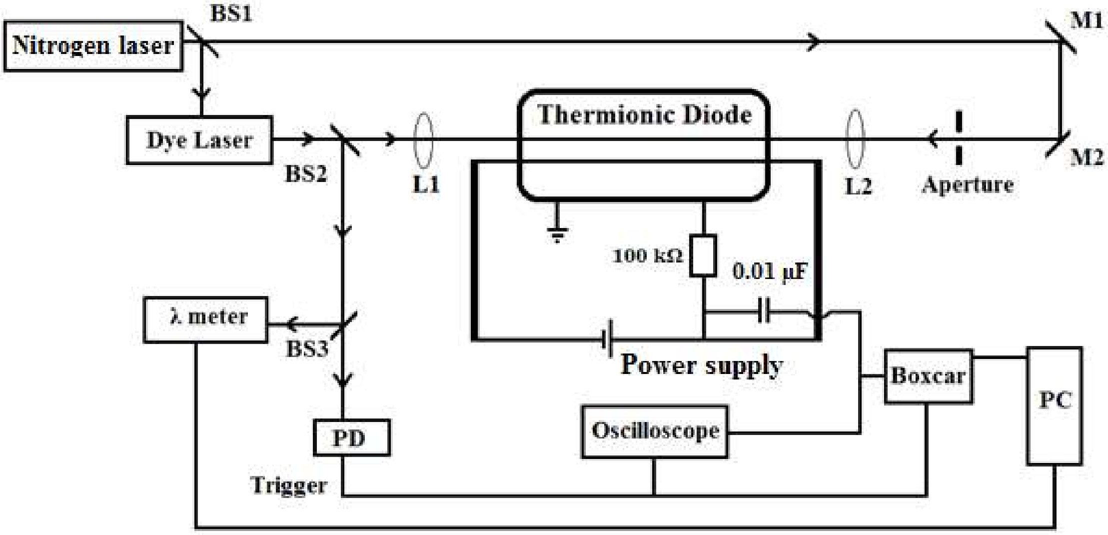

Fig. 5.14 Schematic for two-step selective Li photoionization using TDD

L1 and L2: Convex lens (focal length = 30 and 100 cm), PD: Si-PIN Photodetector, BS1, BS2, BS3: Beam Splitters, M1 and M2: Beam reflecting mirrors, PC: Personal computer,

Actually, an electrical diode is inserted into heat-pipe to detect the Li ions produced by step-wise laser photoionization. The heat-pipe itself acted as cylindrical anode and the straight tungsten wire performed as a cathode of thermionic diode. The block diagram of the developed thermionic diode is shown in Fig. 5.15. The gas pressure in heat-pipe diode is controlled by a special gas & vacuum handling unit. Two units are used, one each for the gas and for vacuum.

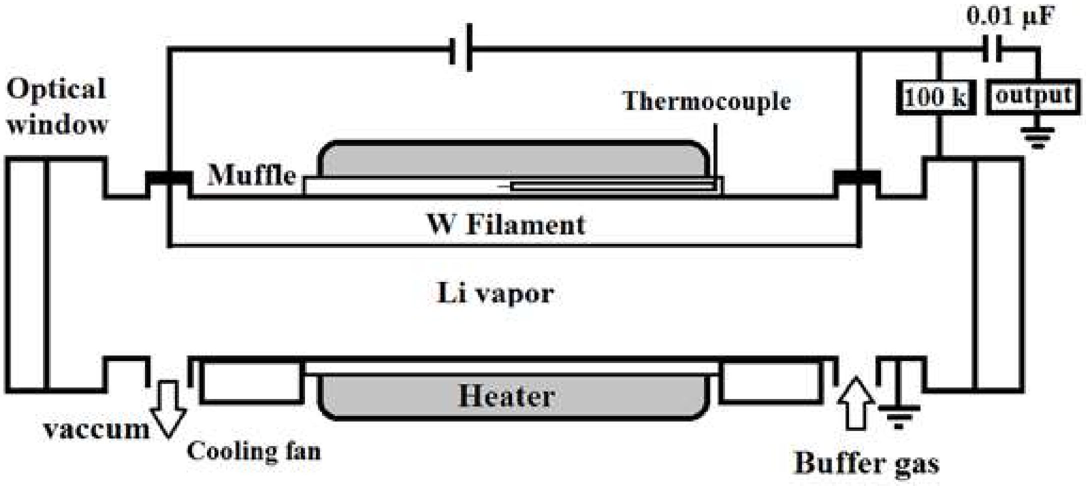

Fig. 5.15 Schematic view of thermionic diode ion-detector

Each one consists of a set of fine controlled needle and shut-off valves. The gas pressure in TD thermionic diode is monitored by a sensitive, capacitance based low pressure gauge (CMR362, Pfeiffer Vacuum) with readout unit. Before loading Li sample, the thermionic diode is cleaned thoroughly. It is also baked for several hours at moderate temperature (~ 200 ^{0}C) and evacuated down to 10^{-5} mbar. This process removed the residual impurities. Neon is used as buffer gas and is filled to 2-3 mbar. Heating the central zone of the heat-pipe, the uniform density vapour column of Li atom is produced. Heat-pipe temperature could be set within ± 1 ^{0}C of desired value (typical ~ 530 ^{0}C). The proportional–integral–derivative (PID) is used for controlling the temperature. The temperature is measured in proximity to heat-pipe outer surface by ‘K’ type thermocouple (see, Fig 5.15). Therefore, temperature of lithium atomic gas inside the heat-pipe possibly will be slightly lower.

The photoionization cross-section measurement are carried out for Li transitions of interest ($^2S_{1/2} \rightarrow {}^2P_{1/2,3/2}$) at 670.802 nm and ($^2S_{1/2} \rightarrow {}^2D_{3/2,5/2}$). The required tunable laser at ~ 639.145 nm is obtained with specific laser grade dye. Most suitable Rhodamine perchlorate-640 dye with good absorption in UV (~ 337 nm) range, high quantum yield at 639 nm and also covering large tuning range beyond 671 nm, is used to accommodate both the transitions.

Therefore, a pulsed dye laser (~ 0.2 cm^{-1}/ 6 GHz, 6 ns, 635-675 nm) pumped by nitrogen laser (~ 337 nm) is used. The pump N_2 laser has peak power ~ 350 kW in 10 ns pulse. The first-step resonant-transition wavelength ~ 671 nm of dye laser is generated by utilizing 60% of N_2 nitrogen laser output. The remaining 40% is utilized to ionize the excited Li atoms. Chapter-2 adequately describes this laser set up. The dye laser is based on a 5.0 mM, Rh-640 dye solution prepared in ethanol. Peak output power of dye laser obtained is ~ 25 kW at ~ 640 nm. The focal size of ionizing laser beam in the interaction zone of TDD is ~ 300 μm. This size is much smaller as compared diameter ~ 1 mm of exciting laser beam. Thereby, both the laser beams effectively overlapping in space. A Si photodiode, verifies the temporal overlapping. However, temporal overlapping of the laser pulses are not very critical. This is owing to the longer lifetime of Li excited states 2p $^2P_{1/2,3/2}$ (~27.2 ns) and 3d $^2D_{3/2,5/2}$ (~14.5 ns) [29, 198]. This is to be compared with exciting laser pulse duration ~ 6 ns. Chapter-2 described, the details of lab-view based computer controlled dye laser wavelength scanner cum data logger [83]. This data acquisition system is utilized to acquire the precise wavelength scanning data in desired narrow spectral range. High resolution λ meter (WS-7), is utilized to precisely monitor the transition wavelengths. The photoionization signal is measured on digital 500 MHz storage oscilloscope. It is also acquired on computer (PC) through boxcar-integrator (SRS-250). The Si PIN photodiode (PD) is used to trigger the boxcar integrator.

5.2.2 Li photoionization pathways and photoionization signal

Lithium is one of the simplest elements after hydrogen, possessing $^2S_{1/2}$ ground state electronic configuration. Li contains single valence electron in 2s orbital with spherical charge distribution. The excited 2p ($^2P_{1/2,3/2}$) & 3d ($^2D_{3/2,5/2}$) states can be studied through single & two-photon excitation, respectively. Figure 5.16 shows the suitable energy levels and ionization potential of Li. It also depicts the two-step photoionization schemes for ionization cross-section measurement near the ionization threshold. The first scheme is based on single photon excitation at 670.78 nm. It excite the Li ground 2s ($^2S_{1/2}$) state population into excited 2p ($^2P_{1/2,3/2}$) energy state. This excited state lie at ~1.84 eV above ground state. As per electric dipole selection rules, this single photon transition ($^2S_{1/2} \rightarrow {}^2P_{1/2,3/2}$) is possible. These rules for allowed transition are, $\Delta l = \pm 1$, $\Delta J = 0, \pm 1$, $\Delta L = 0, \pm 1$, $\Delta S = 0$ & even ↔ odd parity. This is worth mentioning that doublets of both the Li isotopes are almost equal in energy spacing. The $^2P_{1/2}$ and $^2P_{3/2}$ state energy gap is around 10.05 GHz, which is equivalent to $\Delta\lambda \sim 0.0158$ nm. This almost equals their isotopic shift ~ 10.52 GHz for resonance line at 670.780 nm [37,166].

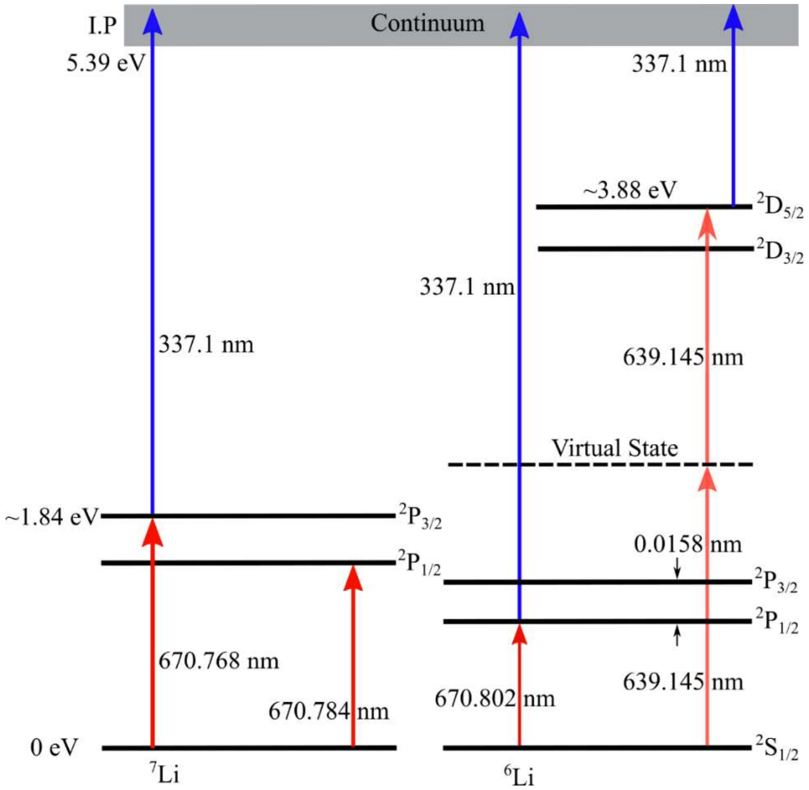

Fig. 5.16 Li two-step selective photoionization by single and two photon excitation

This implies that ^{7}Li ($^2S_{1/2} \rightarrow {}^2P_{1/2}$) transition nearly coincides with ^{6}Li ($^2S_{1/2} \rightarrow {}^2P_{3/2}$) transition. Hence, a narrowband (< 1 GHz dye) dye laser is essential for selective excitation of Li isotopes.

Therefore, in order to measure the ionization cross-section, isotopes need to be selectively excited by tuning dye laser to $^2S_{1/2} \rightarrow {}^2P_{3/2}$ of ^{7}Li or $^2S_{1/2} \rightarrow {}^2P_{1/2}$ of ^{6}Li lines. The first ionization potential of Li is 5.39 eV. Also, ^{2}P state excitation energy is ~ 1.84 eV [126,166]. This means that by utilizing the photons with wavelength shorter than 350 nm, the excited Li atoms can be readily ionized. In this way, nitrogen laser with photon energy ~ 3.68 eV (wavelength ~ 337.1 nm) is good choice for studying the photoionization of Li atoms. The study can be carried out both via single photon and the two photon excitation.

In second photoionization scheme, the Li excited state 3d ($^2D_{3/2,5/2}$) can be populated via intermediate virtual energy states. This can be implemented by two-photon excitation by 639.145 nm radiation. As per selection rules, the two-photon process is allowed for; $\Delta l = 0, \pm 2$, $\Delta J = 0, \pm 1, \pm 2$, $\Delta L = 0, \pm 2$, $\Delta S = 0$ & even ↔ even parity. Selection rules dictate that only 3d ($^2D_{5/2}$) state can be accessed by two-photon excitation from Li ($^2S_{1/2}$) ground state. Figure 5.16 shows the required energy levels with above discussed red and UV transitions [35] to accomplish the photo-ionization of Li atoms. In the atomic vapours produced in TDD, the lithium atoms are laser photo-ionized. This is carried out by the simultaneous interaction of narrowband frequency tuned red dye laser radiation and N_2 laser UV ionizing radiation. The two-photon Li photoionization signal is generated by following process. Counter propagating exciting (~ 639.145 nm) and ionizing (337.1 nm) laser beams overlapped spatially and temporally into TDD. In TDD, this happens in close vicinity of cathode filament. The energy of dye laser is so adjusted that it could produce three-photon ionization signal at 639.145 nm. In best alignment conditions, a strong Li photoionization signal is obtained. The signal is measured across 100 kΩ resistor through 0.01 µF capacitor. The signal is displayed on oscilloscope (see, Fig. 5.17). For the parameters, such as cathode filament current ~ 2.7 A, neon fill gas pressure ~ 5.3 mbar, heat-pipe temperature ~ 520 ^{0}C, maximum strength photo-ion signal is observed. The achieved SNR of photo-ion signal is very high as evident from Fig.

5.17. The rise time of signal is observed as ~ 0.3 ms. This is nearly the time needed for Li ions to diffuse into the detection region from field free region. The signal has a pulse-width ~ 2.4 ms. This corresponded to the typical orbiting time of photo-ions around cathode. The generated photo-ions lower the space charge potential barrier before its neutralization at cathode filament.

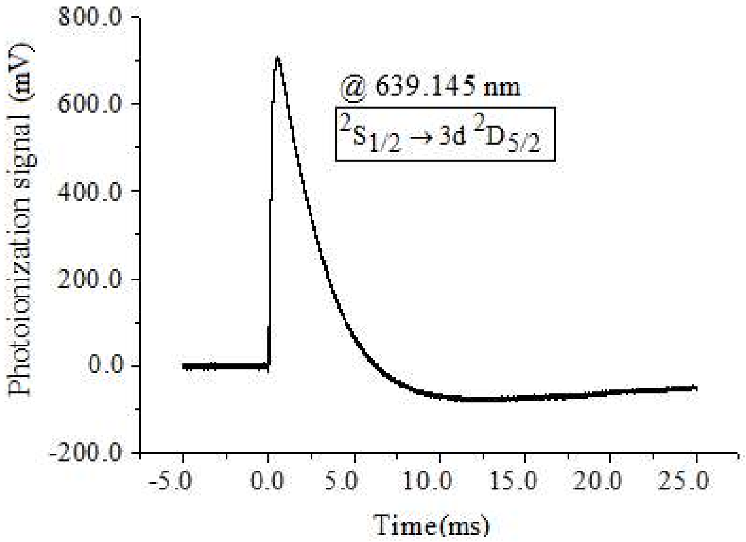

Fig. 5.17 Two-photon excited Li signal ionized by 10 ns UV laser pulse at 337.1 nm

5.2.3 Measurement of photoionization cross-section of Li (2p, 3d) excited states

Burkhardt et al. [131] has devised the most popular and accurate method based on saturation technique to measure the atom density and absolute photoionization cross-section. Similar technique is used in present study to determine the Li (2p & 3d) excited states photoionization cross-section. In this technique, no prior information on either atom density in ground/excited states or number of ionized atoms is needed. Only the ionizing photon flux needs to be calibrated. He et al. [167] used similar method to measure the photoionization cross-section of barium. The photoionization cross-sections of elements such as Ti, Co, Ni, were measured by Cong et al. [112]. The mentioned technique can be applied to study two-step photoionization scheme. The underline assumptions are, linearly polarized laser beams of uniform intensity with enough power to saturate the first resonance transition. Also, during short duration of ionizing laser pulse, the spontaneous decay of excited population from intermediate state is negligible. The ionizing laser energy should be large enough to saturate the photoionization process. The number of ions produced per ionizing pulse [131] is given as,

$$N_i = N_0[1 - \exp\left(-\frac{\sigma E}{2\hbar\omega A}\right)]$$

where, A = Cross-sectional area, E = Ionizing laser pulse energy. The photographic film burn technique is utilized to measure the spot size of laser beam. Then, area of ionizing laser beam in laser interaction zone is calculated. This is ~ 0.0765 mm^2. The uncertainty in measurement of 'A' is less than 20%. N_0 and σ values can be extracted from, N_i vs. E data by adopting least square fitting procedure. This is possible as other parameters are either known or measured.

The effect of ionizing laser pulse energy on photoionization signal is measured. This is carried out to measure an absolute value of photo-ionization cross-section. The Li atomic vapour atom is generated in heat-pipe of TD. Then, these atoms are laser excited from its ground state ($^2S_{1/2}$) to excited state ($^2P_{1/2,3/2}$). This is carried out by tuning the dye laser to resonant wavelength. Subsequently, photon from ionizing laser radiation at ~337 nm ionize the excited population present in '2p' state. Suitable delay (~ ns) is maintained between exciting and ionizing laser pulses. Figure 5.18 shows Li photoionization signal across 670.780 nm ($^2S_{1/2} \rightarrow {}^2P_{1/2,3/2}$) against the fine tuning of dye laser wavelength. This signal is the boxcar averaged output measured with wavelength meter WS-7. Except, inherent space charge diode amplification (~ 10^4 electrons/ion), no signal amplification is used in signal processing. Nearly the noise free signals are obtained by optimizing the gate-width of boxcar. The signal is averaged over 100 samples. The sensitivity was 50 mV sensitivity. Li isotopes are resolved with high resolution. At the same time, there is substantial overlap in ^{7}Li, D_1 line ($^2S_{1/2} \rightarrow {}^2P_{1/2}$) and ^{6}Li, D_2 line ($^2S_{1/2} \rightarrow {}^2P_{3/2}$). It is due to large Li Doppler broadening effects as well as the broad linewidth of dye laser. An additional peak between the two main peaks is seen.

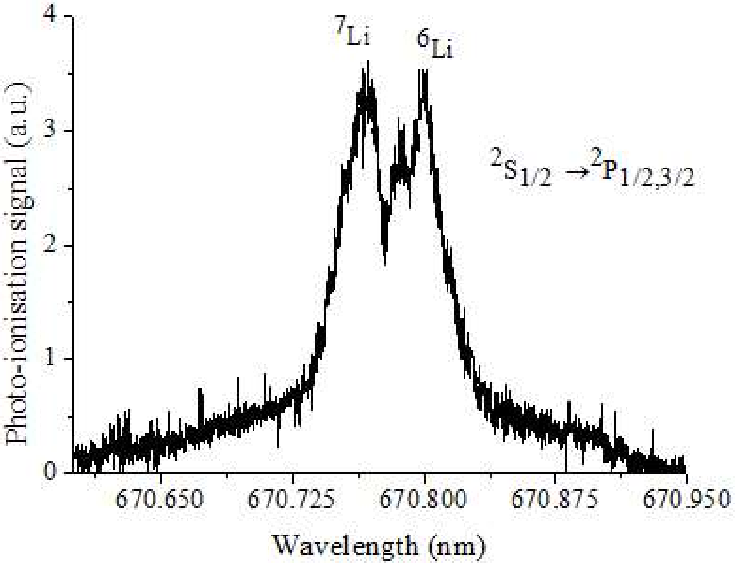

Fig. 5.18 Two-step Li photoionization signal for dye laser tuning across 670.780 nm

This is mainly due to the cumulative effect of photoionization from two nearby (< 1 GHz) ^{7}Li ($^2P_{1/2}$) and ^{6}Li ($^2P_{3/2}$) energy states. The measured spacing between first and the second peak (Fig. 5.18) of photoionization signal is ~ 10.05 GHz. This is consistent with the energy levels as shown in Fig. 5.16. For the isotopes ^{6}Li and ^{7}Li, energy separation between $^2P_{3/2}$ and $^2P_{1/2}$ excited states are nearly same [166]. Between lithium isotopes for 2p states, the measured average value of isotopic shift is ~ 10.53 GHz. This is very close to the reported data [35]. ^{6}Li signal is observed as high as that of ^{7}Li. This is despite lower abundance of ^{6}Li. The structure of Li isotopes D_1 and D_2 lines, may explain this trend. Near the wings, ^{6}Li (D_2) absorption line partially overlaps with that of ^{7}Li (D_1) [128]. There also exist near resonance charge exchange ($^6Li^+ \leftrightarrow ^7Li^+$) collisions. The other responsible factor may be collisions between Li isotopes which mutual transfer of energy. This process is highly probable due to their high cross-section (~ 10^{-14} cm^2) [168-170]. In the experiment, photoionization cross-sections for Li (2p & 3d) excited states are also measured. For single photon excitation, it is carried out at Li ($^2S_{1/2} \rightarrow ^2P_{1/2}$) transition for 670.802 nm. This data is recorded by varying the intensity of ionizing laser beam. This is carried out at fixed intensity of exciting laser beam. Figure 5.19, shows the experimental photo-ionization data for ^{6}Li ($^2P_{1/2}$) excited atoms. Initially, there is exponential rise of photoionization signal. Then, the exhibition of saturation nature with increase in ionizing laser intensity is observed. This experimental data fitted to Eq. (4.11) gives the photoionization cross-section σ = 15.40 ± 2.8 Mb. The value obtained is very near to that of published data [111,132]. Uncertainty in measurements of interaction cross-section area *(A)* and laser energy *(E),* are the prime factors responsible for errors in experimental results. The uncertainty in ionizing laser energy measurement is ± 3%. This is due to resolution of energy meter employed. Further, around ± 5% error is due to pulse to pulse variation in laser energy. Asymptote of data plot curve as per Eq. (4.11) yields $N_i \rightarrow N_0$ as $E \rightarrow \infty$ In this way, the excited state population is estimated as $N_0 \sim 5.6 \times 10^8$ (cm^{-3}) using the saturation of Li resonant transition.

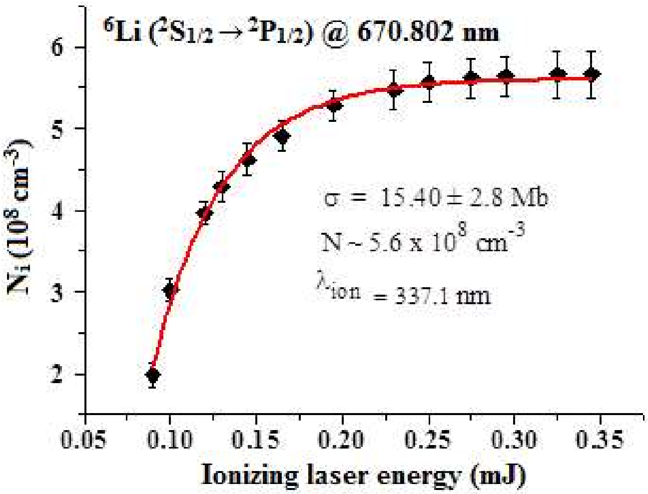

Fig. 5.19 Photoionization cross-section data for ^{6}Li (2p $^2P_{1/2}$) state

Fig. 5.20 shows the photoionization data for 3d ($^2D_{5/2}$) excited state. This corresponds to two-photon excitation at 639.145 nm. As observed earlier in these experiments, initially, there is exponential rise of photoionization signal. Then, ionization signal exhibits the saturation with further increase in ionizing laser intensity. As usual, the least square fitting process is carried out. The photoionization cross-section σ = 8.04 ± 1.6 Mb, is estimated based on the best fit.

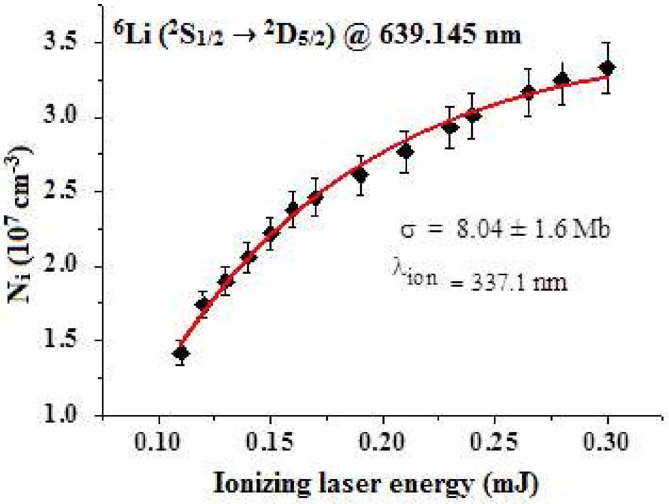

Fig. 5.20 Photoionization cross-section data for ^{6}Li (3d $^2D_{5/2}$) state

These values agree with the reported data [35]. The two-photon excitation photoionization cross-section needs to be compared with that of single photon excitation of Li transition. The ionization cross-section for two-photon excitation (2s $^2S_{1/2} \rightarrow$ 3d $^2D_{5/2}$) at 639.145 nm is found to be nearly half (8.04 ± 1.6 Mb) of that measured for Li single photon excitation (2s $^2S_{1/2} \rightarrow$ 2p $^2P_{1/2}$) at 670.802 nm. Two photon excitation, leads to one order of magnitude smaller photoionization yield as compared to that in single photon excitation. The different methods of photoionization cross section measurement produced almost same uncertainty in the final data. The emphasis of this study as compared to the earlier used more complex methods [111,132] such as TOFMS, MOT etc. is that low cost and simpler design thermionic diode can be effectively employed in the photoionization cross-section measurement. For comparison of the present work data with available experimental data on Li photoionization cross-section for its different excited states, at different ionizing radiation and using different techniques, are also listed in table 5.1.

Table 5.1: Photoionization cross-section of ^{6}Li for different energy states and ionizing radiation

Authors	Method	Cross-section σ (Mb)	Energy states	λ_{ion} (nm)
		^{6}Li		
Wippel et al. [132],	Saturation (MOT)	15 ± 1.5	2p	334.4
Saleem et al. [111],	Saturation (TOFMS)	15 ± 2.5	2p	335.4
Present work,	Saturation (TDD)	15.40 ± 2.8	2p	337.1
Present work,	Saturation (TDD)	8.04 ± 1.6	3d	337.1
Present work,	Saturation (TDD)	7.8 ± 1.6	3d	639.1

5.3 Conclusion

In summary, a positive ion-detector is developed. The device (thermionic diode, TD) enabled high gain (~10^4) and large SNR (~10^6) photoionization signals. High sensitivity of detector (TD) is attributed to its very small electrical noise (~1 pA) and the overall charge collected, which is of many folds of the charge generated by photo-ions. This is due to the increased diode current integrated over long trapping time (~10 ms). Thermionic diode is fully operational in dual mode, as a heat-pipe as well as positive ion-detector. As a heat-pipe, it provided a long isotherm of Li vapour column of uniform density, optimum for absorption experiments. The heat-pipe furnace is designed in a special way. The bifilar electrical windings of heating wire in furnace, take care of unwanted magnetic effects. This would, otherwise, may perturb the energy levels of sample (Li). The proper and accurate performance of the developed thermionic diode is ascertained by its optical and electrical characterization. The developed TD is easy to repair and maintain. This brings in an additional advantage of portability to the device. The excess heat is removed by thin & narrow grooves on TD surface and mini heat-radiator mounted externally. This is contrast to traditional complex and rigid water cooling arrangement generally done.

Large photoionization signals obtained with high SNR, is the evidence of TDD high detection sensitivity. The selective photoionization of Li atoms is carried out in space charge region of thermionic diode. The photo-ion signals are detected with high detection sensitivity. Li photoionization cross-section ($\sigma = 7.8 \pm 1.6$ Mb) is measured for single colour, three-photon ionization at 639.145 nm. This agreed well with the literature reported. Li photoionization cross-sections are studied for other excited states via different photoionization routes. The studied Li excited states are 2p ($^2P_{1/2}$) and 3d ($^2D_{5/2}$) by employing two-step photoionization scheme. For both the single and two photon excitation, the TD produced high SNR photoionization signals. This study concluded that thermionic diode ion detector is a sensitive, simple and cost-effective device to study the Li photoionization process. Photo-ionization cross section for Li 2p ($^2P_{1/2}$) and 3d ($^2D_{5/2}$) excited states are measured. The measured values, of 15.40 ± 2.8 Mb and 8.04 ± 1.6 Mb respectively, are in agreement with reported data, by other methods. The ionization cross-section for two-photon excitation (2s $^2S_{1/2} \rightarrow$ 3d $^2D_{5/2}$) at 639.145 nm is nearly half (8.04 ± 1.6 Mb) of that measured for Li single-photon excitation (2s $^2S_{1/2} \rightarrow$ 2p $^2P_{1/2}$) at 670.802 nm. The isotopic shift of ~ 10.53 GHz is measured between two Li isotopes for 2p states. In addition to measurements of photoionization cross-section of alkalis, the TD with minor improvements can be useful for photoionization studies and Rydberg atoms spectroscopy of other elements also such as lanthanides [159]. The advantage of developed thermionic diode is its sturdy, simple and cost-effective design with high gain.

Chapter 6

Isotope Selective Photoionization of Li using TOF Mass-spectrometer

6.0 Introduction

The studies on Li photoionization spectroscopy in hollow cathode discharge lamp (chapter-4) and thermionic diode (chapter-5) are further extended to atomic beam based mass spectrometer (MS) setup. The TOFMS is a very accurate and sensitive technique for studying the isotope selective photoionization/enrichment. In this chapter, in-house developed linear TOFMS has been utilized for studying the Li isotopes. This chapter, first present the brief working details of the utilized TOFMS and then describe the two and three step isotope-selective photoionization studies on Li. The proper functioning of the TOFMS is first ascertained by adjusting its various control and operational parameters in a non-resonant Li photoionization experiment that allows an accurate measurement of relative compositions of natural Li isotopes. The two-step photoionization is carried out using nitrogen laser pumped dye laser with output in visible range and the UV radiation obtained from nitrogen laser. The effects of precise tuning of dye laser on isotope-selective photo-ion signal is studied. Photoionization cross-section for both the Li isotopes is experimentally measured and the concentration of less abundant ^{6}Li isotope is enhanced upto 72% in is achieved. Three-color, three-step photoionization is carried out using the two high repetition rate tunable dye lasers required one each for the first and second resonant steps. These dye lasers are pumped by copper vapour laser (CVL) master-oscillator/power-amplifier operating at high repetition rate of 6.5 kHz. In this photoionization scheme, third and the final non-resonant step utilize the 578.2 nm radiation directly obtained from CVL. This photo-ionizes the Li atoms from its excited state. Performance of the proposed photoionization schemes are evaluated in terms of photoionization yield and selectivity of the isotopes. Selected three-step photoionization pathway enabled high photoionization yield and high selectivity with large enhancement in desired isotope concentration. The ^{6}Li isotope natural abundance is enhanced upto 92% with high selectivity of ~ 164 by tuning the wavelength of respective dye lasers to 2p ($^2P_{1/2}$) and 3d ($^2D_{3/2}$) energy levels. In the similar way, ^{7}Li abundance is enhanced upto ~ 100%.

6.1 Laser assisted isotope separation of Li by two-step photoionization

6.1.1 Experimental setup

Fig. 6.1 shows the experimental setup used for two-step laser isotope separation studies and measurement of photoionization cross-section. It mainly contains a vacuum chamber, Li atomic beam source and TOFMS. The TOFMS is equipped with vacuum pumping stations with liquid nitrogen baffles at both the ion-source and detector ends. N_2 laser pumped tunable dye laser is used as Li atom exciter. The dye laser relevant parameters are as, ~ 0.2 cm^{-1} (linewidth), 6 ns (pulse duration) and 640-680 nm (tuning range). Nitrogen laser (337.1 nm) is also used as an ionizer. Nitrogen laser operated with a peak power ~500 kW in 10 ns pulse.

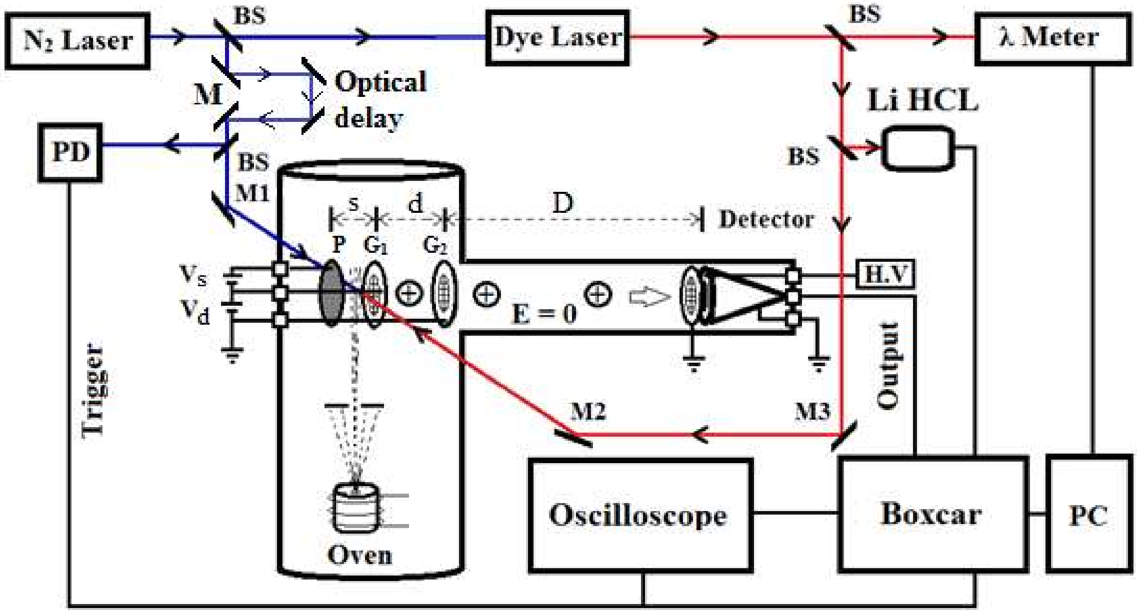

Fig. 6.1 Experimental setup for TOFMS based two-step photoionization of Li isotopes

In ion source vacuum chamber, low pressure ~ 10^{-6} mbar is maintained. This assembly is connected to 1.2 meter long field free (E = 0) flight tube with ion-detector placed at its far end. The vacuum in TOFMS is created by two sets of oil diffusion pump driven by rotary pumps. An atomic beam oven is installed in vacuum chamber. This oven with inner diameter 12 mm and depth 25 mm, is made from corrosion resistant high quality steel (SS 316). The oven has capacity to hold ~ 1.5 gm of lithium sample. Resistive heating of oven generated the effusive Li atomic beam. The oven was placed just below the ionization/extraction region of MS. 'K' type of thermocouple directly mounted on oven surface. This measured the temperature of atomic gas with an accuracy of ± 1 ^{0}C. The small fluctuations in atomic beam flux are controlled precisely. This is carried out by regulating the dc current in heating filament using PID. The PID (proportional- integral-derivative) are the most accurate and stable controller. This uses the feedback control loop mechanism to regulate the process variables. The atomic beam emits through an exit hole of ~ 1 mm diameter. The oven was held at an operating temperature of 525 ^{0}C. At this temperature, the mean free path (= 1/nσ) is ≈ 24 cm. This is much larger than the size of exit hole. This ensured the effusive Li atoms flow without collisions through oven exit hole. The Li atom density generated by oven is estimated to be ~ 3.7 x 10^{16} atoms/sec. The atom moves with at an average speed of ~ 1.35 x 10^{5} cm/sec. A set of 2 mm diameter apertures are used to collimate the atomic beam. The collimated atomic density in laser interaction region is estimated to be ~ 6.85 x 10^{11} atoms/cm^{3}. Li temperature versus vapour pressure curve is used to estimate Li atom density. Emanating from the oven, Li atomic beam reach the ionization/extraction region of MS. Here atomic vapor interacts orthogonally with exciting and ionizing laser beams. The ionizing laser is optically delayed by about 2 ns. In this process, Li photo-ions are produced. These photo-ions are extracted into accelerating region of MS. This is carried out by applying an electric field of 300 V/cm in small laser ionization region (s = 8 mm). The ions are, then, accelerated to high kinetic energy. This energy is achieved by applying an electric field ~ 450 V/cm. The length of acceleration region is ~ 35mm. Then ions travel through 1.2 meter long field free flight region (D = 1.2 m). In this region, the ions are separated as per their mass to charge (m/z) ratio. An ion-detector (SJUTS, KBL-25) is operated in linear region at 2 kV negative potential. This is utilized to collect the produced Li^+. A digital oscilloscope (Lecroy-6050A, 500 MHz) measured the photo-ion current. The optical delay (~2 ns) between exciting and ionizing laser beams is set to optimize the photo-ion signal. Maximum population from excited state, needs to be extracted before its decay to ground state. This necessitates that the ionizing laser pulse should appear just after an exciting laser pulse. This way, the higher photo-ionization efficiency for each Li isotopes is achieved. Data averaging over 100 acquisitions is also carried out. This is to average out the effects of pulse to pulse laser energy change on photo-ionization signal. To average out the noise, the detector signal is processed via boxcar-integrator. Finally signals were recorded on computer for further analysis. The ion detector assembly and connecting cable wires are well shielded and grounded. This was essential to substantially reduce the role of electro-magnetic as well as back ground noise on photo-ion signal.

For studies on Li isotope separation, a suitable dye laser is used. The crucial parameters of dye laser are narrow bandwidth (~ 6 GHz) and wavelength tunablity from 640 to 680 nm, as described in chapter-2 (Fig. 2.17). A dye cell employed has cylindrical dimensions with length = 60 mm and diameter = 20 mm. The dye cell was fabricated form high quality UV grade glass. DCM dye was dissolved in dimethyl sulphoxide (DMSO) solvent, is used. Dye laser cavity has grazing incidence grating (GIG) geometry. The resonator contained, an output coupler (R = 20%), holographic grating (2400 lines/mm) and a plane reflecting mirror. The N_2 laser output is divided by a partial reflector with 40% beam being used to pump the dye laser. The remaining 60% is utilized as ionizing beam. The dye laser is operated at optimized DCM dye concentration of ~ 3.5 mM. This ensured sufficient large power to saturate the Li transitions. Intra-cavity prism beam-expander (10 X) coupled with a Littrow grating (in place of tuning mirror) further reduced the dye laser bandwidth. The cavity length is kept as short (~ 18 cm) as possible, to increase number of round-trips of circulating radiation in the available ~ 6 ns dye laser duration. A homemade Li hollow cathode lamp [171] is used to ensure the resonant excitation of Li. The exciting (670.78 nm) and ionizing (337.1 nm) laser beams interacted in TOFMS ionization-region. These exciting and ionizing laser beams are incident from opposite sides after suitable collimation and focusing. A computer controlled dye laser scanner cum data logger [83] is used to acquire and analyse data. It contained personal computer, wavelength meter (WS-7, HighFinesse), photo-diode and boxcar-integrator (SRS-250). Dye laser wavelength slow scanning speed was slow (~ 0.002 nm/s) during the isotopic signals recording. This was essential in order to capture the every small change in ^{6}Li and ^{7}Li photo-ion signals. The intensity of incident exciting and ionizing laser beams is controlled by a set of neutral density filters.

6.1.2 Multiphoton ionization of Li atoms

In the first part of this study, the isotopes ratio of a natural Li sample is measured. This is carried out to calibrate and optimize the operating parameters of TOFMS. In this experiment, dye laser beam is blocked and only the nitrogen laser UV beam at 337.1 nm, is passed through the ionization region of MS. The ionizing UV beam is focused in the ionization region, by convex lens of short (25 cm) focal length. The ionizing beam interacted with collimated Li atomic beam. The temperature of oven is enhanced suitably upto 625 ^{0}C. This is to achieve the high vapour density (~10^{17} atoms/cm^{3}). In beginning, with low ionizing laser beam energy, no ion-signal is observed. However, a signal of appreciable strength (~ 20 mV) is obtained by increasing ionizing laser energy from 1 to 2 mJ, in small steps. The observed signal is attributed to multiphoton ionization (MPI) of Li atoms. High photon flux density is the need of such experiments, as the photoionization cross-section is very low for non-resonant process. This is achieved by tight focussing of the ionizing laser beam. The MPI yield of the atoms, is related to multiple parameters. Energy density, polarization and pulse duration are the guiding laser parameters. The value of n-photon excitation cross-section (σ_n) is also a very important parameter. The magnitude of σ_n also depends upon incident wavelength and its polarization. The non-resonant MPI cross-section σ_n for an atom can be determined from the numbers of radiation quanta 'n' required, as defined by a relation,

$$\mathrm{n} = \left(\frac{\mathrm{V_{pot}}}{\hbar\omega} + 1\right) \tag{6.1}$$

where, V_{pot} is the ionization potential, '*n*' is rder of multiphoton ionization. In case of Li, for MPI, two photons each of energy 3.67 eV, as obtained from nitrogen laser at 337.1 nm, are enough. The ionizing rate (*R*) of Li is related to the incident laser flux density *(Φ)* as,

$$\mathrm{R} = \sigma_2\Phi^2 \tag{6.2}$$

where σ_2 denotes two-photon ionization cross-section. In whole ionization process, the ion concentration (N_i) varies in time as,

$$\frac{\mathrm{dN_i}}{\mathrm{dt}} = \mathrm{R}(\mathrm{N_0} - \mathrm{N_i}) \tag{6.3}$$

N_0 denotes the Li atom density. For laser pulse duration *(τ)*, ion yield attains a value as,

$$\mathrm{N_i} = \mathrm{N_0}\left[1 - \exp\left(-\int_0^{\tau} \mathrm{R\,dt}\right)\right] \tag{6.4}$$

Practically, all the ions produced are not detected as TOFMS grids transmittance is < 100%.

6.1.3 Isotopic composition of Li atoms

Fig. 6.2(a) shows photo-ion signal and isotopic distribution of Li atoms. These results are obtained by simultaneous absorption of two-photon of 337.1 nm wavelength. Figure 6.2(b) explains the two-photon ionization of Li atoms through its intermediate virtual energy state.

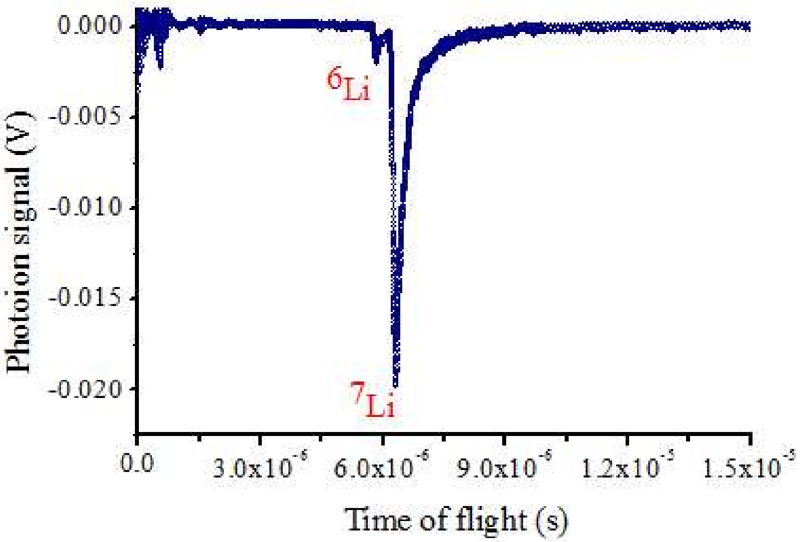

Fig. 6.2(a) Results on Li isotopes by two-photon non-resonant ionization

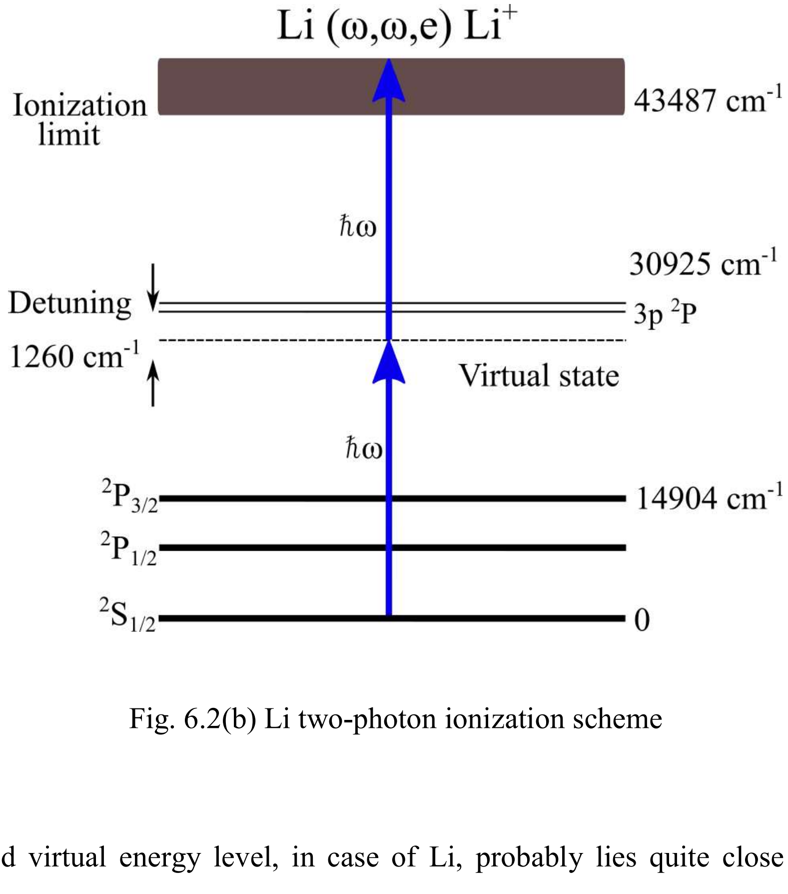

Fig. 6.2(b) Li two-photon ionization scheme

The mentioned virtual energy level, in case of Li, probably lies quite close (~ 1260 cm^{-1} away) to its resonance level (3p ^{2}P) at 30925 cm^{-1}. It is well known that when virtual level lies close to resonant states, the probability of ionization increases substantially [172]. This explains, the relatively strong Li photoionization signal, as achieved low photon density, see Fig. 6.2(a). Hence, non-resonant MPI method, turns out to be good scheme to determine the Li isotope ratio as it ionizes both the isotopes, simultaneously with same efficiency. A similar MPI method is demonstrated by Talwar et al. [67] on isotopes of samarium (Sm). The study was carried out for validating the developed TOFMS of reflectron type. In present research work, the linear TOFMS is calibrated to optimise the ratio of natural abundant Li isotopes. This is carried out by proper adjustment of ion-extraction and accelerating electric fields. The ion-detector voltage was also optimized. In this way, sharp peak of Li isotopic signal are obtained. The isotope ratio is measured by calculating area under the respective isotopic peak and is also cross checked by their peaks heights. The measured relative isotopic abundance (^{6}Li/^{7}Li) is ~ 0.080. This value is very close to Li isotopic ratio reported in the literature [173]. Although, minor variation (- 0.002) is noticed, possibly due to small relative systematic error ($\delta = 0.024$) of the system used. The systematic error is calculated as [1- (^{6}I/^{7}I) / (^{6}Li/^{7}Li)]. The ^{6}I & ^{7}I are signal intensities proportional to the ionic current due to respective isotope masses. This data accuracy is comparable to that reported in similar studies involving resonance ionization mass-spectrometry [174]. The probable dominant source of systematic error are as, 1) Spread of laser beam in interaction zone and 2) Temporal distribution of laser pulse intensity. Other limiting factors also bring in small error in relative isotope abundance measurements. These are, space charge effects, isotopic charge exchange and scattering of ions. These error causing factors can be minimized by laser beam pulse shaping and operating the atomic beam oven at moderate temperature. Once, all these precautions are taken and the ion-extraction/acceleration electric fields as well as ion-detector voltage etc. are set properly, the mass-spectrometer reproduced nearly the precise and correct isotopic ratio. This study confirmed that TOFMS is now ready for further measurements on isotope selective photoionization studies. The method devised may also be very useful for investigating the isotopes involved in environmental, nuclear and biological processes. [175-177]. In comparison to emission and absorption techniques, the mass-spectrometry is highly beneficial for these types of studies [178].

6.1.4 Selective Li isotope separation

The separation of its isotopes (^{6,7}Li) seems feasible using red and UV transitions. This is evident from the energy levels and ionization potential of Li atoms. This is carried out by employing the dye laser and nitrogen laser radiation in two-step photoionization process. Figure 6.3 shows the energy levels for Li isotopes with red (~ 671 nm) and UV (~ 337 nm) transitions [35]. The nuclear spin (I) values for Li isotopes are, 1 for ^{6}Li and 3/2 for ^{7}Li. Both the Li isotopes have doublets and hyperfine structures (HFS). This originates due to their non-zero nuclear spins. The presently used dye laser of line-width ~ 0.2 cm^{-1} was not able to resolve the hyperfine lines. The separation between $^2S_{1/2} \rightarrow {}^2P_{1/2}$ (D$_1$ line) and $^2S_{1/2} \rightarrow {}^2P_{3/2}$ (D$_2$ line), of each isotope is ~ 0.0158 nm [37]. For resonance line at 670.78 nm, D$_1$ and D$_2$ line spacing, is close to the isotopic shift 0.0154 nm (~ 10.54 GHz) [88,126]. This implies that $^2S_{1/2} \rightarrow {}^2P_{1/2}$ transition of ^{7}Li nearly coincides with $^2S_{1/2} \rightarrow {}^2P_{3/2}$ transition of ^{6}Li. This demands for the very small linewidth (< 0.33 cm^{-1}/1 GHz) of the dye laser. Then, only the Li isotopes will be selectively excited from ground state ($^2S_{1/2}$) to the doublets $^2P_{1/2}$ or $^2P_{3/2}$ level of each isotope. In present experiment, dye laser bandwidth is ~ 6 GHz/0.2 cm^{-1}. It is necessary to selectively excite each isotope to attain large isotope separating factor. This is possible with existing dye laser by tuning wavelength to either ^{7}Li ($^2S_{1/2} \rightarrow {}^2P_{3/2}$) or ^{6}Li ($^2S_{1/2} \rightarrow {}^2P_{1/2}$) resonance levels. These levels have a relatively large energy spacing with wavelength difference of $\Delta\lambda$ ~ 0.0315 nm. The Li ionization potential (I.P) is 5.39 eV and its ^{2}P state energy is ~ 1.84 eV [126]. Therefore, the resonantly excited Li atom can be suitably ionized by photons of wavelength < 349 nm. Hence, N_2 laser (~ 337 nm) and dye laser tunable around ~ 671 nm, are proper choice for Li isotope separation via two-step photoionization scheme.

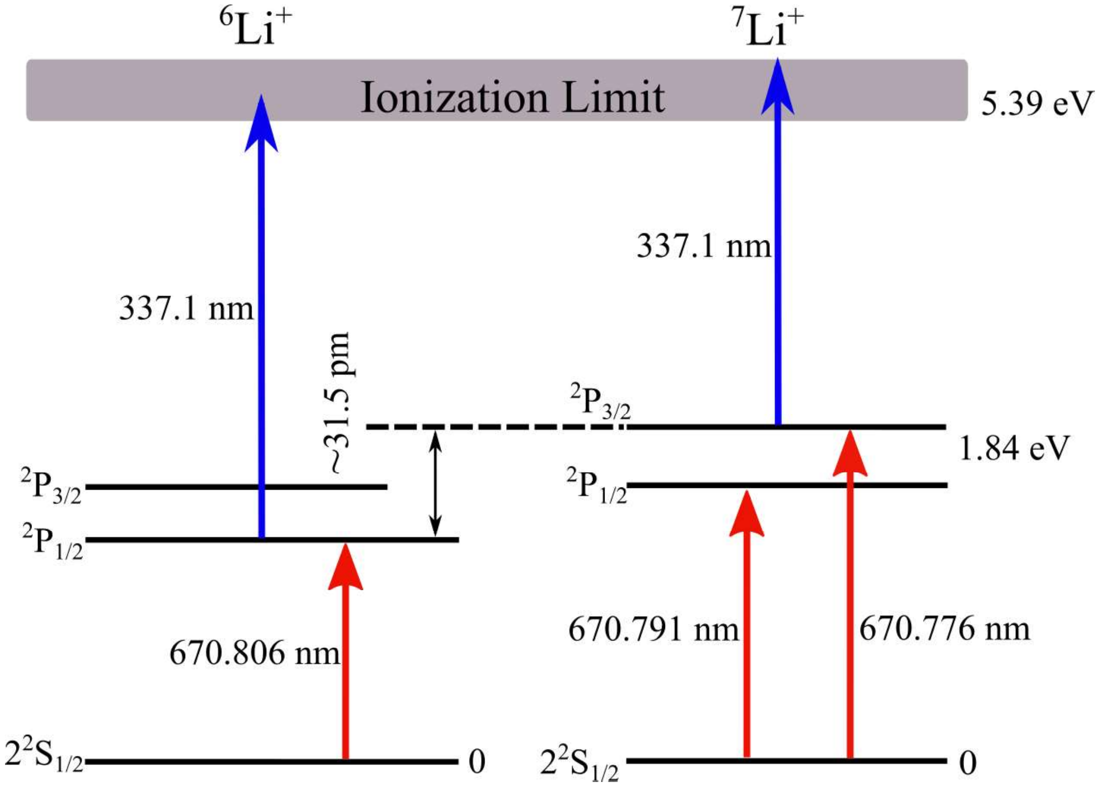

Fig. 6.3 Energy levels of Li, relevant to isotope-selective two-step photoionization

In next set of studies, the photo-ionization yield and cross-section for ionization are measured. Accurate measurement of photoionization cross-section is needed to quantify the isotope enrichment. In present research work, two-step photo-ionization scheme is utilized. The scheme is, $^2S_{1/2} \xrightarrow{\sim 671\ nm} {}^2P_{1/2,3/2} \xrightarrow{\sim 337\ nm} {}^1S_0$ (Li^+). Figure 6.1 shows an experimental setup to implement this two-step resonant photoionization scheme. In the experiment, the excitation laser (~ 670.78 nm) and ionizing laser (~ 337.1 nm), interact orthogonally with Li atomic beam. The resonant transitions are saturated due to sufficient exciting laser pulse energy (~ 30 μJ). The ionizing laser beam energy is reduced significantly to avoid the possibility of two-photon ionization. This is accomplished by inserting neutral density filters. First, the Li atoms are excited from ground ($^2S_{1/2}$) to excited state ($^2P_{1/2,3/2}$). Then, the excited Li atoms are photo-ionized by ionizing laser radiation, subsequently. The produced Li photo-ions are finely separated by their respective flight times in TOFMS according to isotope masses. Finally, these are collected by TOFMS at detector. Such ionic signals are recorded on oscilloscope. For this purpose, dye laser wavelength is scanned over ^{7,6}Li transitions at 670.776 and 670.806 nm, respectively. This resulted in isotope-selective Li photoionization signals of high strength (~120 mV) and good resolution (see, Fig. 6.4).

Figure 6.4(a) shows the high selectivity obtained for ^{7}Li. As the exciting laser wavelength is tuned away the ^{7}Li transition and approaches towards ^{6}Li, another small peak evolves. This is just before (~ 450 ns) the ^{7}Li signal as shown in Fig. 6.4(b). This peak corresponds to ^{6}Li. This is verified from the consistency of flight time data with its mass. This is well known that in a TOFMS, ions flight time is related to square root of the masses [63]. Tuning the dye laser wavelength further, inversion of Li isotopes signal strength is observed. ^{6}Li signal overtakes ^{7}Li peak. This happens as the wavelength tuning approaches towards ^{6}Li resonance level as seen in Fig. 6.4(c). In this way, an optimum condition is reached (Fig. 6.5), when exciting laser is accurately tuned to ^{6}Li ($^2S_{1/2} \rightarrow {}^2P_{1/2}$) transition. Good enrichment in ^{6}Li concentration over its natural abundance is obtained. The enrichment is estimated for the expression [^{6}Li/ (^{6}Li + ^{7}Li)] x 100. Isotope ^{6}Li is selectively enhanced over its natural abundance from 7.5% to 72%. This enrichment achieved far exceeds that reported (~ 47%) by Saleem et al. [42] et al. The isotopes concentration is measured by integrating area under isotopic signal peak. This area calculation process is carried out using 'Origin-8' data analysis. It is well known that by employing very narrow linewidth lasers, much higher selectivity can be obtained. However, it is usually at the cost of compromised photoionization yield.

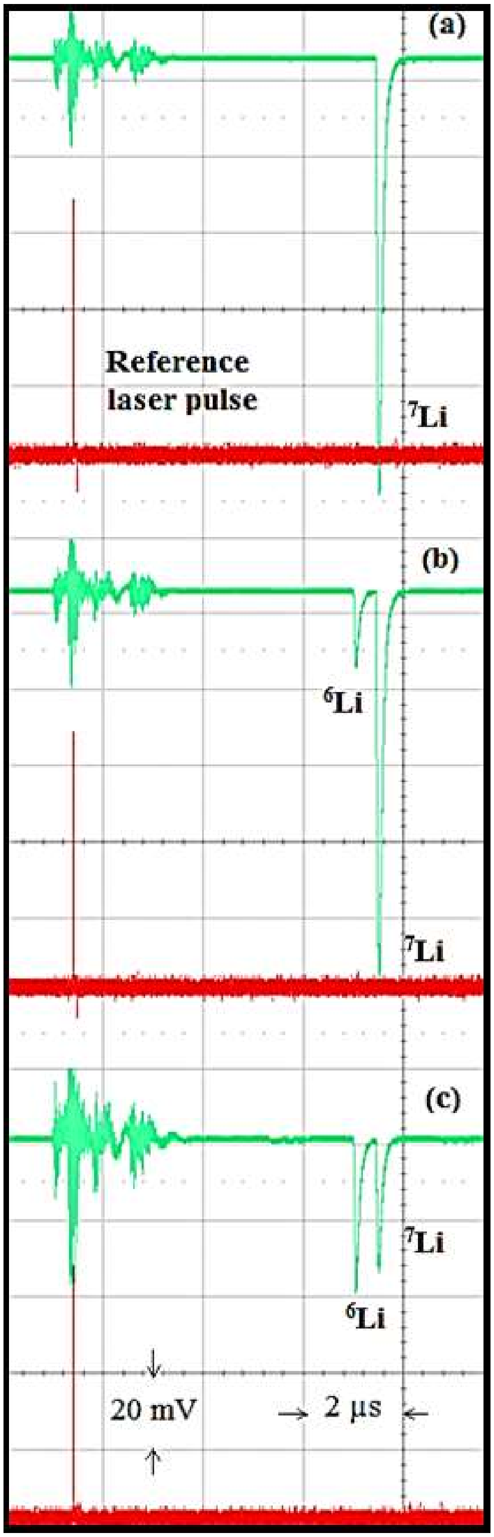

Fig. 6.4 Two-step, isotope-selective, TOF signals of Li for (a) 670.772 nm, (b) 670.782 nm, (c) 670.792 nm wavelength obtained by scanning dye laser wavelength across 671 nm

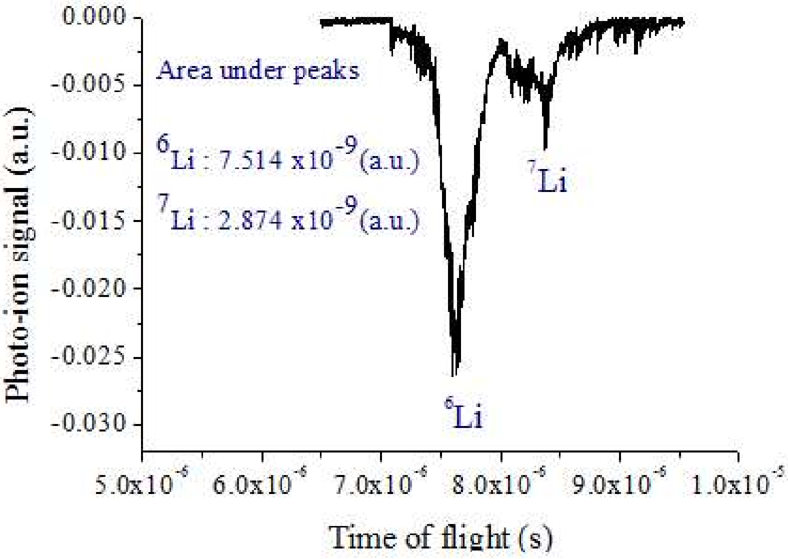

Fig. 6.5 Li isotopes distribution produced by two-step resonant photoioniztion when exciting laser is tuned to ^{6}Li ($^2S_{1/2} \rightarrow {}^2P_{1/2}$) resonance transition at ~ 670.806 nm

In present experiment, about ~10 folds enhancement in the concentration of lowest abundant ^{6}Li is obtained. This is coupled with fairly high selectivity (S = 32.27) calculated as $[(^6Li/^7Li)_{product} / (^6Li/^7Li)_{feed}]$. This expression for selectivity (S) is valid for the elements with only two isotopes such as lithium. The same conforms to that used by Pulhani et al. [179] and references therein. The time resolved Li isotopic signals (Fig. 6.4) measured earlier directly on oscilloscope, are reproduced again to observe the dependence of ^{7}Li and ^{6}Li photo-ion signals on exciting laser wavelengths (Fig 6.6). A boxcar integrator is used to measure the respective isotopes photoionization signal. Figure 6.6 shows the ^{7}Li and ^{6}Li photo-ion yield dependence on exciting laser wavelength, when all other experimental parameters are kept constant. The photo-ion signals are measured by boxcar integrator with 150 ns gate-width, 30 samples and at 20 mV sensitivity. Indication of substantially overlapped two peaks in ^{7}Li signal profile are observed with precise tuning of exciting dye laser wavelength. This corresponded to its fine structure components. Such fine peaks could not be observed for ^{6}Li isotope. This is due to low natural abundance of ^{6}Li. Both the isotopes could not be observed separately. This is most likely due to the residual Doppler broadening in the transitions and very small (< 1 GHz) energy spacing between the ^{7}Li (D_1) and ^{6}Li (D_2) lines. This is beyond the reach of presently used dye laser bandwidth (~ 6 GHz/0.2 cm^{-1}). However, two separate isotope peaks at an interval of ~ 450 ns are repeatedly observed at TOFMS detector (see Fig. 6.4). This is due to the additional mass selectivity offered by TOFMS. It is the beauty of atomic beam based time of flight mass spectrometer photoionization setups. It means, little bit compromise is possible at dye laser linewidth side to obtain separate peaks of the isotopes.

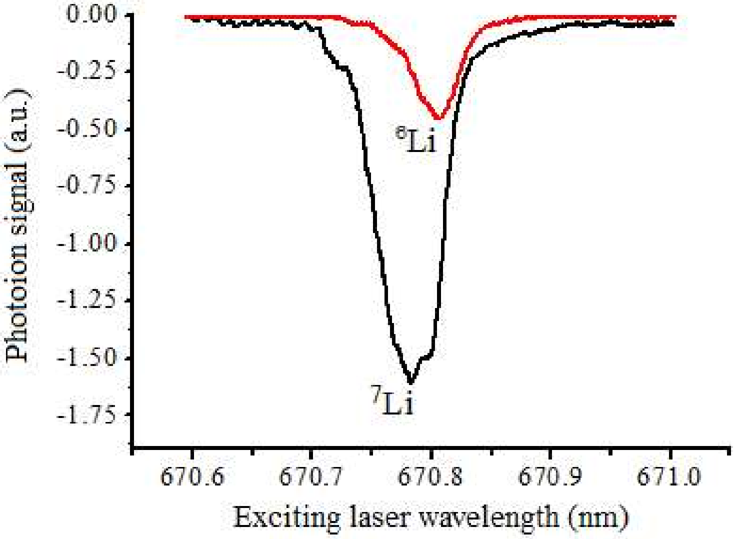

Fig. 6.6 Li isotope photo-ion signals vs exciting laser wavelength

So, it can be concluded that atomic beam based time-of-flight mass spectrometry setups are although costly and complex, however much better than the previously studied low cost HC discharge lamp and thermionic diode based photoionization setups. Although, these simple setups have their own merits in other aspects such as exploring the required spectroscopic data and finalizing the efficient photoionization schemes, needed for high isotope separation/enrichment.

6.1.5 Measurement of Li photoionization cross-section

To measure the Li isotopes photoionization cross-section, the effect of ionizing laser pulse energy on photoionization signals is studied. The ^{7}Li and ^{6}Li photo-ion signal as function of ionizing laser density is shown in Fig. 6.7(a) and Fig. 6.7(b), respectively.

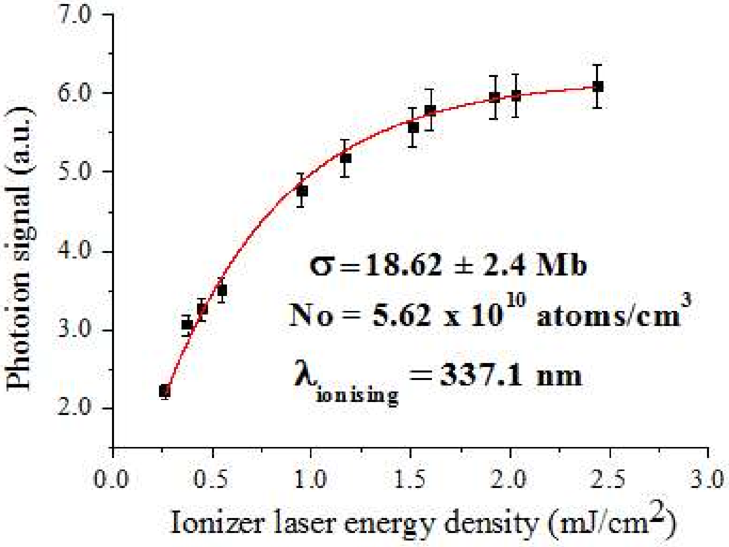

Fig. 6.7(a) Photoionization cross-section data for ^{7}Li ($^2P_{3/2}$) excited state

At low energy density (< 1 mJ/cm^2), the photo-ion signal is almost linear for both the isotopes. However, at higher ionizing energy, it deviates from linear nature and tend to saturate. Almost all the atoms excited into 2p states are ionized, at saturation. The strength of photo-ion signal does not increase further with rise in ionizing laser energy. From this curve, photoionization cross-section can be calculated. This is based on rate equations as described below. Ambartzumian et al. [116] pioneered a technique to measure the photoionization cross-section of excited atomic levels. Burkhardt et al. [131], further, improved upon this technique. Several groups/authors used the improved technique e.g. Saleem et al. [42], Zheng et al. [180] and Mende et al. [181] to measure the photoionization cross-section.

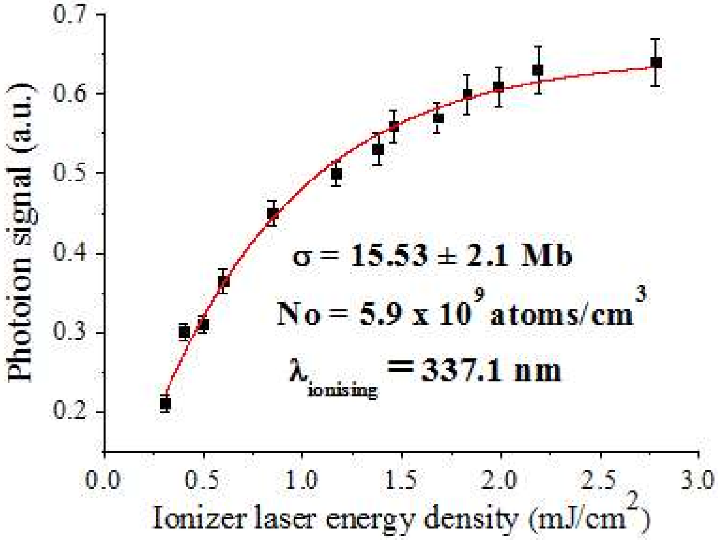

Fig. 6.7(b) Photoionization cross-section data for ^{6}Li ($^2P_{1/2}$) excited state

In two-step photoionization process as used in present Li studies, the population N_1, N_2 and N_i in respective energy states, can be determined from,

$$\frac{d}{dt}N_1(t) = -R_{12}[N_1(t) - N_2(t)] + \frac{N_2(t)}{\tau_{21}}, \qquad N_1\,(t=0) = N_0 \qquad (6.5)$$

$$\frac{d}{dt}N_2(t) = R_{12}[N_1(t) - N_2(t)] - R_i\,N_2\,(t) - \frac{N_2(t)}{\tau_{21}}, \qquad N_2\,(t=0) = 0 \qquad (6.6)$$

$$\frac{d}{dt}N_i(t) = R_i\,N_2\,(t) \qquad (6.7)$$

here R_{12} denotes the excitation rate from ground to excited state, τ_{21} the relaxation time to ground state. For easy calculations, few assumptions are made. These are, 1) No collisions occurs between the atoms, 2) The R_{12} and R_i are much larger than the relaxation rate $1/\tau_{21}$, 3) Since, the duration of ionizing laser pulse (~ 10 ns) is much shorter than Li relaxation time τ_{21} (~ 27 ns). Then, the radiative decay term (N_2/τ_{21}) in Eq. (6.5) may be ignored. Also, under saturation of Li ($^2S_{1/2} \rightarrow {}^2P_{1/2,3/2}$) transition throughout laser pulse duration, it is possible that,

$$N_1(t) = N_2(t) = \frac{N_T(t)}{2} \qquad (6.8)$$

Here N_1 (t) and N_2 (t) are ground and excited states atom density, respectively. N_T (t) is their net sum. Addition of Eqs. 6.5 & 6.6, gives the loss rate due to photo-ionization as,

$$\frac{d}{dt}N_T(t) = -R_i N_2(t) = -\frac{I(t)\sigma}{2\hbar\omega}N_T(t) \tag{6.9}$$

where R_i [= I (t)σ/ħω] is rate of ionization, 'I' is time-dependent ionizing laser intensity. σ(cm^2) is the photoionization cross-section of resonance (2p) state. This state is connected to Li continuum by ionizing radiation (337.1 nm) of photon energy (~3.67 eV). The Eq. (6.9) integration yields,

$$N_T(t) = N_0 \exp[-\frac{\sigma}{2\hbar\omega}\int_0^t I(t')dt'] \tag{6.10}$$

where $N_0 = N_T$ (at t = 0). N_0 denotes the atom density in ground state before an arrival of the exciting laser pulse. The exponential term is connected to decrease in excited atoms after arrival of ionizing laser pulse. The total ionic charge (Q) produced per ionizing laser pulse and finally detected by the TOFMS is given by,

$$\frac{Q}{e} = \int_0^\tau R_i N_2(t) V_{vol.} dt$$

$$\frac{Q}{eV_{vol.}} = N_i = N_0 \int_0^\tau \frac{I(t)\sigma}{2\hbar\omega} \exp[-\frac{\sigma}{2\hbar\omega}\int_0^t I(t')dt']dt \tag{6.11}$$

where *e* (Coulomb) is electronic charge, $V_{vol.}$ (cm^3) is laser-interaction volume and τ (sec) laser pulse duration. Integration of Eq. 6.11 gives an expression for the number of ions (N_i) produced per unit volume by each laser pulse with $\int_0^\tau I(t)dt = E/A$ as,

$$N_i = N_0\left[1 - \exp\left(-\frac{\sigma E}{2\hbar\omega A}\right)\right] \tag{6.12}$$

Here A (cm^2) is the laser interaction cross-sectional area, E (Joule) the total energy per ionizing pulse, ħω (Joule) the energy per photon of ionizing laser beam, N_0 (atoms/cm^3) the number density in ground state. This equation is valid with few assumptions that exciting laser beam intensity is high enough for saturating the resonance transition. In above expression, except N_0 and σ, all other parameters are known or measurable. These parameters can be evaluated from Figs. 6.7(a) and (b), by least-square fitting. At sufficiently high E values, determination of N_0 is independent of ionization cross-section. This is due to the fact that $N_i \rightarrow N_0$ as $E \rightarrow \infty$. Hence, N_0 is estimated from the asymptotic value of N_i. Similarly, σ is estimated from N_i vs. E plot. The measurement error bar in Fig. 6.7 is ~ 5%. Here, the fluctuation in ionizing laser pulse energy is responsible for this error. The resulting photoionization, produced the total ionic charge (Q). This can be correlated with photoionization signal as,

$$Q = \left(\frac{\text{Voltage signal}}{\text{R}}\right)\Delta\text{t} \tag{6.13}$$

Where, R is the load resistor of 50 Ω, and Δt (~130 ns) is FWHM pulse-width of the measured Li isotopes signals. Hence, by knowing accurate laser-atom interaction volume, the value of N_i can be calculated. The spatial overlap of exciting and ionizing laser beams with collimated atomic beam define the interaction volume. In the present case, this cylindrical volume defined, in TOF ionization region, is estimated to be ~ 0.0058 cm^3. For both the isotopes ^{7}Li and ^{6}Li, the least-square fitted experimental data is shown in Figs. 6.7(a) and (b). These are used to calculate the atom density and photoionization cross-section of ^{7}Li and ^{6}Li isotopes as $N_0 = 5.62 \times 10^{10}$ atoms/cm^3, $\sigma = 18.62 \pm 2.4$ Mb and $N_0 = 5.9 \times 10^9$ atoms/cm^3, $\sigma = 15.53 \pm 2.1$ Mb, respectively. The uncertainty in measurements of ionizing laser beam energy (E) and laser interaction cross sectional area (A), dictates the accuracy of measured photo-ionization cross section. A photographic film burn spot due to ionizing laser beam is recorded and used in estimating the cross-sectional area. This comes out to be, $A \approx 0.00968$ cm^2. X. Zheng et al. [180] used similar method to measure the photoionization cross-section of cobalt. In the present experiment, the uncertainty in cross-section (A) determination is estimated to be ~20%. The laser pulse energy measurement further adds around ± 3% uncertainty. Around ± 2% uncertainty is added by statistical errors. In totality, ~ 25% is the maximum uncertainty in estimation of photoionization cross-section. The measured, Li (2p) state, photoionization cross-section for both the isotopes are in excellent agreement with recent published data [42]. Figure 6.8 presents, a graphical comparison of the available experimental [42,129,132] and theoretical data [32] with present work. The theoretical calculations from Lahiri and Manson [32], for Li (2p) state, are shown here as continuous photoionization curve. This covered the excess energy (ϵ) up to 0.075 R_y from Li first ionization threshold. Here, $1R_y$ is equal to 13.60 eV. All the experimentally measured ionization cross-section by different research groups, lies within small region upto 0.011 $\epsilon(R_y)$ of the excess energy. Also, the measured values by us in the present research work for ^{7}Li (2p $^2P_{3/2}$) excited state, is close to those reported by Wippel et al. [132].

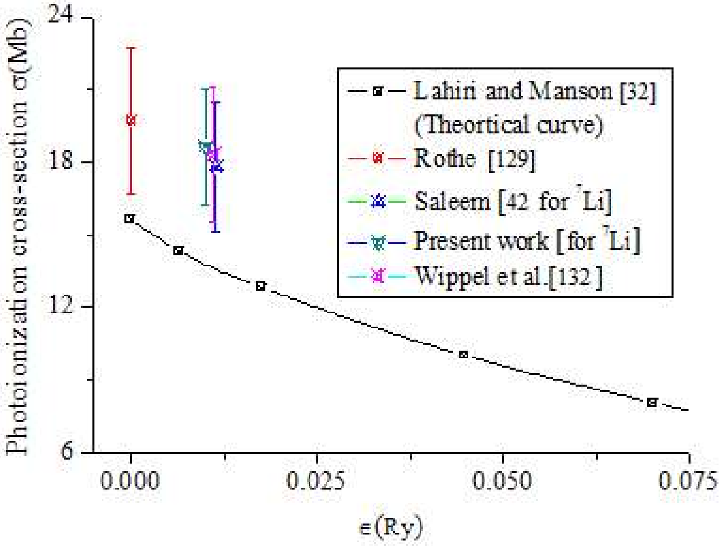

Fig. 6.8 Comparison of experimental and theoretical cross-section of ^{7}Li ($^2P_{3/2}$) state

Table 6.1 Ionizing wavelength wise comparison of cross-section for ^{6,7}Li for 2p state

Authors	Method	Photoionization cross-section σ (Mb)		λ_{ion} (nm)
		^{6}Li	^{7}Li	
Arisawa et al. [41],	Saturation (QMS)	5 ~ 30	……	266
Wippel et al. [132],	Saturation (MOT)	15 ± 1.5	16 ± 2.5	334.4
Saleem et al. [42],	Saturation (TOFMS)	14.8 ± 2.2	17.8 ± 2.7	335.4
Present work,	Saturation (TOFMS)	15.53 ± 2.1	18.62 ± 2.4	337.1

To compare the photoionization cross-section data obtained by different techniques at different ionizing wavelengths, at a glance, is listed in Table 6.1. The knowledge of such photoionization cross-section data is very relevant in many fields. This includes, laboratory as well as astrophysical produced plasma in addition to laser isotope separation.

6.2 Isotope-selective studies by three-step, three-color photoionization of Li

The demand of Li has increased many fold since last few decades because of its extensive use in power backups for electronic devices and electrical vehicles. In addition, the important applications of Li are associated with its isotopes (^{6,7}Li) that can be used in nuclear industry as described in details in chapter-2. A high level of isotope separation/enrichment near to mono-isotopic purity of one of its isotope (^{6}Li) with large thermal neutron cross-section (~ 940 barns) is required in the production of clean fusion energy while high purity over 99.9%, ^{7}LiOH.H$_2$O, is required to adjust the coolant pH factor [182] for safe operation of pressurized water nuclear reactors.

The atomic and molecular spectroscopy is gaining increasing attention in this modern era to obtain highly pure isotopes from their mixtures. Numerous traditional methods as detailed in chapter-2 have been tried to separate and enrich the lithium isotopes. These methods offer higher yield. However, they suffer from low separation factor. This results into poor isotopic purity [183]. Laser based separation methods particularly the resonant ionization spectroscopy (RIS) that utilizes the tunable lasers, are more attractive in terms of high selectivity, isotope purity and capital cost [184-186]. In general, the spectral width of tunable lasers needs to be smaller than isotopic shift of the element to obtain the high selectivity for getting extraordinary isotopic purity. However, the higher selectivity can be obtained with moderate narrowband tunable dye lasers through multi-step excitation/ionization of collimated atomic beam. The large power density of these laser affects the selectivity. This is due to power broadening of atomic transitions and/or multi-photon ionization. This in a way leads to the loss of isotope purity in enrichment [41]. Large power densities are advantageous for higher photo-ionization yield and efficiency. Hence, both the isotope selectivity and photo-ionization efficiency need to be simultaneously optimized. These are prime requirements for LIS methods.

Alkali metals have been studied extensively using the two-step resonant photoionization schemes with narrowband lasers [37,116]. However, the use of time-of-flight (TOF) mass-spectrometer is less reported in such studies. When the RIS technique is coupled with TOF mass-spectrometers, the overall selectivity of process can be suitably enhanced by taking an advantage of the differences in flight time of lighter and heavier isotopes through mass-filter. In this way, the elements with isotopic shift comparable with spectral-width of tunable lasers can be investigated easily. There is a limitation in obtaining the high selectivity and hence in high enrichment of the isotopes with two-step photoionization process [42,187]. In this study three-step, three-color isotope-selective photoionization of Li is investigated with in-house built advanced atomic beam based photoionization setup using the CVL pumped dye lasers in combination with TOF mass-spectrometer. The dependence of photo-ionization yield, selectivity and isotope enrichment factor on laser power density are studied. An advantage of using high repetition rate laser system for Li three-step photoionization over the earlier reported two-step photoionization with low repetition rate laser [42,187], is anticipated in terms of higher isotope selectivity, photoionization yield and high enrichment.

6.2.1 Experimental details

Figure 6.9 shows the layout of an experimental setup. This was utilized to accomplish three-step, three-color photoionization scheme for Li isotope separation/enrichment. The set-up consists of copper vapor laser master-oscillator/power-amplifier (CVL-MOPA), pulsed tunable dye lasers, an oven for generating collimated Li atomic beam, TOF spectrometer for analyzing Li photo-ions, PC- based data acquisition and the dye laser tuning electronics as described in chapter-2. Dichroic mirror ‘BS-1’ separate the green and yellow light components from CVL output to be used for pumping the dye lasers. The laser system consist of CVL pumped high repetition rate tunable dye lasers, one each for the first and second step of Li resonant excitation. The CVL is a useful nano-second pulse pump source in visible region when high pulse repetition rate and high average power are required [44].

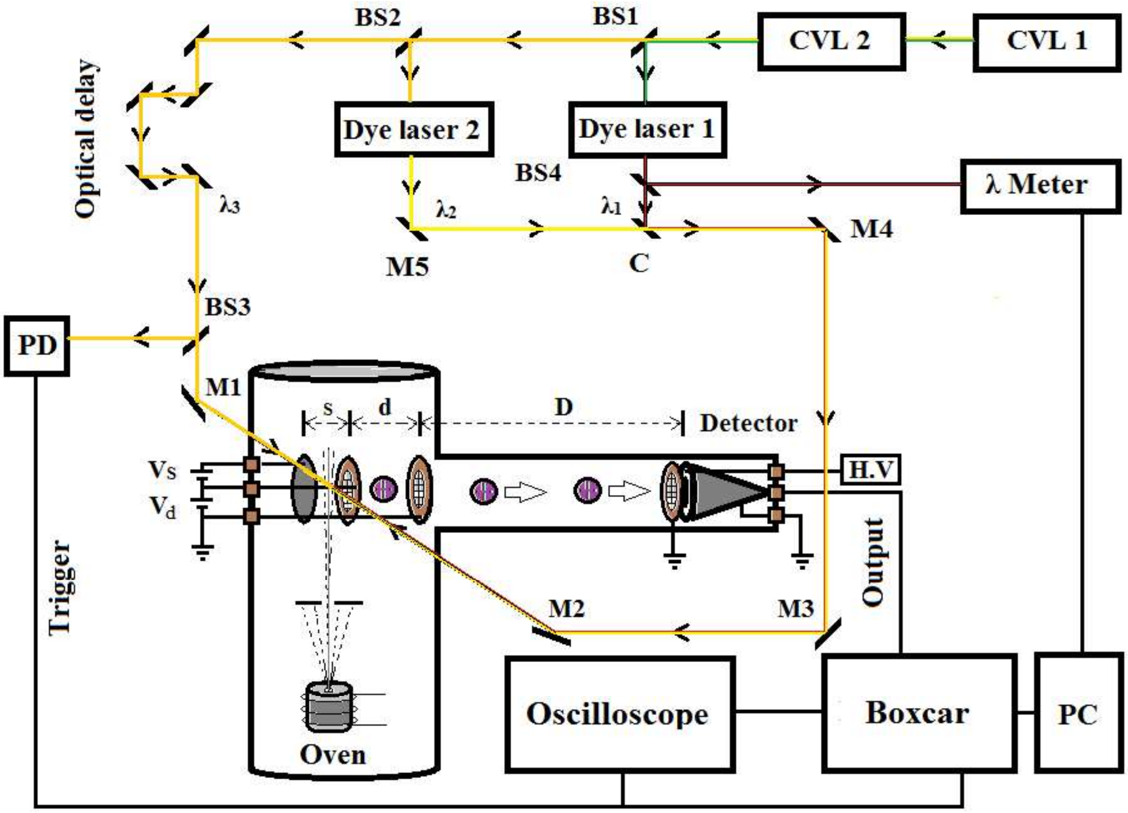

Fig. 6.9 Experimental setup for three-step photoionization of Li isotopes

In Fig. 6.9, the different abbreviations and terminology used are as follows; 1. Dye laser-1 (~2.5 GHz, 20 ns, 635-680 nm, 2.6 mM, DCM dye), 2. Dye laser-2 (~2.5 GHz, 20 ns, 600-625 nm, 0.16 mM, Rh-640 dye), 3. CVL-1 (oscillator 20 W), 4. CVL-2 (amplifier 35 W), 5. λ-meter (WS-7), 6. Boxcar Integrator (SRS-250), 7. PD: Si PIN photodiode, 8. Oscilloscope (Lecroy, 500 MHz), 9. TOFMS parameters: ionization region (s = 8 mm), acceleration region (d = 35 mm), field free flight region (D = 1.2 m), ion-detector: KBL-25 operated @ -2.0 kV, 10. PC: Personal computer. The CVL has unique advantage for pumping the dye lasers in present setup. A CVL produce good quality green (510.6 nm) and yellow (578.2 nm) radiations. The intensity ratio of green and yellow radiation is approximately 2:1. The yellow pulse is slightly delayed (~20) ns from green laser pulse. CVL operates at large pulse repetition frequency (~ 6.5 kHz) with pulse durations ~ 40 ns. It can be operated at pulse energies of several mJ/pulse. The CVL-MOPA schemes are used to further increase the pulse energies. Both the pump laser as well as tunable dye lasers are developed in-house as described in chapter-2. The CVLs are driven by solid state power supplies that utilize insulated gate bipolar transistors (IGBT) in place of costly high voltage hydrogen based thyratron switches and the indigenous ferrite cores based magnetic pulse compressors (MPC) to improve the desired jitter problem in output laser pulse [188]. In laser isotope separation, low jitter is required in order to synchronize the laser light pulses when CVL is operated in MOPA configuration. Poor jitter may affect the stability of laser output pulse energy. The CVL-MOPA used in the present study is operated at low jitter (± 2 ns) and delivers the high average power up to 45 W with ~ 1% stability.

Tunable dye laser-1 (an oscillator-amplifier) with an average high output power of 550 mW at 671 nm wavelength is developed for Li first-step resonant excitation. Its detailed description is given in chapter-2. In brief, a homemade flowing type of dye-cell [57] is used as described earlier. Same dye cells are utilized in both the dye laser-1 and dye laser-2 units. The dye cell has a provision to be pumped transversally from both the sides for strong pumping. The fluorescence emitted through its circular windows along the horizontal axis of dye cell resonates through the dye gain medium. The geometry of dye laser is kept simple with a pair of prism for beam expansion, plane reflecting mirror in combination with holographic grating (2400 l/mm) for tuning the laser and an output coupler. DCM dye in dimethyl sulfoxide (DMSO) solvent is used as gain medium in oscillator as well as amplifier to obtain a strong laser output at ~ 671 nm wavelength. This corresponds to Li first step resonant excitation. Dye concentration in oscillator and amplifier is optimised to 2.6 and 1.2 mM, respectively. The pump laser power for oscillator and amplifier are typically 3.5 W and 10 W of CVL radiation at 510.6 nm, respectively. Cylindrical lenses of short focal length (+ 10 cm) are used to focus the pump laser beam into oscillator as well as amplifier dye cells. The grating is aligned in grazing-incidence-grating (GIG) mode. The overall resonator length is kept short (~15 cm). The oscillator output power is optimized at ~ 671 nm wavelength within its tuning range 630-675 nm, by adjusting the dye concentration and optics alignment. The oscillator output is then focused by a large focal length spherical lens (f = + 50 cm) into the amplifier after spatial filtering through a small pinhole of size ~ 500 μm. This ensures the reduction in the amplified spontaneous emission (ASE). An average power of more than 550 mW is achieved at 671 nm. The bandwidth of dye laser-1 measured by wavelength meter (WS-7) is less than 2.5 GHz. On the same lines, second dye laser based on Rh-640 dye is developed for Li second-step resonant excitation. It has the parameters, ~ 2.5 GHz, 20 ns, 0.16 mM, ~ 150 mW, and 600-625 nm. This dye laser is pumped by the yellow component (578.2 nm) of CVL-MOPA. Such tunable dye lasers find the important applications in spectroscopy and photoionization experiments [189,190].

The TOF mass-spectrometer consist of a round (65 mm dia.) and thin stain less steel back plate followed by two extraction/acceleration grids made of electroformed fine nickel mesh with transmission greater than 90% and an ion-detector. These grids lies at s = 8 mm, (s + d) = 43 mm and (s + d + D) = 1243 mm distance apart from the back plate. A reasonably low pressure (~ 10^{-6} mbar) is produced in TOF vacuum chamber. This is connected with a 1.2 meter long field free flight tube. An effusive type of Li atomic beam source as described in chapter-2 is installed in vacuum chamber. Lithium atomic beam reaches the ionization/extraction region of mass-spectrometer. Here, the Li beam interacts nearly orthogonal with incident exciting and ionizing laser beams focused by the convex lenses of

20 and 50 cm focal length, respectively. As a result, lithium photo-ions are generated. An electric field of ~ 300 V/cm extracts these photo-ions in 8 mm small ionization region. The photo-ions are subsequently accelerated to high kinetic energy by an electric field of 450 V/cm applied in 35 mm long acceleration region (d). These ions then travel through 1.2 meter long field free flight region, where they get separated according to their mass to charge ratio (m/z). The produced ionic-charge are collected by ion detector (SJUTS, Channeltron). The detector operated in the linear region at 2 kV negative potential. The photo-ion current from detector is measured directly on digital oscilloscope. The photo-ion signal is optimised at an appropriate delay (2-5 ns) between the first (red) and second (yellow) resonant step excitation laser beams.

To reduce the Doppler broadening effects, a well collimated Li atomic beam is required. Detailed description of this set up is given in chapter-2. For good signal to noise ratio (S/N) of photoionization signal, the Li atom density in laser interaction region should be typically in the range of 10^8 to 10^{13} atoms/cm^3. The energy transfer effects due to collision between the atoms should be negligible. This set the upper limit of atom density. The lower limit of atom density is determined by the S/N ratio which in turn depends upon the atomic beam cross-section and the properties of detector, such as its angular acceptance, transmission and detection efficiency. In order to obtain the suitably high atom density, it is advantageous to position the oven orifice close to laser interaction point. However, this arrangement may lead to poor beam collimation. The increased spacing between oven and laser interaction region allows good collimation as well as reduce the detrimental effects, such as the thermal radiation, electric and magnetic stray fields generated by oven heating current. Therefore, oven is installed just beneath the ionization/extraction region of mass-spectrometer at an optimum distance around 50 mm. The Li atomic beam from oven is emitted through an exit hole of small (~ 1 mm) diameter. The quality of atomic beam produced is judged by the parameters, such as the rate of liberated Li atoms that effuse without collisions through oven exit hole and their transparent flow. The effusive rate at which material leaves the oven is calculated as 3.7 x 10^{16} atoms/sec at an average speed of 1.35 x 10^5 cm/sec. At an operating temperature 525 ^{0}C, the mean free path calculated by a relation [191] as,

$$L = \frac{7.321\, x\, 10^{-20}\, T}{\sigma P} \qquad (6.14)$$

is found much higher (L ≈ 24 cm) than oven exit hole (~ 1mm) diameter. This ensures the transparent outward flow of Li atoms from the oven. Here, T(k) is the temperature, P (mm of Hg) the vapour pressure and σ (cm^2) the collision cross-section of Li atoms. The selection of suitable exit hole diameter of oven and its operation in a regime where Knudsen number (K_n) is greater than unity, determines the degree of atomic beam directionality. The Knudsen number is defined as the ratio of mean free path to exit hole diameter.

In present experiment, atom density in interaction region is estimated from oven atomic gas temperature and corresponding Li vapor pressure curves readily available from literature. The small fluctuations in atomic beam flux are monitored using PID control of oven heating current to maintain its temperature. The stability of atomic beam in time and space are crucial for such experiments. These are ensured by taking few operational precautions, such as oven temperature should be raised slowly through small steps and for beam stability, the temperature equilibrium reached must be maintained for at least several hours. However, in initial stage the oven temperature is raised slightly in excess of required operating temperature, to avoid the spurious signals due to material oxidation. Especially, the new sample loaded has to be outgassed before reaching their temperature. Dramatic instabilities in atomic beam are observed during the initial melting and boiling of lithium along with ejection of few lumps of Li sample. The overlap of atomic beam, both in time and space, with interaction laser beams, are the main limiting factor that limits the efficiency of

TOFMS. In present experiment, the temporal overlap determined by an expression $F_t = d_L \nu_{rep}/\bar{\upsilon}$ gives a small fraction value $F_t = \sim 0.005$ for CVL pulse repetition rate $\nu_{rep} = 6.5$ kHz, average thermal speed of Li atoms $\bar{\upsilon} = 1.35 \times 10^5$ cm/sec and laser beam diameter $d_L \sim 1$ mm for working temperature of 525 ^{0}C. Similarly, spatial overlap is estimated by the fraction of atoms entering into interaction zone as $Fs \sim 0.012$, using a relation $Fs = (\kappa/\pi)\, \Delta\Omega$ described in details in chapter-2. Here, Fs denotes the atom fraction entering the interaction region within a solid angle $\Delta\Omega$ ($\Delta\Omega \leq 2\pi$) at $\theta \approx 0^0$ to the total number of atoms evaporated from source. The 'κ' term is related to the geometry of source [68]. The θ is the angle with limiting aperture symmetry axis. Thus, total fraction of evaporated atoms into interaction zone is found to be as $F_{tot} = Fs \times F_t \approx 5.7 \times 10^{-5}$. This leads to the overall atom density in laser interaction region within permissible limit of 2.1×10^{12} atoms/cm^3.

6.2.2 Three-color Li photoionization scheme

It is evident that there are different energy pathways to selectively photo-ionized Li isotopes. This process is multi-step. In the first stage, selective excitation of one or more intermediate atomic levels is carried out. In the next, the ionization of the excited atoms take place. This ionization can be accomplished with either an additional laser radiation, electric field or through collisions with other particles [185,186]. Two-step photoionization, is relatively straight forward, in absence of external fields and collisions. However in absence of auto-ionization levels, the selectivity remains limited [42,192]. This situation exist in lithium. Higher value of selectivity is feasible in multi-step resonant photoionization schemes. Here, number of steps involved are decided by two factors, 1) the ionization potential (I.P) of the element and 2) the photons energy of the laser radiation. Larger the number of resonant intermediate states, higher is selectivity of the process [193]. Also, selectivity of multistep photoionization process is limited by the resonant transfer of energy from excited atoms to unexcited ones [194]. This decrease in selectivity can be managed by limiting the atom density up to certain value ($\leq 10^{12}$ cm^{-3}) [193]. The resonance-ionization transitions and the available energy pathways, dictate the isotope selectivity and photoionization efficiency [186]. Other main factors which determine the isotope selectivity, are the transitions isotope-shift and hyperfine components. Theoretical isotope selectivity (S), is given by [186] as,

$$S = \left[\frac{2\Delta\nu}{\Gamma_{nat}}\right]^2 \tag{6.15}$$

here Γ_{nat} denotes the natural linewidth, $\Delta\nu$ the isotope-shift. The recipe to attain the higher selectivity, in photoionization schemes, is related with many characteristics. These are, large isotopic shift, small natural linewidth and non-overlapping hyperfine structure. Further, the reduced Doppler width may effectively enhance the selectivity of process. In the present case of Li, three step, three-color scheme is adopted. In such case, the resulting selectivity can be increase as given by the expression,

$$S = S_1.S_2.S_3 \tag{6.16}$$

where S_i is i_{th} step excitation selectivity. But, the overall selectivity will be smaller if the laser linewidth exceeds the linewidth of absorption transitions.

The spectral features of Li isotopes consists of doublets and hyperfine fine structures (HFS). This originates due to their non-zero nuclear spins. The presently used dye laser of linewidth ~ 2.5 GHz/ 0.08 cm^{-1} is not able to resolve the Li hyperfine lines. In terms of excitation wavelength, the separation between $^2S_{1/2} \rightarrow {}^2P_{1/2}$ (D_1 line) and $^2S_{1/2} \rightarrow {}^2P_{3/2}$ (D_2 line) of each isotope is $\Delta\lambda \sim 0.0158$ nm [37]. For resonance line at 670.78 nm, D_1 and D_2 line spacing, is close to its isotopic shift 0.0154 nm (~ 10.54 GHz) [88,195]. This implies that $^2S_{1/2} \rightarrow {}^2P_{1/2}$ transition of ^{7}Li nearly coincides with $^2S_{1/2} \rightarrow {}^2P_{3/2}$ transition of ^{6}Li. This demands for very good linewidth (< 1 GHz/ 0.33 cm^{-1}) of the dye laser. Then, only the Li isotopes can be selectively excited from ground state ($^2S_{1/2}$) to the doublets $^2P_{1/2}$ or $^2P_{3/2}$ level of each isotope. For large isotope separation factor, it is necessary to selectively excite each of the isotope, separately. This is possible with presently used dye laser by tuning its wavelength either to ^{7}Li ($^{2}S_{1/2} \rightarrow ^{2}P_{3/2}$) or ^{6}Li ($^{2}S_{1/2} \rightarrow ^{2}P_{1/2}$) resonance levels, having the large energy spacing with difference in their excitation wavelengths as $\Delta\lambda \sim 0.0315$ nm. The Li has moderate I.P ~ 5.39 eV [126] with energy of excitation for its 2p and 3d resonance states around 1.84 and 3.87 eV, respectively. Hence, the laser photons of wavelength shorter than 820 nm can ionize the Li atoms, present in excited 3d levels to its continuum.

In photoionization process, high laser power is generally required for obtaining high photo-ionization probability and all the laser beams are set to interact with the atoms simultaneously. The photoionization efficiency in most cases remains low leading to waste of laser power. In laser isotope separation, large photoionization efficiency at low laser powers are desirable [196]. There are few important considerations to achieve this. High oscillator strength, large absorption cross-section etc. ascertain the suitability of resonant atomic levels, to be utilized in highly efficient photoionization schemes [196,197]. With these factors in background a specific three-color, three-step photoionization scheme is adopted in the present research work. This scheme contains two resonance levels as shown in Fig. 6.10. For lithium, both for the first and second resonance transitions, the relevant parameters are well known and favorable. These are, the oscillator strength ($f_1 = 0.746$, $f_2 = 0.638$), lifetime ($\tau_1 = 27.1$ ns, $\tau_2 = 14.5$ ns) and absorption cross-section ($\sigma_{1,2} = 10^{-12}$ to 10^{-11} cm^{2}) [29,35,198]. Three-step photoionization scheme for ^{7}Li has an excitation process as, 2s $^{2}S_{1/2}$ (0 cm^{-1}) → 2p $^{2}P_{3/2}$ (14908.11 cm^{-1}) → 3d $^{2}D_{5/2}$ (31292.55 cm^{-1}). This is followed by a third color non-resonant ionization using a photon with energy >1.5 eV. In present experimental setup, this photon is directly obtained from yellow component (578.213 nm) of CVL. On the same line, for ^{6}Li, the excitation 2s $^{2}S_{1/2}$ (0 cm^{-1}) → 2p $^{2}P_{1/2}$ (14907.42 cm^{-1}) → 3d $^{2}D_{3/2}$ (31291.85 cm^{-1}) is utilized. This is followed by non-resonant photo-ionization using an extra photon of 578.213 nm. Strong saturation of each steps transition is required to achieve the high photoionization efficiency. The possibility to saturate the transitions with available laser power can be estimated by considering above mentioned parameters [35]. Only a few tens of mW of tunable dye lasers average power is needed to saturate the first and the second resonant transitions. However, the third step which is non-resonant, laser power ~ 5 W is required at 578.2 nm. Much higher laser powers can be used to increase the photoionization efficiency but at the cost of poor selectivity [192,194,196].

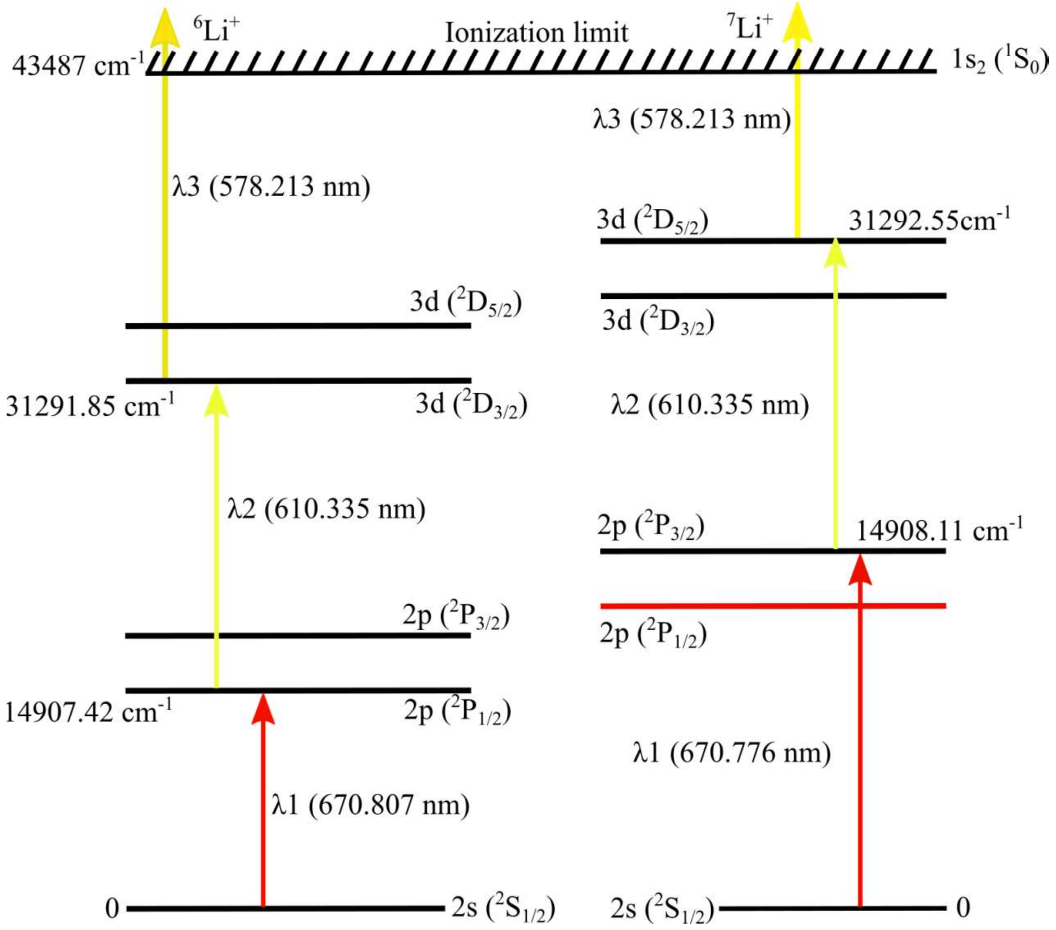

Fig. 6.10 Ionization pathways for three-color photoionization of Li isotopes

Kramer et al. [34] used two-color resonant ionization scheme for a detection of single Li atom. In present experiment, it is extended to three-color with two steps in resonance using the high repetition rate lasers. As per our knowledge, this scheme has not been explored earlier. The isotope shift for Li first and second resonant transitions are sufficiently large [126,195]. Therefore, the proposed three-color photoionization scheme is anticipated to yield high enrichment and large isotope separation factor. This scheme is implemented utilizing the dye lasers developed with moderate power at narrow spectral bandwidth (~ 2.5 GHz). The third and final step utilizes the non-selective non-resonant photoionization. Hence, no selectivity (S = 1) is expected in this step. As the experiment is carried out at suitably high Li atom density (~10^{12}) in laser interaction region [42] with kHz repetition rate of lasers, therefore high photoionization yield is expected.

6.2.3 Results on three-color, three-step photoionization

The atomic beam of naturally abundant Li isotopes produced, in vacuum chamber of TOFMS, is irradiated in sequence by 670.780 nm to populate the Li (2p) levels and then by suitably delayed (~5 ns) 610.335 nm radiation to reach the 3d levels. In this way population accumulated in 3d levels is finally photo-ionized by an extra photon of an energy with 578.213 nm radiation. The ions thus produced are detected by TOFMS as described in experimental section. A typical Li mass-spectrogram with it two isotopes (^{6}Li & ^{7}Li) using the discussed three-colour, three-step photoionization scheme is recorded (Fig. 6.11). Tuning the wavelength of dye laser-1 to first-step within 670.756 to 670.820 nm spectral range, we can excite the Li atoms of either one or both the isotopes, resulting in proportionate photo-ion current. When excitation wavelength (λ_1) to 1st resonance is scanned from 670.750 to 670.850 nm, with excitation wavelength (λ_2) to 2nd resonance being fixed at 610.335 nm, photo-ion signals of ^{6}Li & ^{7}Li with varying peak heights are observed. Maximum signal strength is obtained at the coincidence of excitation and absorption centres of Li. This is due to the fact that dye laser spectral width and transition absorption profile, which is a function of angular distribution of atom's velocity, are ~ 0.04 Å and 0.01Å, respectively.

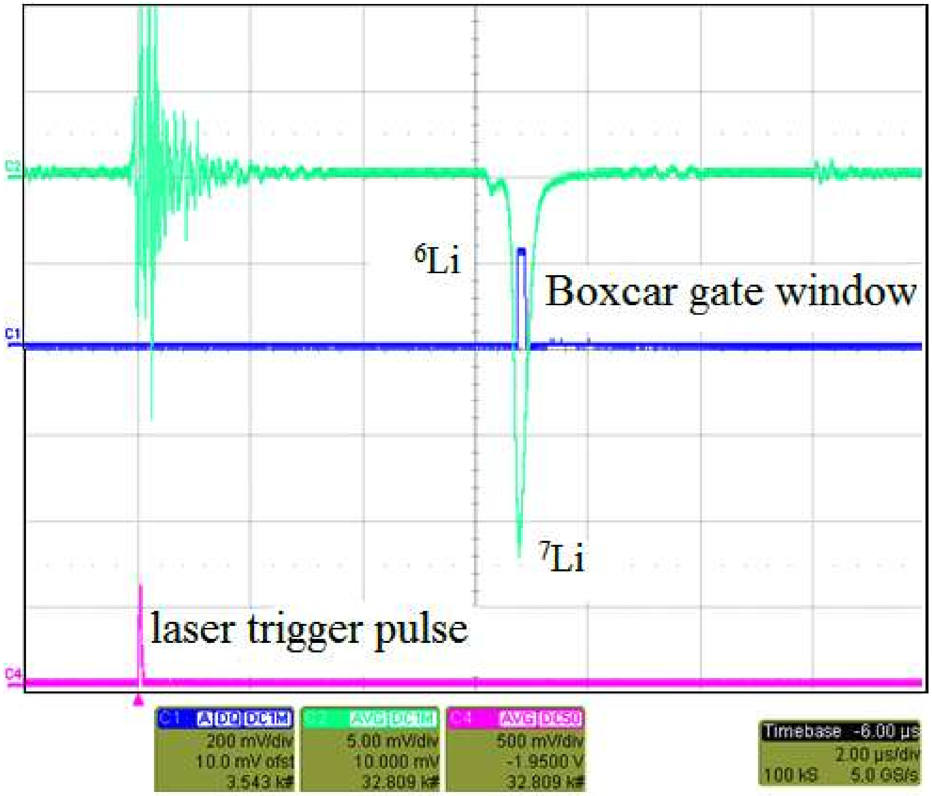

Fig. 6.11 Three-step isotope-selective photo-ionization of Li produced by TOFMS using three-color (λ_1: 670.765 nm, λ_2: 610.335 nm, λ_3: 578.213 nm)

Selected signal samples from recorded mass-spectrum, during dye laser wavelength scanning are shown in Fig. 6.12. This figure shows the effects of fine tuning of dye laser-1 on photo-ion signals. 1st Li transition ($^2S_{1/2} \rightarrow {}^2P_{1/2,3/2}$) is studied in spectral range, 670.756 to 670.820 nm. In this case, wavelength of dye laser-2 is fixed at 610.335 nm corresponding to 2nd Li transition $^2P_{1/2} \rightarrow {}^2D_{3/2,5/2}$ and non-resonant ionizing laser pulse at 578.213 nm wavelength is applied for 3rd step. The typical average powers used for different steps are as follows; P_1 = 42 mW, P_2 = 15 mW and P_3 = 6 W. The extreme high selectivity obtained for ^{7}Li, on tuning dye laser-1 to exciting radiation at 670.756 nm, leads to ~ 100% enrichment, see Fig. 6.12(a). On slight red detuning, an additional weak signal, just around 450 ns before the strong ^{7}Li ion-signal, appears at 670.792 nm excitation wavelength, see Fig. 6.12(b). This corresponds to ^{6}Li isotope. Further tuning to higher wavelengths side, the strength of ^{6}Li ion-signal increases. Finally it overtakes ^{7}Li signal significantly at 670.807 nm, as shown in Fig. 6.12(c). In this condition, a relative small peak of ^{7}Li isotope is also observed in addition to ^{6}Li, however only the ^{6}Li ($^2S_{1/2} \rightarrow {}^2P_{1/2}$) transition is possibly excited. Most likely, this is owing to the transition saturation broadening at high laser powers used in experiment. To investigate the facts, dye laser powers for 1st and 2nd resonant transitions, are reduced in steps gradually, see Figs. 8(d) to 8(f) using the neutral density filters.

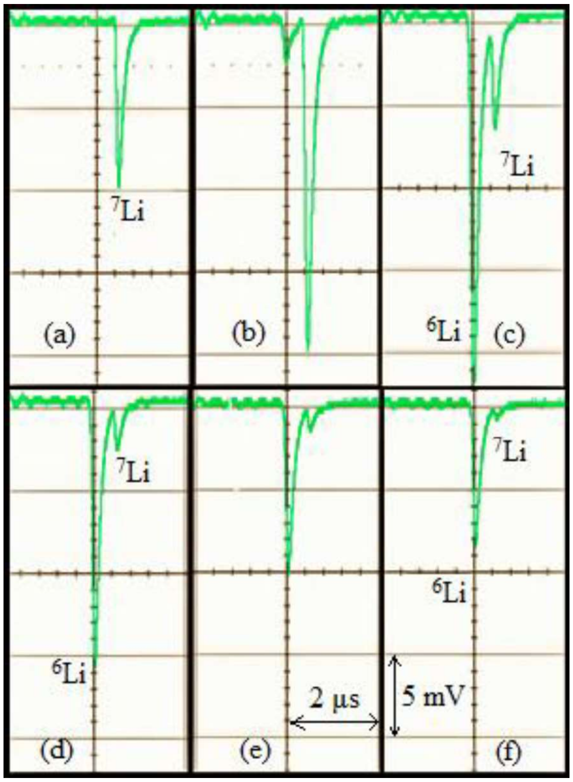

Fig. 6.12 Effect of precise tuning of dye laser-1 on Li three-color photoionization signal

The signals in Fig. 6.12(d) is recorded at (P_1: 20 mW, P_2: 15 mW, P_3: 6 W). In another set of experiment, further successive decrease in both the dye laser powers upto (P_1:

5.5 mW, P_2: 5.2 mW, P_3: 6 W) lead the strong ^{6}Li photo-ion signal only a very small trace of ^{7}Li, see Fig. 6.12(f). The possibility of resonant charge transfer [196] between the isotopes due to slightly high atom density in interaction region may be responsible for small ^{7}Li signal even at low incident laser powers. However, the results obtained clearly confirms that power or saturation broadening at high laser powers severely affects the selectivity of LIS process. At high laser power levels, although the yield of photoionization is higher but selectivity of process reduced significantly. In the pursued three-color photoionization scheme, an investigation is also made on the dependence of photo-ion signal on laser power for the first resonance excitation. The obtained results are shown for both the isotopes in Fig. 6.13. An uncertainty (± 5%) is observed in measurement of ion-signals due to pulse to pule variation (~ 3%) in laser powers.

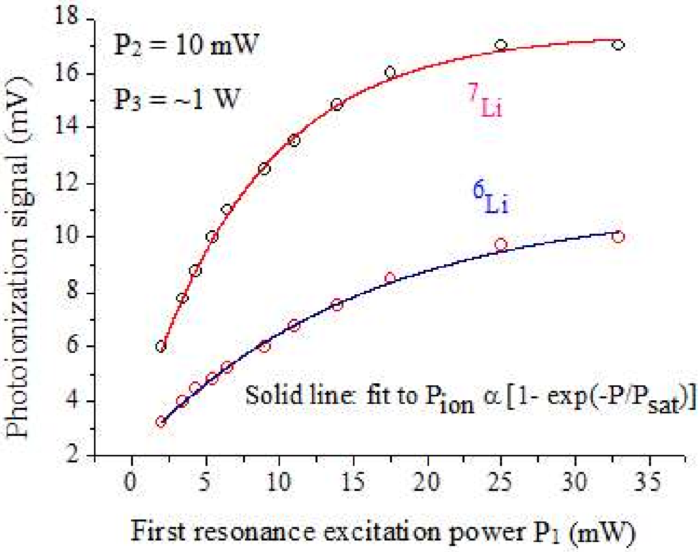

Fig. 6.13 Li photo-ion yield vs laser power for first step resonance transition

The analysis of saturation behaviour of the transition involved is also carried out. This is the study of respective photo-ion signals with increase in laser excitation powers. As the dye laser-1 power is enhanced, initially the ion-signal (for both the isotopes) increases exponentially. After that it undergoes saturation at higher laser power near to 20 mW. The governing relation is an exponential function given as,

$$P_{ion}\ \alpha\ [1- \exp(- P/P_{sat})] \qquad (6.17)$$

This relation closely fits the observed photo-ion signals. The change in ion-yield (P_{ion}) vs laser power curve slope indicate the saturation of resonance transition. The saturation value (P_{sat}) for both the isotopes ion signal for 1st resonance transition is found to be ~ 32 mW. Also, the similar study is performed for second step resonance transition (Fig. 6.14). In this study, the ion-signal for both the isotopes increase almost in linear fashion up to 8 mW. After that saturation sets in beyond 10 mW. Thus transition saturation is reached near 32 mW for first resonance transition. However, second resonance steps is reached at near 10 mW of laser power. The laser irradiation area is ~ 2 mm^2 in both the cases. Similar trends and values for Li isotopes were observed in Ref. [35, 42].

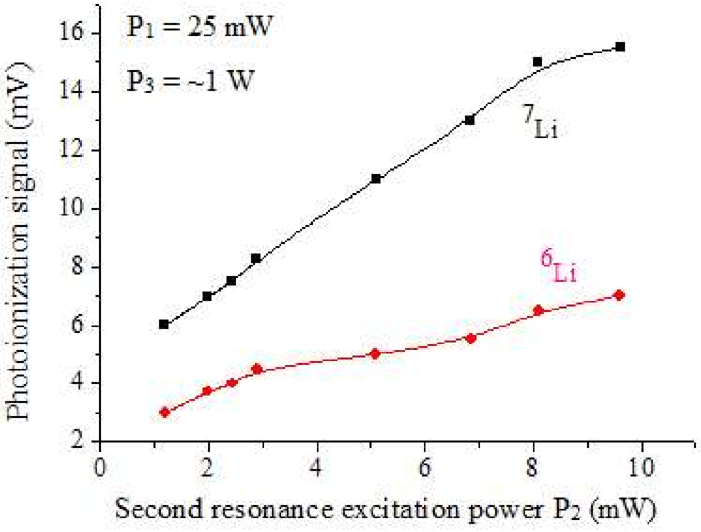

Fig. 6.14 Li photo-ion yield vs laser power for second step resonance transition

In a further continued study, involving the third non-resonant step, the laser power at 578.213 nm radiation is increased from 1 to 6 W. However, the dye laser power remained fixed at transition saturation level for both the first and second resonance steps. It is found that ion-signal strength increased almost linearly up to around 30 mV. Beyond laser power of 6 W, the ion-signal is nearly saturated. However, at still larger power (typ. ~ 14 Watts), the multi-photon ionization artefacts are visible on photo-ion signal. In this way, performance analysis of three-color photo-ionization can be carried out by studying the transition saturation in all the steps. Although, laser powers are optimized for the first, second and third steps to attain the large photoionization yield but at what cost?

For investigation of this issue, an experiment is carried out at two different dye laser excitation powers for the 1st and 2nd resonance steps, keeping the laser power fixed for third non-resonant step. In Fig. 6.15(a), the excitation frequency dependent ^{6}Li photo-ion signal profile is displayed by scanning the wavelength of dye laser-1 for 1st resonance transition. The laser power used are moderately high i.e. P_1= 22 mW, P_2 = 14 mW, P_3 = 6W and Li vapour temperature is 505 ^{0}C. In these conditions, the increase in homogeneous line broadening, arising from transition saturation effects, is given as,

$$\Delta\nu(\mathrm{fwhm}) = \Delta\nu_N \, (1 + I/Isat)^{1/2} \qquad (6.18)$$

Here, the saturation parameter S_0 (= I/Isat) compares the laser fluence with Isat. These values are related with average laser power P and Psat for constant laser focus irradiation area (~2 mm^2). Although line broadening effects due to both the first and second Li resonance steps are included in Δν parameter. The saturation parameter ($S_0 \sim 5.81 \times 10^6$) is evaluated using the natural linewidth ($A_{21} = 2\pi\Delta\nu_N$ = 5.89 MHz) for the 1st transition. This sets the lower limit on line broadening. At these power levels, overall isotope selectivity S (= 32.88) is measured as $[(^6Li/^7Li)_{product}/(^6Li/^7Li)_{feed}]$ from the recorded mass-spectrogram, see Fig. 6.15(b). It gives an enhancement factor of 72.72% for ^{6}Li, which is calculated as $[^6Li/ (^6Li+^7Li)] \times 100$.

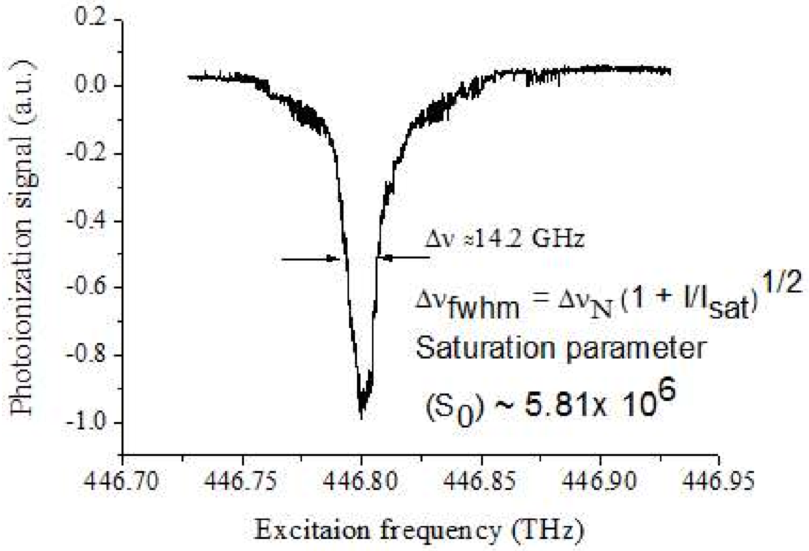

Fig. 6.15(a) First-step resonant frequency vs photoionization signal profile of ^{6}Li for laser powers (P_1: 22 mW, P_2: 14 mW, P_3: 6W)

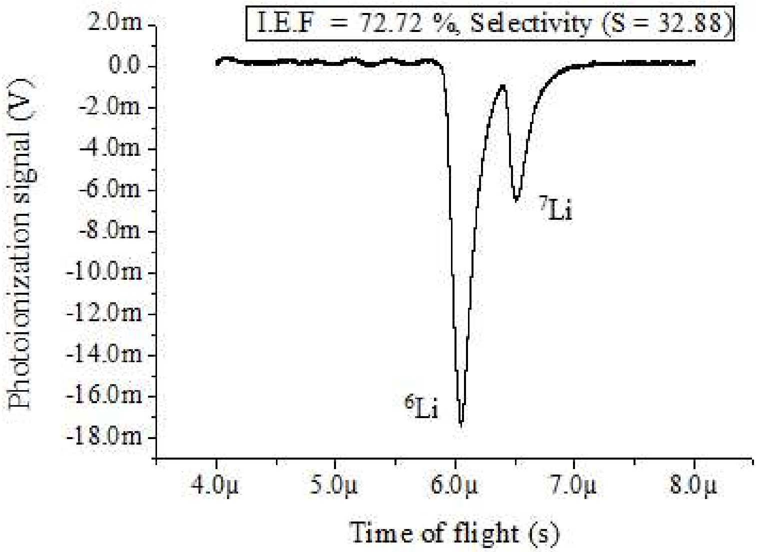

Fig. 6.15(b) Li isotopes distribution for laser powers (P_1: 22 mW, P_2: 14 mW, P_3: 6W)

When laser power of both the dye lasers are reduced considerably i.e. P_1= 5.5 mW, P_2= 5.2 mW, P_3= 6 W), the homogeneous line broadening is minimized up to Δv (fwhm) = 6.45 GHz. This reduced the saturation parameter S_0 value (= 1.2 x 10^6) by a large factor (~5). At reduced power levels (Fig. 6.16(b), the selectivity S (= 160.34) is increased significantly. Also, the isotope enhancement factor (I.E.F) of 92.86% is obtained for ^{6}Li. The present study clearly demonstrates that although the large laser power is favourable to high photoionization yield, however the selectivity is reduced considerably at high laser powers.

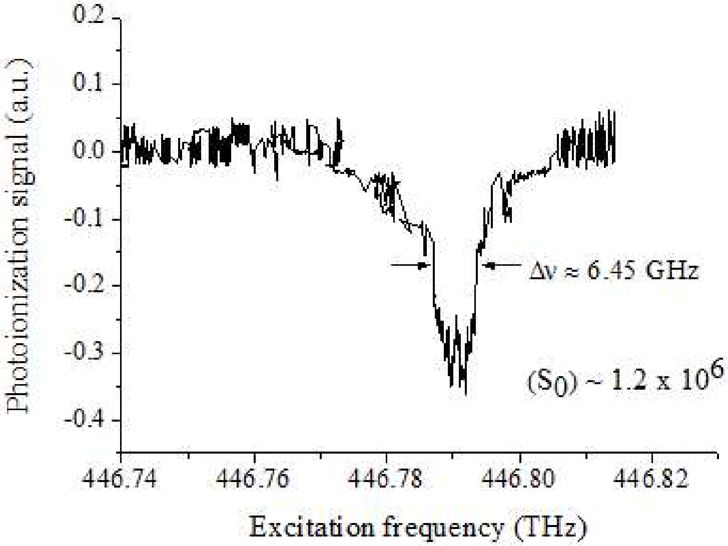

Fig. 6.16(a) First-step resonant frequency vs photoionization signal profile of ^{6}Li for laser powers (P_1: 5.5 mW, P_2: 5.2 mW, P_3: 6W)

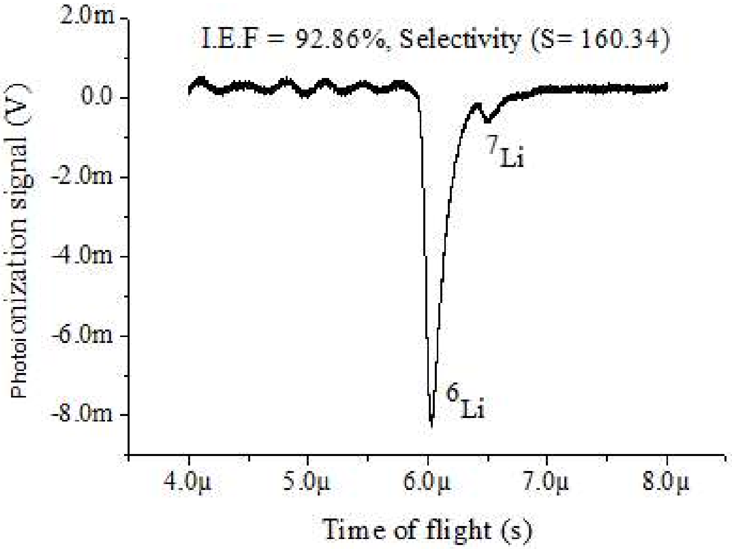

Fig. 6.16(b) Li isotopes distribution for laser powers (P_1: 5.5 mW, P_2: 5.2 mW, P_3: 6W)

This study infers that laser isotope enrichment by multistep selective-photoionization method is a convenient and cost-effective technique by which high selectivity and high enrichment can be ensured. The LIS technique may be applicable for other class of elements also [112, 192,196].

6.3 Conclusion

In summary, separation of Li isotopes by laser technique is demonstrated. In the whole research work, in-house built tunable dye lasers and time-of-flight mass-spectrometer are utilized. The developed TOFMS mass resolution (m/Δm) is around 24. The TOFMS is calibrated with non-resonant photoionization technique that ionizes both the isotopes as per their natural abundances. It provided the relative isotope composition of Li. The measured Li isotope ratio is ~ 0.080. This agreed well with its averaged natural abundance ratio (^{6}Li/^{7}Li: 7.5/92.5: 0.081). The major outcomes are, well resolved isotopic photo-ion signals and high selectivity (~ 32) for ^{6}Li. The developed photoionization setup produced large photo-ion signals for both the isotopes ^{6}Li & ^{7}Li, on the precise tuning of dye laser wavelength to their resonance levels. Simultaneous photoionization cross-section measurement for both Li isotopes and their quantitative isotope enrichment, are demonstrated at TOFMS detector. The Li isotopes photoionization cross-sections for 2p excited states are measured with good fidelity. These values are as ^{7}Li (18.62 ± 2.4 Mb) and ^{6}Li (15.53 ± 2.1 Mb). In addition, high photoionization yield and large isotope enhancement factor (~10 folds) is achieved. The study pointed out that the selected energy pathway through Li (2p) excited state, near the ionization threshold, is an efficient path to enrich the ^{6}Li isotope. Remarkable enhancement in natural abundance of Li isotopes by three-colour photoionization using the high repetition rate (~ 6.5 kHz) lasers and time-of-flight mass-spectrometer is also demonstrated. Performance of the proposed photoionization scheme is evaluated. It is learnt that photoionization yield and selectivity are the two important competing factors that ascertains the high enrichment factor. The selected three-color photoionization pathway $[{}^2S_{1/2} \rightarrow^{\sim} \xrightarrow{671\text{ nm}} {}^2P_{1/2,3/2} \rightarrow^{\sim} \xrightarrow{610\text{ nm}} {}^2D_{3/2,5/2} \xrightarrow{\sim 578\text{ nm}} {}^1S_0\ (\mathrm{Li}^+)]$ enabled the high photoionization yield and large isotope enhancement factor (I.E.F >12 fold). It is found that concentration of naturally less abundant ^{6}Li is enhanced upto over 92%. This is accomplished by the precise tuning dye lasers wavelength to 2p ($^2P_{1/2}$) and 3d ($^2D_{3/2}$) levels of ^{6}Li. High selectivity obtained for ^{7}Li isotope leads to its ~ 100% enrichment in optimum operating conditions.

References

[1] A. Klix, K. Ochiai, S. Sato, Y. Terada, Y. Morimoto, J. Hori, M. Yamauchi, M. Wada, T. Nishitani, “Blanket experiments using enriched Li_2TiO_3/Ferritic steel/Beryllium assemblies and D-T fusion neutrons,” J. Plasma Fusion Res. SERIES **5**, 565-569 (2002).

[2] T. Suzuki, Y. Tachibana, M. Nomura, Y. Fujii, “Lithium isotope separation using cation exchange resin and cross-linkage effect on isotope fractionation,” J Plasma Fusion Res Series **11**, 45-48 (2015).

[3] A. A. Palco, J. S. Drury, J. M. Begun, “Lithium isotope separation factors of some two-phase equilibrium systems,” J. Chem. Phys. **64**, 1828-1837 (1976).

[4] T. Hoshino, T. Terai, “High efficiency technology for lithium isotope separation using an ionic-liquid impregnated organic membrane,**”** Fusion Eng. and Design **86**, 2168-2171 (2011).

[5] J. R. Black, G. Umeda, B. Dunn, W. F. Mcdonough, A. Kavner, “Electrochemical isotope effect and lithium isotope separation,” J. Am. Chem. Soc. **131**, 9904-9905 (2009).

[6] C. Shi, Y. Jia, J. Xiao, X. Wang, Y. Yao, Y. Jing, “Lithium isotope separation by liquid-liquid extraction using ionic liquid system containing dibenzo-14- crown-4,” J. Mol. Liq. **224**, 662–667 (2016).

[7] S. Honda, K. Shin-Mura, K. Sasaki, “Lithium isotope enrichment by electrochemical pumping using solid lithium electrolytes,” J. Cer. Soc. Japan **126**, 331-335 (2018).

[8] F. M. Penning, “Demonstratie van ecn nieuw photoelectrisch effect,” Physica **8**, 137-140 (1928).

[9] B. Barbieri, N. Beverini, A. Sasso, “Optogalvanic spectroscopy,” Rev. Mod. Phys. **62**, 603-644 (1990).

[10] V. K. Saini, V. K. Shrivastava, R. Khare, “Anomalous behavior of optogalvanic signal in a miniature neon discharge lamp,” Opt. Comm. **281**, 129-134 (2008).

[11] R. Khare, V. K. Saini, V. K. Shrivastva, U. Nundy, "Observation of Penning ionization in Zr–Ne discharge by optogalvanic effect," Opt. Comm. **283**, 542-546 (2010).

[12] V. K. Saini, P. Kumar, S. K. Dixit, S. V. Nakhe, "Studies on pulsed optogalvanic effect in Eu/Ne hollow cathode discharge," Appl. Optics **53**, 4320-4326 (2014).

[13] G. Erez, S. Lavi, E. Miron, "A simplified theory of the optogalvanic effect," IEEE J. Quant. Elect. QE-**15**, 1328-1332 (1979).

[14] A. Ben-Amar, G. Erez, R. Schuker, "Pulsed resonant optogalvanic effect in neon discharges," Appl. Phys. **54**, 3688-3698 (1983).

[15] M. Broglia, F. Catoni, A. Montone, P. Zampetti, "Galvanic detection of laser photoionization in hollow-cathode discharges: Experimental and theoretical study," Phys. Rev. A **36**, 705-714 (1987).

[16] O. Axner, "Laser enhanced ionization spectroscopy," (Chalmers Press, Holland, 1987).

[17] R. A. Keller, B. E. Warner, E. F. Zalewski, P. Dyer, R. Engleman, Jr., B. A. Palmer, "The mechanism of the optoglvanic effect in hollow cathode discharge," J. Phys. (Paris) Colloques **44**, C-7, 23-33 (1983).

[18] D. Zhechev, V. I. Zhemenik, S. Tileva, G. V. Mishinsky, N. Pyrvanova, "A hollow cathode discharge modification as a source of sputtered atoms and their ions," Nucl. Inst. and Methods in Phys. Research, B **204**, 387-391 (2003).

[19] M. N. Reddy, "Laser optoglavanic spectroscopy: Experimental details and potential applications in R&D.," Defence Science Journal, **44**, 279-293 (1994).

[20] G. S. Hurst, V. S. Letokhov, "Resonant ionization spectroscopy," Physics Today **47**, 38-45 (1994).

[21] J. D. Fassett, J. C. Travis, "Analytical applications of resonance mass spectrometry (RIMS)", Spectrochimica Acta Part B: Atomic spectroscopy **43**, 1409-1422 (1988).

[22] J. P. Young, R. W. Shaw, D. H. Smith, "Resonance ionization mass spectrometry,"

Analytical Chemistry **61**, 1271A-1279A (2008).

[23] G. S. Hurst, M. G. Payne, S. D. Kramer, J. P. Young, “Resonance ionization spectroscopy and one-atom detection,” Revi. Mod. Phys. **51**, 767-819 (1979).

[24] A. P. Thorne, Spectrophysics (Chapman and Hall, London, 1988).

[25] M. Göppert-Mayer, “Über Elementarakte mit zwei Quanten-sprüngen,” Ann. Physik. **9**, 273-295 (1931).

[26] V. Hughes, L. Grabner, “Energy levels, selection rules, and line intensities for molecular beam electric resonance experiments with diatomic molecules,” Phys. Rev. **79**, 829-836 (1950).

[27] A. Thorne, U. Litzen and S. Johansson, Spectrophysics, principle and applications (Springer-Verlag, Berlin, 1999).

[28] M. Aymar, E. L. Koenig and F. C. Farnoux, “Theoretical investigation on photoionization from Rydberg states of lithium, sodium and potassium,” J. Phys. B: At. Mol. Phys. **9**, 1279-1291 (1976).

[29] Z. C. Yan, G. W. F. Drake, “Theoretical lithium 2 ^{2}S → 2 ^{2}P and 2 ^{2}P → 3 ^{2}D oscillator strengths,” Phys. Rev. A **52**, R4316-4319 (1995).

[30] Q. I. Yue-Ying, W. U. Yong, W. Jian-Guo, D. Pei-Zhu, “Calculations of Photo-Ionization Cross Sections for Lithium Atoms,” Chin. Phys. Lett. **25**, 3620-3623 (2008).

[31] M. Shimazu, Y. Takubo, Y. Maeda, “Selective two-step photoionization of lithium atoms,” Japan. J. Appl. Phys. **16**, 1275-1276 (1977).

[32] J. Lahiri, S. T. Manson, “Radiative recombination and excited-state photoionization of lithinm,” Phys. Rev. A **48**, 3674-3679 (1993).

[33] N. V. Karlov, B. B. Krynetskiĭ, V. A. Mishin, A. M. Prokhorov, “Selective atomic photoionization and its use in isotope separation and spectroscopy,” Sov. Phys. Usp. **22**, 220-235 (1979).

[34] S. D. Kramer, J. P. Young, G.S. Hurst, M.G. Payne, "Resonance ionization spectroscopy of lithium," Opt. Comm. **30**, 47-50 (1979).

[35] E. B. Saloman, "A resonance ionization spectroscopy/ resonance ionization mass spectrometry data service: IV-Data sheets for Be, In, Li, K, Rb, Ag, Ti and V and an update of the data sheet for Ni," Spectrochimica Acta. **48B**, 1139-1203 (1993).

[36] M. A. Baig, M. Akram, S. A. Bhatti, N. Ahmad, "Two-colour three photon resonance excitation spectra of lithium," J. Phys. B: At. Mol. Opt. Phys. **27**, L351-L357 (1994).

[37] I. E. Olivares, A. E. Durate, "Resonance ionization spectroscopy in a thermal lithium beam by means of diode lasers," Appl. Opt. **38**, 7481-7485 (1999).

[38] M. A. ul-Haq, S. Mahmood, M. Riaz, R. Ali, M. A. Baig, "On the first ionization potential of lithium," J. Phys. B: At. Mol. Opt. Phys. **38**, S77–S86 (2005).

[39] N. Amin, S. Mahmood, M. Saleem, M. A. Kalyar, M. A. Baig, "Photoionization cross-section measurements from the 2p, 3d and 3s excited states of lithium," Eur. Phys. J. D **40**, 331-337 (2006).

[40] A. M. Il'n, A. P. Moschevikin, A. D. Khakhaev, "Li isotopes photoionization in two-frequency laser field," Physcia Scripta **56**, 587-591 (1997).

[41] T. Arisawa, Y. Maruyama, Y. Suzuki, K. Shiba, "Lithium isotope separation by laser," Appl. Phys. B **28**, 73-76 (1982).

[42] M. Saleem, S. Hussain, M. Rafiq, M. A. Baig, "Laser isotope separation of lithium by two-step photoionization," J. Appl. Phys. **100**, 053111 (2006).

[43] C. E. Little, Metal vapor laser-Physics, engineering and applications (John Wiley & Sons Ltd, England, 1999).

[44] J. K. Mittal, P. K. Bhadani, B. Singh, L. Abhinandan, R. Bhatnagar, "Design and performance of a 20 watt copper vapour laser," J. Phys. E **21**, 388-392 (1988).

[45] C. Yamanaka, E. Fujiwara, T. Naka, T. Takeda, T. Yamanaka, C. Yamanaka, "Technology reports of the Osaka University," **36**, 353 (1986).

[46] T. C. Wang, C. V. Yang, W. S. Lee, Y. Y. Hwang, M. W. Shea, F. B. Luoh, C. H. Chen, M. Chen, H. H. Luo., "A 25-W longitudinal, discharge-heated copper vapor laser," Rev. Sci. Instrum. **60**, 3351-3352 (1989).

[47] R. K. Mishra, S. V. Nakhe, G. N. Tiwari, J. K. Mittal, "Development of insulated gate bipolar transistor-based power supply for elemental copper vapor laser," Pramana - J. Phys.**75**, 967-973 (2010).

[48] R. Hargrove, R. Grove, T. Kan, "Copper vapor laser unstable resonator oscillator and oscillator-amplifier characteristics," IEEE Jour. of Quant. Elect. **15**, 1228-1233 (1979).

[49] N. A. Lyabin, V. V. Zubov, A. D. Chursin, "Active element utilizing copper vapor for high-power master-oscillator-amplifier laser systems," Sov. J. Quant. Electron. **20**, 20-23 (1990).

[50] J. J. Chang, "Time-resolved beam-quality characterization of copper vapor lasers with unstable resonators," App. Opt. **33**, 2255-2265 (1994).

[51] D. W. Coutts, "Time-resolved beam divergence from a copper vapor laser with unstable resonator," IEEE J. Quant. Electron. QE**-31**, 330-342 (1995).

[52] O. Prakash, S. K. Dixit, R. Bhatnagar, "On the role of the coherence width and its evolution in a short-pulse fundamental beam in second harmonic generation from beta-barium borate," IEEE J. Quant. Electron. **38**, 603-613 (2002).

[53] P. P. Sorokin, J. R. Lankard, "Stimulated emission observed from an organic dye, chloroaluminum phthalocyanine," IBM Journal of Res. and Development **10**, 162-163 (1966).

[54] Dye laser principles with applications, ed. by F. J. Durate, L.W. Hillman (Academic Press Inc., New York 1990) chap 4-6.

[55] F. J. Duarte, J. A. Piper, “A double-prism beam expander for pulsed dye lasers,” Optics Comm. **35**, 100-104 (1980).

[56] T. W. Hensch, “Repetitively pulsed tunable dye laser for high resolution spectroscopy,” Appl. Optics **11**, 895-898 (1972).

[57] J. Kumar, P. Shukla, U. Kumbhkar, O. Prakash, R. Khare, S. K. Dixit, J. K. Mittal, “Design & development of a flowing dye-cell and its performance evaluation in a dye laser oscillator pumped by a copper-vapor laser,” National laser symposium-09 (BARC Mumbai, 2010).

[58] M. G. Littman, H. J. Metcalf, “Spectrally narrow pulsed dye laser without beam expander,” Appl. Opt. **17**, 2224–2227 (1978).

[59] R. Beigang, W. Makat, A. Timmermann, “A thermionic ring diode for high resolution Rydberg state spectroscopy,” Opt. Comm. **49**, 253-257 (1984).

[60] S. Dushman, “Thermionic emission,” Rev. Mod. Phys. **2**, 381-476 (1930).

[61] I. Langmuir, **“**The effect of space charge and initial velocities on the potential distribution and thermionic current between parallel plane electrodes,” Phys. Rev. **21** 419-435 (1923).

[62] W. E. Stephens, “A pulsed mass spectrometer with time dispersion,” Phys. Rev. **69,** 691 (1946).

[63] W. C. Wiley, I. H. McLaren, “Time-of-Flight Mass Spectrometer with Improved Resolution,” Rev. Sc. Instr. **26**, 1150-1157 (1955).

[64] R. J. Cotter, “Time-of-flight mass spectrometry for the structural analysis of biological molecules,” Anal. Chem. **64**, 1027A–1039A (1992).

[65] M. Guilhaus, “Principles and instrumentation in time-of-flight mass spectrometry,” J. Mass Spectrometry **30**, 1519-1532 (1995).

[66] B. A. Mamyrin, "Time-of-Flight Mass Spectrometry (Concepts, achievements, and prospects)," International Journal of Mass Spectrometry **206**, 251-266 (2001).

[67] S. Talwar, V. V. V. Subrahmanyam, V. K. Saini, K. K. Sarangpani, S. V. Nakhe, "Development of time of flight mass-spectrometer for studies on lithium isotopes," Adv. Sci. Lett. **21**, 2556-2560 (2015).

[68] N. Ramsey, Molecular beams (Oxford Univ. Press, London, 1969).

[69] S. M. Rossnagel, J. J. Coumo, W. D. Westwood, ed. Handbook of plasma processing technology (Noyes Publication, Park Ridge, New Jersey, 1990).

[70] S. Caroli, O. Senofonte, *Glow discharge spectroscopies*, edited by R. K. Marcus (Plenum Press, New York, 1993), Chap 6.

[71] S. Levesque, F. Babin, J. M. Gagne, "Calibration of pulsed laser wavelength by optogalvanic spectroscopy in hollow cathode discharges," IEEE Transactions on Instr. and Meas. **42**, 251-254 (1993).

[72] Y. Oki, T. Izuha, M.Maeda, C. Honda, Y. Hasegawa, H. Futami, J. Izumi, K. Matsuda, "Optogalvanic wavelength calibrator for an automatic tunable laser system," Jpn. J. Appl. Phys. **30**, L1744-L1746 (1991).

[73] N. J. Dovichi, D. S. Moore, R. A. Keller, "Use of the optogalvanic effect and the uranium atlas for wavelength calibration of pulsed lasers," Appl. Opt. **21**, 1468-1473 (1982).

[74] W. DeGraffenereid, C. J. Sansonetti, "Reference lines in the optogalvanic spectra of uranium and thorium over the wavelength range 694–755 nm," J. Opt. Soc. Am. B **19**, 1711-1715 (2002).

[75] S. Yamaguchi, M. Suzuki, "Simultaneous stabilization of the frequency and power of an AlGaAs semiconductor laser by use of the optogalvanic effect of krypton," IEEE J. Quant. Elect. **19**, 1514-1519 (1983).

[76] V. K. Saini, P. Kumar, S. K. Dixit, S. V. Nakhe, “Studies on laser-assisted Penning ionization by the optogalvanic effect in Ne/Eu hollow cathode discharge,” Appl. Opt. **54**, 595-602 (2015).

[77] P. Bueno, A. R. Victor, J. R. D. Santos, L. F. N Barreta, M. G. Destro, M. E. Sbampato, J. W. Neri, C. A. B. Silveira, “Spectroscopic studies of neutral erbium in a hollow cathode lamp: Electronic temperature and two-step optogalvanic spectroscopy,” Spectrochemica Acta Part B: Atomic Spectroscopy **118,** 14-19 (2016).

[78] M. H. Begemann, R. J. Saykally, “Color center laser optogalvanic spectroscopy of lithium, barium, neon and argon Rydberg states in hollow cathode discharges,” Opt. Comm. **40**, 277-282 (1982).

[79] Z. Yuan, H. Zhang, R. Ye, J. Zhou, Y. Wei, Q. Lou, “Wavelength calibration of narrowband ArF laser with iron hollow cathode lamp,” Chin. Opt. Lett. **15**, 071402 (2017).

[80] R. B. Green, R. A. Keller, G. C. Luther, P. K. Schenck, J. C. Travis, “Galvanic detection of optical absorptions in a gas discharge,” Appl. Phys. Lett. **29**, 727-729 (1976).

[81] P. Kumar, J. Kumar, O. Prakash, V. K. Saini, S. K. Dixit, S. V. Nakhe, “Studies on the optogalvanic effect and isotope-selective excitation of ytterbium in a hollow cathode discharge lamp using a pulsed dye laser,” Appl. Spectroscopy **67**, 1036-1041 (2013).

[82] V. K. Saini, “Laser-induced optogalvanic signal oscillations in miniature neon glow discharge plasma, “Appl. Opt. **52**, 4404-4411 (2013).

[83] A. Mokhariwale, S. K. Agrawal, V. K. Saini, S. V. Nakhe, “Wavelength scanner for precision tuning of pulsed dye laser,” J. Instrum. Soc. India **43**, 5-6 (2013).

[84] J. E. Sansonetti, W. C. Martin, Handbook of Basic Atomic Spectroscopic Data, J. Phys. Chem. Ref. Data **34**, 1559-2259 (2005).

[85] B. N. Chapman, Glow Discharge Processes: Sputtering and Plasma Etching (Wiley, New York, 1980).

[86] N. Bundaleska, Z.Tomova, V. Steflekova, D.Zhechev, "Ion sputtering of cathode surface in a hollow cathode discharge," Vacuum **82**, 455-458 (2008).

[87] G. Erez, S. Lavi, E. Miron, "A simplified theory of the optogalvanic effect," IEEE J. Quant. Elect. QE-**15**, 1328-1332 (1979).

[88] P. Kumar, V. K. Saini, G. S. Purbia, O. Prakash, S. K. Dixit, S. V. Nakhe, 'Saturation absorption spectroscopy of lithium in hollow cathode lamp," Adv. Sci. Lett. **21**, 2548-2550 (2015).

[89] G. Racah, "On a new type of vector coupling in complex spectra," Phys Rev. **61**, 537-537 (1942).

[90] NIST Atomic Spectra Database (ver. 5.3), Online available: http://physics.nist.gov/asd for atomic transitions and emission line intensity.

[91] K. C. Smyth, P. K. Schenck, "Opto-galvanic spectroscopy of a neon discharge: Mechanism studies," Chem. Phys. Lett. **55**, 466-472 (1978).

[92] X. L. Han, M. C. Blosser, P. Misra, C. Haridass, "Abrupt changes in neon discharge plasma detected via the optogalvanic effect," Thin Solid Films **521**, 155-157 (2012).

[93] R. Shuker, A. Ben-Amar, G. Erez, "Optogalvanic spectroscopy of quasi-resonant Penning ionization," J. Appl. Phys. **54**, 5685-5690 (1983).

[94] R. Shuker, A. Ben Amar, G. Erez, "Inverted population observation using pulsed optogalvanic effect," Opt. Comm. **42**, 29-33 (1982).

[95] R. A. Keller, R. Engleman, Jr., B. A. Palmer, "Atlas for optogalvanic wavelength calibration," Appl. Opt. **19**, 836-837 (1980).

[96] J. R. Nestor, "Optogalvanic spectra of neon and argon in glow discharge lamps," Appl. Opt. **21**, 4154-4157 (1982).

[97] X. Zhu, A.H. Nur, P. Misra, "Laser optogalvanic wavelength calibration with a commercial hollow cathode iron-neon discharge lamp,"J. Quant. Spectroc. Radiat. Transfer. **2**, 167-177 (1994).

[98] K. C. Smyth, R. A. Keller, F. F. Crim, "Photon-induced ionization changes in a neon discharge," Chem. Phy. Lett. **55**, 473-477 (1978).

[99] A. Mirage, A. Scalabrin, D. Pereira, N. D. Vieira Jr., "Population inversion measurements in a hollow-cathode discharge by optogalvanic spectroscopy," Optics Comm. **129**, 358-360 (1996).

[100] R. Shuker, A. Gallagher, A.V. Phelps, "Models of high-power discharges for metal-Xe excimer lasers,' J. Appl. Phys. **51**, 1306-1320 (1980).

[101] W. R. Bennet Jr., P. J. Kindlmann, "Radiative and collision-induced relaxation of atomic states in the $2p^5 3p$ configuration of neon," Phys. Rev. **149**, 38-51 (1966).

[102] A. A. Radzig, B. M. Simrnov, Reference Data on Atoms, Molecules and Ions, (Springer, New York, 1985).

[103] A. M. Frolov, "On the hyperfine structures of the ground state (s) in the ^{6}Li and ^{7}Li atoms," JETP Letters **103**, 739–742 (2016).

[104] F. C. Cruz, A. Mirage, A. Scalabrin, D Pereira, "Optogalvanic sub-Doppler spectroscopy in titanium," J. Phys. B: At. Mol. Opt. Phys. **27**, 5851-5861 (1994).

[105] D. Das, V. Natrajan, "High-precision measurement of hyperfine structure in the D lines of alkali atoms," J. Phys. B: At. Mol. Opt. Phys. **41**, 035001 (1-12) (2008).

[106] D. K. Doughty, S. Salih, J. E. Lawler, "Two-step optogalvanic effect using intersecting laser beams: a pinpoint discharge diagnostic," Phys. Lett. **103A**, 41-44 (1984).

[107] F. Babin, J. M. Gagne, "Hollow cathode discharge (HCD) dark space diagnostics with laser photoionization and galvanic detection," Appl. Phys. B **54**, 35-45 (1992).

[108] M. Broglia, F. Catoni, A. Montone, P. Zampetti, “Galvanic detection of laser photoionization in hollow-cathode discharges: Experimental and theoretical study,” Phys. Rev. **36**, 705-714 (1987).

[109] G. Stockhausen, W. Mende, M. Kock, “Laser-induced photoionization in the dark space of a hollow cathode,” J. Phys. B: At. Mol. Opt. Phys. **29**, 665-675 (1996).

[110] V. Dev, M. L. Shah, A. K. Pulhani, B. M. Suri, “Two-color photoionization spectroscopy of uranium in a U–Ne hollow cathode discharge tube,” Appl. Phys. B **80**, 587-594 (2005).

[111] M. Saleem, N. Amin, H. Hussain, M. Rafiq, S. Mahmood, M. A. Baig, “Alternate technique for simultaneous measurement of photoionization cross-section of isotopes by TOF mass spectrometer,” Eur. Phys. J. D **38**, 277-283 (2006).

[112] R. Cong, Yi. Cheng, J. Yang, J. Fan, G. Yao, X. Ji, X. Zheng, Z. Cui, “Measurement of photoionization cross sections of the excited states of titanium, cobalt and nickel,” J. App. Phys. **106**, 013103 (1-6) (2009).

[113] Y. Maruyama, Y. Suzuki, T. Arisawa, K. Shiba, “Laser isotope separation of titanium by two-step photoionization,” Appl. Phys. B **44**, 163-166 (1987).

[114] I. E. Olivares, A. E. Duarte, E. A. Saravia, F. J. Duarte, “Lithium isotope separation with tunable diode lasers,” Appl. Opt. **41**, 2973-2977 (2002).

[115] W. Mende and M. Kock, “Oscillator strengths of Ba I and Sr I Rydberg transitions,” J. Phys. B: At. Mol. Opt. Phys. **29**, 655–663 (1996).

[116] R. V. Ambartzumian, N. P. Furzikov, V. S. Letokhov, A. A. Puretsky, “Measuring photoionization cross-sections of excited atomic states,” Appl. Phys. **9**, 335-337 (1976).

[117] M. Shimazu, Y. Takubo, Y. Maeda, “Selective two-step photoionization of lithium atoms,” Japan. J. Appl. Phys. **16**, 1275-1276 (1977).

[118] S. Levesque, J. M. Gagne, F. Babin, “Optogalvanic photoionization spectroscopy,” J. Phys. B: At. Mol. Opt. Phys. **30**, 1331-1346 (1997).

[119] B. B. Rossi, H. H. Staub, Ionization chambers and counters (McGraw-Hill, New York, 1949), pp. 20-71.

[120] F. Babin, J. M. Gagne, “Characterization of an atom beam produced with the help of a hollow cathode discharge,” Rev. Sc. Instrum. **57**, 1536-1541 (1986).

[121] J. Alessi, E. Beebe, C. Carlson, D. McCafferty, A. Pikin, J. Ritter, “A hollow cathode ion source for production of primary ions for the BNL electron beam ion source,” Rev. Sci. Instrum. **85**, 02C107 (1-3) (2014).

[122] D. Carazzato, M. J. Bertrand, “Characterization of a glow discharge ion source for the mass spectrometric analysis of organic compounds,” J. Am. Soc. Mass Spectrom. **5**, 305-315 (1994).

[123] D. Scarpa, A. Barzakh, D. Fedorov, A. Andrighetto, E. Mariotti, P. Nicolosi, A. Tomaselli, “First results on Ge resonant laser photoionization in hollow cathode lamp,” Rev. Sci. Instr. **87**, 02B708 (1-3) (2016).

[124] L. Sottili, D. Scarpa, E. Mariotti, P. Nicolosi, A. Tomaselli, A. Monetti, A. Andrighetto, S. Corradetti, F. Borgna, M. Manzolaro, M. Lollo, M. Rossignoli, R. Silingardi, A. Mozzi, E. Boratto, M. Ballan, G. Vivian, N. Sattin, L. Martin, D. Conventi, G. Prete, L. Biasetto, R. Oboe, G. Meneghetti, P. Colombo, M. Guerzoni, R. Michinelli, A. Margotti, I. Cristofolini, M. Ferrari, A. Zenoni, “First measurements of laser photoionization on Sn atoms in a time of flight mass spectrometer at SPES laser laboratory,” SPES: Project study of an advanced facility for exotic beams at LNL, LNL-INFN (REP) **145/99**.

[125] L. Windholz, C. Umfer, “Measurement of the transition wavelengths of the lithium resonance lines,” Z. Phys. D **29**, 121-123 (1994).

[126] G. Herzberg: Atomic Spectra and Atomic Structure, (Dover Publications, Inc., New York, 1994).

[127] C. J. Sansonetti, B. Richou, R. Engleman Jr, and L. J. Radziemski, “Measurements of the resonance lines of ^{6}Li and ^{7}Li by Doppler-free frequency modulation spectroscopy,” Phys. Rev. A **52**, 2682-2688 (1995).

[128] V. K. Saini, P. Kumar, K. K. Sarangpani, S. K. Dixit, L. Abhinandan, S. V. Nakhe, “Studies on pulsed and CW optogalvanic effects in in-house developed see-through lithium hollow cathode,” Adv. Sci. Lett. **21**, 2609-2612 (2015).

[129] D. E. Rothe, “Radiative electron-ion recombination into the first excited state of lithium,” J. Quant. Spectrosc. Radiat. Transfer **11**, 355-365 (1971).

[130] N. V. Karlov, B. B. Krynetskii, O. M. Stelmakh, “Measurement of the photoionization cross section of the Li atom at the 2P level,” Sov. J. Quantum Electron. **7**, 1305-1306 (1977).

[131] C. E. Burkhardt, J. L. Libbert, J. Xu, J. J. Leventhal, “Absolute measurement of photoionization cross sections of excited atoms: Application to determination of atomic beam densities,” Phys. Rev. A **38**, 5949-5952 (1988).

[132] V. Wippel, C. Binder, W. Huber, L. Windholz, M. Allegrini, F. Fuso, E. Arimondo, “Photoionization cross-sections of the first excited states of sodium and lithium in a magneto-optical trap,” Eur. Phys. J. D **17**, 285-291 (2001).

[133] G. S. Hurst, M. H. Nayfeh, J. P. Young, ‘A demonstration of one-atom detection,” Appl. Phys. Lett. **30**, 229-231 1977.

[134] A. R. Victor, M. G. Destro, M. E. Sbampato, J. W. Neri, C. A. B. Silveira, A. C. Oliveira, N. A. S. Rodrigues, “Neodymium two-step optogalvanic spectroscopy in a hollow cathode lamp,” Spectrochemica Acta Part B **66**, 748-753 (2011).

[135] W. I. McAlexander, E. R. I. Abraham, R. G. Hulet, Radiative lifetime of the 2P state of lithium,” Phy. Rev. A **54**, R5-R8 (1996).

[136] R. A. Keller, B. E. warner, E. F. zalewski, P. Dyer, R. Engleman, Jr., B.A. Palmer, “The mechanism of the optogalvanic effect in a hollow-cathode discharge,” J. De Phys. Coll. **C7-44, C7-23** (1983).

[137] K. C. Harvey, “Shielded thermionic diode detector for precision spectroscopy,” Rev. Sci. Instrum. **52**, 204-206 (1981).

[138] D. C. Thompson, B. P. Stoicheff, “Study of the characteristics of thermionic ionization detectors,” Rev. Sci. Instrum. **53**, 822-828 (1982).

[139] K. Niemax, C. J. Lorenzen, “The thermionic double-diode, an efficient detector in excited state laser spectroscopy,” Opt. Comm. **44**, 165-169 (1982).

[140] R. Beigang, W. Makat, A. Timmermann, “A thermionic ring diode for high resolution Rydberg state spectroscopy,” Opt. Comm. **49**, 253-257 (1984).

[141] K. Niemax, “Spectroscopy using thermionic diode detectors,” Appl. Phys. B **38**, 147-57(1985).

[142] P. P. Herrmann, N. Schlumpf, V. L. Telegdi, “A. Weis, Design, performance, and theory of long thermionic diodes,” Rev. Sci. Instrum. **62**, 609-623 (1991).

[143] J. Franzke, D. Veza, K. Niemax, “An improved thermionic diode detector for analytical laser spectroscopy,” Spectrochimica Acta Part B: Atomic Spectroscopy **47B**, 593-599 (1992).

[144] T. Chin-Chun, T. B. Jhon, C. S. William, “Shielded cylindrical space-charge-limited diode ionization detector,” Rev. Sci. Instrum. **63**, 5576-5581 (1992).

[145] K. K. Kingdon, “A method for the neutralization of electron space charge by positive ionization at very low Gas pressures,” Phys. Rev. **21**, 408-418 (1923).

[146] F. L. Mohler, P. D. Foote, “Photo-electric ionization of caesium vapour,” Phys. Rev. **26**, 195-207 (1925).

[147] D. Popescu, C. B. Collins, B. W. Johnson, I. Popescu, “Multiphoton excitation and ionization of atomic cesium with a tunable dye laser,” Phys. Rev. A **9**, 1182-1187 (1974).

[148] M. E. Koch, C. B. Collins, "Space-charge ion detection of multiphoton absorption phenomena in lithium vapor," Phys. Rev. A **19**, 1098-1105 (1979).

[149] A. Kallenbach, M. Kock, G. Zierer, "Absolute cross sections for photoionization of laser-excited BaI states measured on a thermionic diode," Phys. Rev. A **38**, 2356-2360 (1988).

[150] S. Shahzada, P. Ijaz, M. Shah, S.U. Haq, M. Ahmed, A. Nadeem, "Photoionization studies from the 3p ^{2}P excited state of neutral lithium," J. Opt. Soc. Am. B **29,** 3386-3392 (2012).

[151] A. Nadeem, M. Shah, S. Shahzada, M. Ahmed, S. U. Haq, "Spectroscopic investigation of the odd-parity 3d ^{2}D → nf ^{2}F transitions of neutral sodium, J. Appl. Spectroscopy **82**, 719-725 (2015).

[152] M. W. McGeoch, R. E. Schlier, G. K. Chawla, "Associative Ionization with Cold Rydberg Lithium," Atoms Phys. Rev. Lett. **61**, 2088-2091 (1988).

[153] M. P. A. Jones, L. G. Marcassa, J. P. Shaffer, "Special issue on Rydberg atom physics," J. Phys. B: At. Mol. Opt. Phys. **50**, 060202 (1-7) (2017).

[154] L. A. Bloomfield, H. Gerhardt, T. W. Hansch, "Ultraviolet-infrared double-resonance laser spectroscopy of nd (n =12→17) Rydberg states in He," Phys. Rev. A **27**, 850-856 (1983).

[155] J. Neukammer, H. Rinneberg, "Optical-optical double resonance in barium," J. Phys. B: At. Mol. Phys. **15**, 2899-2910 (1982).

[156] K. C. Harvey, B. P. Stoicheff, "Fine structure of the n^{2}D series in rubidium near the ionization limit," Phys. Rev. Lett. **38**, 537-540 (1977).

[157] R. Beigang, E. Matthias, A. Timmermann, "Influence of singlet-triplet mixing on the hyperfine structure of 5snd Rydberg states in ^{87}Sr," Phys. Rev. Lett. **47**, 326-329 (1981).

[158] S. G. Nakhate, M. A. N. Razvi, S. A. Ahmad, "New odd-parity energy levels of europium atoms in the 43 200-45 000 cm^{-1} region by laser photoionization spectroscopy," J. Phys. B: At. Mol. Opt. Phys. **33**, 191-200 (2000).

[159] S. G. Nakhate, M. A. N. Razvi, J. P. Connerade, S. A. Ahmad, "Investigation of Rydberg states of the europium atom using resonance ionization spectroscopy," J. Phys. B: At. Mol. Opt. Phys. **33**, 5191-5202 (2000).

[160] C. R. Vidal, J. Cooper, "Heat-Pipe Oven: A new well-defined metal vapor device for spectroscopic measurements," J. Appl. Phys. **40**, 3370-3374 (1969).

[161] M. M. Hessel, P. Jankowski, "Two-Metal heat-pipe oven: Operation, dynamics, and use in spectroscopic investigations," J. Appl. Phys. **43**, 209-211 (1972).

[162] H. Dennis, D. Mark, T. Erik, L. Casey, E. M. Richard, M. F. Mark, "Construction of a heat pipe oven on a small budget," Am. J. Phys. **65**, 1017-1022 (1997).

[163] H. B. Michaelson, "Work functions of the elements," J. Appl. Phys. **21**, 536-540 (1950).

[164] G. C. Tisone, P. J. Hargis Jr., "Laser absorption and fluorescence studies of the lithium 2S-3D transition," AIP Conf. Proc. **160**, 404-417 (1987).

[165] V. K. Saini, A. Kak, S .K. Dixit, "Selective photoionization of lithium isotopes in a hollow cathode lamp: a feasibility study for a laser ion source and detector," Appl. Opt. **57**, 6808-6816 (2018).

[166] C. E. Moore, Atomic energy levels NSRDS-NBS vol. 1 Washington, DC: U; 1971.

[167] L. W. He, C. E Burkhardt, M. Ciocca, J. J. Leventhal, S. T. Manson "Absolute cross sections for the photoionization of the 6s6p ^{1}P excited state of barium," Phy. Rev. Lett. **67**, 2131-2134 (1991).

[168] P. Zhang, E. Bodo, A. Dalgarno, "Near resonance charge exchange in ion−atom collisions of lithium isotopes," J. Phys. Chem. A **113**, 15085-15091 (2009).

[169] V. S. Letokhov, C. B. Moore. "Laser isotope separation (review)," Sov. J. Quant. Electron. **6**, 129-150 (1976).

[170] D. C. Lorents, G. Black, "Charge transfer between Li ions and Li atoms in the 14-1000 eV energy region," Phys. Rev. **137**, A1049-A1053 (1965).

[171] V. K. Saini, P. Kumar, K. K. Sarangpani, S. K. Dixit, S. V. Nakhe, "Development of a see-through hollow cathode discharge lamp for (Li/Ne) optogalvanic studies," Rev. Sc. Instrum. **88**, 093101 (1-9) (2017).

[172] T. N. Chang, R. T. Poe, "Calculation of multiphoton ionization processes," J. Phys. B: Atom. Mol. Phys. **9**, L311-L315 (1976).

[173] K. J. R. Rosman, P. D. P. Taylor, "Atomic weights of the elements 1997 (Technical report)," Pure Appl. Chem. **71**, 1593-1607 (1999).

[174] A. A. Sysoev, V. B. Artaev, V. V. Kashcheev, "Errors in isotope ratios measured on a laser mass spectrometer with photographic recording," J. Anal. Chem. **55**, 9-13 (2000).

[175] M. B. Rabinawitz, G. W. Wetherill, 'Identifying sources of lead contamination by stable isotope techniques," Environ. Sci. Tech-nol. **6**, 705-709 (1972).

[176] J. A. Goleb, "The determination of uranium isotopes by atomic absorption spectrophotometry," Anal. Chim. Acta **34**, 135-145 (1966).

[177] V. Middelboe, "On accuracy and sensitivity in optical 15 N-analysis," Appl. Spectroscopy **24**, 608-609 (1970).

[178] F. E. Lichte, R. K. Skogerboe, "Emission spectrometric determination of isotopic concentrations of lithium," Appl. Spectroscopy **28**, 354-355 (1974).

[179] A. K. Pulhani, G. P. Gupta, B. M. Suri, "Isotopic selectivity calculations for multi-step photoionization of calcium atoms using narrow-band lasers," J. Phys. B: At. Mol. Opt. Phys. **35**, 3677-3688 (2002).

[180] X. Zheng, X. Zhou, Z. Cheng, D. Jia, Z. Qu, G. Yao, X. Zhang, Z. Cui, "Photoionization cross section measurements of the excited states of cobalt in the near-threshold region," AIP Advances **4**, 107120 (1-10) (2014).

[181] W. Mende, K. Bartschat, M. Kock, "Near-threshold photoionization from the Sr I (5s5p) $^1P^o_1$ state," J. Phys. B: At. Mol. Opt. Phys. **28**, 2385-2393 (1995).

[182] K. D. Kok, Nuclear Engineering Handbook (Mechanical Engineering Series, CRC Press, Taylor & Francis, 6000 Broken Sound Parkway NW, Suite 300, 2010).

[183] Y. Kanzaki, N. Suzuki, R. Chitrakar, T. Ohsaka, M. Abe, "^{7}Li/^{6}Li isotope separation on inorganic ion-exchangers and NMR study of the H+/Li+ ion-exchange reaction," J. Phys. Chem. B **106**, 988-995 (2002).

[184] B. A. Bushaw, W. Nortershauser, K. Wendt, "Lineshapes and optical selectivity in high-resolution double-resonance ionization mass spectrometry," Spectrochimica Acta B **54**, 321-332 (1999).

[185] G. S. Hurst, M. G. Payne, Principles and applications of resonance ionization spectroscopy (Adam Hilger, Bristol, 1988).

[186] V. S. Letokhov, "Laser Photoionization Spectroscopy (Academic Press, New York, 1987).

[187] V. K. Saini, S. Talwar, V. V. V. Subrahmanyam, S. K. Dixit, "Laser assisted isotope separation of lithium by two-step photoionization using time of flight mass-spectrometer," Optics & Laser Tech. **111**, 754-761 (2019).

[188] R. K. Mishra, D. V. S. Raju, S. V. Nakhe, "A novel and robust circuit for jitter reduction in copper vapour laser system," Rev. Sci. Instr. **86**, 116107 (1-3) (2015).

[189] M. Broyer, J. Chevaleyre, G. Delacrétaz, L. Wöste, "CVL-pumped dye laser for spectroscopic application," Appl. Phys. B **35**, 31-36 (1984).

[190] R. Khare, S. R. Daulatabad, H. S. Vora, R. Bhatnagar, "A tunable three-wavelength copper-vapor laser pumped dye laser with collinear output," Opt. Comm. **114**, 275-279 (1995).

[191] K. J. Ross, B. Sonntag, "High temperature metal atom beam sources," Rev. Sci. Instr. **66**, 4409-4433 (1995).

[192] C. R. Locke, T. Kobayashi, T. Fujiwara, K. Midorikawa, "Selective photoionization of palladium isotopes using a two-step excitation scheme," Appl. Phys. B **123**, 123-240 (2017).

[193] V. S. Letokhov, V. I. Mishin, "Highly selective multistep ionization of atoms by laser radiation," Opt. Comm. **29**, 168-171 (1979).

[194] N. V. Karlov, Y. B. Konev, A. M. Prokhorov, "Selectivity of two-stage photoionization of atoms," Sov. J. Quant. Elect. **5**, 1336-1338 (1975).

[195] J. Walls, R. Ashby, J. J. Clarke, B. Lu, W. A. Van Wijngaarden, 'Measurement of isotope shifts, fine and hyperfine structure splitting of the lithium D lines," Eur. Phys. J. D **22**, 159-162 (2003).

[196] N. V. Karlov, A. M. Prokhorov, "Laser isotope separation," Usp. Fiz. Nauk **118**, 583-609 (1976).

[197] M. G. Payne, L. Deng, N. Thonnard, "Applications of resonance ionization mass spectrometry," Rev. Sci. Instrum. **65**, 2433-2459 (1994).

[198] J. Heldt, G. Leuchs, "Lifetime measurements of lithium D states," Z. Phys. A **291**, 11-13 (1979).

Summary

Lithium (Li) has two stable isotopes, namely ^{6}Li and ^{7}Li with the natural abundances of about 7.5% and 92.5%, respectively. Both the Li isotopes are important for nuclear industry. ^{6}Li is used in breeding of tritium for D-T reaction in fusion reactors, development of thermonuclear weapons and compact solid state neutron detector. The effectiveness of all these processes greatly improves with the enriched ^{6}Li beyond its natural abundance of 7.5%. Highly enriched ^{7}Li is used in pressurized water nuclear reactors as a pH-stabilizer of coolant and in molten salt (lithium fluoride) nuclear reactors. Most often, the chemical separation methods such as ion exchange, chemical exchange and electrolysis have been used for Li isotopes. These methods offer good yield but are limited by low isotope separation factor per stage, resulting in separation with poor isotopic purity. Laser based isotope separation (LIS) is a very popular and attractive technique in terms of attaining high isotope selectivity and purity. In the present thesis, a comprehensive study on the isotope-selective photoionization of Li leading to separation/enrichment of its isotopes by laser method is presented. Overall, the thesis research work consists of development, characterization and utilization of low (~ Hz) and high (~ kHz) repetition rate tunable dye lasers, hollow cathode (HC) discharge lamp, thermionic diode ion-detector and time-of-flight mass-spectrometer (TOFMS) for studying different photoionization pathways of Li isotopes, measurement of photo-ionization cross-section & ionization yield and enhancement in abundance of respective Li isotopes. The studied photoionization pathways include multi-step, multi-color (multi-wavelengths) schemes applied in different atomic vapor source cum ion-detector setups. An enhancement in isotopic abundance up to 92% for ^{6}Li and ~ 100% for ^{7}Li have been demonstrated using TOFMS photoionization setup.

As part of the present research work, the HC lamp and thermionic diode ion-detector with high gain and sensitivity are developed. The developed Li HC lamp has been used for dye laser wavelength calibration, investigation of suitable Li energy levels, measurement of

fine/hyperfine structure & isotopic-shift and to carry out multi-step selective photoionization studies. Both the HC dark space and negative glow region have been utilized for Li OG studies. The developed thermionic diode is used to measure the photoionization cross-section of Li in excited states. The linear TOFMS is used for isotope-selective photoionization studies to measure the Li natural isotope ratio, photoionization cross-section and enrichment of its isotopes. The laser assisted Li isotope separation is carried out by isotope-selective two / three-step photoionization schemes using TOFMS. Two-step $[{}^2S_{1/2} \xrightarrow{\sim 671\ \text{nm}} {}^2P_{1/2,\,3/2} \xrightarrow{\sim 337\ \text{nm}} {}^1S_0\,(\text{Li}^+)]$ scheme offered large (~ 10 folds) enhancement in ^{6}Li natural abundance with isotope selectivity of ~ 32. Three-step $[{}^2S_{1/2} \xrightarrow{\sim 671\ \text{nm}} {}^2P_{1/2,3/2} \xrightarrow{\sim 610\ \text{nm}} {}^2D_{3/2,5/2} \xrightarrow{\sim 578\ \text{nm}} {}^1S_0\,(\text{Li}^+)]$ scheme has demonstrated ^{6}Li enhancement upto 92% with selectivity of ~ 164. The present research work thus vastly extends the limited studies reported earlier on Li photoionization.

Salient points of the thesis

- *Lithium HC lamp, thermionic diode, dye lasers and associated instrumentation & data acquisition system are developed as part of the present research work.*
- *Dye lasers wavelength calibration, Li atom energy levels, fine/hyperfine structure, isotopic shift are studied in HC lamp.*
- *Two-step and three-step isotope selective Li photo-ionization are studied.*
- *Photoionization cross-sections are measured for different Li excited states.*
- *Isotopic selectivity and purity are studied in two and three step schemes using TOFMS.*
- *High enrichment of ^{6}Li (7.5% → 92%) and ^{7}Li (92.5% → ~ 100%) are achieved on TOFMS detector by optimized photoionization scheme.*
- *As an outcome of present research work, a facility is developed to study the laser based isotope separation processes of different useful elements.*
- *The research emanating from thesis work is published as a number of publications in reputed journals.*

LIST OF FIGURES

LIST OF TABLES

Highlights of the thesis

- Lithium HC lamp, thermionic diode, dye lasers and associated instrumentation & data acquisition system are developed as part of the present research work.

- Dye lasers wavelength calibration, Li atom energy levels, fine/hyperfine structure, isotopic shift are studied in HC lamp.

- Two-step and three-step isotope selective Li photo-ionization are studied.

- Photoionization cross-sections are measured for different Li excited states.

- Isotopic selectivity and purity are studied in two and three step schemes using TOFMS.

- High enrichment of ^{6}Li (7.5% → 92%) and ^{7}Li (92.5% → ~ 100%) are achieved on TOFMS detector by optimized photoionization scheme.

- As an outcome of present research work, a facility is developed to study the laser based isotope separation processes of different useful elements.

- The research emanating from thesis work is published as a number of publications in reputed journals.